Université de Strasbourg

UNIVERSITÉ DE STRASBOURG

École doctorale Sciences de la vie et de la santé | ED 414 Université de Strasbourg

*Ecole doctorale 414 des sciences de la vie et de la santé*

**Transcription co-activators • UMR 7104 • IGBMC**

# DISSERTATION presented by :


**Victor HANSS**


defended on : **28 janvier 2025**

to obtain the grade of **:**
**Strasbourg University Doctor**

Specialty : Structurale Biology

# Sample preparation and method development towards new nanometric probes for cryo electron tomography

**DISSERTATION supervisor :**

| | |
|---|---|
| **SCHULTZ Patrick** | Doctor, Université de Strasbourg |
| **ELTSOV Mikhail** | Professor, Université de Strasbourg |

**RAPPORTEURS :**

| | |
|---|---|
| **BERTIN Aurélie** | Doctor, Sorbonne Université |
| **ZUBER Benoît** | Professor, University of Bern |

**OTHER MEMBERS OF THE JURY :**

| | |
|---|---|
| **LEFORESTIER Amélie** | Doctor, Université Paris-Saclay |
| **FAESSLER Florian** | Professor, Université de Strasbourg |

# Avertissement au lecteur / Warning to the reader

Ce document est le fruit d'un long travail approuvé par le jury de soutenance et mis à disposition des membres de la communauté universitaire. Il est soumis à la propriété intellectuelle de l'auteur. Cela implique une obligation de citation et de référencement lors de l'utilisation de ce document. D'autre part, toute contrefaçon, plagiat, reproduction ou représentation illicite encourt une poursuite pénale.
This document is the result of a long process approved by the jury and made available to members of the university community. It is subject to the intellectual property rights of its author. This implies an obligation to quote and reference when using this document. Furthermore, any infringement, plagiarism, unlawful reproduction or representation will be prosecuted.

**Code de la Propriété Intellectuelle**

**Article L122-4** :

Toute représentation ou reproduction intégrale ou partielle faite sans le consentement de l'auteur ou de ses ayants droit ou ayants cause est illicite. Il en est de même pour la traduction, l'adaptation ou la transformation, l'arrangement ou la reproduction par un art ou un procédé quelconque.
Any representation or reproduction in whole or in part without the consent of the author or his successors in title or assigns is unlawful. The same applies to translation, adaptation or transformation, arrangement or reproduction by any art or process whatsoever.

**Articles L335-1 à L335-9**. : Dispositions pénales / Penal provisions.

# Licence attribuée par l'auteur / Licence attributed by the author

# Acknowledgement

**Eltsov Team**
Mikhail Eltsov, Nathalie Troffer-Charlier, Fadwa Fatmaoui, Gurudatt Patra, Mohammad Harastani

**Schultz Team**
Maximilien Werderer (impression 3D), Alexandre Frechard (vision positive de la fin de thèse), Danièle Spehner, Gabor Papai, Corinne Crucifix, Patrick Schultz

**Klaholz Team**
Léo Frechin, Charles Barchet, Samuel Holvec, Bruno Klaholz

**EM platform**
Alexandre Durand, Nils Marchal, Sasha Ballet, Marie-Christine Poterszman, Catherine Birck

**Poterszman Team**
Arnaud Poterszman, Charlotte Schnitzler, Jules Loup-Forest

**Ex Zuber-Weiss team and Torbeev team in ESBS**
Guy Zuber, Nadja Groysbeck, Vladimir Torbeev, Dominique Desplancq, Manuela Chiper, Mohammed Banni, Bruno Chatton, Etienne Weiss

**Micro opto-mécanique platform**
Didier Hentsch, Serge Taubert, Victor Priolo de Metz

**Institute's electronics and electromechanical staff**
And in particular Régis Vonscheidt, Alain Litt, Jean-Philippe Erb, Luc Weil

**IT Team**
And in particular Jeanne Lavaud, Guillaume Seith, Matthieu Distelzwey, J.C. Haessig,

**Microscopie électronique cellulaire**
Nadia Messaddeq, Chadia Nahy

**CSI jury members**
Fabien Alpy, Jacky Goetz accepted to go through all my four thesis follow up meetings and had to cope with this administrative work. I thank them for their advice and comments.

**Individually**
Anna Steyer, Véronique Mallouh, Mariel Donzeau, Bruno Kieffer, were the former gave me priceless advice on FIB-SEM acquisition and sample preparation, the second introduced me to segmentation and shared nice moment of exchange, the third gave me positive energy by induction and stimulated creativity with interesting discussions and developments and the last trusted my skills and competences in handling python practicals for students which resulted in well needed self satisfaction.

**Friends**
Fadwa, Ana, Franck, Christelle, Abir

**Famille**
Pere, mere, frere, soeur, Masha, Youki, Sashok, la famille Dinte

# Abbreviations

| | |
|---|---|
| **Au** | Gold |
| **AuNp** | Gold Nanoparticles |
| **BSE** | Back Scattered Electrons |
| **ChiP** | Chromatin Immuno Purification |
| **CEMOVIS** | Cryo Electron Microscopy Of Vitreous Sections |
| **Cryo-EM** | Cryo Electron Microscopy |
| **Cryo-ET** | Cryo Electron Tomography |
| **CTD** | C-Terminal Domain |
| **EC** | Elongation Complex |
| **EM** | Electron Microscopy |
| **ET** | Electron Tomography |
| **FAB** | Fragment Antigen-Binding region |
| **FIB** | Focused Ion Beam |
| **GIS** | Gaz Injection System |
| **HPF** | High Pressure Freezing |
| **ITC** | Initial Transcribing Complex |
| **MD** | Molecular Dynamics |
| **MED-SEM** | Multi-Energy Deconvolution - Scanning Electron Microscopy |
| **mRNA** | messenger RNA |
| **NA** | Numerical Aperture |
| **PALM** | Photoactivated Localization Microscopy |
| **PIC** | Pre-Initiation Complex |
| **Pol II** | RNA Polymerase II |
| **rDNA** | ribosomal DNA |
| **SBF-SEM** | Serial Block Face - Scanning Electron Microscopy |
| **SE** | Secondary Electrons |
| **SEM** | Scanning Electron Microscopy |
| **ssET** | serial sectioning Electron Tomography |
| **ssTEM** | serial sectioning Transmission Electron Microscopy |
| **STED** | Stimulated Emission Depletion |
| **TADs** | Topologically Associated Domains |
| **TEM** | Transmission Electron Microscopy |

# Table of Content

# Résumé de thèse

Université de Strasbourg E.D. 414

**Développement de sondes nanométriques pour détecter des macromolécules en microscopie cryo électronique par tomographie.**


HANSS Victor


**Discipline** Sciences de la vie et de la santé

**Spécialité** Biophysique et biologie structurale

**Unité de recherche**

Transcription co-activators • UMR 7104 • IGBMC

**Directeur de thèse**

Dr. SCHULTZ Patrick [1] ● Director

**Co-directeur de thèse**

ELTSOV Mikhail [1] ● Professor

***Rapporteurs***

Dr. Aurélie Bertin [2]

Pr. Benoît Zuber [3]

***Examinateurs***

Dr. Amélie Leforestier [4]

Pr. Florian Faessler [1]


1. Department of Integrated Structural Biology, Institut de Génétique et de Biologie Moléculaire et Cellulaire (IGBMC), INSERM U964, CNRS UMR 7104, University of Strasbourg, Illkirch, France
2. Laboratoire Physico Chimie Curie, Institut Curie, PSL Research University, CNRS UMR168, Sorbonne Université, 75005 Paris, France
3. Institute of Anatomy, Medical Faculty, University of Bern, Bern Switzerland
4. Université Paris-Saclay, CNRS, Laboratoire de Physique des Solides (LPS), 91405, Orsay, France

# Introduction

La cellule eucaryote est un système compact et hétérogène où des éléments compartimentées comme les mitochondries, le noyau, l'appareil de Golgi et différents organites coexistent au sein de milieux hydratés denses en biomolécules : le cytosol et le nucléosol. L'imagerie à haute résolution par cryo-tomographie électronique (cryo-ET) a permis de révéler des aspects structurels macromoléculaires dans leur contexte cellulaire *in situ* qui ne pouvait être atteint par l'analyse de molécules isolées *in vitro*. Cependant, dans cet environnement cellulaire encombré, l'identification de biomolécules est une tâche difficile puisqu'elle ne se base que sur la reconnaissance de forme. Le marquage fluorescent des protéines *in vivo* permet de suivre leur distribution spatiale et temporelle, ainsi que leur dynamique. Néanmoins, les limitations de résolution spatiale et le manque d'informations contextuelles des images de microscopie optique rendent difficile son utilisation dans le repérage de molécules individuelles pour l'imagerie à haute résolution. Pour y parvenir, les macromolécules sont ciblées *in vivo* avec des sondes nanométriques directement reconnaissables en cryo-ET. Mon projet de thèse porte sur le développement de cette approche en utilisant des nanoparticules d'or biocompatible pour la localisation de molécules d'intérêt dans le noyau de cellule humaine. Le noyau a été sélectionné en raison de son organisation complexe en condensats dépourvus de frontières structurelles définies. Cet environnement rend particulièrement difficile la localisation des molécules.

Nous avons choisi l'ARN polymérase II (pol II) comme cible, en tentant de localiser cette protéine dans le noyau cellulaire. La pol II est chargée de transcrire l'information stockée sous forme d'ADN en ARN messager chez les organismes eucaryotes. Cette protéine est essentielle à la survie de la cellule mais l'organisation spatiale des unités de transcription ainsi que l'interaction avec des protéines de maturation de l'ARN messager restent mal connues. L'immunomarquage de sections cellulaires incluses en résine a révélé l'existence d'agrégats clairsemés de pol II actives, appelées usines de transcriptions ou condensats. Ces observations ont récemment été corroborées par la microscopie à fluorescence à super-résolution. Cependant, aucune image à ce jour n'a permis de visualiser ou de localiser directement la pol II dont la structure atomique à pourtant été déterminée par cristallographie des rayons X et par cryo microscopie électronique de molécules isolées. La détermination de l'organisation tridimensionnelle des condensats de Pol II et leur interaction avec la chromatine et les machineries d'épissage fournirait des informations essentielles sur la transcription eucaryote. Pol II est une protéine globulaire de taille moyenne et rare en dehors des sites de transcription. Ces caractéristiques rendent cette protéine difficile à observer en cryo-ET à haute résolution. Le développement de procédures de marquage de la Pol II avec des sondes nanométriques permettrait de surmonter cette limitation et d'obtenir sa localisation, fournissant ainsi les premières images de l'organisation des sites de transcription *in situ*. Pour atteindre ces objectifs, j'ai abordé les défis techniques suivants :

**Marquage *in vivo* avec des sondes conjugué à des particules d'or :** Le marquage de protéines endogènes à l'aide d'anticorps couplés à des éléments métalliques de numéro atomique élevé tel que l'or, à été utilisé de manière fiable en microscopie électronique conventionnelle pour localiser des cibles moléculaires dans des échantillons inclus en résine. Pour appliquer ces protocoles de marquage, le matériel biologique est d'abord fixé chimiquement à l'aide d'aldéhydes, contrasté avec des éléments lourds, inclus en résine, découpé en fines sections avant d'être placé sur une grille de microscopie électronique. Toutes ces étapes entraînent des artefacts de structure qui sont incompatibles avec la visualisation directe des macromolécules en cryo-EM dans un état quasi-natif. De plus, les échantillons cryo-immobilisés doivent être maintenus dans des conditions cryogéniques où aucune réaction d'affinité et de marquage n'est possible. Le premier objectif de ma thèse était de résoudre ce problème en développant un protocole de marquage *in vivo* approprié permettant à la sonde dense en électrons d'interagir avec sa cible en amont de la cryo-immobilisation, dans la cellule vivante.

**Vitrification complète de la cellule.** La glace amorphe est constituée d'eau en phase solide dépourvue de cristaux de glace (souvent référé comme vitreux). Les structures biologiques congelées dans un liquide cellulaire amorphe sont préservées sans dommage, immobilisées dans un instant de leur évolution. Le refroidissement doit être suffisamment rapide pour empêcher la formation de cristaux de glace qui altèrent les structures intra- et intermoléculaires. De plus, les cristaux de glaces induisent des artéfacts d'imagerie en interférant avec le faisceau d'électrons ce qui dégrade fortement la qualité des images enregistrées et les étapes de traitement d'image ultérieures. Les méthodes de congélation par immersion, utilisées en routine pour la cryo-ET des régions cytoplasmiques, ne sont pas entièrement efficaces pour le noyau cellulaire qui est généralement la partie la plus épaisse des cellules de mammifères. J'ai relevé ces défis en essayant plusieurs méthodes et systèmes de congélation jusqu'à obtenir de la glace de qualité suffisante pour imager les structures cellulaires.

**Amincissement des cellules pour la collecte de données en cryo-ET.** Les cellules vitrifiées sont trop épaisses pour l'imagerie par microscopie électronique ; elles sont opaques aux électrons. La fourchette d'épaisseur cellulaire utile est comprise entre 70 et 200 nm et résulte d'un compromis entre la conservation d'une haute résolution spatiale en cryoET et une épaisseur suffisante pour voir l'ensemble de la structure d'intérêt. Deux méthodes existent pour obtenir des segments de cellule vitrifiée. La méthode de microscopie cryo-électronique de sections vitreuses ou CEMOVIS a été développée en premier. Des échantillons volumineux congelés à haute pression (HPF) sur des portes objet en métal sont découpés en rubans de sections minces (50-100 nm) à l'aide d'un couteau en diamant. Une seconde stratégie d'affinement des échantillons utilise la gravure par faisceau d'ion. Le cryo-FIB-SEM est un instrument qui combine deux faisceaux : un faisceau d'ion gallium (FIB pour focussed ion beam) et un faisceau d'électron (SEM pour Scanning Electron Microscope. Le FIB concentre les ions gallium en un faisceau très énergique qui permet d'éroder la matière et enlève le matériel cellulaire congelé jusqu'à affiner une région centrale de la cellule. Les lamelles créées sont d'une épaisseur inférieure à 200 nm pour être exploitables par l'imagerie en cryo-ET. J'ai exploré les deux techniques d'amincissement et investi beaucoup de temps dans le déploiement du cryo-FIB-SEM au sein de l'institut : j'ai mené un atelier international sur la tomographie par microscopie électronique de cryo-lamelles pendant deux années consécutives.

Au cours de mes quatre années de thèse, j'ai relevé ces défis et développé un ensemble d'étapes d'optimisation et de procédures pour la préparation de sondes d'affinité, leur délivrance *in vivo*, la vitrification complète des échantillons, leur amincissement pour l'imagerie cryo-ET et le traitement des données. Toutes ces étapes ont été intégrées dans le workflow suivant.

**Workflow.** L'or est un élément neutre et dense aux électrons. Les cellules vivantes s'accommodent de la présence de cet élément *in vivo* après transfection sans affecter les taux de mortalité cellulaire. Le protocole de synthèse d'or que j'ai utilisé m'a permis d'obtenir des nanoparticules en phase aqueuse avec un diamètre homogène entre 2 et 3 nm. Le revêtement réactif de ces nanoparticules s'échange efficacement pour former une liaison de coordination thiol-or, où le système protéine-thiol•or est alors appelé un conjugué. Plusieurs systèmes d'affinité peuvent être choisis pour former ce conjugué (mAb, Fab, Nanobody, Spycatcher). Le conjugué est introduit dans des cellules vivantes via électroporation. L'efficacité de transfection du conjugué et du marquage après électroporation sont validées par immunofluorescence, qui marque la protéine d'affinité et par amplification à l'argent, qui révèle la position des nanoparticules d'or. Si ces deux marquages co-localisent l'échantillon est préparé pour la cryo-ET. Les cellules électroporées sont alors ensemencées sur des grilles de microscopie électronique, plongées dans l'éthane liquide, et amincies par cryo-FIB-SEM ou culottées, congelées à haute pression, et traitées par CEMOVIS. Les échantillons amincis sont imagés dans un microscope électronique cryogénique Titan Krios à haute résolution, où une série de tilt est enregistrée puis reconstruite en volumes 3D par rétroprojection pondérée. Les volumes peuvent alors être manipulés par des algorithmes utilisant des architectures de réseaux de neurones pour améliorer leur rapport signal-bruit. La réduction de bruit améliore l'efficacité de sélection de particules par des logiciels dédiés à la reconstruction de structures moléculaires.

## Résultats

**Optimisation de la transfection et de la visualisations des sondes à l'aide du conjugué Au•NLS.** J'ai synthétisé et purifié des nanoparticules d'or de 2 à 3 nm et utilisé un peptide de signal de localisation nucléaire (NLS) avec un groupe thiol disponible pour construire un conjugué Au•NLS facile à produire de manière reproductible en grande quantité. Une fois électroporé, le NLS est reconnu par la machinerie d'import nucléaire de la cellule qui le transporte activement dans le noyau. Cette sonde m'a permis d'optimiser efficacement l'étape d'électroporation en fonction du tampon d'électroporation, du voltage, du nombre de pulsations et du nombre de cellules pour des applications en cryo-ET. La sonde Au•NLS peut être électroporé en grande quantité sans impacter le taux de vitalité cellulaire : les noyaux des cellules apparaissent alors noir après amplification à l'argent (Figure 1a). Un signal négligeable est présent dans le cytoplasme ce qui indique que le conjugué est suffisamment pur et robuste. (Figure 1a). Les cryo-sections obtenues à partir de ces cellules ont fourni la preuve de concept pour la visualisation de l'or dans des images de projection 2D avec une localisation préférentielle dans le noyau **[1]**. Malheureusement, la faible adhésion des cryo-sections aux grilles de microscopie m'a empêché de les imager par tomographie. Pour faire face à cette limitation, j'ai usiné des lamelles, par cryo-FIB-SEM, de ces cellules électroporé avec la sonde Au•NLS. J'ai imagé ces lamelles par tomographie où j'ai pu visualiser les particules d'or (Figure 1b, c, d). J'ai constaté que le débruitage basé sur l'apprentissage profond facilite la visualisation du context cellulaire (Figure 1c), tandis que le filtrage basé sur l'écart-type est optimal pour localiser des particules d'or au sein d'un volume (Figure 1d).

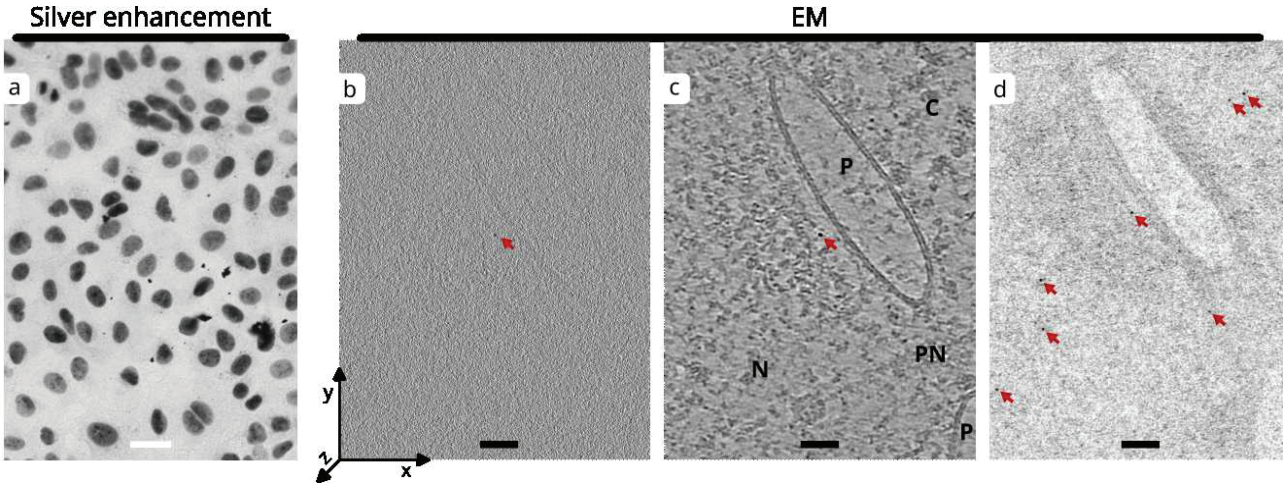


**Figure 1. a** : Image en champ clair de cellules U20S électroporées avec la sonde Au•NLS, fixées et révélées par amplification à l'argent. **b** : Tranche centrale brute, d'un tomogramme dévoilant l'espace périphérique d'un noyau de cellule U2OS électroporée avec la sonde Au•NLS. **c** : La même tranche après débruitage avec cryoCARE. **d** : Une projection du tomogramme dont est issue la coupe, le long de l'axe Z, montrant l'écart type de chaque rangée Z de pixels. **PN** : pore nucléaire, **P** : paroie nucléaire, **C** : cytoplasme, **N** : noyau, **flèches rouges** : conjugués AU•NLS. La barre d'échelle blanche représente 40 µm et les barres d'échelle noir représentent 100 nm de distance.

**Sondes Anti-Pol II.** La présence d'un agent réducteur en quantités contrôlées avec un mAb favorise la protonation partielle des ponts disulfure en thiol, permettant à la nanoparticule d'or d'interagir entre les chaîne de l'anticorps et de former un conjugué mAb•Au. La production et la purification des mAbs sont coûteuses et se traduisent souvent par un rendement et une pureté limités. Par conséquent, nous avons préféré utiliser des fragments de liaison à l'antigène (Fab), qui sont produits de manière recombinante et peuvent être purifiés avec un rendement et une pureté plus élevés. Les Fab sont dérivés des mAb et se composent d'une demi-chaîne lourde interagissant avec une chaîne légère via des ponts disulfures. J'ai réussi à conjuguer le Fab f7G5 dérivé du mAb 7G5, ciblant le domaine C terminale de la Pol II, en adaptant la stratégie de réduction partielle appliquée aux mAb. Après électroporation, le f7G5 devrait interagir avec la Pol II fraîchement traduite dans le cytoplasme. L'importation active de la Pol II transporterait alors le Fab conjugué à l'or dans le noyau. Après

électroporation, le f7G5 se localise principalement dans le noyau. Cependant, la réduction partielle du Fab affecte son intégrité structurelle et, potentiellement, la quantité de conjugués actifs purifiés. Nous avons constaté que l'ajout d'un groupe -SH externe à l'une des chaînes du Fab fournit un point d'interaction supplémentaire avec la nanoparticule d'or et limite l'impact structurel de la conjugaison sur le Fab. Cette solution pourrait être appliquée à l'avenir à toute protéine ne possédant pas de groupe -SH disponible pour interagir avec la nanoparticule d'or.

**Développement de sondes polyvalentes :** Les nanobodies sont uniquement constitués de la partie variable des chaînes lourdes des anticorps, ce qui les rend plus faciles à produire de manière recombinante que les Fab. J'ai choisi un système de conjugaison existant et fonctionnel, le système d'assemblage E3-K3, qui est utilisé comme lien dans la conjugaison de l'or à un nanobody ciblant la GFP (nGFP) dans une construction Au•K3-E3nGFP. E3-K3 éloigne l'or du paratope afin de réduire l'impact potentiel de son encombrement sur la fonction du nGFP. J'ai électroporé une lignée cellulaire U2OS modifiée exprimant la nucléoporine de fusion NUP96-GFP avec Au•K3-E3nGFP. Mes données préliminaires provenant des contrôles en immunofluorescence et amplification à l'argent montrent qu'une partie de la sonde se localise en périphérie du noyau (Figure 2a, d) où l'autre partie a été encapsulée dans des endosomes. Cette sonde a été développée à la fin de ma thèse, et je n'ai pas eu le temps de la valider en cryo-ET. Nous montrons que ce conjugué n'est pas cytotoxique et qu'il pourrait être utilisé sur n'importe quelle lignée cellulaire modifiée exprimant la GFP, pour des approches de fluorescence corrélative en cryo-ET.

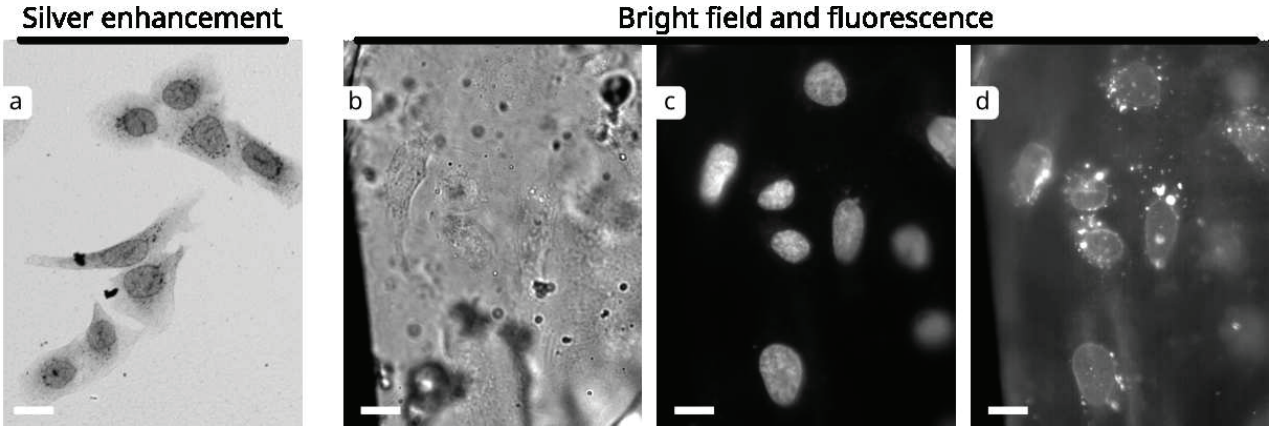


**Figure 2. a** : Microscopie en champ clair de cellules U20S électroporées avec la sonde anti-GFP, fixées et révélées par amplification à l'argent, montrant un marquage à la périphérie du noyau. **b** : Cryo-microscopie à champ clair de cellules U20S électroporées avec la sonde anti GFP, incubées avec du colorant Hoechst 33342 et cryo immobilisée. **c** : Cryo-microscopie à fluorescence avec un filtre DAPI du même échantillon montrant l'ADN. **d** : Cryo-microscopie à fluorescence avec un filtre GFP du même échantillon montrant un marquage à la périphérie du noyau. Les barres d'échelle représentent 20 µm.

## Conclusion

Dans mon projet de thèse, j'ai développé et optimisé des protocoles pour créer des sondes d'or nanométrique pour le marquage *in vivo* et l'imagerie par Cryo-ET. Cela m'a permis d'obtenir des images *in situ* de cellules humaines à partir de cryo-sections et de cryo-lamelles. À condition d'obtenir une glace vitreuse de haute qualité, mes résultats ont confirmé la visualisation et localisation spécifique par cryo-ET de particules d'or entre 2 et 3 nm dans un environnement nucléaire encombré. Mes résultats ont démontré que ce protocole est fonctionnel pour le marquage *in situ* de protéines en cryo-tomographie électronique. Toutes les étapes du workflow ne sont pas au même stade de développement. La purification du conjugué de l'excès d'or après la synthèse reste une étape limitante. Cependant, ce workflow s'est avéré efficace pour la sonde Au•NLS. Nous avons optimisé la sonde pour le marquage de la Pol II en ajoutant un groupe -SH externe à l'une des chaînes du Fab dirigé contre cette protéine, bien que la Cryo-ET soit en cours de développement. Nos résultats préliminaires avec le conjugué basé sur le nanobody Au•K3-E3nGFP indiquent que cette construction peut être la direction préférentielle à prendre pour de futurs développements vers une sonde polyvalente adaptable à une large gamme de cibles marqué à la GFP *in vivo* pour de futurs développements d'imagerie multimodale.

## Publications


[1] N. Groysbeck *et al.*, « Bioactivated and PEG-Protected Circa 2 nm Gold Nanoparticles for in Cell Labeling and Cryo-Electron Microscopy », *Small Methods*, vol. 7, nº 6, p. 2300098, 2023, doi: 10.1002/smtd.202300098.

[2] N. Groysbeck *et al.*, « 1.4 nm gold nanoparticle-antibody conjugates for *in situ* gold immunolabeling after transduction into living human cells », *Comptes Rendus Chim.*, vol. 26, nº S3, p. 1-14, 2023, doi: 10.5802/crchim.251.

# Introduction

## Exploring the invisible

Considering a human in his mid twenties of normal sight with a maximum accommodation power of 8 diopters and a minimum visual angle of 1 minute of arc, the smallest object this person could resolve would be about 35 μm diameter or half the diameter of a thin human scalp hair (Buffoli et al., 2014; Garner and Yap, 1997; Kniestedt and Stamper, 2003). Below this dimension, size limits all objects that are merged beyond recognition. Most unicellular microorganisms are way smaller than 35 um and despite that, assembly of micro-organisms can be visualized as contaminated turbid liquids, moisture, or other biofilms. However, human vision is not able to identify that they are made of millions of copies of cells that share common structural features and function using the same macromolecular building blocks. These elements remain elusive without the help of a magnifying device that resolves smaller dimensions. A mammalian fibroblast cell, for instance, can extend itself over a hundred micrometers by using long protrusions that are only below a micrometer in thickness. Two cells of this size placed side by side would be indistinguishable from each other, appearing instead as a tiny dot or a hair-thin line if cells were opaque to visible light. The smallest unit of life would be ignored without the development of magnifying apparatus: the vast field of microscopy finds its essence here, in exploring environments beyond distances that can be resolved by the naked human eye.

The word “microscope” was first used by Giovanni Faber in 1625 and referred to a two lens device created by Galileo in 1609: an objective and an ocular lens magnified the specimen image (Wollman et al., 2015). Although the term cells was inherited from 1665 Robert Hooke’s observation of cork’s pores through the first design of a 3 lens compound microscope, this word was not describing the nowadays called living cells (Masters, 2020). Despite having a design close to the actual tabletop microscope, the lenses used had too many inbuilt aberrations to get a proper sharp and focused image of an object as small as a cell.

The dynamic life diversity from the microworld was first unveiled by Antoni van Leeuwenhoek using a simpler, but more powerful self-made apparatus consisting of a refined single ball lens. The single lens design generated less optical aberrations and allowed him in 1665 to observe moving organisms that he named little animals or “animalcules” (Porter, 1976; Van Leeuwenhoek, 1677). His animalcules observations are the first descriptions of bacteria and protozoa. Although his magnifying apparatus was far from the resolving power of actual laboratory light microscopes, it could magnify up to 200 times, resolving objects down to 1 um. An example of Van Leeuwenhoek instrument is exhibited in the Utrecht University Museum and has a magnification power of 275 times.

Nowadays educational tools similar to van Leeuwenhoek's overall design reaches the limit resolving power of visible light with a magnification power up to 2000 times, using only a single tiny ball lens (Cybulski et al., 2014). Nevertheless, multi-lens microscopes continue their development towards more versatile and convenient devices. They overcame single ball lens microscopes designs by using better lenses with less aberration. The first aberration-corrected lens dealt with chromatic aberration and was described in 1830: the achromatic lens (Lister, 1830). From 1873 when Abbe released his theory of image formation and onward, microscopes production shifted from empirical variable quality design towards better systems with improved glass lens quality, less optical aberration from optical assemblies, better light sources shifting from the sun / candle light to stable electric light sources. This advancement marked a pivotal moment in microscopy, laying the foundation for modern illumination techniques such as Köhler illumination in 1893, that provides even illumination of the field of view and which remains a standard in light microscopy today (Somssich, 2022).

At nearly the same time, sample preparation improved with the development of microtomes and dedicated dyes to investigate life in tissues or micro-organisms (Titford, 2009). However, most individual cells such as bacteria, protozoa, cells or biological tissues are translucent, difficult to observe under optical microscopes. Antoni van Leeuwenhoek and early microscope enthusiasts used staining elements available at hand such as saffron, madder or indigo. Light microscope optical quality improvement in the second half of the nineteenth century fed a growing interest in histological description of unwell known tissues and increased the need to develop proper staining protocol to observe them. In a quick lapse of time many staining procedures were developed: in 1856 the aniline industry proposed a wide range of synthetic dyes that quickly found use in histology, in 1863 Wilhelm von Waldeyer used hematoxylin to identify cellular components, procedure that was improved in 1876 by Wissowzky who observed tissues using the still-in-use today hematoxylin and eosin treatment. Microorganism staining procedures improved after 1875 shifting from mainly carmine to bismarck-brown then to methylene blue in 1881 to still commonly used gram staining, introduced in 1884 by Hans Christian Gram (Titford, 2009; Yoshimura et al., 2023). Nevertheless, staining procedures are usually toxic in a way that prevents the observation of living specimens. The demand of overcoming this limitation initialized development of contrasting approaches that do not use chemical treatments. In 1932, Frits Zernike's invention of phase-contrast imaging enabled visualization of structural features of transparent biological objects like cells and tissues without staining, thus opening up ways for live specimen imaging.

At that moment in time the optical microscopy reached a “local maximum”. The improvement of lens quality could not further help to improve the resolution, because of the physical properties of light. The criterion for light microscopy resolution was introduced by Ernst Abbe much earlier in 1873. Abbe linked the limit of resolution to the diffraction limit of light (Abbe, 1873) and showed a relationship between the wavelength of light, the numerical aperture (NA) of the objective lens, and the smallest resolvable distance (d) in the following formula:

$$d = \frac{\lambda}{2 \cdot \mathrm{NA}}$$

This expression dictates that photons in the visible light range (380-750nm) are limiting the resolution of objects or features to about 200 nm (Vangindertael et al., 2018). This value represents the classical resolution limits of conventional light microscopes and many cell organelles and macromolecular assemblies are smaller than 200 nm. This observation provided the driving force for the development of higher resolution determination techniques, such as x-ray crystallography, NMR or electron microscopy. Nevertheless, light microscopy improvements didn’t stop there. Fluorescence properties of fluorophores molecules were applied to light microscopy creating a new area of fluorescence microscopy. It enabled development of a confocal microscopy, whose concept was proposed in the early 1950s by Dr. Marvin Minsky (Minsky, 1988; Somssich, 2022). The filtration of unfocused light using an aperture enabled for the confocal microscopy to get about 30% improvement of resolution. This breakthrough had a particular impact in the early 2000s with the development of superresolution microscopy approaches. Nowadays super-resolution light microscopy represents an imaging field composed of a range of techniques overcoming Abbe’s diffraction limit by modifying the timing or the patterns of fluorescence emission. Stefan Hell, who pioneered STED (Stimulated Emission Depletion) microscopy, earned the Nobel Prize in Chemistry in 2014 alongside Eric Betzig and William Moerner for their collective advancements in super-resolution imaging (Willig et al., 2006). These imaging methods reach a point-to-point resolution below 100 nm, however its application to life imaging is challenging because of the phototoxicity coming from the high dose of photons required. Super-resolution methods based on stochastic emissions of fluorophores such as PALM (Photoactivated Localization Microscopy) and STORM (Stochastic Optical Reconstruction Microscopy) could achieve resolutions below 10 nanometers, enabling localization of individual proteins within the cell (Betzig et al., 2006; Rust et al., 2006). However, microscopy can only provide images of fluorescently labeled features and only limited cellular objects can be labeled using fluorescent probes. Fluorescent microscopy cannot provide images of the complete cellular structural landscape in which fluorescent labeled proteins, organelles or other cellular features are evolving. The development of electron microscopy (EM) has revolutionized our ability to observe materials and biological specimens. The diffraction limit of electrons for nowadays 300 keV electron microscopes is 25.000 times smaller than the theoretical one of light: electron based imaging offers

great magnification power to image objects smaller than an atom in principle. The development of electron imaging gave rise to two major fundamental systems: Transmission Electron Microscopy (TEM) and Scanning Electron Microscopy (SEM). The first one was introduced by Ernst Ruska in 1930, the second was reported by Max Knoll in 1935 as a SEM prototype while the first working system was presented by Zworykin in 1942 (Bogner et al., 2007). When these methods were just introduced, the actual resolution of electron microscopy could not meet the resolving power of optical microscopes available at that time. Decades of technical development eventually led to EM imaging of samples preserved at cryogenic temperatures (cryo-EM). This breakthrough supported the direct visualization of biological molecular structures *in vitro* at near-atomic resolution without the need of contrasting electron dense stains. Recent advancements in cryo-electron tomography (cryo-ET) demonstrated that near-atomic resolution can be also achieved in cellular samples *in situ*, establishing a bridge between molecular and cellular scales. *In situ* cryo-ET is the first method that enabled visualization of macromolecules together with their cellular structural context (Hell, 2009).

## Revolutionizing resolution: the power of electrons

In 1924, Louis de Broglie proposed that all particles have wave-like properties. His equation stated:

$$\lambda = \frac{h}{p}$$

where: λ is the wavelength (known as the de Broglie wavelength); h is Planck's constant ($6.626 \times 10^{-34}$ J); p is the momentum of the particle, p=mv, where m is the mass and v is the velocity of the particle (Williams and Carter, 1996). The wave properties of electrons were independently confirmed experimentally by Davisson and Germer, as well as Thomson and Reid, in 1927 through the demonstration that an electron beam can diffract. Shortly after, the concept of the electron microscope was proposed by Knoll and Ruska in 1932 (Figure 1A) (Knoll and Ruska, 1932).

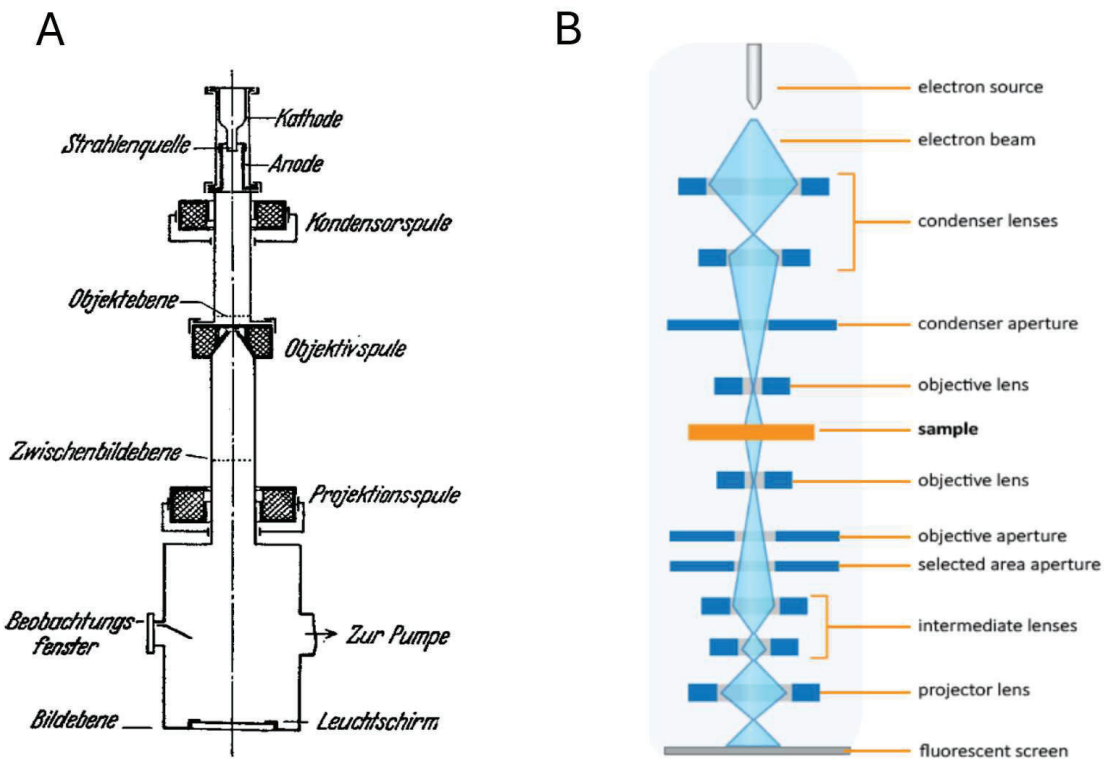


**Figure 1. (A)** The concept of EM from Knoll and Ruska's publication (Knoll and Ruska, 1932). **(B)** A schematic drawing of the main optical elements and the electron beam path of a more modern TEM (scheme taken from https://www.nanoscience.com/techniques/transmission-electron-microscopy/). The main magnetic lens components (condenser, objective, projector) are common.

## Imaging in TEM

TEM is based on collecting the electrons that pass through a thin semi-transparent specimen. Parallel illumination over a wide sample area is possible using high energy electrons (usually 300 keV) that are beneficial to achieve high-resolution imaging. SEM applied to biology uses an electron beam with the lowest usable energy, and generates an image by focusing the electron beam into a tiny spot illuminating successive positions over a complete field of view to screen the desired sample surface.

High-energy electrons (100–300 keV) have wavelengths on the order of magnitude of picometers, as predicted by de Broglie's principle in agreement with the wave-like behavior of particles. This extremely short wavelength (λ) is far beyond the diffraction limit of light and with corrections for the relativistic speed, λ=0.124 Å for a 100 keV electron beam, and 0.0719 Å for 300 keV (Penczek, 2010). Nevertheless, the highest routinely achievable resolution of EM is at the angstrom scale due to the challenges of creating perfect magnetic lenses for focusing electrons.

Importantly, the gain of resolution provided by EM for biological imaging comes with side-effects: electrons interact strongly with matter. This property leads to two key limitations: (i) the electron beam requires high vacuum to be emitted and avoid unwanted scattering, and (ii) the beam damages samples during imaging. These constraints are particularly problematic for biological specimens, as the water content in living samples boils under vacuum, collapsing and denaturing cellular structures, the electron beam would take care of damaging what remains. Consequently, as is, EM cannot be used for imaging living organisms.

Practical solutions have been developed to preserve structure of tissues, cells or macromolecules in vacuum. They either consist in hardening biological samples while preserving the structural features that are heavy metal stained (this will be discussed later in the **Three dimensional electron microscopy**) or to embed a preparation of purified macromolecules with amorphous precipitate of heavy metal salts to image their metallic shell or footprints as the proteins collapse under the microscope vacuum. The latter allows investigating biological objects at the molecular level using this sample preparation strategy known as “negative staining”. This preparation procedure can be used both to stabilize the structure or as a contrasting agent to enhance visibility. However, we are not observing directly the biological features as the TEM image is, here, mainly formed due to heavy metal contrasting agents and neither of these methods is capable of achieving high resolution of detailed macromolecular organization. They are also prone to artefacts resulting from chemical treatments, dehydration, embedding and binding of heavy metal salts (Dubochet, 2012). A major breakthrough in the preservation and observation of sample’s high resolution features came with instruments and methods development enabling EM imaging of samples processed, preserved and maintained at cryogenic temperatures (Dubochet, 2018).

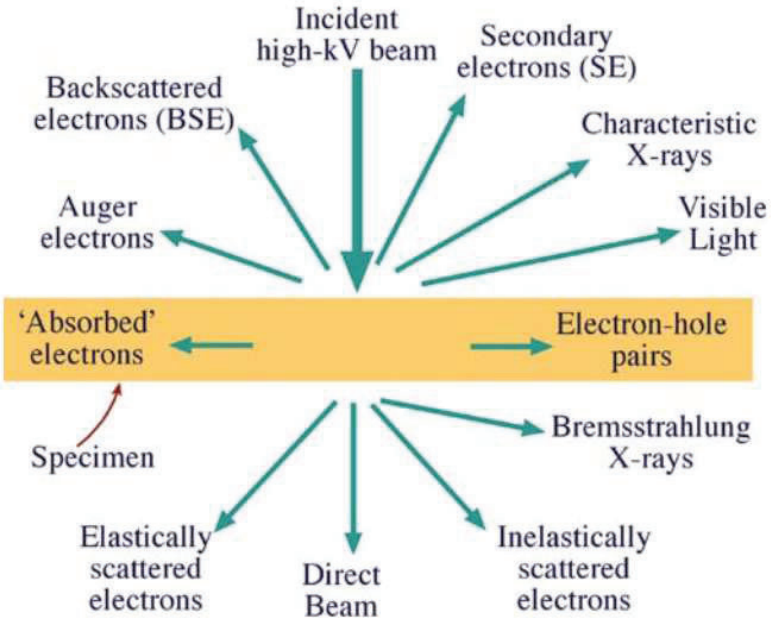


**Figure 2.** Main secondary signals resulted from interaction of incident high-energy electrons with a sample, adapted from (Williams and Carter, 1996).

Interaction of high-energy electrons with the sample results in a wide range of secondary signal events (Figure 2). TEM and SEM use different modalities to generate an image. In the case of TEM, electrons are scattered at the low angles providing so-called amplitude contrast that is predominant in conventional EM and negative staining. Amplitude contrast originates from a strong scattering of electrons by heavy atoms (Au, Pt, Pb, W), that are removed by a physical barrier, objective aperture, placed in the back focal plane of the objective lens in a way that this electrons will filtered out of the image formation (Williams and Carter, 1996) (Figure 3).

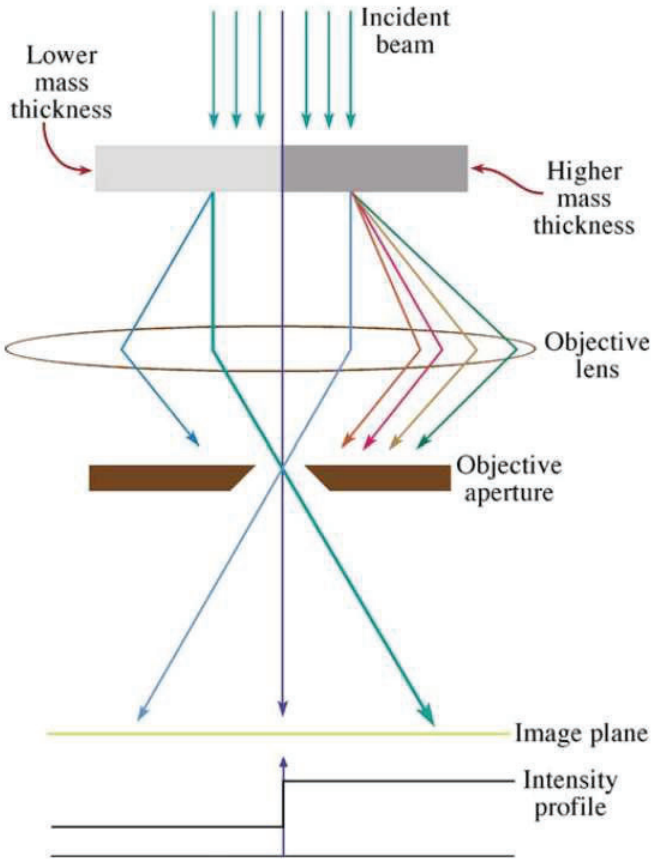


**Figure 3.** Aperture-based “amplitude” contrast (adapted from Williams and Carter, 1996)

## Phase Contrast

The water-rich vitrified native biological samples do not contain heavy atoms, they are mainly made of organic molecules featuring the following atoms (H,C,O,N,S,P). Such composition does not provide a sufficient mass difference from the rest of the cellular environment (solid amorphous water, ions and mineral molecules) for the generation of a substantial amplitude contrast. Cryo-EM imaging is taking advantage of phase contrast in order to visualize biological features. It is based on a phase shift of electrons induced by their interaction with atoms of a sample. Some of the electrons passing through vitrified biological samples will experience a phase shift. However the phase shift generated by the interaction of the incident beam with the atoms of a biological sample is usually too weak to be reliably detected in noisy conditions (Nagayama and Danev, 2008). The usual way for inducing differential phase shift is based on the optical aberrations introduced by the objective lens when it applies defocus. The spherical aberration and defocus effects have opposite signs, resulting in frequency-dependent constructive or destructive interference of the “scattered” electron wave passing through the sample without interaction (Figure 4). This frequency-dependent modulation can be described as a function defined by the wavelength λ of electrons, defocus, and spherical aberration of the objective, this function is called the Contrast Transfer Function (CTF).

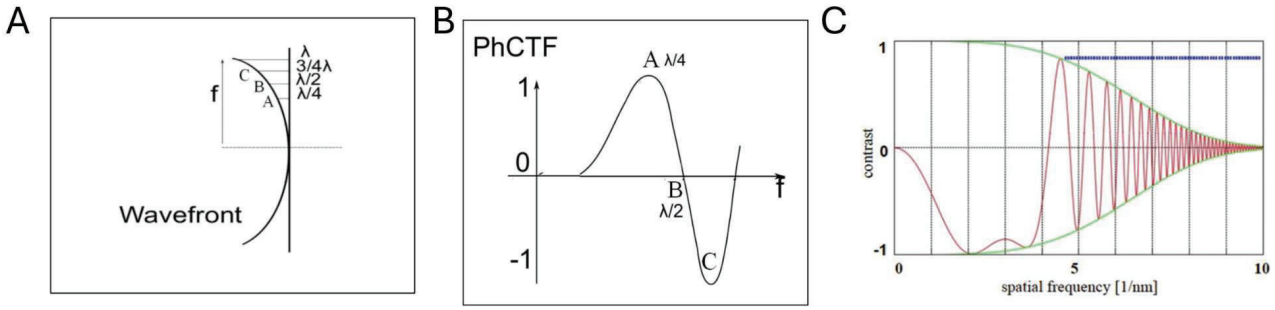


**Figure 4.** Schematic drawing of the CTF formation. (A) In the case of introduced defocus, the scattered wave remains bent and undergoes interference with the direct wave, which is flat at the back focal plane of the objective. At position A, the phase is delayed by 90° with respect to the phase at the optical axis, leading to positive interference and (positive) phase contrast. At position B, the total phase delay is 180°, resulting in destructive interference, where no information remains. At position C, the total phase difference is 270°, leading to negative phase contrast, and so on (adapted from Martiv van Heel lectures http://www.single-particles.org/methodology/MvH_Phase_Contrast.pdf). (C) A frequency dependent amplitude decay: the “envelope” function (adapted from Costa et al., 2017).

The presence of the CTF introduces challenges in the direct interpretation of images because the information is suppressed, completely lost, or phase-inverted depending on the spatial frequency. Additionally, various imperfections in imaging experiments, such as spatial and temporal incoherence of the electron beam, lens aberrations, stage vibrations, and sample thickness, contribute to the decay of signal amplitudes at higher spatial frequencies. This decay is typically described by the "envelope" function (Figure 4C). The frequency dependent contrast loss of the CTF is directly impacting the features that can be extracted from the images. Another method is to introduce phase shift contrast while imaging the sample on the focal plane by the addition of an optical part within the microscope that will separate scattered electron waves from unscattered ones at the back focal plane of the objective lens (Costa et al., 2017). This new hardware part, called a phase plate, would add additional phase shift either to scattered or unscattered electrons. Volta phase plates are the most advertised ones (Danev et al., 2014) but the phase shift produced by them is not reproducible. There are recent developments of laser phase plates (Schwartz et al., 2019) aiming to provide stable and reproducible phase shifts.

Inelastically scattered electrons (Figure 2) formed during imaging in cryo-TEM are unwanted because they contribute to noise. They can be removed using energy-filtering devices, which selectively eliminate electrons that have lost, usually more than 10 eV energy during scattering. Such filters are essential for *in situ* cryo-ET, which utilizes thicker samples (100–300 nm) compared to SPA (<50 nm) (Neselu et al., 2023). Furthermore, the effective thickness of the sample increases significantly during tilting, approximately doubling at a tilt angle of 60°.

## Imaging in SEM

SEM imaging benefits from a great range of field of views from a few centimeter long to sub micrometer objects. Upon irradiation with the direct electron beam, the specimen is emitting multiple signals from which we can extract information about the properties of the sample. SEM generates inelastic secondary electrons, backscattered electrons, and X-rays emitted as the primary beam interacts with the sample. These signals are collected by dedicated detectors that will record these signals, extracting information or creating an image of the sample surface. Secondary electrons (SE), generated by inelastic scattering as the incident electron beam excites the specimen's surface atoms, are the primary signal used in SEM imaging. These low-energy electrons (typically less than 50 eV) originate from a shallow depth of the sample making them highly sensitive to surface features. By scanning the beam across the sample and measuring the spatial distribution of emitted secondary electrons, SEM produces detailed images of surface topography. Electron permeable objects such as resins or biological material will absorb most of the direct emitted electrons, leading to weak contrast and sample damages. To maximize contrast and minimize undesired charging effects, the sample surface is covered with a thin conductive metallic coat of platinum for instance. Electron dense objects such as metal will interact strongly with the direct electron beam and generate more SE signals.

Backscattered electrons (BSE) are emitted deeper inside the sample surface and will be less impacted by the sample surface deformation (Figure 5). They are used for imaging as they carry information about the sample surface electron opacity, but are less abundant than SE. Deeper than the BSE generation layer, X-rays are formed, they carry chemical sample properties and can be used to map the different elements present in the sample using Energy-dispersive X-ray spectroscopy. BSE and SE based images can be combined with more weight attributed to one or the other detectors in order to get sharp information from the BSE images compensated for the noise with the SE strong signal images. The accelerating voltage of the electron beam will impact the image resolution (Figure 5). High energy electrons will penetrate deeper within the sample increasing the size of the interaction pear giving rise to signals coming from a larger volume inducing blurry micrographs. On the contrary, less energetic electrons, accelerated below 2 to 1 kV will interact within a small interaction pear increasing the imaging resolution but increasing the proportions of electrons "absorbed" leading to noisier images.

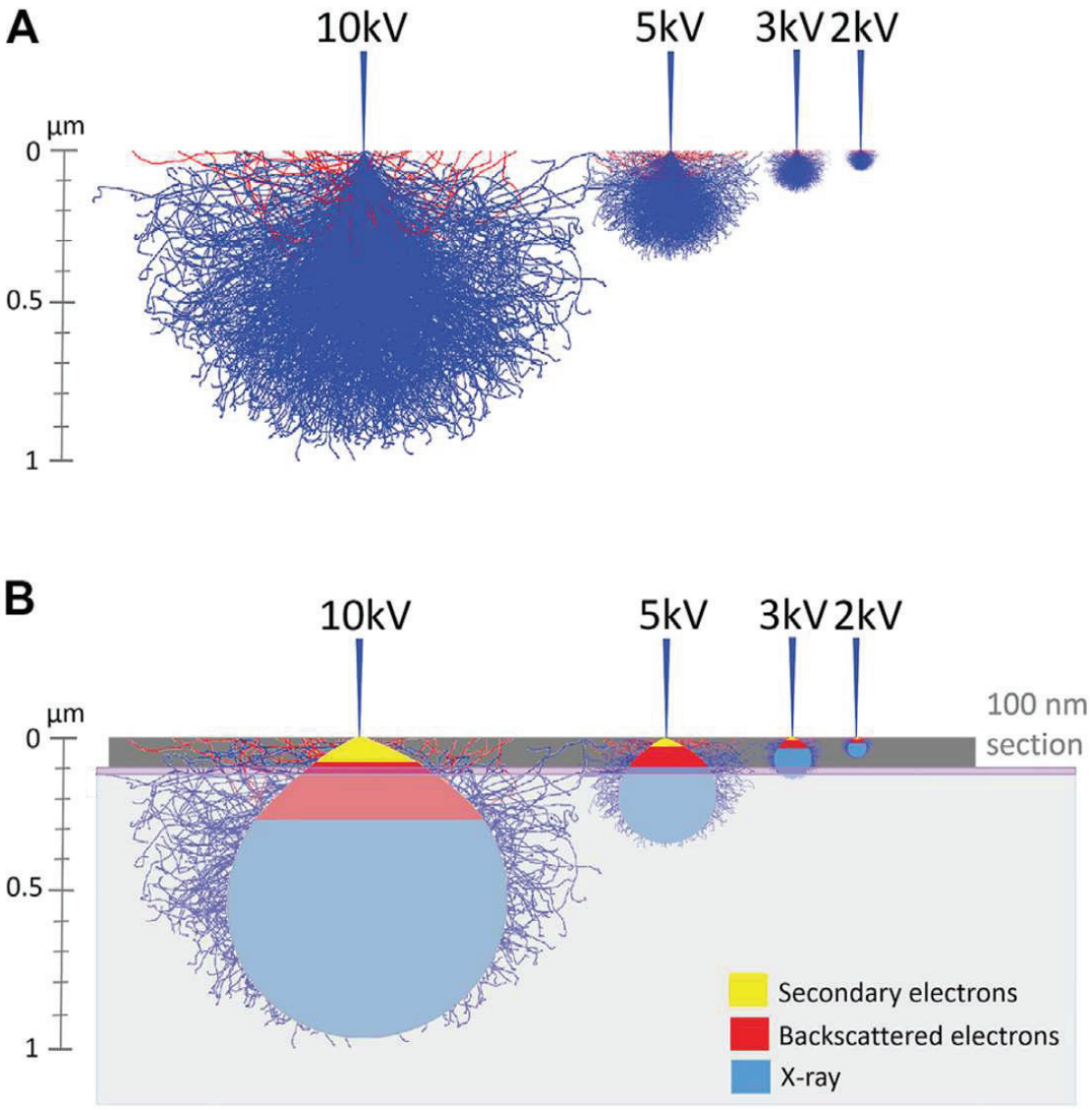


**Figure 5.** Monte Carlo simulations, adapted from Baatsen et al. (2021), illustrate the interaction volume of electrons with a biological sample during imaging. **(A)** The simulations reveal that most electrons from the beam are absorbed by the sample without generating secondary electrons (SE) or back-scattered electrons (BSE). Reducing the acceleration voltage can help to minimize sample damage while also enhancing imaging resolution. This trade-off underscores the importance of optimizing beam parameters for biological imaging. **(B)** Unlike BSE, SE are generated within a very superficial layer of the sample. This characteristic makes SE particularly advantageous for achieving high-resolution imaging, as their production is localized and closely tied to surface features.

## Three dimensional electron microscopy

EM methods are only providing 2D images of volumetric samples: TEM micrographs represent 2D projections of semi-transparent samples and SEM only images sample surfaces. To obtain three dimensional representation of the sample, the information from multiple 2D images has to be computationally processed to reconstruct 3D volumes. This collection of 2D images can either sample the surface of a specimen of interest at different depth or regroup multiple transmission micrographs of the same thin specimen but recorded at different tilt angles (Figure 6).

As discussed before, hydrated living biological samples cannot be introduced inside a TEM or a SEM microscope, the sample preparation has first to deal with biological specimens's liquid state while using heavy metal stains to generate contrast. We previously introduced the negative staining that is used to image macromolecules *ex situ* where the cellular environmental and structural information is absent.

Practical solutions have been developed to preserve structure of cells and tissues in vacuum. Briefly, the sample preparation includes chemical fixation, replacement of water by a mix of alcohol and contrasting heavy atoms that are finally exchanged by a liquid resin that will slowly polymerise and embed contrasted cellular features. This method is nowadays often referred to as a conventional EM sample preparation and maintains structural features down to the organelle scale (Figure 6AB). Molecular information is lost due to the chemical fixation, substitution of water using alcohol and heavy metal stains processing steps that are all introducing artefacts and damages. However, resin embedded stained samples are a good starting material for both TEM and SEM volume imaging provided that they undergo further processing steps to fit these 3D imaging methods (Figure 6C). In essence, for TEM based volumetric imaging, the bulky resin samples will be thinned down using an ultra microtome into a ribbon of successive sections that are collected on an EM grid. This way, the resin embedded specimen is sampled in 3D with a step according to the section's thickness. A cutting step between 50 to 100 nm is selected to perform serial sectioning TEM (ssTEM) imaging where each section will be recorded individually in transmission. They will be later gathered in a stack before alignment and segmentation of each slide from which a volume is reconstructed.

Transmission images of 50 to 100 nm thick sections have the inconvenience of flattening all the 3D information within each plastic section in a 2D projection. Serial sectioning electron tomography (ssET) is an alternative method that keeps the 3D information within each section by imaging successive slices at different angles. In a classic recording setup the specimen holder is tilted from -70 to 70 degrees, the section is imaged in steps of 2 degrees resulting in a collection of different 2D projections influenced by the tilted 3D data within the section. The stack of tilted micrographs, referred to as a tilt series, is aligned and processed to reconstruct a 3D image stack, revealing the internal volume of the section (Figure 6D). Colloidal gold nanoparticles, typically 10 nm in diameter,

are applied to the surface of the sections and/or the supporting EM grid's plastic film prior to tomographic imaging. These gold particles, due to their high contrast and consistent size and shape, serve as fiducial markers for aligning the tilt images. Once aligned, the volume is reconstructed using Fourier space based weighted back-projection algorithms, such as those available in the IMOD software package (Kremer et al., 1996). This recording and reconstruction scheme is then applied to all the remaining sections and each section's reconstructed volumes are concatenated in a bigger resulting volume (Peddie et al., 2022). The sections width used in ssET are thicker, about 200 -300 nm, as the aim is to get the biggest reconstructable volume using ET without facing too much resolution loss. TEM based volumetric images benefit from high resolution but require time consuming dedication as the number of possible recorded sections is limited by the size of EM grids and involves the preparation of multiple of them (Denk and Horstmann, 2004). Additionally, identification of structural features within stitched regions of a section and the alignment of all the stitched sections together for 3D volume reconstructions can be challenging (Weber et al., 2014).

Scanning electron microscopes are extensively used for volumetric images. Large resin embedded specimens can be introduced inside their chamber and the SEM optics allows for the recording of a wide field of views. Using low voltage imaging around 1 keV, only electrons coming out of the surface of the specimen (secondary or backscattered electrons) are used to form an image. In principle, TEM volume imaging relies on imaging successive sections of a sample to reconstruct a 3D volume but as SEM only images surfaces, every material lying in the thickness of a section beyond its surface will not contribute to the images and will be lost. For this reason, thin sections are particularly important for SEM based volume imaging.

Array tomography will take advantage of the wide specimen holder to insert a huge collection of sections that will be recorded in parallel with the use of a splittable electron beam that allows for fast imaging with great throughput. The z resolution is however quite large with sections of about 30 nm thick at best. In a related manner, some SEM apparatus are fitted with an ultra microtome in chamber where the sample block face is scanned between consecutive microtome cuts, thus exposing a freshly cut block face before each SEM image. In the serial block face SEM apparatus (SBF-SEM), this iterative cutting-imaging process goes on until the desired volume is recorded (Peddie et al., 2022). A new commercially available SBS-SEM apparatus image each slice using multi-energy deconvolution SEM (MED-SEM), this recording process is using multiple images of the same block face taken at different electron beam energy, therefore formed at multiple optical depths close to the surface, to recover 3D information of the block face's near surface volume (De Goede et al., 2017). This imaging method compensates to some extent the data lost in 30 nm thick slices by bringing down the z resolution to 10 nm. This principle is implemented in the new Volumescope 2 SEM (Thermofisher scientific ®). Methods relying on the imaging of ultra microtome sections are coping with compression problems due to mechanical slicing. SBS-SEM ,

however, scans the block face between sections and is free from sectioning-related issues like compression and section deformations.

Focused ion beam (FIB) and scanning electron microscopes (SEM) are generating a beam made of different probes that can be combined for volumetric imaging purposes. Ion miller apparatus are able to precisely polish or mill a surface through the emission of an energetic focused beam of ions. This milling process, also referred as cathodic sputtering or sputter-etching, precisely degrades matter by ejecting out the molecules of the exposed sample's surface upon interaction with the system's incident focused ion beam. Nowadays referred to as focused ion beam (FIB) this apparatus was initially developed to prepare thin foils of metal for TEM analysis and imaging and was later extensively used for the preparation of semiconductor (Ballerini et al., 2001).

In 1993, Young et al, reported to have used a FIB apparatus to mill regions of adults and larva Halarachne as a processing step for later SEM imaging in a separated microscope (Young et al., 1993). Dual beam apparatus FIB-SEM, available since the late 80's, found good application in slice-and-view usage to analyse semiconductor architecture of semiconductor. The FIB was used to expose a newer deeper layer of the sample by etching that will be scanned by a SEM. In a similar way as SBF-SEM, this slice and view process happens iteratively until a desired volume is imaged. Its first application in biology was reported in 2006 where resin embedded yeast pellets were sliced and viewed using a step of 100 nm (Heymann et al., 2006). Nowadays apparatus can reach below 5 nm in slicing step resolution, making the FIB-SEM the most resolutive apparatus in the z axis for large EM volume imaging. FIB-SEM is a relatively slow imaging method but allows the processing of huge volume, recently a modified FIB-SEM microscope could record Drosophila optic lobes volumes as big as 180 x 100 x 50 µm using a sampling rate down to 8 nm isotropic voxels (8 nm pixel size in the x and y axis and a slice step width of 8 nm) after 100 days of constant recording (Xu et al., 2017). In 2003, Mulders showed in a small paper that at -140°C, the FIB could be used as a trimmer in an alternative for cryo facture to investigate life (Mulders, 2003). Quickly after the idea of using FIB-SEM at lower temperature to mill into vitreous ice to produce an *in situ* thin lamella for cryo-TEM imaging was investigated. In 2005, Marko et al, stated after their observation that with an appropriate sample temperature, the heat transfer during etching of the vitreous water embedded sample seems to be small enough to prevent the formation of transformed ice (Marko et al., 2006, 2005). From this point on, the cryo FIB-SEM kept on being developed as an alternative to cryo ultramicrotome for the preparation of samples for *in situ* cryo ET. These developments fueled by modern Cryo-EM microscopes hardware advances allowed direct visualization of cellular features preserved in a near native state down to the molecular scale. Cryo FIB-SEM with good SEM optics can be used to produce *in situ* volumetric images of vitrified biological samples using slice-and-view without any addition of heavy atoms (Schertel et al., 2013; Spehner et al., 2020) but the image resolution and the completeness of environmental description doesn't match the one reached by cryo-ET.

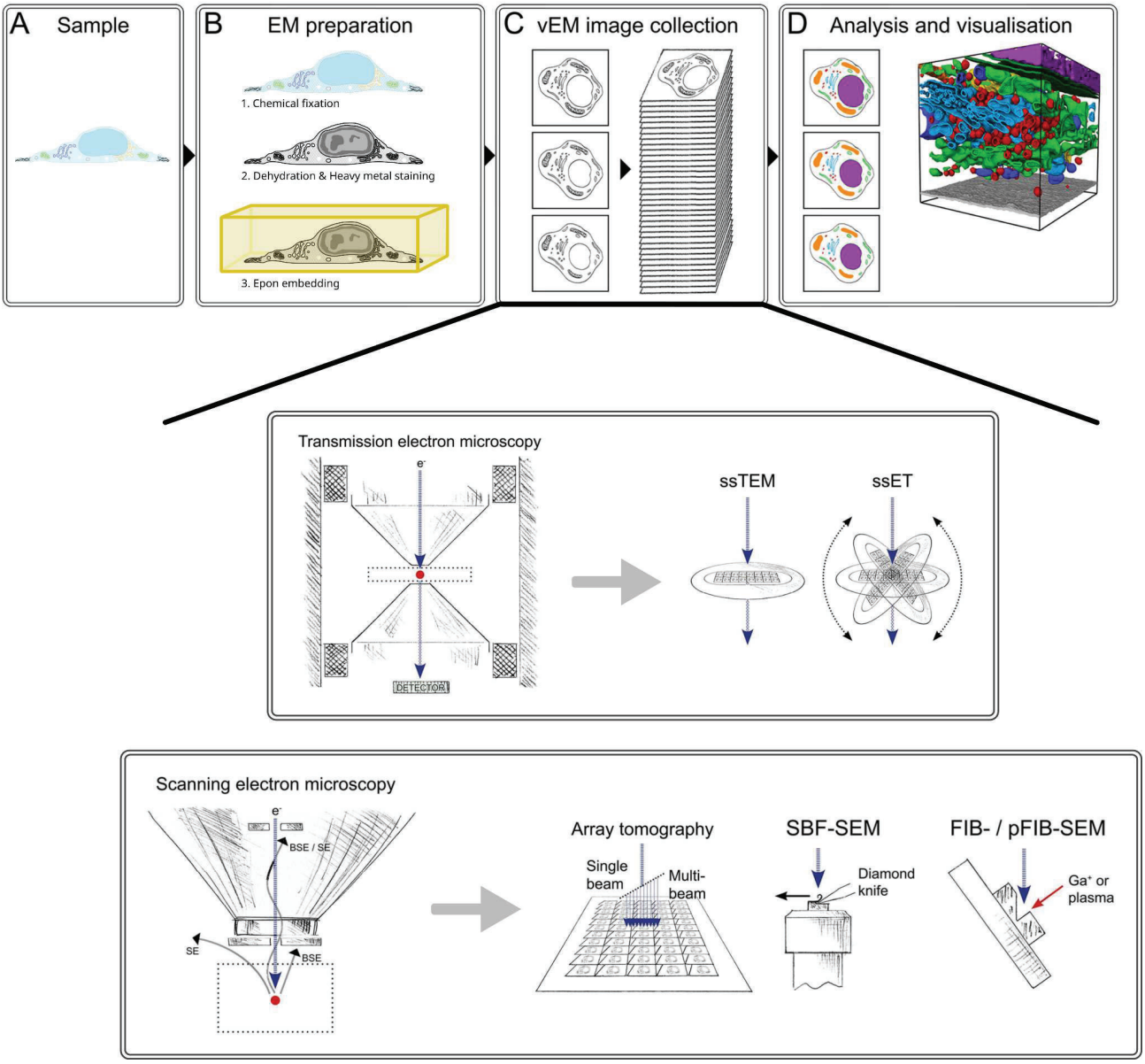


**Figure 6.** Basic workflow and main methods of volumetric imaging (adapted from Peddie et al., 2022). Live cells or tissues (A) are chemically fixed, dehydrated, and contrasted with heavy-metal salts for electron imaging. The sample is then embedded in resin. (C) Volumetric data are collected from the sample using various methods based on TEM or SEM. For TEM, serial sections are cut with a diamond knife and collected on EM grids. Serial 2D images (ssTEM) or serial tomograms (ssET) are then acquired. SEM imaging relies on secondary electrons (SE) and backscattered electrons (BSE), which are detected using different detectors. The washer-like detector for BSE and the in-lens detector are shown in the figure. Array tomography involves collecting serial sections on silicon wafers, which are scanned using single or multi-beam systems. The serial block-face SEM (SBF-SEM) approach uses a diamond knife to shave thin sections from the block face, followed by scanning with an electron beam. Dual-beam machines (FIB-SEM) combine gallium ions or gas plasma beams to ablate layers of material with an electron beam for imaging. (D) The obtained image or volume stacks are reconstructed and segmented by computation methods.

## Cryogenic electron microscopy: resolution revolution

Recent advances in cryo-electron microscopy (cryo-EM) transformed it into a leading technique of structural biology. This methodology shift is often termed the "Resolution Revolution" but actually integrates a large range of conceptual and technological advances. Cryo-EM has its origin in early 1980th from pioneering experiments performed by Jacques Dubochet team at EMBL Heidelberg that demonstrated the possibility to transform liquid water into an amorphous solid, named vitreous water, by fast cooling at atmospheric pressure (Dubochet and McDowall, 1981). This discovery initiated the development of cryo-EM as a technique that preserves samples in a close to native hydrated state.

In the 2010s, direct electron detectors were introduced and dramatically improved the signal-to-noise ratio of the recorded images thus enabling high-quality imaging at low electron doses, which is critical to minimize radiation damage. This, together with development of more stable cryo-sample holders, more stable electro-magnetic lenses, electron energy filters that further improved image quality, provided altogether major resolution improvement. Development of plunge-freezing devices from the initial guillotine introduced by Marc Adrian made the plunge-freezing more reproducible (Dubochet et al., 1982). The regular perforated carbon films made it possible for automated acquisition of data in a majority of SPA experiments (Adrian et al., 1984). Additional factors also contributed to improve data quality: fully automated processes for image acquisition in low-dose conditions, remote microscope operation, and of course the development of 3D single particle image analysis.

As of today, after all these improvements, performing a single particle cryo-EM experiment is rather streamlined and mainly depends on sample purity, macromolecular flexibility and physico-chemical stability at the air-water interface. In sharp contrast, *in situ* cryo-EM on cellular samples remains highly challenging.

## Challenges of *in situ* cryo-EM

As previously discussed and despite their great resolution power, electron microscopes are not adapted to explore life and living organisms. Liquid water is one of the main compounds of life as it acts as an essential solvent for all biochemical reactions that occur within the cell environment. Water conditions all hydrophilic/hydrophobic based structural features and interactions, and it also encapsulates the cell's overall ultrastructure (Westall and Brack, 2018).

Classical EM on solid state samples was formerly mentioned. However, studies on cellular systems are using EM to get information on liquid phase specimens. A very specialized field of EM is working on imaging liquid phase samples to get rid of sample preparation artifacts and damages of solid phase EM on biological specimens. This field provided ultrastructures images of cells but it seems that this technology is limited and cannot reach sub nanometer high resolution images (Caffrey et al., 2024; Egelman, 2024; Rutten et al., 2023). Cryo-immobilization, on another hand, will embed the sample in its own water, cooled down to reach the state of solid vitreous ice, allowing for sub nanometric imaging while avoiding sample reorganization caused by chemical cross-linking. This breakthrough quickly led to the emergence of several freezing methods such as plunge freezing, slam freezing or high pressure freezing.

Eukaryotic cells are in their vast majority much thicker than the maximum sample thickness allowing high-resolution imaging: 300 nm. In addition, proper vitrification with the help of plunge-freezing is possible only for very narrow cytoplasmic outgrowths of most eukaryotic cells. Yeasts are one of the exceptions, they also are small cells which contain a high concentration of polysaccharides acting as an internal cryoprotectant. Thus, *in situ* cryo EM should always address two problems: achieving vitrification and reducing cell thickness to make structures transparent enough for electron tomography.

### Complete cell vitrification

The need for complete vitrification of the cell for *in situ* cryo-EM was proposed as a requirement as early as in the pioneering work of Jacques Dubochet. Too slow freezing results in the accumulation of ice crystals whose size is inversely related to the cooling rate. Ice crystal formation excludes macromolecules and perforates membranes thus altering cellular ultrastructures. Plunge frozen human eukaryotic cells would only guarantee proper vitrification in thin peripheral cytoplasmic areas. The complete vitrification of bulkier specimens, up to 200 micron in thickness, can be achieved by high-pressure freezing. The concept of high-pressure freezing (HPF) introduced by Riehle in the late 1960s, is based on changes of physical properties of water at 2100 barr that improves the vitrification depth (Riehle, 1968).

Nevertheless, many recent and current studies using cryo-ET have actually been performed on samples containing small areas of crystalline ice, the presence of which is obvious when looking at tilt-series. In several cases, such inefficient vitrification did not prevent from obtaining sufficiently high resolution for a number of cell structures, raising the question of how complete vitrification is necessary to extract useful information. Our observations indicate that the cell nucleus is highly sensitive to damage caused by crystalline ice. Since our target structure is RNA polymerase II, achieving complete vitrification of the sample has been our primary objective.

## Making thin cellular windows

In a similar way as for resin embedded samples Jacques Dubochet and his collaborators addressed the problem of thickness for EM imaging of cryo-immobilized samples by adapting sectioning using diamond knives to high-pressure frozen samples. This method gave rise to the first *in situ* cryo-EM images (McDowall et al., 1983). They named their workflow Cryo Electron Microscopy Of VItreous Sections (CEMOVIS) where vitrified sections thinner than 100nm can be obtained. However mechanical sectioning with a diamond knife at low temperature introduces structural deformations (Al-Amoudi et al., 2004) with the formation of crevices and shrinkage of about 30% of the sample in the direction perpendicular to the knife's blade. These limitations combined with the requirement for a long training time and dedicated operator have been detrimental to the cryo-sectionning approach which is currently under-used. Relatively recently, a micromanipulator-assisted cryo-sectioning system was introduced by Diatome (Studer et al., 2014). In combination with electrostatic section attachment to EM grids, it provides a more robust and less-laborious success rate of obtaining cryo-sections. The compression induced by the sectioning process leads to thickening in the z direction and shortening along the sectioning direction. Interestingly, these deformations seem to be non-uniform: large features such as cell shape or organelles are strongly affected, while small molecules such as nucleosomes are not deformed (Eltsov et al., 2018). Furthermore cryo-sectioning is currently the best method to obtain high resolution information on large cellular depths by cryo serial sectioning. In my project, I used the CEMOVIS protocol to produce sections of cut Hela cells frozen in dense suspensions by HPF.

As introduced previously, the cryo FIB-SEM provides a great alternative approach to thin bulky samples as the production of thin lamella is streamlined in an efficient automatic procedure on the latter commercially available dual beam microscopes. The easiest way for obtaining such lamellae consists in milling adherent cells directly grown on EM grids and frozen by plunge-freezing. One lamella is milled per cell, and then the grid is transferred to a cryo-TEM. Bulky frozen specimens prepared by HPF can also be thinned down in cryo FIB-SEM using the so-called lift-out approach that was inherited from the extraction of specific zones of bulky resin embedded samples for later TEM imaging (Parmenter and Nizamudeen, 2021; Rubino et al., 2012; Zachman et al., 2016). The initially rather thick lamella is milled within the freezing carrier, then moved out and attached to the

EM grid by a micromanipulator. The final FIB thinning takes place on the grid. Implementation of these methods requires specific lift out equipment that are not default to cryo-FIB-SEM as well as dedication and sharp skills from the operator as it is not fully automated. With this information in mind, cryo serial lift out would be science fiction but later workflow improvements proved otherwise (Schiøtz et al., 2024).

Recently, another HPF-based method, the Waffle approach, was introduced (Kelley et al., 2022). In this method, cells in suspension are placed in between bars of an EM grid and vitrified by high-pressure freezing. This allows for the complete vitrification of large eukaryotic cells while simultaneously enabling FIB lamella milling directly on the grid without the need of a lift-out process.

Cryo-FIB lamellae do not show any spatial deformation artefacts typical for CEMOVIS, however accelerated Galium ions transfer energy to the sample during the milling process resulting in molecular structure damage in the peripheral layers of lamellas (Lucas and Grigorieff, 2023). Recently gas plasma systems were introduced which offer faster milling and a lower structural damage compared to Ga based beams (Berger et al., 2023). The main current challenge of cryo-FIB lamellae is to reproducibly obtain lamellae thinner than 200 nm. Even in the case of thin lamellae, using lower energy ion beams, macromolecules in the 30–50 nm thick layers on both surfaces are likely to be damaged by the milling process (Yang et al., 2023). In this regard, cryo-sectioning is still a solution that should not be overlooked.

## Recording Electron tomograms

Tomographic data collection from vitrified sections or lamellas is also presenting a challenge on its own. Electron tomography, as explained in the **Three dimensional electron microscopy** part, is based on the recording of tilt series typically comprising 40 to 60 images. Applied to cryo lamellae or sections, the complete recording scheme has to be imaged at a very low electron dose per tilt (usually 2–3 electrons per Å²) to prevent sample destruction before the entire tilt series is recorded. This is achieved using a low-dose acquisition approach, which is based on tracking and focusing outside the recording area to minimize the damage in the recording area. The implementation of computer-controlled, high-precision goniometers made it possible to collect tilt series semi-automatically (Mastronarde and Held, 2017). Nevertheless, cumulative continuous damage to the recording area occurs during tilt series collection, resulting in a progressive resolution decay in the tilt images. To optimize the dose distribution between the tilt angles, Wim Hagen introduced a dose-symmetric data collection scheme (Hagen et al., 2017). In this case, the tilt series acquisition starts from an untitled flat position and then alternates in steps between increasingly positive and negative tilts. This approach creates more favorable conditions for preserving high-resolution information at lower tilt angles, enabling reliable high-resolution subtomogram averaging

(Hoffmann et al., 2022; Xue et al., 2022). Recently, the throughput of *in situ* data collection was increased by introduction of PACE-tomo approach (Eisenstein et al., 2023). Instead of recording tilt series sequentially one after another, this software sets up the recording of multiple areas of interest within a given range and at a given angle using beam shifts. This process iterates at each stage tilt, recording in parallel multiple tilt series, which greatly speeds up data collection. It is important to note that the use of fiducials to align successive tilted images on high contrast points of interest is generally not possible in cryo-ET experiments. As a result, cryo tilt series alignment relies mainly on fiducial-less approaches. These methods involve comparing and aligning sets of local patches within consecutive tilt images based on cross-correlation (Mastronarde and Held, 2017). Raw reconstructed tomograms (weighted ramp filter) from defocused cryo immobilized samples usually have a low signal to noise ratio preventing limiting the recognition of non membrane based features. Current highly sensitive direct electron detectors fragment each micrograph in a series of images called sub frames. Each tilt frame can therefore be divided into two subseries of sub frames, representing the same sample but with different noise patterns. As a result, two reconstructions of the same volume can be generated and used to train deep-learning models to remove partial noise (Bepler et al., 2020; Buchholz et al., 2019). This approach facilitates the denoising of cryo-ET reconstructions, improving both structural feature interpretation and particle picking.

## Identification of molecular targets in EM data

Conventional resin-embedded cellular EM used to provide sufficient structural preservation and, correspondingly, the resolution necessary to distinguish cellular organelles, highly ordered macromolecular assemblies such as cytoskeletal elements, viruses or nuclear pore complexes. Unfortunately, as discussed before the structural preservation and the use of heavy metal stains prevents the localization of isolated molecular complexes within the cell, with the rare exception of ribosomes. Obviously, the ability to localize specific poorly stained stained target molecules significantly enhances the applicability and impact of EM in cell biology. Consequently, the development of EM-based localization techniques began shortly after the introduction of affinity probes such as antibodies. The primary prerequisite for the effective use of such probes in EM is their ability to stand out within the context of the contrasting stains used in conventional EM imaging. As heavy metals were already used as diffused stains, the idea to direct heavy metal probes to specific locations quickly emerged and found its application by coupling antibodies with heavy metal ions. In the 1960s, the coupling of antibodies with iron, mercury, uranium, was explored, pioneering EM immunocytochemistry (Koike et al., 1964; Pepe and Finck, 1961; Singer, 1959; Sternberger et al., 1965). However, due to its size, iron-protein complexes like ferritins could not penetrate inside the sample. Mercury and uranium are toxic, chemically reactive, and require specific protective layers around the probes. The solution came from colloidal gold particles (usually 5-15 nm), which were first used for immunogold labeling in 1971 (Faulk and Taylor, 1971).

The high contrast of gold particles and their stability turned them into the main type of the particle probe in structural immunocytochemistry (Griffiths, 1993). Electron dense labels can be introduced at different moments within the EM sample preparation protocol, depending on the timing, they are defined as pre-embedding and post-embedding labelings. In the case of post-embedding, the labeling is performed on sections of the resin-embedded sample. On frozen hydrated samples, existing post-embedding methods cannot be used as they require incubation of the probes in liquid phase which is obviously incompatible with cryogenic samples. Pre-embedding nevertheless is performed before any embedding. It is first performed after mild fixation of the cell, followed by permeabilization using detergents to break the cytoplasmic membrane and allow the probe to reach the internal space of the cell (Griffiths, 1993). The cells are then incubated with the label, the excess is washed away followed by a final fixation and resin-embedding. The pre-embedding approaches required the probe to penetrate well into subcellular structures, which inspired the development of smaller gold particles (<5 nm). These probes were generally invisible when visualized in the context of conventional EM samples and required further aggregation of heavier atoms (silver or gold) around the original gold particle (Bienz et al., 1986; Namork and Heier, 1989). In my project, I aim to expand the concept of pre-embedding labeling method for cryo-ET by using small gold particles (nanogold) as probes for *in situ* molecular localization. This opens the way for the localisation of any molecular target within its cellular environment at molecular resolution.

## Delivering probes in living cells

Molecular labeling of biological samples for *in situ* cryo-EM imaging requires the delivery of specific electron-dense molecular probes *in vivo* because none of the approaches developed for conventional EM can be applied for vitrified samples (see the chapter above). *In vivo* labeling, however, poses significant challenges. First, the probe must pass through the external cell's plasma membrane and remain soluble without being captured by the endo-lysosomal pathways for degradation. Then, the probe should not only maintain its specific recognition properties for its target in the crowded environment of the living cell but also be "physiologically" compatible. This is why the cytotoxicity of the probe is a major limiting factor.

Two main concepts exist for generating *in vivo*-compatible probe delivery: (i) genetically encoded tags and (ii) transfection methods. Currently, the available genetic tools enable the design of structurally recognizable molecular complexes that can be combined with protein probes or can accumulate physiologically relevant metallic atoms, as presented in the following papers (Fung et al., 2023; Jiang et al., 2020; Roozbahani et al., 2024; Silvester et al., 2021; Wang et al., 2024). Nevertheless, in all the previous methods, the authors emphasized that the efficiency of the localization of such probes depends on macromolecular crowding and requires particularly high

data quality. Additionally, the design of such probes would require the creation of dedicated cell lines for each protein or element to target, requiring a tremendous time and investment.

The second concept to deliver probes *in vivo* implies the use of more or less invasive delivery methods such as lipid-based transfection, microinjection or electroporation. Low-invasive lipid based systems for probe delivery often lead to poor endosomal escape where the probe is trapped in endosomes until degradation in mature lysosomes. This phenomenon is mainly studied in the context of nucleic acid delivery with growing understanding on how to favor their endosomal escape Maugeri et al., 2019; Patel et al., 2017). Liposomal encapsulation of nucleic acid is facilitated by electrostatic attraction of cationic lipid cargo to negatively charged nucleic acids. The overall charge of a protein is dependent on its amino acid sequence and varies greatly from one protein to another and for this reason and the fact that proteins that are encapsulated have low rates of endosomal escape, lipid based transfection methods are not the most efficient to deliver proteins inside living cells. Nevertheless, there are still some attempts to generalize lipid-based transfection methods by fusing it with a negative charge boosted GFP to favor encapsulation (Zuris et al., 2015). However, this method does not improve the rates of endosomal escape of the fusion protein.

In the context of the mechanical approaches of probe delivery, I will focus on electroporation, because microinjection has an extremely low throughput, and is therefore exclusively applied to specialized systems like embryos that are not in the scope of my work (Meacham et al., 2014). Electroporation is the most efficient way for the delivery of molecules into the cell. Electroporation was introduced by Neumann et al. (Neumann et al., 1982) for transfection of mouse cancer cells, then it was optimized for different eukaryotic cells and also for bacteria (Gehl, 2003). It is based on reversible permeabilization of cytoplasmic membrane by short pulses of high-voltage field. Once membranes are permeabilized, various molecules can enter the cells, either by passive diffusion (for small molecules), equilibration of different osmotic pressure or in case of charged molecules, through an electrophoretic process. The second case is likely more relevant for the subject of my research, because gold nanoparticles coupled to proteins are relatively large assemblies, showing electrophoretic properties (details are provided in the discussion part about **electrophoretic properties** of the gold nanoparticles used in my work.). The exact mechanism of the electric field induced membrane permeabilization remains under debate. Eukaryotic cells have a difference in electric potential across the plasmatic membrane that is maintained and regulated by ion pumps embedded in the plasma membrane. This transmembrane voltage ranges from -40 to -70 mV (Kotnik et al., 2019). In an electroporation mix, every cell would behave like a small capacitor with accumulation of negative charges at the inner side of the plasma membrane and therefore, stacking of positive charges at the outer side. When a growing outer electric field is applied to an electroporation mix, the plasma membrane of cells will condense positive and negative charges until it saturates, the number of charges on both sides of the lipid bilayer remain constant. At a certain electric field strength, the force applied on the charges will break down the plasma

membrane with the creation of a “pore”. Electropermeabilization is modeled to happen in 5 stages: the initiation of the permeable state, the pore expansion, the stabilization, the membrane resealing, and finally residual memory effects corresponding to slow the recovery of the cell’s altered physiological processes. The speed and the intensity at which the previous steps happen will drive the transfection efficiency and eventually the cytotoxicity of electroporation. For the membrane to recover and stabilize after electroporation, the electric field should not be greater than a certain critical threshold. Molecular dynamic (MD) simulations modeled the effect of an electric pulse across a simple lipid bilayer. Although pure lipid bilayer is not representing transmembrane proteins, cholesterol and the remaining heterogeneity embedded within the plasma membrane, it is good enough to give insights about electric field induced pore formation. According to MD, a strong enough electric field will induce water molecules to form small clusters on both sides of the membrane that will extend until they bridge over the plasma membrane into a water finger protrusion. Depending on the electric field strength, the protrusion will expand into a pore or not (Kotnik et al., 2019). After electroporation, if the electric field did not reach the critical high threshold, the plasma membrane returns to its standard transmembrane voltage values under which pores are not stable and collapses quickly. It is assumed that electric-field induced membrane permeabilization takes place in parts of the cell membrane, where potential difference has been brought at its critical value around 200–300 mV (Escoffre et al., 2009).

In my thesis project, I focus on application of electroporation of biocompatible gold nanoparticle base probes into living cells. I used the Neon™ transfer system (Invitrogen, Figure 7B). This apparatus was initially developed to transform cells with nucleic acids but it has been shown previously that proteins are also successfully delivered (Freund et al., 2013). This apparatus is based on a device developed by Jeong Ah Kim and collaborators (Kim et al., 2008). A special tip with an inner gold rod is used to act both as a piston to draw in the electroporation mix and as an electrode in direct contact with the mix (Figure 7A). The sample is sucked inside the tip and stays between the piston/electrode and the edge of the loaded tip which is placed in an electrolytic buffer; millimeters away from a second electrode (Figure 7C). Upon electroporation, the electric field is conducted inside the special tip to the gold piston. After electroporation, cells can directly be released in culture plates or flasks in media free of any antibiotics. By getting free of cuvettes, or electroporation plates, these methods get rid of additional pipetting steps that can increase possible contamination and harm the very fragile cells post electroporation. There are also many advantages of having the electroporation happening in a tip compared to a large volume cuvette: tips are channeling the electric field within them by minimizing the surface area of the electrodes. This system is advertised as having a more uniform electric field compared to classical cuvette based electroporation implying a more uniform transfection rate on the overall set of cells.

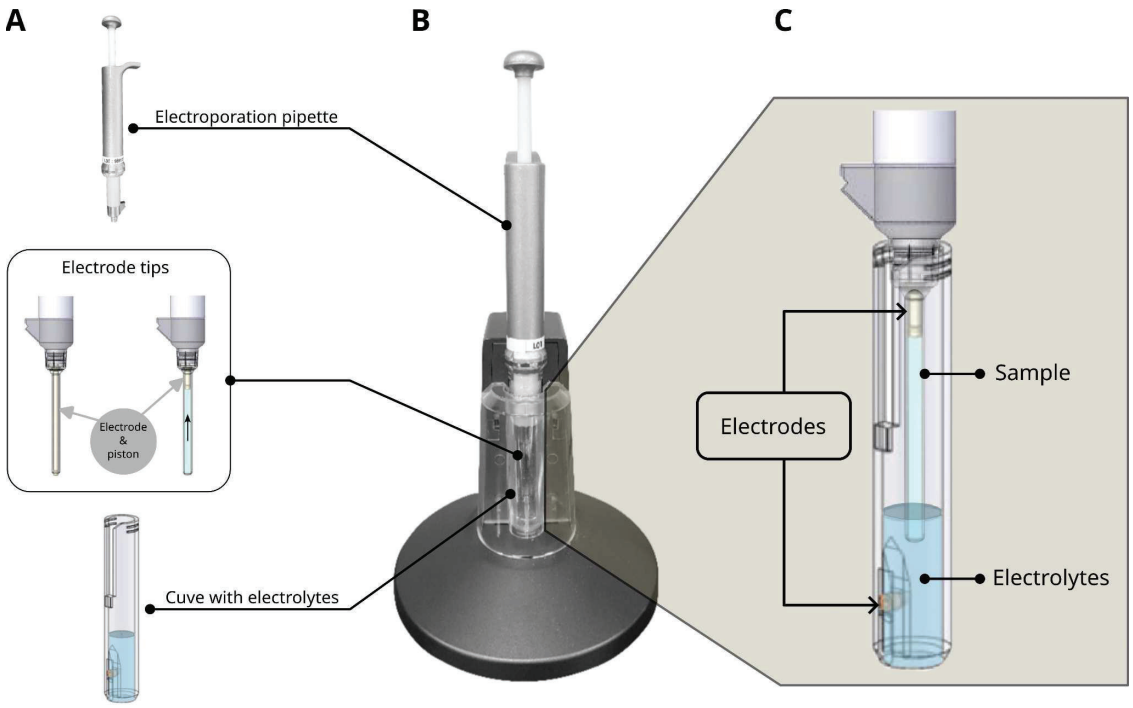


**Figure 7 .** Neon™ electroporation system. The system uses a pipette to hold the electroporation mix into a 10 µl electrode tip (A). The pipette is inserted into a stand and the electrode tip is placed in a cuvette with electrolyte (B). The electrical potential is then applied to the electrodes, one at the base of the tip and the other in the cuvette (C ) (adapted from the Neon™ Electroporation System User Manual).

## Case study: Polymerase II

In eukaryotes, RNA polymerase II (Pol II) is the enzyme responsible for the transcription of DNA into messenger RNA (mRNA) within the cell's nucleus. This vital cellular function is one of the two main steps of the molecular biology dogma and is highly regulated. The atomic structure of Pol II has been determined through x-ray crystallography by the group of Roger Kornberg in 2000 (Cramer et al., 2001, 2000) and this outstanding achievement was rewarded by a Nobel Prize in Chemistry in 2006. More than 10.000 liters of yeast cell culture was needed to perform all the crystallisation trials and this tour de force aligned with the improved performance of cryo electron microscopy. With a few exceptions, all further structural studies of functional Pol II complexes were performed by single particle cryo electron microscopy. Among its various states, the structure of an inactive non crystallized Pol II in its monomeric form remains unsolved. This lack of structural information leaves questions about how Pol II is maintained in an inactive state and the possible roles of its monomeric form in transcription regulation or enzyme storage. Pol II is a globular ellipsoid-like protein with dimensions of 12 nanometers for its semi-major axis and 10 nanometers for its semi-minor axis. The complete Pol II holoenzyme is assembled from 12 sub-units from which 10 constitute the core enzyme, sufficient to transcribe (Figure 8 ; Armache et al., 2003).

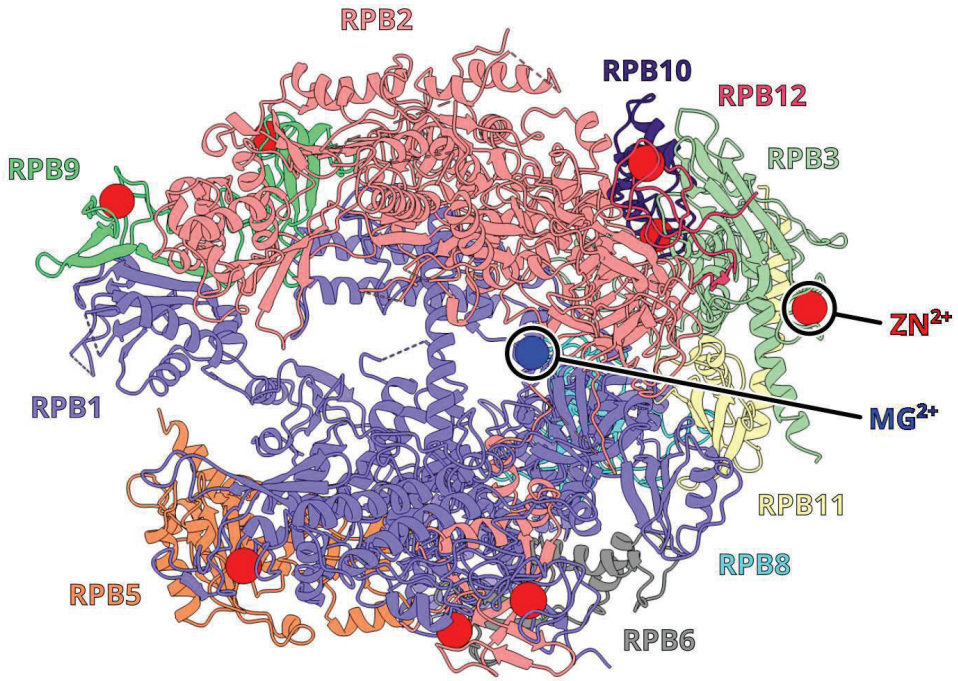


**Figure 8 .** The structural complexity of eukaryotic RNA Pol II (Pol II) is exemplified by the 10-subunit yeast Pol II (PDB ID: 1I50; Cramer et al., 2001). In addition to the subunits highlighted in different colors, the positions of functionally important magnesium and zinc atoms are shown.

Transcription is a multi state process undergoing closed pre-initiation, open initiation, abortive initiation or promoter escape into elongation, pausing and termination (Wade and Struhl, 2008). Pol II is first recruited to gene promoters through the combined action of gene-specific transcription factors that bookmask the gene of interest and transcription coactivators that modify the structure of chromatin to facilitate transcription. The binding of the general transcription factor TBP to the gene promoter triggers the sequential assembly of a pre-initiation complex (PIC) formed by the general transcription factors TFIIA, TFIIB, TFIIC, TFIID, TFIIE and TFIIH. The transition from an inactive state to transcriptionally active Pol II requires the kinase enzymatic activity of TFIIH that phosphorylates specific residues of the C-terminal domain (CTD) repeat of the largest Pol II subunit.

Several high-resolution structures of Pol II within the PIC (Aibara et al., 2021b) reveals its interactions with general transcription factors and promoter DNA (He et al., 2016, 2013; Louder et al., 2016; Murakami et al., 2013; Schilbach et al., 2021, 2017). These studies highlight the intricate coordination required for transcription initiation, including the precise positioning of Pol II at the promoter and the unwinding of DNA to allow RNA synthesis. These structural studies provide critical insights into Pol II's regulatory states, from its inactive forms to its central role in initiating transcription, underscoring the complexity of transcriptional control (Figure 8). Although the general structural framework has been confirmed by genome wide colocalization studies using Chromatin Immuno Purification (ChIP) approaches followed by massive sequencing, alternative assembly pathways have been proposed. No structural data is currently available on *in vivo* assembled PICs and even less so about PICs in their native *in situ* state. In a test tube, TFIIA, B,D,E,F,H, triphosphate ribonucleotides, pol II and double strand linear DNA are the minimum requirements for transcription to happen. In the cell environment, the transcription is taking place in the middle of a sea of molecules densely packed in the nucleus where DNA is not directly accessible as it is organized in regions of varying density interacting with proteins to form chromatin.

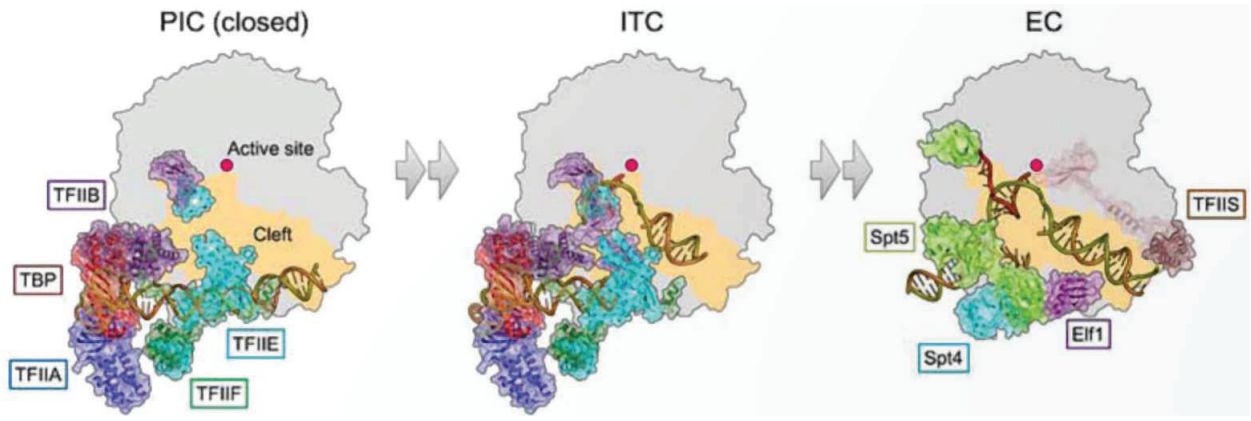


**Figure 8.** Transcription requires a transition from the pre-initiation complex (PIC) to the initial transcribing complex (ITC) and then to the elongation complex (EC). (adapted from Ehara and Sekine, 2018)

## Chromatin organization

In eukaryotes, the genetic information is packaged through a hierarchy of folding events. At the first level DNA is wrapped around an histone octamer to form the nucleosome core particle whose atomic structure has been unveiled (Luger et al., 1997). The fundamental repeated element of chromatin, the nucleosome, is composed of the core particle flanked by linker DNA which connects successive nucleosomes and variable amounts of linker histone H1 (Figure 9).

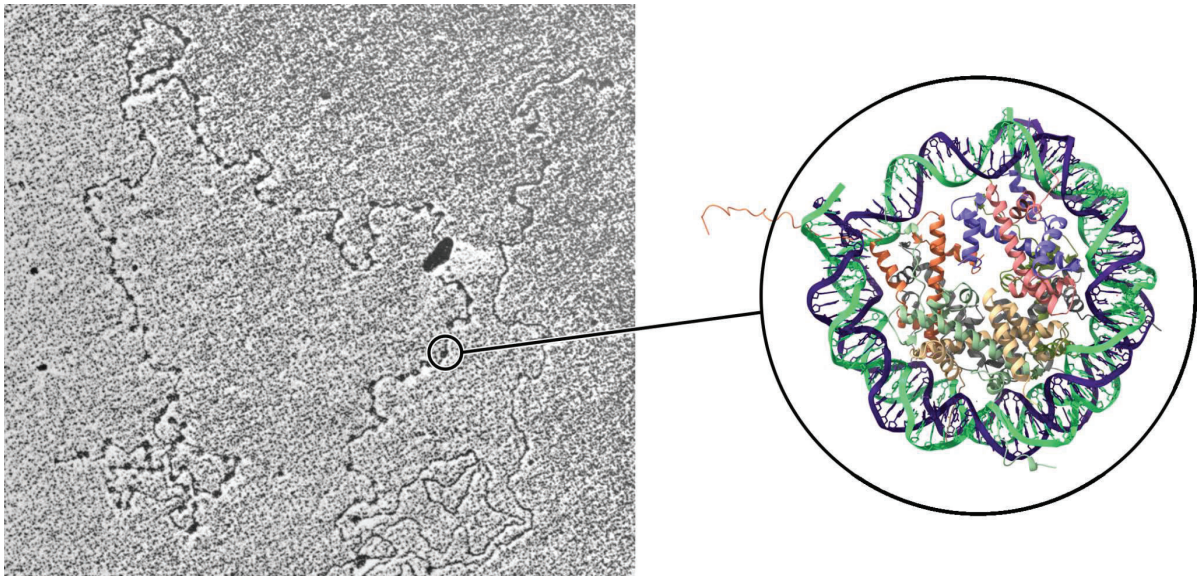

**Figure 9.** One of the pioneering EM visualizations of isolated chromatin fibers (adapted from Oudet et al., 1975). In this low-resolution image, nucleosomes look like beads on a string. The structure of the nucleosome (right) was later determined at the atomic level by X-ray crystallography (PDB ID : 1AOI; Luger et al., 1997).

In low ionic strength solutions, purified chromatin appears as an extended 11 nm fiber formed by a linear beads-on-a-string nucleosomal array that compacts into 30 nm fibers in physiological ionic strength and in the presence of histone H1 (Oudet et al., 1975; Thoma and Koller, 1977). Higher order chromatin organization in intact nuclei is still a matter of debate. Direct electron microscopy imaging of nuclear sections described highly compact electron dense chromatin compartments corresponding mostly to transcriptionally inactive chromatin and a variety of packing modes ranging from less compact to extended domains. An interchromatin space, loaded with soluble complexes involved in transcription, epigenetic modifications, RNA maturation and DNA replication factors is surrounding the chromatin domains. These observations have provided little information on the precise higher order chromatin organization and in particular the 30 nm fibers could not be

confirmed as the fundamental *in vivo* secondary structure of chromatin (Bouchet-Marquis et al., 2006; Eltsov et al., 2008). The current conception, based initially upon cryo-EM of cryo-sections, is that the 30-nm chromatin fiber represents a rather peculiar form of the compact chromatin that may be found in highly specialized terminally differentiated cell types, such as chicken erythrocytes, starfish spermatozoids (Scheffer et al., 2011), while the 30-nm chromatin fiber does not exist in the majority of tissues *in vivo*. Furthermore, histones are modified by a plethora of post translational modifications which can affect nucleosome stability, higher order chromatin organization or contribute to the recruitment of specific proteins that will either stimulate nuclear functions or maintain repressed chromatin states. Little is known about the chromatin structures of defined epigenetic states as induced directly or indirectly by these histone modifications, especially the chromatin structures that govern the constitutively and transiently repressed states.

Higher levels of chromatin organization were revealed by chromosome conformation capture (3C to 5C) experiments (Dekker et al., 2002) which identify and map preferential associations between co-regulated genes at long distances (Schoenfelder et al., 2010). Interchromosomal interaction maps disclosed topologically associated chromatin domains (TADs) with a relatively conserved dimension of 400-500 kbp suggesting that these domains may constitute universal chromosome building blocks (Figure 10, topologically associated domains). These interaction data have been modelled to provide a map of the whole genome but up-to-now these structural elements, as well as the associated chromatin loops, have not been visualized *in situ*. One possible reason is that the size of these structures is challenging to resolve in transmission electron microscopy. A characteristic TAD would contain around 2000 nucleosomes which, if organized as a random coil, would generate chromatin domains 100 to 200 nm in size. Such irregular structure could well have been overlooked in 70 to 100 nm thick sections and need to be reinvestigated in the context of the whole nucleus by FIB-SEM microscopy and at molecular resolution by cryo-electron tomography.

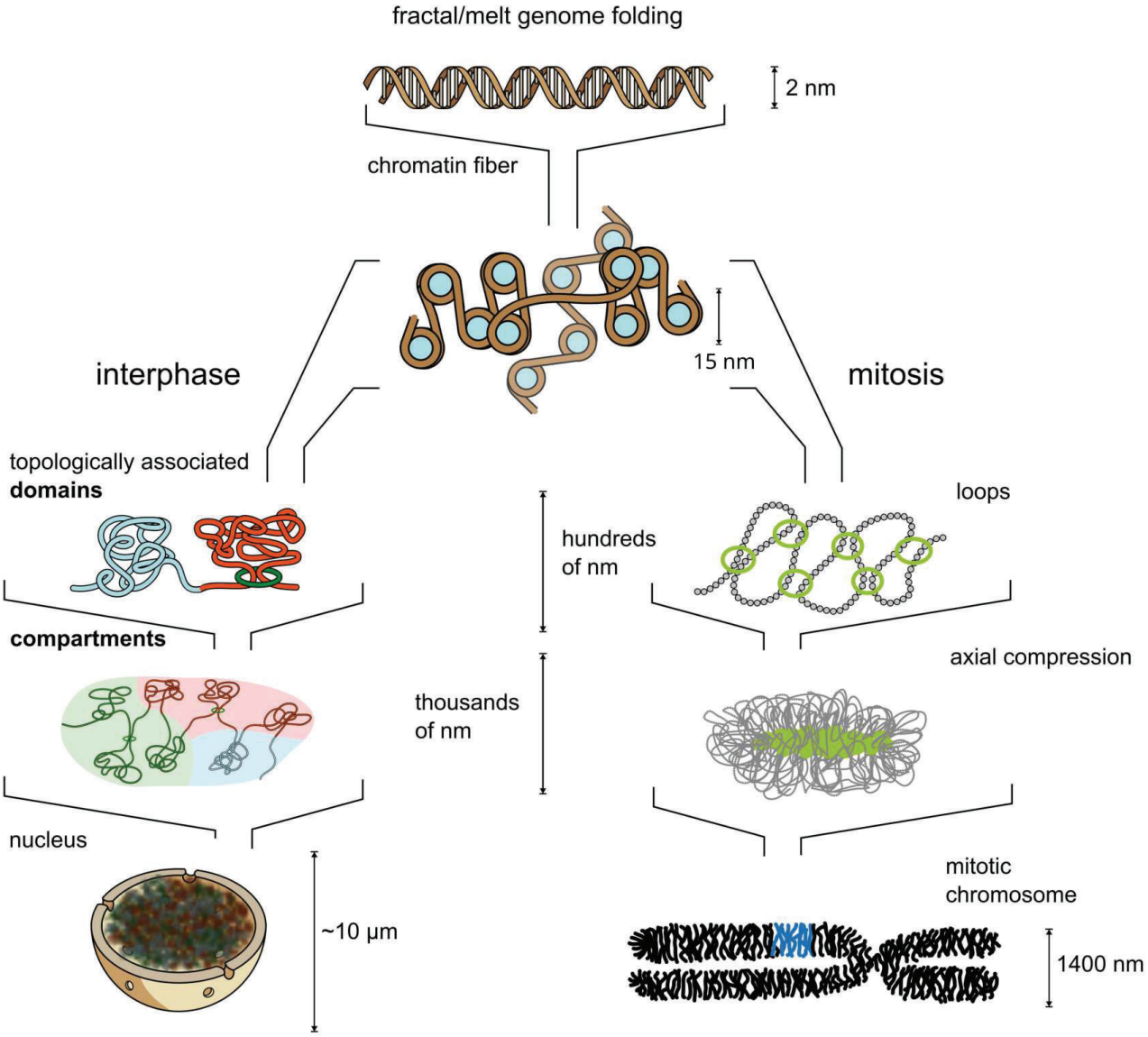


**Figure 10**. A current model of chromatin organization in interphase and mitosis (Moraru and Schalch, 2019).

## Chromatin and transcription

Chromatin is considered as a general transcriptional repressor that impedes access of transcription factors and RNA pol II to the genetic information. Chromatin structure acts as a fundamental player of epigenetic processes that regulate cell fate and permit the establishment of a cell-type specific gene expression program by limiting the fraction of the genome that can be transcribed. Little is currently known about the specific chromatin structures established for constitutively versus transiently repressed transcriptional states and the precise molecular interactions between epigenetically modified nucleosomes and regulatory proteins. On top of the different chromatin states, poorly understood long range chromatin interactions between transcriptional enhancers play a crucial role in regulated gene expression. These interactions are particularly important in hormonal regulation of gene expression networks where most of the active nuclear hormone responsive elements are placed more than 5 kbp or hundreds of nucleosomes away from the transcription start site of the target gene. In cancer it was further shown that chromosomal translocations often reorganize such regulatory genomic regions and perturb the gene expression profiles. Such long range chromatin loops have been postulated but were never imaged directly at high resolution.

The structural organization of transcription units within the cell has been actively studied for more than five decades (Monneron and Bernhard, 1969). Pioneering electron microscopy approaches identified the border of condensed chromatin domains as the major site for transcription (Kizilyaprak et al., 2010) and perichromatin fibrils as the *in situ* form of the nascent transcript reviewed in (Fakan and Puvion, 1980). However to date the molecular organization of a transcription unit, the identification of a short-lived transcription initiation event or the actual chromatin structure of a transcribed gene have never been imaged *in cellulo*.

The number of proteins and processes involved in the transcription machinery is substantial and the organization of such events within the compact but diffuse environment of the cell nucleus raises questions. It was first observed that nascent mRNA of resin embedded cells was localized in discrete spots (Jackson et al., 1993) and later confirmed *in vivo* by super resolution fluorescence (Figure 11 ; Cisse et al., 2013). These live cell imaging revealed the nuclear distribution of the transcription reaction and its dynamics (Darzacq et al., 2009; Hübner et al., 2013), and led to changes in paradigm where promoters are recruited towards transcription condensates. These condensates were baptised transcription factories and are suspected to gather polymerases, general transcription factors and everything needed for the transcription machinery to function in a determined anchored place within the nucleus that can coordinate the transcription of sets of genes located on different chromosomes (Pombo et al., 2000). These observations lead to new concepts such as the presence of nuclear sub-compartments associated with particular gene expression and chromatin states (Fraser and Bickmore, 2007; Gasser, 2002; Taddei et al., 2006).

Part of the transcription process is dictated by the pol II C-terminal domain which incorporates a sequence with 52 tandem repeats of an heptapeptide with the following consensus sequence YSPTSPS (Hsin and Manley, 2012). The activity of pol II is regulated by specific phosphorylation patterns of the CTD's repeated amino acids with serine 2 and serine 5 as preferential targets of transcription factors to regulate the enzyme activity. The unphosphorylated CTD tail of inactive pol II is compacted in space with an overall length of 100 Å, whereas the phosphorylated CTD of active polymerase forms a floating tail that can reach 650 Å in length (Hsin and Manley, 2012).

In recent studies the intrinsically disordered CTD tail is suspected to induce pol II and mediator clustering in a liquid-like phase separation (Flores-Solis et al., 2023; Schuster et al., 2020). In this model the transcription machinery would be phase separated in different condensates depending on the transcription phase with initiation and elongation dedicated condensates (Cramer, 2019). In liquid phase separated condensates molecular interactions are different as the content of water is reduced leading to smaller dielectric constant than in the cellular diffuse area. This particular environment was shown to be prone to transcription with partially disassembled histones, easy to open DNA strands and boosted enzyme activity (Palacio and Taatjes, 2022). Multiple studies are providing proof consistent with whether liquid phase separation induces the formation of dynamic transcription condensates or within a hub where transcription would be organized within rather fixed transcription factories.

A compromise exists where the flexibility of condensates are needed to bear with highly transcribing genes whereas transcription factories might be predominant for other less expressed genes with hubs rapidly created to support transcription on a case-by-case basis (Palacio and Taatjes, 2022). Finally, to this day, the transcription machinery organisation *in vivo* is still under investigation with no molecular scale high resolution image to represent it. Transcription factories or phase separated condensates are however highly controversial because the clustering of RNA Pol II molecules seems to be short lived and not compatible with actively transcribed genes but might be correlated with transcription initiation (Cisse et al., 2013). The possibility to visualize such a cluster at molecular resolution would shed new light on this debate.

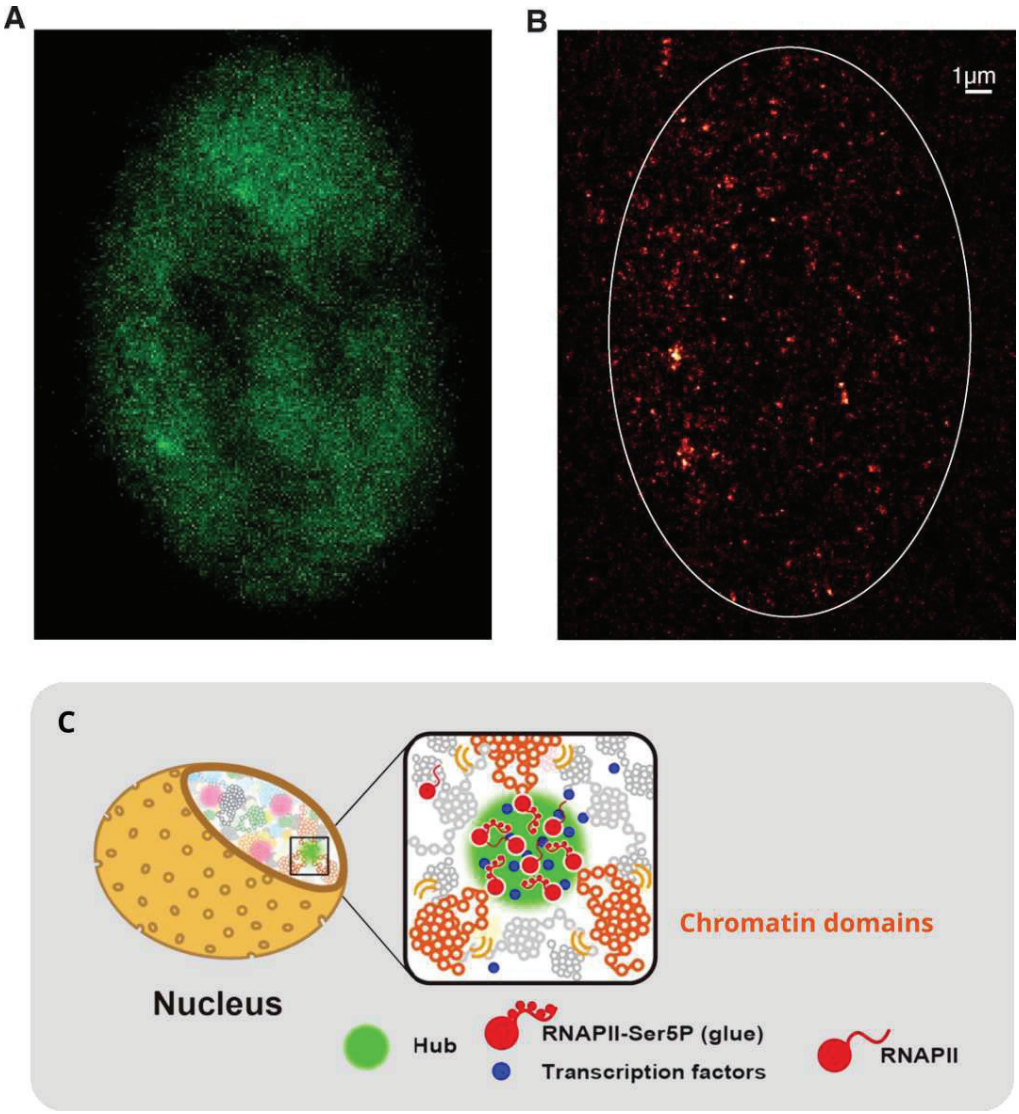


**Figure 11 .** Live super-resolution imaging of Pol II's rpb1 subunit tagged with the photoconvertible Dendra2 fluorescent protein. (A) Diffuse green fluorescence signal from Dendra2 before photo-activation resulting in a classical resolution limited fluorescence image. (B) Super resolution reconstruction of PALM images of photo-activated Dendra2 reveals the presence of Pol II clusters (adapted from Cisse et al., 2013). (C) A model of transcription -related condensate, also called transcription factories, postulating that active genes expand from chromatin domains and enter the condensates accumulating transcription factors and POL II, adapted from (Hansen et al., 2021).

*In vitro* studies failed up to now to explain the mechanisms of long range interactions between distant genomic loci that play essential roles in the regulation of gene expression. Pol II is likely to exist in different functional states, some of which have been described: the free enzyme or the enzymes stalled downstream of the promoter waiting for regulatory signals to start transcription, others are still poorly described. In the cellular context transcription and RNA processing are co-transcriptional processes and the spliceosome is likely to be associated with the transcribing enzyme forming a yet uncharted structure much larger than the current models of a transcribing Pol II enzyme.

Interestingly, structural insights have been gained for the inactive floating Pol II dimer. The study of (Aibara et al., 2021a) provides a detailed view of the dimeric configuration. It reveals the molecular interfaces that stabilize the Pol II dimer, suggesting potential physiological roles, such as a reservoir state or a regulatory mechanism for the enzyme. This dimeric form may represent an intermediate state in Pol II assembly or a response to specific cellular conditions. Insights for a similar mechanism was suggested for RNA polymerase I, responsible for ribosomal DNA (rDNA) transcription; the dimerization was shown to be regulated *in vitro* by the Rrn3 transcription factor (Pilsl et al., 2016). There is currently no evidence that such a regulatory mechanism exists *in vivo* and whether Pol II dimers are present in the cell nucleus.

# Objectives

As discussed above, the organization of *in situ* transcription remains poorly understood, and key questions related to the existence of inactive Pol II dimers, the long-range organization of transcriptional units, their binding to chromatin, the coupling of transcription to mRNA processing, and the role of transcriptional condensates remain largely unanswered.

Pol II, being a relatively small molecule, interacts with numerous other components during transcription. This, combined with the crowded nuclear environment, presents a significant challenge for its direct shape-based identification. These limitations underscore the need for *in situ* probes capable of visualizing and localizing Pol II at molecular resolution by cellular cryo-ET.

At the beginning of my PhD project, my primary goal was to gain initial insights into Pol II distribution within the cell nucleus at molecular resolution using cryo-ET. However, numerous technical challenges emerged, particularly concerning the preparation and application of nanogold probes for *in vivo* labeling. These challenges highlighted unexpected limitations of existing approaches and shifted my focus as multiple steps needed to be optimized to move forward. While *in situ* mapping Pol II remains a long-term objective, I prioritized the development of robust pipelines for *in vivo* labeling with nanogold probes using electroporation and their subsequent localization in cryo-tomograms.

The key axes of my methodology improvement work are outlined below:

- Bringing evidence that 2 nm gold nanoparticles are visible *in situ* by cryoET of cryo sections (Chapter I, Publication 1)
- Optimization of the probe delivery using the Au•NLS probe (Chapter I, Section 1.3)
- Optimization of Anti-Pol II nanogold probe preparation (Chapter I, Publication 2, Section 1.4 )
- Initial experiments towards the development of universal probes based on anti-GFP nanobodies (Chapter I, Section 1.4.5)
- Post transfection sample preparation and optimization for Cryo-ET (Chapter I, Section 1.5)
- Optimization of volumetric imaging on the available FIB-SEM instrument (Carl Zeiss Auriga 60, Chapter II), detectors use in cryogenic conditions for cell localization and sample quality assessment (Chapter I, Section 1.5.3), and development of approaches for cryo-FIB lamella preparation towards improved structure preservation (Chapter I, Section 1.5.4)

These advancements aim to establish a foundation for high-resolution transcription studies while addressing broader challenges in *in vivo* labeling and cryo-ET visualization. The protocols I developed are designed for general applicability, enabling their use of mapping for different molecular targets and their localization in cryo-ET data.

## Bibliography


Abbe, E., 1873. Beiträge zur Theorie des Mikroskops und der mikroskopischen Wahrnehmung. Arch. Für Mikrosk. Anat. 9, 413–468. https://doi.org/10.1007/BF02956173

Adrian, M., Dubochet, J., Lepault, J., McDowall, A.W., 1984. Cryo-electron microscopy of viruses. Nature 308, 32–36. https://doi.org/10.1038/308032a0

Aibara, S., Dienemann, C., Cramer, P., 2021a. Structure of an inactive RNA polymerase II dimer. Nucleic Acids Res. 49, 10747–10755. https://doi.org/10.1093/nar/gkab783

Aibara, S., Schilbach, S., Cramer, P., 2021b. Structures of mammalian RNA polymerase II pre-initiation complexes. Nature 594, 124–128. https://doi.org/10.1038/s41586-021-03554-8

Al-Amoudi, A., Chang, J.-J., Leforestier, A., McDowall, A., Salamin, L.M., Norlén, L.P.O., Richter, K., Blanc, N.S., Studer, D., Dubochet, J., 2004. Cryo-electron microscopy of vitreous sections. EMBO J. 23, 3583–3588. https://doi.org/10.1038/sj.emboj.7600366

Armache, K.-J., Kettenberger, H., Cramer, P., 2003. Architecture of initiation-competent 12-subunit RNA polymerase II. Proc. Natl. Acad. Sci. U. S. A. 100, 6964–6968. https://doi.org/10.1073/pnas.1030608100

Ballerini, M., Milani, M., Batani, D., Squadrini, F., 2001. Focused ion beam techniques for the analysis of biological samples: A revolution in ultramicroscopy?, in: Conchello, J.-A., Cogswell, C.J., Wilson, T. (Eds.), . Presented at the BiOS 2001 The International Symposium on Biomedical Optics, San Jose, CA, p. 92. https://doi.org/10.1117/12.424523

Bepler, T., Kelley, K., Noble, A.J., Berger, B., 2020. Topaz-Denoise: general deep denoising models for cryoEM and cryoET. Nat. Commun. 11, 5208. https://doi.org/10.1038/s41467-020-18952-1

Berger, C., Dumoux, M., Glen, T., Yee, N.B. -y., Mitchels, J.M., Patáková, Z., Darrow, M.C., Naismith, J.H., Grange, M., 2023. Plasma FIB milling for the determination of structures in situ. Nat. Commun. 14, 629. https://doi.org/10.1038/s41467-023-36372-9

Betzig, E., Patterson, G.H., Sougrat, R., Lindwasser, O.W., Olenych, S., Bonifacino, J.S., Davidson, M.W., Lippincott-Schwartz, J., Hess, H.F., 2006. Imaging Intracellular Fluorescent Proteins at Nanometer Resolution. Science 313, 1642–1645. https://doi.org/10.1126/science.1127344

Bienz, K., Egger, D., Pasamontes, L., 1986. Electron microscopic immunocytochemistry. Silver enhancement of colloidal gold marker allows double labeling with the same primary antibody. J. Histochem. Cytochem. 34, 1337–1342. https://doi.org/10.1177/34.10.3745912

Bogner, A., Jouneau, P.-H., Thollet, G., Basset, D., Gauthier, C., 2007. A history of scanning electron microscopy developments: Towards “wet-STEM” imaging. Micron 38, 390–401. https://doi.org/10.1016/j.micron.2006.06.008

Bouchet-Marquis, C., Dubochet, J., Fakan, S., 2006. Cryoelectron microscopy of vitrified sections: a new challenge for the analysis of functional nuclear architecture. Histochem. Cell Biol. 125, 43–51. https://doi.org/10.1007/s00418-005-0093-x

Buchholz, T.-O., Jordan, M., Pigino, G., Jug, F., 2019. Cryo-CARE: Content-Aware Image Restoration for Cryo-Transmission Electron Microscopy Data, in: 2019 IEEE 16th International Symposium on Biomedical Imaging (ISBI 2019). Presented at the 2019 IEEE 16th International Symposium on Biomedical Imaging (ISBI), IEEE, Venice, Italy, pp. 502–506. https://doi.org/10.1109/ISBI.2019.8759519

Buffoli, B., Rinaldi, F., Labanca, M., Sorbellini, E., Trink, A., Guanziroli, E., Rezzani, R., Rodella, L.F., 2014. The human hair: from anatomy to physiology. Int. J. Dermatol. 53, 331–341. https://doi.org/10.1111/ijd.12362

Caffrey, B.J., Pedrazo-Tardajos, A., Liberti, E., Gaunt, B., Kim, J.S., Kirkland, A.I., 2024. Liquid Phase Electron Microscopy of Bacterial Ultrastructure. Small 20, 2402871. https://doi.org/10.1002/smll.202402871

Cisse, I.I., Izeddin, I., Causse, S.Z., Boudarene, L., Senecal, A., Muresan, L., Dugast-Darzacq, C., Hajj, B., Dahan, M., Darzacq, X., 2013. Real-Time Dynamics of RNA Polymerase II Clustering in Live Human Cells. Science 341, 664–667. https://doi.org/10.1126/science.1239053

Costa, T.R.D., Ignatiou, A., Orlova, E.V., 2017. Structural Analysis of Protein Complexes by Cryo Electron Microscopy, in: Journet, L., Cascales, E. (Eds.), Bacterial Protein Secretion Systems, Methods in Molecular Biology. Springer New York, New York, NY, pp. 377–413. https://doi.org/10.1007/978-1-4939-7033-9_28

Cramer, P., 2019. Organization and regulation of gene transcription. Nature 573, 45–54. https://doi.org/10.1038/s41586-019-1517-4

Cramer, P., Bushnell, D.A., Fu, J., Gnatt, A.L., Maier-Davis, B., Thompson, N.E., Burgess, R.R., Edwards, A.M., David, P.R., Kornberg, R.D., 2000. Architecture of RNA Polymerase II and Implications for the Transcription Mechanism. Science 288, 640–649. https://doi.org/10.1126/science.288.5466.640

Cramer, P., Bushnell, D.A., Kornberg, R.D., 2001. Structural basis of transcription: RNA polymerase II at 2.8 angstrom resolution. Science 292, 1863–1876. https://doi.org/10.1126/science.1059493

Cybulski, J.S., Clements, J., Prakash, M., 2014. Foldscope: Origami-Based Paper Microscope. PLoS ONE 9, e98781. https://doi.org/10.1371/journal.pone.0098781

Danev, R., Buijsse, B., Khoshouei, M., Plitzko, J.M., Baumeister, W., 2014. Volta potential phase plate for in-focus phase contrast transmission electron microscopy. Proc. Natl. Acad. Sci. 111, 15635–15640. https://doi.org/10.1073/pnas.1418377111

Darzacq, X., Yao, J., Larson, D.R., Causse, S.Z., Bosanac, L., De Turris, V., Ruda, V.M., Lionnet, T., Zenklusen, D., Guglielmi, B., Tjian, R., Singer, R.H., 2009. Imaging Transcription in Living Cells. Annu. Rev. Biophys. 38, 173–196. https://doi.org/10.1146/annurev.biophys.050708.133728

De Goede, M., Johlin, E., Sciacca, B., Boughorbel, F., Garnett, E.C., 2017. 3D multi-energy deconvolution electron microscopy. Nanoscale 9, 684–689. https://doi.org/10.1039/C6NR07991A

Dekker, J., Rippe, K., Dekker, M., Kleckner, N., 2002. Capturing Chromosome Conformation. Science 295, 1306–1311. https://doi.org/10.1126/science.1067799

Denk, W., Horstmann, H., 2004. Serial block-face scanning electron microscopy to reconstruct three-dimensional tissue nanostructure. PLoS Biol. 2, e329. https://doi.org/10.1371/journal.pbio.0020329

Dubochet, J., 2018. On the Development of Electron Cryo-Microscopy (Nobel Lecture). Angew. Chem. Int. Ed. 57, 10842–10846. https://doi.org/10.1002/anie.201804280

Dubochet, J., 2012. Cryo-EM--the first thirty years. J. Microsc. 245, 221–224. https://doi.org/10.1111/j.1365-2818.2011.03569.x

Dubochet, J., Lepault, J., Freeman, R., Berriman, J.A., Homo, J. -C., 1982. Electron microscopy of frozen water and aqueous solutions. J. Microsc. 128, 219–237. https://doi.org/10.1111/j.1365-2818.1982.tb04625.x

Dubochet, J., McDowall, A.W., 1981. Vitrification of pure water for electron microscopy. J. Microsc. 124, 3–4. https://doi.org/10.1111/j.1365-2818.1981.tb02483.x

Egelman, E.H., 2024. The myth of high-resolution liquid phase biological electron microscopy. Protein Sci. 33, e5125. https://doi.org/10.1002/pro.5125

Ehara, H., Sekine, S., 2018. Architecture of the RNA polymerase II elongation complex: new insights into Spt4/5 and Elf1. Transcription 9, 286–291. https://doi.org/10.1080/21541264.2018.1454817

Eisenstein, F., Yanagisawa, H., Kashihara, H., Kikkawa, M., Tsukita, S., Danev, R., 2023. Parallel cryo electron tomography on in situ lamellae. Nat. Methods 20, 131–138. https://doi.org/10.1038/s41592-022-01690-1

Eltsov, M., Grewe, D., Lemercier, N., Frangakis, A., Livolant, F., Leforestier, A., 2018. Nucleosome conformational variability in solution and in interphase nuclei evidenced by cryo-electron microscopy of vitreous sections. Nucleic Acids Res. 46, 9189–9200. https://doi.org/10.1093/nar/gky670

Eltsov, M., MacLellan, K.M., Maeshima, K., Frangakis, A.S., Dubochet, J., 2008. Analysis of cryo-electron microscopy images does not support the existence of 30-nm chromatin fibers in mitotic chromosomes in situ. Proc. Natl. Acad. Sci. 105, 19732–19737. https://doi.org/10.1073/pnas.0810057105

Escoffre, J.-M., Portet, T., Wasungu, L., Teissié, J., Dean, D., Rols, M.-P., 2009. What is (Still not) Known of the Mechanism by Which Electroporation Mediates Gene Transfer and Expression in Cells and Tissues. Mol. Biotechnol. 41, 286–295. https://doi.org/10.1007/s12033-008-9121-0

Fakan, S., Puvion, E., 1980. The Ultrastructural Visualization of Nucleolar and Extranucleolar RNA Synthesis and Distribution, in: International Review of Cytology. Elsevier, pp. 255–299. https://doi.org/10.1016/S0074-7696(08)61962-2

Faulk, W.P., Taylor, G.M., 1971. An immunocolloid method for the electron microscope. Immunochemistry 8, 1081–1083. https://doi.org/10.1016/0019-2791(71)90496-4

Flores-Solis, D., Lushpinskaia, I.P., Polyansky, A.A., Changiarath, A., Boehning, M., Mirkovic, M., Walshe, J., Pietrek, L.M., Cramer, P., Stelzl, L.S., Zagrovic, B., Zweckstetter, M., 2023. Driving forces behind phase separation of the carboxy-terminal domain of RNA polymerase II. Nat. Commun. 14, 5979. https://doi.org/10.1038/s41467-023-41633-8

Fraser, P., Bickmore, W., 2007. Nuclear organization of the genome and the potential for gene regulation. Nature 447, 413–417. https://doi.org/10.1038/nature05916

Freund, G., Sibler, A.-P., Desplancq, D., Oulad-Abdelghani, M., Vigneron, M., Gannon, J., Van Regenmortel, M.H., Weiss, E., 2013. Targeting endogenous nuclear antigens by electrotransfer of monoclonal antibodies in living cells. mAbs 5, 518–522. https://doi.org/10.4161/mabs.25084

Fung, H.K.H., Hayashi, Y., Salo, V.T., Babenko, A., Zagoriy, I., Brunner, A., Ellenberg, J., Müller, C.W., Cuylen-Haering, S., Mahamid, J., 2023. Genetically encoded multimeric tags for subcellular protein localization in cryo-EM. Nat. Methods 20, 1900–1908. https://doi.org/10.1038/s41592-023-02053-0

Garner, L.F., Yap, M.K.H., 1997. Changes in ocular dimensions and refraction with accommodation. Ophthalmic Physiol. Opt. 17, 12–17. https://doi.org/10.1111/j.1475-1313.1997.tb00518.x

Gasser, S.M., 2002. Visualizing Chromatin Dynamics in Interphase Nuclei. Science 296, 1412–1416. https://doi.org/10.1126/science.1067703

Gehl, J., 2003. Electroporation: theory and methods, perspectives for drug delivery, gene therapy and research. Acta Physiol. Scand. 177, 437–447. https://doi.org/10.1046/j.1365-201X.2003.01093.x

Griffiths, G., 1993. Fine Structure Immunocytochemistry. Springer Berlin Heidelberg, Berlin, Heidelberg. https://doi.org/10.1007/978-3-642-77095-1

Groysbeck, N., Donzeau, M., Stoessel, A., Haeberle, A.-M., Ory, S., Spehner, D., Schultz, P., Ersen, O., Bahri, M., Ihiawakrim, D., Zuber, G., 2021. Gold labeling of a green fluorescent protein (GFP)-tag inside cells using recombinant nanobodies conjugated to 2.4 nm thiolate-coated gold nanoparticles. Nanoscale Adv. 3, 6940–6948. https://doi.org/10.1039/d1na00256b

Hagen, W.J.H., Wan, W., Briggs, J.A.G., 2017. Implementation of a cryo-electron tomography tilt-scheme optimized for high resolution subtomogram averaging. J. Struct. Biol., Electron Tomography 197, 191–198. https://doi.org/10.1016/j.jsb.2016.06.007

Hansen, J.C., Maeshima, K., Hendzel, M.J., 2021. The solid and liquid states of chromatin. Epigenetics Chromatin 14, 50. https://doi.org/10.1186/s13072-021-00424-5

He, Y., Fang, J., Taatjes, D.J., Nogales, E., 2013. Structural visualization of key steps in human transcription initiation. Nature 495, 481–486. https://doi.org/10.1038/nature11991

He, Y., Yan, C., Fang, J., Inouye, C., Tjian, R., Ivanov, I., Nogales, E., 2016. Near-atomic resolution visualization of human transcription promoter opening. Nature 533, 359–365. https://doi.org/10.1038/nature17970

Hell, S.W., 2009. Microscopy and its focal switch. Nat. Methods 6, 24–32. https://doi.org/10.1038/nmeth.1291

Heymann, J.A.W., Hayles, M., Gestmann, I., Giannuzzi, L.A., Lich, B., Subramaniam, S., 2006. Site-specific 3D imaging of cells and tissues with a dual beam microscope. J. Struct. Biol. 155, 63–73. https://doi.org/10.1016/j.jsb.2006.03.006

Hoffmann, P.C., Kreysing, J.P., Khusainov, I., Tuijtel, M.W., Welsch, S., Beck, M., 2022. Structures of the eukaryotic ribosome and its translational states in situ. Nat. Commun. 13, 7435. https://doi.org/10.1038/s41467-022-34997-w

Hsin, J.-P., Manley, J.L., 2012. The RNA polymerase II CTD coordinates transcription and RNA processing. Genes Dev. 26, 2119–2137. https://doi.org/10.1101/gad.200303.112

Hübner, M.R., Eckersley-Maslin, M.A., Spector, D.L., 2013. Chromatin organization and transcriptional

regulation. Curr. Opin. Genet. Dev. 23, 89–95. https://doi.org/10.1016/j.gde.2012.11.006

Jackson, D.A., Hassan, A.B., Errington, R.J., Cook, P.R., 1993. Visualization of focal sites of transcription within human nuclei. EMBO J. 12, 1059–1065.

Jiang, Z., Jin, X., Li, Y., Liu, S., Liu, X.-M., Wang, Y.-Y., Zhao, P., Cai, X., Liu, Ying, Tang, Y., Sun, X., Liu, Yan, Hu, Y., Li, M., Cai, G., Qi, X., Chen, S., Du, L.-L., He, W., 2020. Genetically encoded tags for direct synthesis of EM-visible gold nanoparticles in cells. Nat. Methods 17, 937–946. https://doi.org/10.1038/s41592-020-0911-z

Kelley, K., Raczkowski, A.M., Klykov, O., Jaroenlak, P., Bobe, D., Kopylov, M., Eng, E.T., Bhabha, G., Potter, C.S., Carragher, B., Noble, A.J., 2022. Waffle Method: A general and flexible approach for improving throughput in FIB-milling. Nat. Commun. 13, 1857. https://doi.org/10.1038/s41467-022-29501-3

Kim, J.A., Cho, K., Shin, M.S., Lee, W.G., Jung, N., Chung, C., Chang, J.K., 2008. A novel electroporation method using a capillary and wire-type electrode. Biosens. Bioelectron. 23, 1353–1360. https://doi.org/10.1016/j.bios.2007.12.009

Kizilyaprak, C., Spehner, D., Devys, D., Schultz, P., 2010. In Vivo Chromatin Organization of Mouse Rod Photoreceptors Correlates with Histone Modifications. PLoS ONE 5, e11039. https://doi.org/10.1371/journal.pone.0011039

Kniestedt, C., Stamper, R., 2003. Visual acuity and its measurement. Ophthalmol. Clin. N. Am. 16, 155–170. https://doi.org/10.1016/S0896-1549(03)00013-0

Knoll, M., Ruska, E., 1932. Das Elektronenmikroskop. Z. F�r Phys. 78, 318–339. https://doi.org/10.1007/BF01342199

Koike, M., Nagayama, A., Nakayama, H., Amako, K., Matsuo, T., 1964. A new immuno-electron microscope technique with use of metal chelate antibody (MCA). J. Electron Microsc. (Tokyo) 13, 133–138.

Kotnik, T., Rems, L., Tarek, M., Miklavčič, D., 2019. Membrane Electroporation and Electropermeabilization: Mechanisms and Models. Annu. Rev. Biophys. 48, 63–91. https://doi.org/10.1146/annurev-biophys-052118-115451

Kremer, J.R., Mastronarde, D.N., McIntosh, J.R., 1996. Computer Visualization of Three-Dimensional Image Data Using IMOD. J. Struct. Biol. 116, 71–76. https://doi.org/10.1006/jsbi.1996.0013

Lister, 1830. On some properties in achromatic object-glasses applicable to the improvement of the microscope. Philos. Trans. R. Soc. Lond. 120, 187–200. https://doi.org/10.1098/rstl.1830.0015

Louder, R.K., He, Y., López-Blanco, J.R., Fang, J., Chacón, P., Nogales, E., 2016. Structure of promoter-bound TFIID and model of human pre-initiation complex assembly. Nature 531, 604–609. https://doi.org/10.1038/nature17394

Lucas, B.A., Grigorieff, N., 2023. Quantification of gallium cryo-FIB milling damage in biological lamellae. Proc. Natl. Acad. Sci. 120, e2301852120. https://doi.org/10.1073/pnas.2301852120

Luger, K., Mäder, A.W., Richmond, R.K., Sargent, D.F., Richmond, T.J., 1997. Crystal structure of the nucleosome core particle at 2.8 Å resolution. Nature 389, 251–260. https://doi.org/10.1038/38444

Marko, M., Hsieh, C., Moberlychan, W., Mannella, C.A., Frank, J., 2006. Focused ion beam milling of vitreous water: prospects for an alternative to cryo-ultramicrotomy of frozen-hydrated biological

samples. J. Microsc. 222, 42–47. https://doi.org/10.1111/j.1365-2818.2006.01567.x

Marko, M., Hsieh, C.-E., MoberlyChan, W.J., Mannella, C.A., Frank, J., 2005. Feasibility of Focused Ion Beam Milling for Preparation of TEM Specimens of Biological Material Embedded in Vitreous Ice. Microsc. Microanal. 11. https://doi.org/10.1017/S1431927605500709

Masters, B.R., 2020. Superresolution Optical Microscopy: The Quest for Enhanced Resolution and Contrast, Springer Series in Optical Sciences. Springer International Publishing, Cham. https://doi.org/10.1007/978-3-030-21691-7

Mastronarde, D.N., Held, S.R., 2017. Automated tilt series alignment and tomographic reconstruction in IMOD. J. Struct. Biol. 197, 102–113. https://doi.org/10.1016/j.jsb.2016.07.011

Maugeri, M., Nawaz, M., Papadimitriou, A., Angerfors, A., Camponeschi, A., Na, M., Hölttä, M., Skantze, P., Johansson, S., Sundqvist, M., Lindquist, J., Kjellman, T., Mårtensson, I.-L., Jin, T., Sunnerhagen, P., Östman, S., Lindfors, L., Valadi, H., 2019. Linkage between endosomal escape of LNP-mRNA and loading into EVs for transport to other cells. Nat. Commun. 10, 4333. https://doi.org/10.1038/s41467-019-12275-6

McDowall, A.W., Chang, J. -J., Freeman, R., Lepault, J., Walter, C.A., Dubochet, J., 1983. Electron microscopy of frozen hydrated sections of vitreous ice and vitrified biological samples. J. Microsc. 131, 1–9. https://doi.org/10.1111/j.1365-2818.1983.tb04225.x

Meacham, J.M., Durvasula, K., Degertekin, F.L., Fedorov, A.G., 2014. Physical Methods for Intracellular Delivery: Practical Aspects from Laboratory Use to Industrial-Scale Processing. SLAS Technol. 19, 1–18. https://doi.org/10.1177/2211068213494388

Minsky, M., 1988. Memoir on inventing the confocal scanning microscope. Scanning 10, 128–138. https://doi.org/10.1002/sca.4950100403

Monneron, A., Bernhard, W., 1969. Fine structural organization of the interphase nucleus in some mammalian cells. J. Ultrastruct. Res. 27, 266–288. https://doi.org/10.1016/S0022-5320(69)80017-1

Moraru, M., Schalch, T., 2019. Chromatin fiber structural motifs as regulatory hubs of genome function? Essays Biochem. 63, 123–132. https://doi.org/10.1042/EBC20180065

Mulders, H., 2003. The use of a SEM/FIB dual beam applied to biological samples. GIT Imaging Microsc, Imaging and microscopy 5, 8–10.

Murakami, K., Elmlund, H., Kalisman, N., Bushnell, D.A., Adams, C.M., Azubel, M., Elmlund, D., Levi-Kalisman, Y., Liu, X., Gibbons, B.J., Levitt, M., Kornberg, R.D., 2013. Architecture of an RNA polymerase II transcription pre-initiation complex. Science 342, 1238724. https://doi.org/10.1126/science.1238724

Nagayama, K., Danev, R., 2008. Phase contrast electron microscopy: development of thin-film phase plates and biological applications. Philos. Trans. R. Soc. Lond. B. Biol. Sci. 363, 2153–2162. https://doi.org/10.1098/rstb.2008.2268

Namork, E., Heier, H.E., 1989. Silver enhancement of gold probes (5–40 nm): Single and double labeling of antigenic sites on cell surfaces imaged with backscattered electrons. J. Electron Microsc. Tech. 11, 102–108. https://doi.org/10.1002/jemt.1060110203

Neselu, K., Wang, B., Rice, W.J., Potter, C.S., Carragher, B., Chua, E.Y.D., 2023. Measuring the effects of ice thickness on resolution in single particle cryo-EM. J. Struct. Biol. X 7, 100085.

https://doi.org/10.1016/j.yjsbx.2023.100085

Neumann, E., Schaefer-Ridder, M., Wang, Y., Hofschneider, P.H., 1982. Gene transfer into mouse lyoma cells by electroporation in high electric fields. EMBO J. 1, 841–845. https://doi.org/10.1002/j.1460-2075.1982.tb01257.x

Orlov, I., Schertel, A., Zuber, G., Klaholz, B., Drillien, R., Weiss, E., Schultz, P., Spehner, D., 2015. Live cell immunogold labeling of RNA polymerase II. Sci. Rep. 5, 8324. https://doi.org/10.1038/srep08324

Oudet, P., Gross-Bellard, M., Chambon, P., 1975. Electron microscopic and biochemical evidence that chromatin structure is a repeating unit. Cell 4, 281–300. https://doi.org/10.1016/0092-8674(75)90149-X

Palacio, M., Taatjes, D.J., 2022. Merging Established Mechanisms with New Insights: Condensates, Hubs, and the Regulation of RNA Polymerase II Transcription. J. Mol. Biol. 434, 167216. https://doi.org/10.1016/j.jmb.2021.167216

Parmenter, C.D., Nizamudeen, Z.A., 2021. Cryo-FIB-lift-out: practically impossible to practical reality. J. Microsc. 281, 157–174. https://doi.org/10.1111/jmi.12953

Patel, S., Ashwanikumar, N., Robinson, E., DuRoss, A., Sun, C., Murphy-Benenato, K.E., Mihai, C., Almarsson, Ö., Sahay, G., 2017. Boosting Intracellular Delivery of Lipid Nanoparticle-Encapsulated mRNA. Nano Lett. 17, 5711–5718. https://doi.org/10.1021/acs.nanolett.7b02664

Peddie, C.J., Genoud, C., Kreshuk, A., Meechan, K., Micheva, K.D., Narayan, K., Pape, C., Parton, R.G., Schieber, N.L., Schwab, Y., Titze, B., Verkade, P., Aubrey, A., Collinson, L.M., 2022. Volume electron microscopy. Nat. Rev. Methods Primer 2, 51. https://doi.org/10.1038/s43586-022-00131-9

Penczek, P.A., 2010. Resolution Measures in Molecular Electron Microscopy, in: Methods in Enzymology. Elsevier, pp. 73–100. https://doi.org/10.1016/S0076-6879(10)82003-8

Pepe, F.A., Finck, H., 1961. THE USE OF SPECIFIC ANTIBODY IN ELECTRON MICROSCOPY. J. Cell Biol. 11, 521–531. https://doi.org/10.1083/jcb.11.3.521

Pilsl, M., Crucifix, C., Papai, G., Krupp, F., Steinbauer, R., Griesenbeck, J., Milkereit, P., Tschochner, H., Schultz, P., 2016. Structure of the initiation-competent RNA polymerase I and its implication for transcription. Nat. Commun. 7, 12126. https://doi.org/10.1038/ncomms12126

Pombo, A., Jones, E., Iborra, F.J., Kimura, H., Sugaya, K., Cook, P.R., Jackson, D.A., 2000. Specialized transcription factories within mammalian nuclei. Crit. Rev. Eukaryot. Gene Expr. 10, 21–29.

Porter, J.R., 1976. Antony van Leeuwenhoek: tercentenary of his discovery of bacteria. Bacteriol. Rev. 40, 260–269. https://doi.org/10.1128/br.40.2.260-269.1976

Riehle, U., 1968. Schnellgefrieren organischer Präparate für die Elektronen-Mikroskopie. Die Vitrifizierung verdünnter wäßriger Lösungen. Chem. Ing. Tech. 40, 213–218. https://doi.org/10.1002/cite.330400504

Roozbahani, G.M., Colosi, P., Oravecz, A., Sorokina, E.M., Pfeifer, W., Shokri, S., Wei, Y., Didier, P., DeLuca, M., Arya, G., Tora, L., Lakadamyali, M., Poirier, M.G., Castro, C.E., 2024. Piggybacking functionalized DNA nanostructures into live cell nuclei. https://doi.org/10.1101/2023.12.30.573746

Rubino, S., Akhtar, S., Melin, P., Searle, A., Spellward, P., Leifer, K., 2012. A site-specific focused-ion-beam lift-out method for cryo Transmission Electron Microscopy. J. Struct. Biol. 180, 572–576. https://doi.org/10.1016/j.jsb.2012.08.012

Rust, M.J., Bates, M., Zhuang, X., 2006. Sub-diffraction-limit imaging by stochastic optical reconstruction microscopy (STORM). Nat. Methods 3, 793–796. https://doi.org/10.1038/nmeth929

Rutten, L., Joosten, B., Schaart, J., De Beer, M., Roverts, R., Gräber, S., Jahnen-Dechent, W., Akiva, A., Macías-Sánchez, E., Sommerdijk, N., 2023. A Cryo-to-Liquid Phase Correlative Light Electron Microscopy Workflow for the Visualization of Biological Processes in Graphene Liquid Cells. https://doi.org/10.1101/2023.05.08.539575

Scheffer, M.P., Eltsov, M., Frangakis, A.S., 2011. Evidence for short-range helical order in the 30-nm chromatin fibers of erythrocyte nuclei. Proc. Natl. Acad. Sci. 108, 16992–16997. https://doi.org/10.1073/pnas.1108268108

Schertel, A., Snaidero, N., Han, H.-M., Ruhwedel, T., Laue, M., Grabenbauer, M., Möbius, W., 2013. Cryo FIB-SEM: Volume imaging of cellular ultrastructure in native frozen specimens. J. Struct. Biol. 184, 355–360. https://doi.org/10.1016/j.jsb.2013.09.024

Schilbach, S., Aibara, S., Dienemann, C., Grabbe, F., Cramer, P., 2021. Structure of RNA polymerase II pre-initiation complex at 2.9 Å defines initial DNA opening. Cell 184, 4064-4072.e28. https://doi.org/10.1016/j.cell.2021.05.012

Schilbach, S., Hantsche, M., Tegunov, D., Dienemann, C., Wigge, C., Urlaub, H., Cramer, P., 2017. Structures of transcription pre-initiation complex with TFIIH and Mediator. Nature 551, 204–209. https://doi.org/10.1038/nature24282

Schiøtz, O.H., Kaiser, C.J.O., Klumpe, S., Morado, D.R., Poege, M., Schneider, J., Beck, F., Klebl, D.P., Thompson, C., Plitzko, J.M., 2024. Serial Lift-Out: sampling the molecular anatomy of whole organisms. Nat. Methods 21, 1684–1692. https://doi.org/10.1038/s41592-023-02113-5

Schoenfelder, S., Sexton, T., Chakalova, L., Cope, N.F., Horton, A., Andrews, S., Kurukuti, S., Mitchell, J.A., Umlauf, D., Dimitrova, D.S., Eskiw, C.H., Luo, Y., Wei, C.-L., Ruan, Y., Bieker, J.J., Fraser, P., 2010. Preferential associations between co-regulated genes reveal a transcriptional interactome in erythroid cells. Nat. Genet. 42, 53–61. https://doi.org/10.1038/ng.496

Schuster, B.S., Dignon, G.L., Tang, W.S., Kelley, F.M., Ranganath, A.K., Jahnke, C.N., Simpkins, A.G., Regy, R.M., Hammer, D.A., Good, M.C., Mittal, J., 2020. Identifying sequence perturbations to an intrinsically disordered protein that determine its phase-separation behavior. Proc. Natl. Acad. Sci. U. S. A. 117, 11421–11431. https://doi.org/10.1073/pnas.2000223117

Schwartz, O., Axelrod, J.J., Campbell, S.L., Turnbaugh, C., Glaeser, R.M., Müller, H., 2019. Laser phase plate for transmission electron microscopy. Nat. Methods 16, 1016–1020. https://doi.org/10.1038/s41592-019-0552-2

Silvester, E., Vollmer, B., Pražák, V., Vasishtan, D., Machala, E.A., Whittle, C., Black, S., Bath, J., Turberfield, A.J., Grünewald, K., Baker, L.A., 2021. DNA origami signposts for identifying proteins on cell membranes by electron cryotomography. Cell 184, 1110-1121.e16. https://doi.org/10.1016/j.cell.2021.01.033

Singer, S.J., 1959. Preparation of an Electron-dense Antibody Conjugate. Nature 183, 1523–1524. https://doi.org/10.1038/1831523a0

Somssich, M., 2022. A Short History of Plant Light Microscopy. Curr. Protoc. 2, e577.

https://doi.org/10.1002/cpz1.577

Spehner, D., Steyer, A.M., Bertinetti, L., Orlov, I., Benoit, L., Pernet-Gallay, K., Schertel, A., Schultz, P., 2020. Cryo-FIB-SEM as a promising tool for localizing proteins in 3D. J. Struct. Biol. 211, 107528. https://doi.org/10.1016/j.jsb.2020.107528

Sternberger, L.A., Donati, E.J., Cuculis, J.J., Petrali, J.P., 1965. Indirect immunouranium technique for staining of embedded antigen in electron microscopy. Exp. Mol. Pathol. 4, 112–125. https://doi.org/10.1016/0014-4800(65)90027-4

Studer, D., Klein, A., Iacovache, I., Gnaegi, H., Zuber, B., 2014. A new tool based on two micromanipulators facilitates the handling of ultrathin cryosection ribbons. J. Struct. Biol. 185, 125–128. https://doi.org/10.1016/j.jsb.2013.11.005

Taddei, A., Van Houwe, G., Hediger, F., Kalck, V., Cubizolles, F., Schober, H., Gasser, S.M., 2006. Nuclear pore association confers optimal expression levels for an inducible yeast gene. Nature 441, 774–778. https://doi.org/10.1038/nature04845

Thoma, F., Koller, Th., 1977. Influence of histone H1 on chromatin structure. Cell 12, 101–107. https://doi.org/10.1016/0092-8674(77)90188-X

Titford, M., 2009. Progress in the Development of Microscopical Techniques for Diagnostic Pathology. J. Histotechnol. 32, 9–19. https://doi.org/10.1179/his.2009.32.1.9

Van Leeuwenhoek, 1677. Observations, communicated to the publisher by Mr. Antony van Leewenhoeck, in a dutch letter of the 9th Octob. 1676. here English'd: concerning little animals by him observed in rain-well-sea- and snow water; as also in water wherein pepper had lain infused. Philos. Trans. R. Soc. Lond. 12, 821–831. https://doi.org/10.1098/rstl.1677.0003

Vangindertael, J., Camacho, R., Sempels, W., Mizuno, H., Dedecker, P., Janssen, K.P.F., 2018. An introduction to optical super-resolution microscopy for the adventurous biologist. Methods Appl. Fluoresc. 6, 022003. https://doi.org/10.1088/2050-6120/aaae0c

Vigneron, M., Dietsch, F., Bianchetti, L., Dejaegere, A., Nominé, Y., Cordonnier, A., Zuber, G., Chatton, B., Donzeau, M., 2019. Self-Associating Peptides for Modular Bifunctional Conjugation of Tetramer Macromolecules in Living Cells. Bioconjug. Chem. 30, 1734–1744. https://doi.org/10.1021/acs.bioconjchem.9b00276

Wade, J.T., Struhl, K., 2008. The transition from transcriptional initiation to elongation. Curr. Opin. Genet. Dev. 18, 130–136. https://doi.org/10.1016/j.gde.2007.12.008

Wang, C., Iacovache, I., Zuber, B., 2024. Genetically Encoded FerriTag as a Specific Label for Cryo-Electron Tomography. https://doi.org/10.1101/2024.09.10.612178

Wang, R., Brattain, M.G., 2007. The maximal size of protein to diffuse through the nuclear pore is larger than 60kDa. FEBS Lett. 581, 3164–3170. https://doi.org/10.1016/j.febslet.2007.05.082

Weber, B., Tranfield, E.M., Höög, J.L., Baum, D., Antony, C., Hyman, T., Verbavatz, J.-M., Prohaska, S., 2014. Automated Stitching of Microtubule Centerlines across Serial Electron Tomograms. PLoS ONE 9, e113222. https://doi.org/10.1371/journal.pone.0113222

Westall, F., Brack, A., 2018. The Importance of Water for Life. Space Sci. Rev. 214, 50. https://doi.org/10.1007/s11214-018-0476-7

Williams, D.B., Carter, C.B., 1996. Transmission Electron Microscopy. Springer US, Boston, MA.

https://doi.org/10.1007/978-1-4757-2519-3

Willig, K.I., Rizzoli, S.O., Westphal, V., Jahn, R., Hell, S.W., 2006. STED microscopy reveals that synaptotagmin remains clustered after synaptic vesicle exocytosis. Nature 440, 935–939. https://doi.org/10.1038/nature04592

Wollman, A.J.M., Nudd, R., Hedlund, E.G., Leake, M.C., 2015. From *Animaculum* to single molecules: 300 years of the light microscope. Open Biol. 5, 150019. https://doi.org/10.1098/rsob.150019

Xu, C.S., Hayworth, K.J., Lu, Z., Grob, P., Hassan, A.M., García-Cerdán, J.G., Niyogi, K.K., Nogales, E., Weinberg, R.J., Hess, H.F., 2017. Enhanced FIB-SEM systems for large-volume 3D imaging. eLife 6, e25916. https://doi.org/10.7554/eLife.25916

Xue, L., Lenz, S., Zimmermann-Kogadeeva, M., Tegunov, D., Cramer, P., Bork, P., Rappsilber, J., Mahamid, J., 2022. Visualizing translation dynamics at atomic detail inside a bacterial cell. Nature 610, 205–211. https://doi.org/10.1038/s41586-022-05255-2

Yang, Q., Wu, C., Zhu, D., Li, J., Cheng, J., Zhang, X., 2023. The reduction of FIB damage on cryo-lamella by lowering energy of ion beam revealed by a quantitative analysis. Structure 31, 1275-1281.e4. https://doi.org/10.1016/j.str.2023.07.002

Yoshimura, J., Ogura, H., Oda, J., 2023. Can Gram staining be a guiding tool for optimizing initial antimicrobial agents in bacterial infections? Acute Med. Surg. 10, e862. https://doi.org/10.1002/ams2.862

Young, R.J., Dingle, T., Robinson, K., Pugh, P.J.A., 1993. An application of scanned focused ion beam milling to studies on the internal morphology of small arthropods. J. Microsc. 172, 81–88. https://doi.org/10.1111/j.1365-2818.1993.tb03396.x

Zachman, M.J., Asenath-Smith, E., Estroff, L.A., Kourkoutis, L.F., 2016. Site-Specific Preparation of Intact Solid–Liquid Interfaces by Label-Free *In Situ* Localization and Cryo-Focused Ion Beam Lift-Out. Microsc. Microanal. 22, 1338–1349. https://doi.org/10.1017/S1431927616011892

Zuris, J.A., Thompson, D.B., Shu, Y., Guilinger, J.P., Bessen, J.L., Hu, J.H., Maeder, M.L., Joung, J.K., Chen, Z.-Y., Liu, D.R., 2015. Cationic lipid-mediated delivery of proteins enables efficient protein-based genome editing in vitro and in vivo. Nat. Biotechnol. 33, 73–80. https://doi.org/10.1038/nbt.3081

# Results

## Chapter I

## Electroporation-based workflow for *in situ* labeling of biomolecules

Our objective is to identify biological macromolecules directly within cells preserved in frozen-hydrated conditions and suitable for molecular-scale cryo-electron tomography. This imposes stringent constraints on labeling strategies. Post-sectioning labeling is not feasible without warming the vitrified sample, which must remain cryo-immobilized before and during data collection. Therefore, molecular recognition for identifying the target macromolecule must occur before cryo-immobilization. Consequently, the molecules of interest must be labeled *in vivo* by introducing the label directly into living cells. To fulfill these requirements I focused on *in vivo* labeling methods based on gold nanoparticles.

In my thesis project, I investigated the complete workflow of the preparation and production of nano-gold-based probes, beginning with the synthesis of gold nanoparticles, their functionalization with a variety of protein compounds, and their stabilization to prevent unwanted interactions with the cellular environment. Furthermore, I explored the delivery of the functionalized probes into cells via electroporation and their subsequent detection in cryo-EM/ET data. In this chapter, I present my experimental results and suggestions for optimizations in the following areas:

(i) Transfection optimization and control using robust Au•NLS conjugates

(ii) Improving the Pol-II probes based on antigen-binding fragments (Fab)

(iii) Developing a universal probe based on anti-GFP nanobodies.

## 1.1. Publication 1

My initial task in this project was to validate the feasibility to detect ~2 nm gold probes *in situ* using cryo-EM imaging. In this first experiment, gold-NLS probes and electroporation were performed in the laboratory of Dr. Guy Zuber (UMR7242 Biotechnology and Cell Signalling) by his former PhD student, Nadja Groysbeck. I performed vitrification of the electroporated HeLa cells by high-pressure freezing (HPF, Leica EM PACT 2 apparatus), vitreous cryo-sectioning, and imaging with Titan-Krios.

Here, I summarize my main results:

1. I used EM imaging to explore the size heterogeneity of the nanogold particles used later for conjugation purposes. I performed segmentation of gold particles and their size measurements with ImageJ on EM micrographs. My statistical analysis resulted in 41528 segmented particles with an average diameter of 1.96 nm and a standard deviation of 0.38 nm. (see Figure 1E of the Publication 1).

2. 2 nm gold particles are distinguishable in 2D projection images of 100 nm-thick vitreous sections of HeLa cells. This indicates that the probe will most probably be identifiable in tomographic volumes of similar thickness. Such thickness is standard for vitreous cryosections but is the limit achievable width using cryo-FIB and involves greater technical challenges (see Figure 7-8 of the Publication 1).

The experimental procedures and results are described in detail in the following publication:

N. Groysbeck, **V. Hanss,** M. Donzeau, J.-M. Strub, S. Cianférani, D. Spehner, M. Bahri, O. Ersen, M. Eltsov, P. Schultz, G. Zuber, Bioactivated and PEG-Protected Circa 2 nm Gold Nanoparticles for in Cell labeling and Cryo-Electron Microscopy. Small Methods 2023, 7, 2300098. https://doi.org/10.1002/smtd.202300098.

Check for updates

RESEARCH ARTICLE

small methods
www.small-methods.com

# Bioactivated and PEG-Protected Circa 2 nm Gold Nanoparticles for in Cell Labelling and Cryo-Electron Microscopy

*Nadja Groysbeck, Victor Hanss, Mariel Donzeau, Jean-Marc Strub, Sarah Cianférani, Danièle Spehner, Mounib Bahri, Ovidiu Ersen, Mikhael Eltsov, Patrick Schultz, and Guy Zuber**

**Advances in cryo-electron microscopy (EM) enable imaging of protein assemblies within mammalian cells in a near native state when samples are preserved by cryogenic vitrification. To accompany this progress, specialized EM labelling protocols must be developed. Gold nanoparticles (AuNPs) of 2 nm are synthesized and functionalized to bind selected intracellular targets inside living human cells and to be detected in vitreous sections. As a proof of concept, thioaminobenzoate-, thionitrobenzoate-coordinated gold nanoparticles are functionalized on their surface with SV40 Nuclear Localization Signal (NLS)-containing peptides and 2 kDa polyethyleneglycols (PEG) by thiolate exchange to target the importin-mediated nuclear machinery and facilitate cytosolic diffusion by shielding the AuNP surface from non-specific binding to cell components, respectively. After delivery by electroporation into the cytoplasm of living human cells, the PEG-coated AuNPs diffuse freely in the cytoplasm but do not enter the nucleus. Incorporation of NLS within the PEG coverage promotes a quick nuclear import of the nanoparticles in relation to the density of NLS onto the AuNPs. Cryo-EM of vitreous cell sections demonstrate the presence of 2 nm AuNPs as single entities in the nucleus. Biofunctionalized AuNPs combined with live-cell electroporation procedures are thus potent labeling tools for the identification of macromolecules in cellular cryo-EM.**

## 1. Introduction

Understanding the human cell architecture at the molecular level relies on the availability of advanced microscopes and labeling tools. Developments in cryo-Electron Microscopy (cryo-EM) now enable the recording of cellular images at nanometric resolution detailing multiple molecular components in near native frozen-hydrated conditions.[1] Large protein assemblies such as nuclear pores, ribosomes, microtubules or filaments can be readily visualized, whereas smaller components remain difficult to identify.[2] Gold nanoparticles (AuNPs) with an inner metallic core are popular EM labeling tags, as they efficiently scatter electrons and can be readily functionalized with antibodies to target selected cellular structures/proteins. In most cases, immunogold labeling for cellular EM imaging is performed after resin-embedding on sections of chemically cross-linked cells. However, the visualization of biomolecules in cryo-EM

N. Groysbeck, M. Donzeau, G. Zuber
Université de Strasbourg – CNRS
UMR 7242
Biotechnologie et Signalisation Cellulaire
Boulevard Sebastien Brant, Illkirch F-67400, France
E-mail: zuber@unistra.fr

V. Hanss, D. Spehner, M. Eltsov, P. Schultz
Centre for Integrative Biology (CBI)
Department of Integrated Structural Biology
Institut de Génétique et de Biologie Moléculaire et Cellulaire (IGBMC)
1 rue Laurent Fries, BP10142, Illkirch Cedex F-67404, France

J.-M. Strub, S. Cianférani
Laboratoire de Spectrométrie de Masse BioOrganique
Université de Strasbourg, CNRS, IPHC UMR 7178
Strasbourg F-67000, France

M. Bahri
Albert Crewe Centre
University of Liverpool
4. Waterhouse Building, Block C, 1–3 Brownlow Street, London L69 3GL, UK

O. Ersen
Université de Strasbourg – CNRS
UMR 7504
Institut de Physique et Chimie des Matériaux de Strasbourg (IPCMS)
23 rue de Loess, Strasbourg 67034, France

The ORCID identification number(s) for the author(s) of this article can be found under https://doi.org/10.1002/smtd.202300098

© 2023 The Authors. Small Methods published by Wiley-VCH GmbH. This is an open access article under the terms of the Creative Commons Attribution License, which permits use, distribution and reproduction in any medium, provided the original work is properly cited.

**DOI: 10.1002/smtd.202300098**

relies on the vitrification of living cells and on maintaining the native cell structure in a frozen-hydrated state throughout the sectioning or milling process up to image acquisition. The strict maintenance of the temperature below -140 °C does not allow for gold labeling following the classical process. This implies that labeling can only be performed before vitrification on unfixed living cells. This constraint has motivated a quest for new tags and methodologies.[3,4] Ideally, the labeling tool must be specific for its target, clearly recognized within the specimen and its use should not denature the specimen. In case intracellular proteins are targeted the probes must be able to freely diffuse in the cytosol.

We previously demonstrated that ultra-small 0.8 nm AuNP-antibodies can be transported into living cells using a cationic lipid formulation and label their target, namely in this case, nuclear RNA polymerase II (PolII).[5] The size of gold nanoparticle attached to the probe was however too small to be revealed effectively by cryo-EM in frozen hydrated cell sections (data not shown). The linkage chemistry was furthermore poorly defined, potentially causing an uncertainty in the distance between the detected gold domain and the targeted epitope. We then screened for gold nanoparticles with increased diameters to facilitate their detection. Mercaptobenzoate-coordinated AuNPs of precise composition[6,7] appear extremely attractive in this regard. They can not only be produced with sizes between 1.2 to 3 nm[8] but also can be functionalized with antibodies via thiolate exchange[9] in aqueous phase. The thiolate-for-thiolate exchange tremendously simplifies the preparation of AuNP-conjugates and opens new ways to design advanced AuNP probes[10] for in situ labeling of supramolecular assemblies and cryo-EM analysis.[11–14] By following the synthesis protocol of thiobenzoate-coordinated gold nanoparticles reported by Levi-Kalisman,[7] we discovered that sodium borohydride reduction of gold(III) chloride in the presence of 5,5'-dithio-bis(2-nitrobenzoic acid) led to 1.4 nm AuNPs covered by a Au-S coordination shell consisting of thioaminobenzoates (TABs) and thionitrobenzoates (TNBs).[15] These mixed TAB-, TNB-coated AuNPs (AuZ) appeared extremely pertinent for bioconjugation purposes and intracytosolic live cell applications. First, the gold nanoparticles reacted well in water near pH 7 with excess thiolated peptides mainly by substitution of TNBs to peptides, producing a gold particle functionalized with 8–9 peptides and the zwitterionic TAB. Second, the organic shell did not dramatically alter HeLa cell viability after cytosolic delivery by electroporation and remained bound to the gold particles.[15] Indeed, the human cells rapidly recovered from the transient electric pulse-mediated permeabilization and withstood the cytoplasmic presence of peptide-functionalized AuNPs. The 1.4 nm AuNP probes coated with the capping peptide of sequence CALNNG[16] could diffuse freely in the cytoplasm and did not accumulate in clusters inside cells as was observed for 2 nm particles delivered by cationic lipid formulation[5] or penetrating peptides.[17] Only SV40 Nuclear Localization Signal (NLS)[18]-conjugated nanoparticles were found to accumulate in the nucleus while Nuclear Export Signal (NES)-conjugated AuNPs were exported from the nucleus.

While these previously published data clearly demonstrated that AuZs are attractive platforms for biofunctionalization and production of AuNPs suitable for delivery into living cells, the 1.4 nm sized-particles still fall short for direct detection with the current electron-dose limitations of cryo-EM for biological specimen.[5,19] It was estimated that AuNPs larger than 2 nm are currently needed for direct detection in cryo-vitrified cell sections.[14] However, this size appears to represent a threshold for protein binding.[20]AuNPs below 2 nm display a strong curvature, and therefore the nanoparticle surface available for binding biomolecules by other means than coordination bonds is limited.[21] With increasing size, the AuNP curvature flattens and the exposed surface presents a larger contact area available for non-specific binding of biomolecules.[22] In the crowded cytosol, weak superficial interactions between AuNPs and the cellular components contribute more to slowing down of the diffusion of the particle than the increase of the hydrodynamic diameter associated with the larger size.[23,24] Hints of the toll taken by non-specific binding of 2 nm AuNPs to cellular components are images showing heterogeneous diffusion pattern and clustering of the nanomaterial in subcellular domains[17,25,26] as well as low specific activity when the AuNPs are equipped with functional elements targeting cytosolic enzymes.[27] Minimizing non-specific binding of molecules using surface-protecting components such as high molecular weight polyethyleneglycol (PEG), which is widely used to decrease non-specific binding of nanomaterial to extracellular constituents[28,29] should enhance binding selectivity and improve the trafficking of the nanomaterial following cytosolic entry.

Here, 2 nm AuZs were synthesized and their surface was functionalized with SV40 NLS peptides and surface capping agents, by thiolate to thiolate exchange. Amongst the various tested capping elements, the 2 kDa polyethyleneglycols (PEG) was the most effective and was coordinated to the AuNP surface in combination with a NLS peptide at different proportion. After characterization, the functionalized AuNPs were first incubated with living HeLa cells to assay cytotoxicity and non-specific cellular penetration and distribution. The gold nanoparticles were then delivered into the cytosol of living cells using an electroporation procedure and cell viability, probe distribution, and nuclear import efficiency were assayed. The PEG-,NLS-coated AuNP (AuPEGNLS) with an equal amount of NLS and PEG conjugated to the AuNP surface showed weak non-specific binding to general cellular components while performing highly efficient NLS-mediated nuclear import. We further demonstrate that the 2 nm AuPEGNLSs after electroporation are directly detected within the nucleus in unstained vitreous cell sections by cryo-EM.

## 2. Results and Discussion

### 2.1. Synthesis and Characterization

The AuZs were synthesized in acetonitrile/water mixture[30] by sodium borohydride reduction of auric chloride in the presence of Ellman's reagent.[31] Characterization by gel electrophoresis, transmission electron microscopy, and MALDI-TOF revealed a monodisperse solution of particles with an average diameter of 2.02 nm (SD 0.21, n = 105) and a molecular mass of 60 kDa (Supporting InformationFigure S1, Supporting Information). The gold particles were then reacted with increasing molar ratios of the NLS peptide whose sequence (CALNNGAGP-KKKRKVED) contains the classical SV40 NLS[18] and with

23669608, 2023, 6, Downloaded from https://onlinelibrary.wiley.com/doi/10.1002/smtd.202300098 by Cochrane France, Wiley Online Library on [06/01/2025]. See the Terms and Conditions (https://onlinelibrary.wiley.com/terms-and-conditions) on Wiley Online Library for rules of use; OA articles are governed by the applicable Creative Commons License

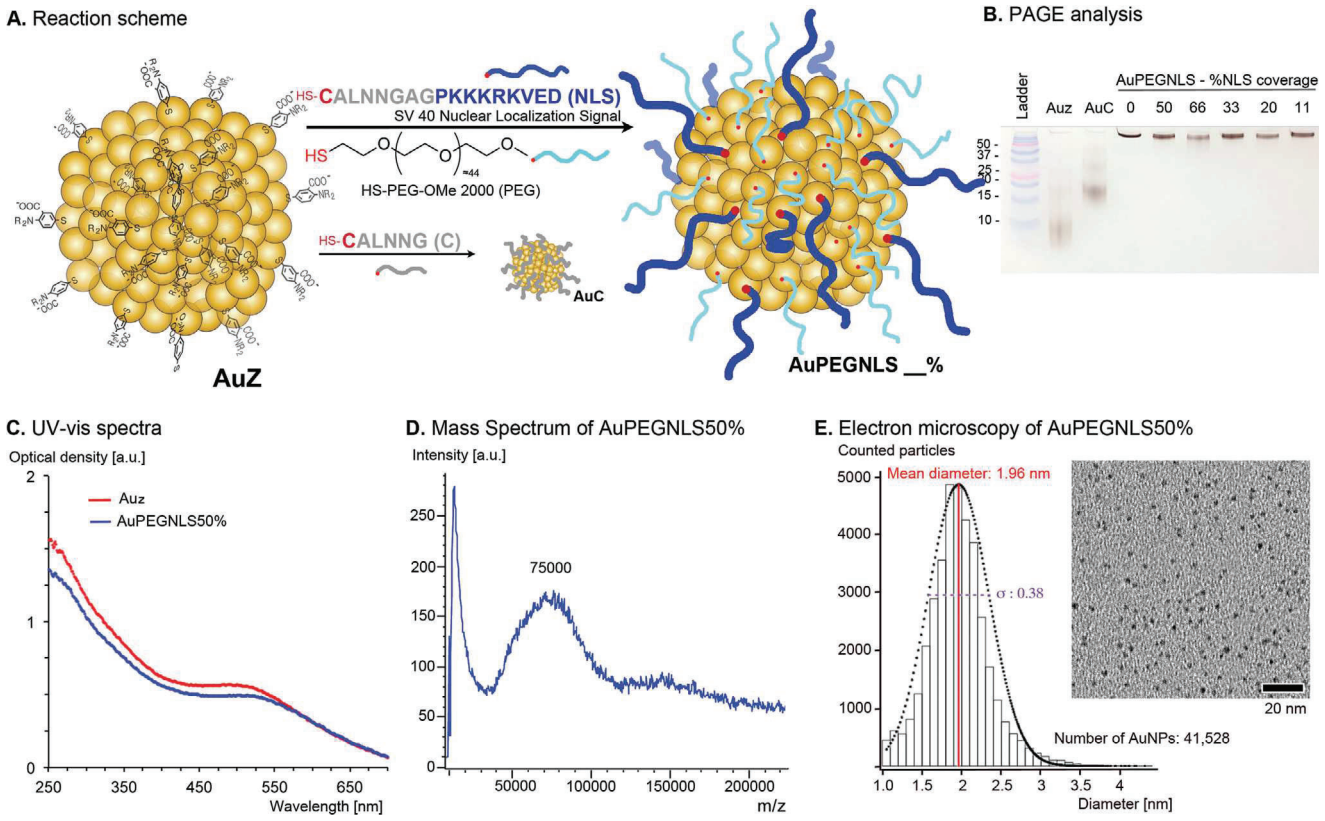


**Figure 1.** Preparation and characterization of polyethyleneglycol -, Nuclear Localization Signal peptide - decorated AuNPs. A) Illustration of the AuNPs and synthesis scheme. The percentage refers to the relative amounts of NLS peptide to total (PEG + NLS) thiolates. As a control, the AuZwas also reacted with CALNNG forming the AuC nanoparticles. B) Polyacrylamide gel electrophoresis analysis of the starting AuZ, purified AuC, and AuPEGNLS at the indicated NLS proportion. C) UV–vis spectrometry of AuZ (in red) and AuPEGNLS50% (in blue). D) MALTI-TOF Mass spectrum of the AuPEGNLS50%. E) Electron microscopy image of AuPEGNLS50% and population analysis of the gold particle diameter.

a previously described gold particle capping peptide whose sequence (CALNNG)[16] carries a reactive Cysteine at its N-terminus. The degree of ligand exchange on the particle surface was analyzed by monitoring stably bound NLS peptides to AuNPs by gel electrophoresis (Figure S2, Supporting Information). Substitution of AuZ-coordinated thiobenzoates by the NLS peptide expectedly increased when the peptide/AuZ ratios rose from 4 to 30. Excess NLS-coating of the 2 nm AuZ particles led to precipitation, which was not observed with the 1.4 nm AuZ.[15] This undesired precipitation is likely a consequence of the surface area of a 2 nm particle (calculated area of 12.6 $nm^2$) that is twice the one of a 1.4 nm particle (area of 6.15 $nm^2$) and prompted us to complement the conjugation of the bioactive NLS with a surface protecting element. Thiolated reagents ensuring effective protection for gold surfaces from associating with biomolecules are scarce. Glutathione[17,27] and 0.6 kDa thiolated PEG[32] were first tested as passivation agents for AuZ. Unfortunately, mixing the glutathione or the 0.6 kDa thiolated PEG with AuZ led to precipitates that were uneasy to re-suspend in aqueous solutions near pH 7.0. In contrast, addition of CALNNG peptide[16] or thiolated 2 kDa PEG to AuZ maintained the gold particles in suspension and formed the AuC and AuPEG components, respectively, via the expected thiolate to thiolate exchange. The NLS peptide was incorporated in the AuPEG shell at relative thiolate amounts of 11, 20, 33, 50, and 66%, thus yielding the AuPEGNLSs with the indicated NLS% (**Figure 1**A).

All functionalized AuNPs were purified by gel filtration chromatography, concentrated by ultracentrifugation, and behaved as stable colloids. Their electrophoretic mobility was different than the starting AuZ (Figure 1B). Regardless of the NLS proportion, the AuPEGNLS did not enter the gel, indicating that the thiolated 2 kDa PEG are coordinated onto the gold surface in a high density. The intensity of Coomassie blue staining of each AuNP grew as a function of increasing NLS proportion, indicating that the number of NLS peptides conjugated per AuNP increased as well (Figure S3, Supporting Information). All AuPEGNLSs show UV–vis spectrum similar to that of AuZ with a similar absorption shoulder at 520 nm (Figure 1C; Figure S4, Supporting Information). The concentration of the gold nanoparticles was determined by spectrometry measurement at 520 nm using an absorption coefficient of 510 000 $M^{-1}$ $cm^{-1}$ according to the formula proposed by Liu et al.[33] The MALDI-TOF Mass spectrum of the AuPEGNLS50% (Figure 1D) was representative of all the other AuPEGNLS spectra (Figures S5–S10, Supporting Information). A broad distribution of masses centered at ≈75 kDa was observed as compared to 60 kDa for AuZ. The roughly 15 kDa difference in mass likely measures the exchange of about ten 0.2 kDa TNBs to ten 2 kDa PEGs and 1.8 kDa NLSs. This

23669608, 2023, 6, Downloaded from https://onlinelibrary.wiley.com/doi/10.1002/smtd.202300098 by Cochrane France, Wiley Online Library on [06/01/2025]. See the Terms and Conditions (https://onlinelibrary.wiley.com/terms-and-conditions) on Wiley Online Library for rules of use; OA articles are governed by the applicable Creative Commons License

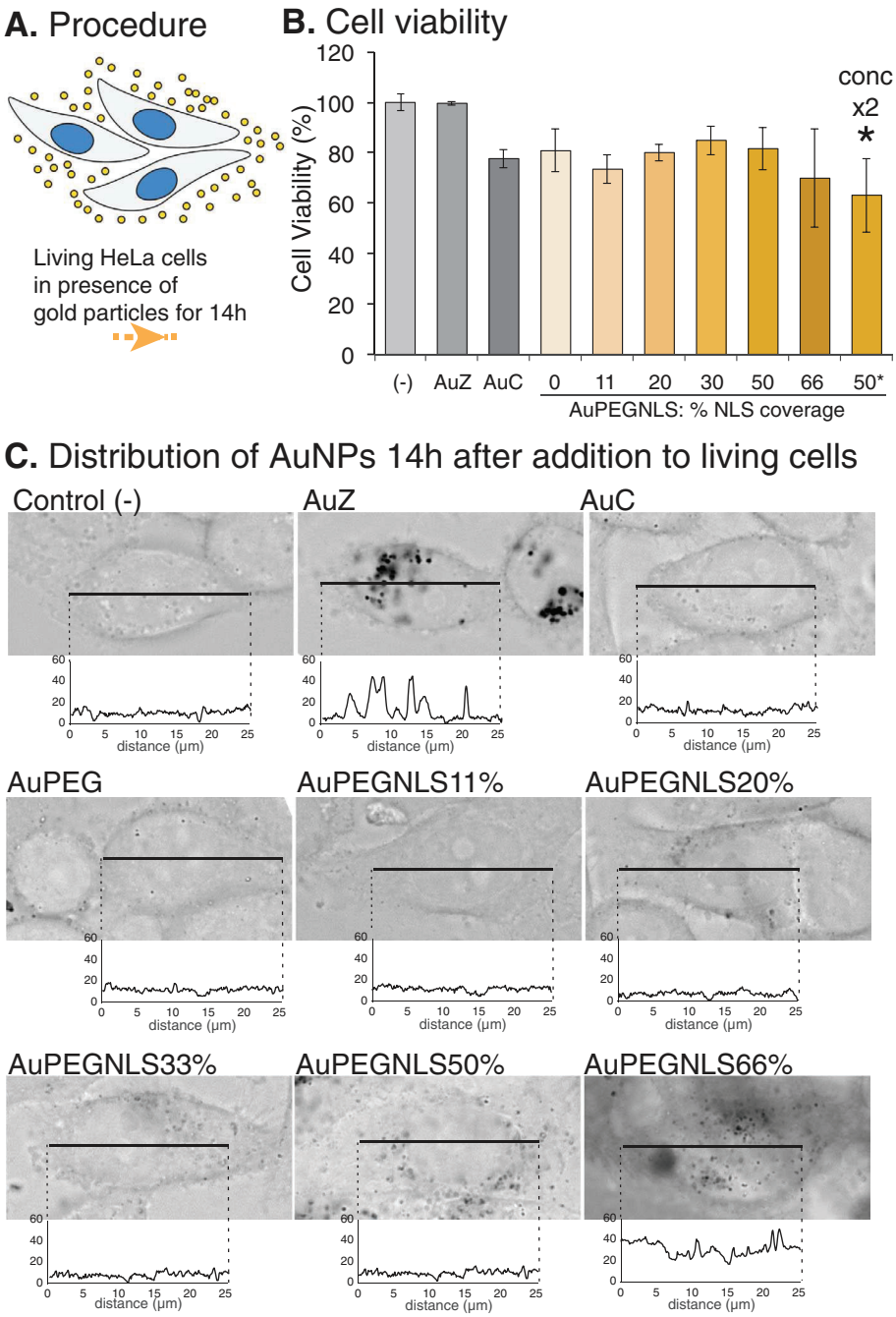


**Figure 2.** Analysis of cell viability and gold particle distribution following their incubation with HeLa cells for 14 h as indicated. A)Freshly trypsinized HeLa cells ($10^5$ cells/10 µL PBS) alone or with 5 µM of each AuNP (10 µM AuPEGNLS50% in the * marked condition), were incubated for 10 min before dilution in 1 mL cell culture medium containing 10% serum. Cells were then dispatched in plates for cell culture at 37 °C during 14 h (final concentration of AuNPs after dilution: 0.5 µM (1 µM for*). B)The cell viability as estimated with the MTT assay.[34] Values are averages and standard deviations of quintuplicates. C)Light microscopy images and distribution profiles of AuNPs along the indicated lines. Cells were fixed with 2% glutaraldehyde, permeabilized with 0.1% saponin and the gold particles were silver-enhanced for detection.

substitution number suggests that the AuPEGNLS50% is grafted with 5 PEGs, 5 NLSs and residual TABs and TNBs. Electron micrographs showed evenly distributed individual particles on the carbon film. Statistical analysis of 41528 imaged particles resulted in an average diameter of 1.96 nm and a standard deviation of 0.38 nm.

### 2.2. Distribution Profiles Upon Addition to Living Cells

The above-characterized AuNPs were then incubated with living HeLa cells for 14 h in order to analyze their cytotoxicity (**Figure 2**). HeLa cells were freshly trypsinized to detach them from the Petri dishes, concentrated to obtain $10^5$ cells in 10 µL of PBS and mixed

23669608, 2023, 6, Downloaded from https://onlinelibrary.wiley.com/doi/10.1002/smtd.202300098 by Cochrane France, Wiley Online Library on [06/01/2025]. See the Terms and Conditions (https://onlinelibrary.wiley.com/terms-and-conditions) on Wiley Online Library for rules of use; OA articles are governed by the applicable Creative Commons License

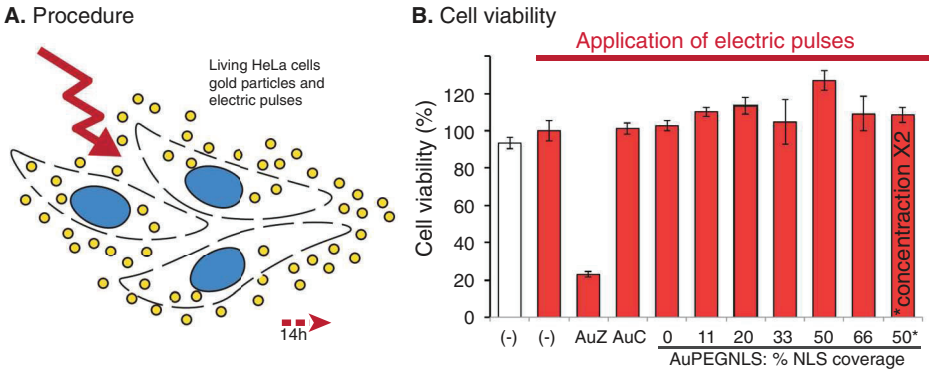


**Figure 3.** Analysis of cell viability following electroporation of HeLa cells incubated with the indicated gold particles. A)Freshly trypsinized HeLa cells ($10^5$ cells/10 µL PBS) alone (-) or with 5 µM of each AuNP (10 µM AuPEGNLS50% in the * marked condition) were subjected to 3 electric pulses of 10 ms at 517 V $cm^{-1}$. Cell suspensions were diluted in 1 mL cell culture medium containing 10% serum and AuNPs remaining in solution were separated from cells by centrifugation. The cell pellets were then re-suspended in cell culture medium for culture during 14 h. B)Cell viability was estimated with the MTT assay.[34] Values are averages and standard deviations of quintuplicates.

with 5 µM of each AuNP. After 10 min of incubation, the cells were diluted in cell medium containing serum and incubated for growth before analysis of cell viability and AuNP localization 14 h latter. HeLa cells with proteolytically removed adhesion receptors (e.g., trypsin cleaves superficial proteins involved in adhesion) but with native plasma membranes tolerate well the presence of the different AuNPs as evidenced by the recovery of <70% viable adhered cells relative to control even in the presence of 1 µM AuPEGNLS50%. (Figure 2B). The localization of the AuNPs was then monitored. The cell culture media containing unbound gold particles were removed. The cells were washed with PBS, fixed with glutaraldehyde and subjected to silver-enhancement (Figure 2C).

The AuZ particles gave rise to intense cytoplasmic aggregates likely because of their ability to react with thiols on the cell surface and their uptake into vesicular compartments. The AuC, AuPEG, AuPEGNLS 11% and AuPEGNLS 22% were barely seen on the cell surface and even less so within cells suggesting that they do not significantly bind to the plasma membrane (Figure 2C). Accumulation into discrete dots at the plasma membrane and within the cytoplasm was observed for AuPEGNLS33%, 50%, and 66%. The staining intensity increased as a function of the NLS content in the AuPEGNLS shell. The AuPEGNLS66% even strongly adhered to the glass support. The electrostatic associations between cationic NLSs and anionic proteoglycans present on the cell surface and the continuous recycling of the plasma membrane into intracellular vesicles may account for the observed gold particle distribution.[35] Regardless of the coverage, the AuNPs did not accumulate in the nucleus and did not diffuse into the cytosol. Intravesicular entrapment of gold particles without cytosolic release upon addition to living cells is expected[15,36] since the rupture of the endosomal bilayer, although possible,[37,38] remains a rare event.

### 2.3. Distribution Profiles after Entry into the Cytoplasm of Living Cells

The cytotoxicity and distribution of the AuNPs within living cells was investigated after having delivered the probe using a commercially available electroporation device[39] and electric pulses that were previously optimized for antibody transduction[15,40] (**Figure 3** and **Figure 4**). AuNPs at the indicated final concentrations were incubated with freshly suspended HeLa cells in PBS. The solutions were then subjected to 3 electric pulses of 10 ms at 517 V $cm^{-1}$ to create transient holes in the plasma membrane and hence cytosolic entry of the extracellular applied components. After the electric pulses, excess AuNPs in solution were removed and the electroporated cells were cultivated for 14 h before testing the recovery of cell viability and the distribution of AuNPs as described above. The cell viability was compared to cells in PBS without application of electric pulses or to cells in PBS treated with electric pulses. Except for AuZ, application of the 3 electric pulses and presence of AuNPs did not affect cell viability (Figure 3B). The highly thiol-reactive AuZ may trap essential cellular components and induce cell death.

The cellular distribution of the electroporated functionalized AuNPs (Figure 4A) was remarkably different than the ones reported in Figure 2C, confirming that the gold particles entered the cell and that their intracellular location was determined by the functions introduced on their outer shell. The non-functionalized AuZ did not diffuse freely but rather accumulated in cell membrane-bound aggregates or within intracellular vesicles.

The mobility of the thiol-reactive AuZ was probably hampered by its ability to react with thiolate-containing cell components and hence be trapped there. The internalized AuCs appeared to distribute throughout the cell, including to some extent in the nucleus. Aggregate formation was also clearly observed in perinuclear vesicles resembling lysosomal compartments. The AuPEGs appeared homogeneously dispersed in the cytoplasm and were mostly excluded from the cell nuclei in agreement with the fact that nuclear import of inert material larger than 5 nm in diameter is severely restricted by the nuclear pore complex.[41,42] In fact, the 2 kDa PEG molecules surrounding the 2 nm gold particles have a contour length of 12.5 nm which increases the maximal diameter of the particles to 27 nm. In contrast to the AuPEG, the NLS functionalized AuPEGNLSs accumulated in the nuclei and preferably in the nucleoplasm rather than in nucleoli. To analyze the nuclear accumulation of AuNPs, we plotted the

23669608, 2023, 6, Downloaded from https://onlinelibrary.wiley.com/doi/10.1002/smtd.202300098 by Cochrane France, Wiley Online Library on [06/01/2025]. See the Terms and Conditions (https://onlinelibrary.wiley.com/terms-and-conditions) on Wiley Online Library for rules of use; OA articles are governed by the applicable Creative Commons License

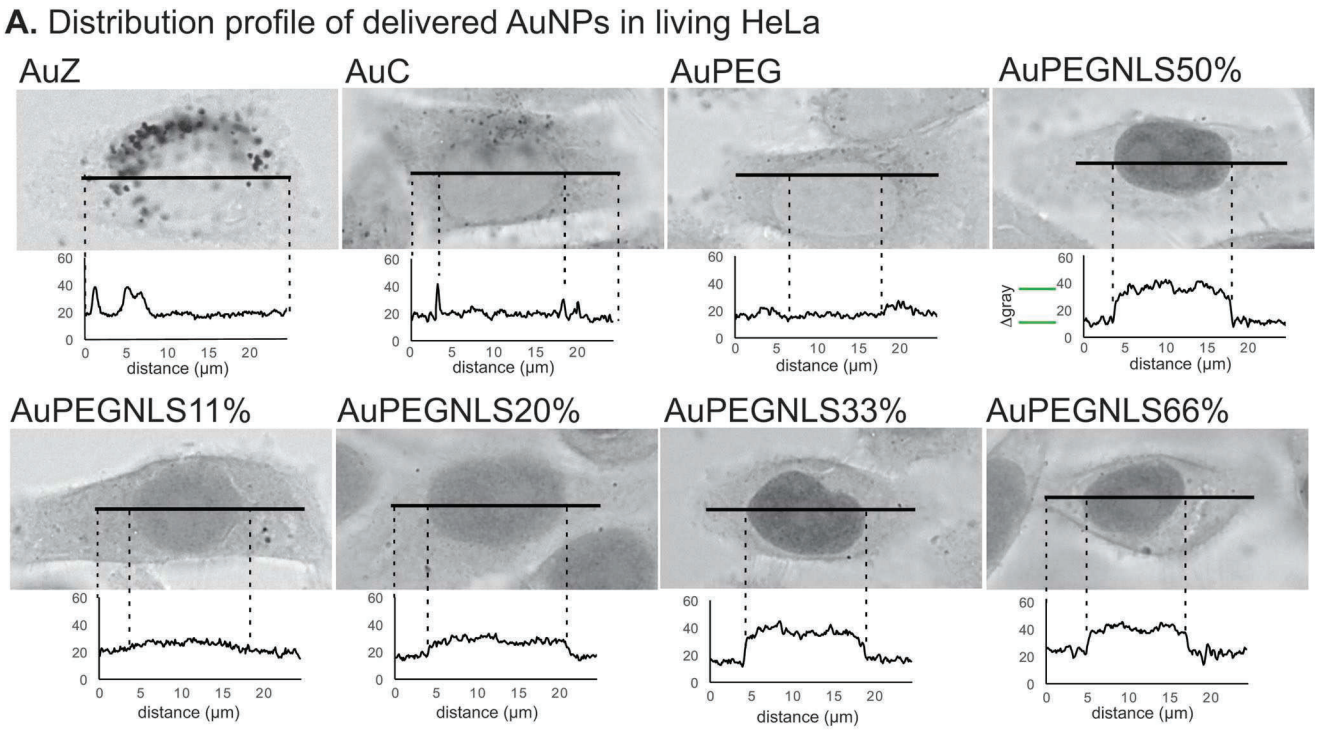


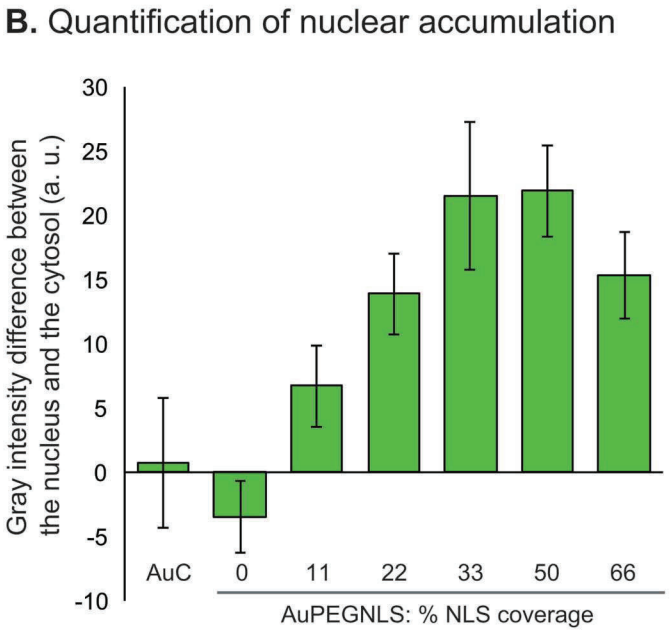


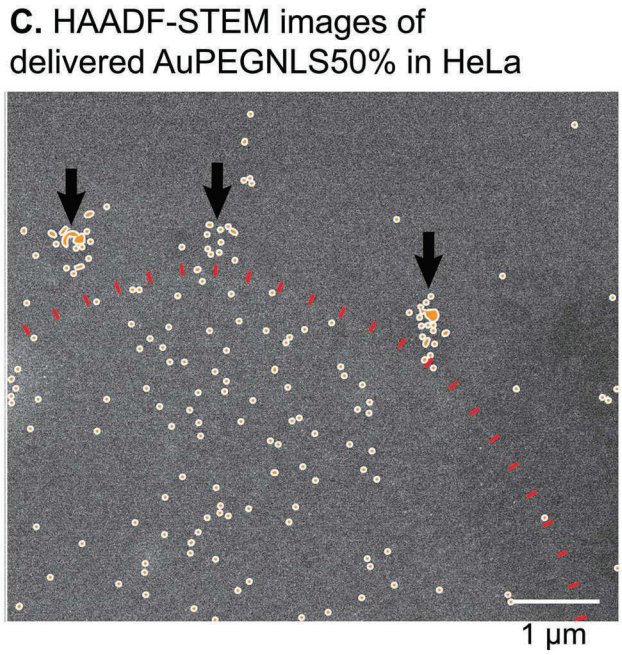


**Figure 4.** Intracellular AuNP distribution after AuNP delivery by electroporation. A) Light microscopy images and distribution profiles of the indicated AuNPs 14 h after transient plasma membrane permeabilization, and subsequently silver enhanced cells. The graphs represent intensity plots along the indicated lines and reveal the AuNP distribution. B) Quantification of nuclear accumulation. Differences in staining between the nucleus and the cytosol were measured using gray plots from silver-enhanced cell images containing the indicated delivered AuNPs. Values are averages and standard deviations of 14 measures. C) HAADF-STEM images of a HeLa section containing delivered AuPEGNLS50%. After delivery and cell culture, the cells were fixed, the AuNPs were enhanced with silver and the specimen embedded in resin for room temperature electron microscopy imaging. For sake of clarity, the nuclear envelope (dotted red line) and the barely visible AuNPs (orange dots) were marked. The 3 black arrows point to AuNPs entrapped in cytoplasmic vesicles.

23669608, 2023, 6, Downloaded from https://onlinelibrary.wiley.com/doi/10.1002/smtd.202300098 by Cochrane France, Wiley Online Library on [06/01/2025]. See the Terms and Conditions (https://onlinelibrary.wiley.com/terms-and-conditions) on Wiley Online Library for rules of use; OA articles are governed by the applicable Creative Commons License

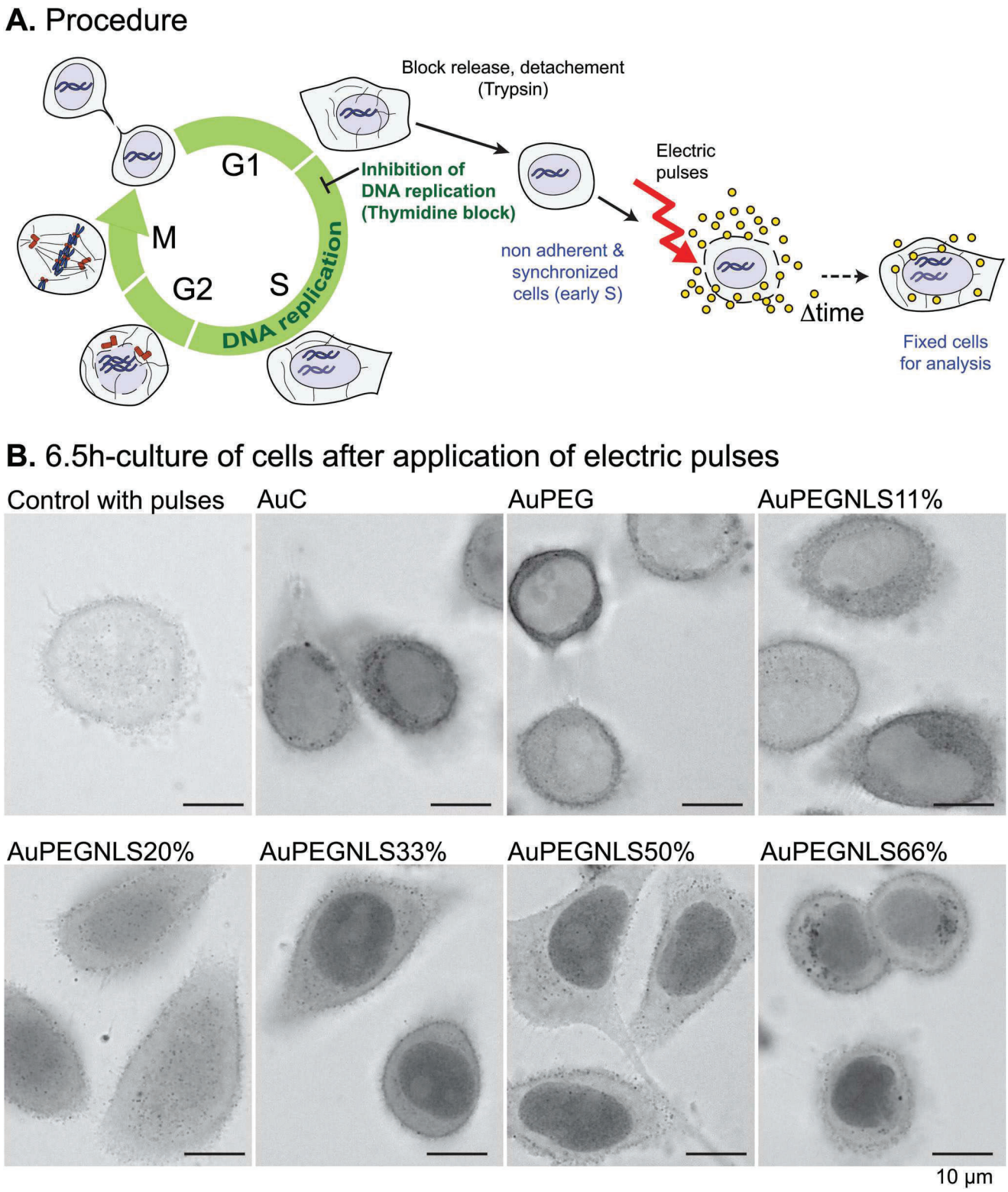


**Figure 5.** Analysis of cell content 6.5 h after application of electric pulses to HeLa cells synchronized to be in early S phase and incubated with the indicated AuNPs. A) Scheme of the procedure. B) Distribution of the indicated gold nanoparticles in synchronized HeLa cells 6.5 h after release of the inhibition of DNA replication and application of the electric pulses (3 pulses of 10 ms at 517 V $cm^{-1}$). The cells were fixed with 2% glutaraldehyde, permeabilized with 0.1% saponin and the gold particles were enhanced with silver for detection by light microscopy.

23669608, 2023, 6, Downloaded from https://onlinelibrary.wiley.com/doi/10.1002/smtd.202300098 by Cochrane France, Wiley Online Library on [06/01/2025]. See the Terms and Conditions (https://onlinelibrary.wiley.com/terms-and-conditions) on Wiley Online Library for rules of use; OA articles are governed by the applicable Creative Commons License

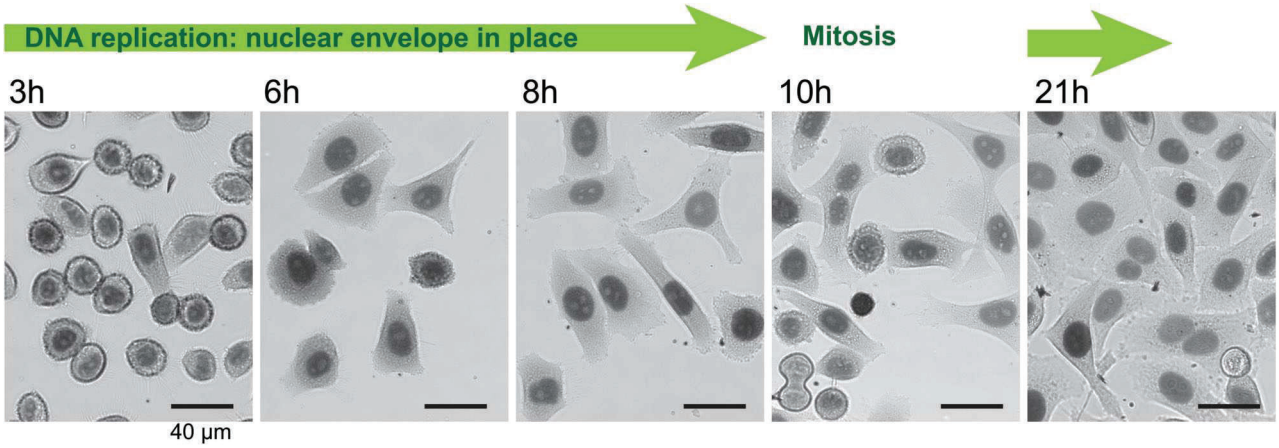


**Figure 6.** Light microscopy images of HeLa cells containing AuPEGNLS50% at different time points after electroporation and release of the inhibition of DNA replication. The cells were fixed with 2% glutaraldehyde, permeabilized with 0.1% saponin and the gold particles were silver-enhanced for detection by light microscopy.

intensity profile along a line crossing cytoplasmic and nuclear regions of the silver enhanced cells (Plots in Figure 4A). The intensity ratios between the average nuclear and cytoplasmic values were then calculated to quantify the nuclear accumulation (Figure 4B). The nuclear accumulation of the AuPEGNLSs consistently increased with the NLS density indicating that nuclear import depends on the NLS coverage. The maximum import was reached with 33% and 50% NLS coverage and was found to decrease for the 66% NLS coverage. This may be related to the intracellular aggregation observed in the control experiments with AuPEGNLS66% nanoparticles. Although the import efficiency was comparable for AuNPs with 33 and 50% coverage, the lower standard deviation of AuPEGNLS50% prompted us to employ them to prepare samples for EM observation. A first HAADF-STEM imaging of the AUPEGNLS50% particles delivered into living HeLa cells was performed at room temperature after silver enhancement and resin embedding (Figure 4C). With the exception of AuNPs entrapped within vesicular compartments at the vicinity of the nuclear envelope (black arrows), only a few particles were detected in the cytoplasm while the vast majority of AuNPs were found in the nucleus as single particles.

### 2.4. Distribution Profiles after Entry into the Cytoplasm of Synchronized Cells

To further demonstrate without ambiguity that the NLS-functionalized AuPEGs are shuttled into the nucleus via the nuclear pores using the importin pathway and not trapped during mitosis,[43] DNA replication was inhibited with a double thymidine block to hold the cells in early S phase (**Figure 5**A).[44] The synchronized cells were then released from the DNA synthesis inhibition just before the electroporation procedure and the AuNP distribution was analyzed after growing the cells for 6.5 h (Figure 5B). At the arrest time, most synchronized cells remained in S phase and did not undergo nuclear envelope breakdown and mitosis. The distribution profiles of the different AuNPs were extremely similar to those obtained 14 h after cytosolic delivery and without thymidine block (Figure 4). The AuPEG, AuC, and AuPEGNLS11% were mainly distributed in the cytosol with clear contact to the cytosolic face of the nuclear envelope. The AuPEGNLS20% entered the nucleus albeit poorly. Darker grains near the nuclear envelope were observed, suggesting that these gold particles, 6.5 h after entry were still proceeding for association to importin and for passage across the gel protecting the hole of the nuclear pores.[41,45] The AuPEGNLS33% and 50% with the highest NLS density were efficiently imported into the nucleus with apparently few nanoparticles remaining in the cytosol. The AuPEGNLS66% also accumulated in the nucleus but was also detected in perinuclear compartments resembling lysosomes, likely because the number of NLS peptides attached to these gold particles favor unspecific binding to the external surface of the plasma membrane and engulfment in intracellular vesicles via the plasma membrane recycling process.

The living cells containing AuPEGNLS50% were then grown for 3,6,8,10, and 21 h in order to analyze the dynamics of intracellular AuNP distribution before and after mitosis (**Figure 6**).

The HeLa cells slowly formed adhesion contacts onto the cell culture dish and the AuPEGNLS50% readily accumulated in the cell nuclei following the electric pulses. Robust and near complete nuclear import was observed during the S phase when the nuclear envelope remains intact (3, 6, and 8 h time points). The cells then entered and exited mitosis without major perturbation, confirming that HeLa cells withstand the transient electric pulse- mediated permeabilization and the intracellular presence of AuPEGNLS50%. The fast nuclear import of the NLS-equipped AuNPs following delivery parallels the behavior of NLS-containing proteins and confirms the relative inertness of the probes.[42] Of note, 2 nm AuPEGNLSs were also efficiently shuttled into the nuclei of U2OS following electroporation without marked cytotoxicity (Figure S11, Supporting Information), indicating that this protocol is applicable to other human cell lines.

### 2.5. Cryo-EM Imaging

In a final experiment, we investigated whether the 2 nm gold particles could be detected without silver enhancement within the



23669608, 2023, 6, Downloaded from https://onlinelibrary.wiley.com/doi/10.1002/smtd.202300098 by Cochrane France, Wiley Online Library on [06/01/2025]. See the Terms and Conditions (https://onlinelibrary.wiley.com/terms-and-conditions) on Wiley Online Library for rules of use; OA articles are governed by the applicable Creative Commons License

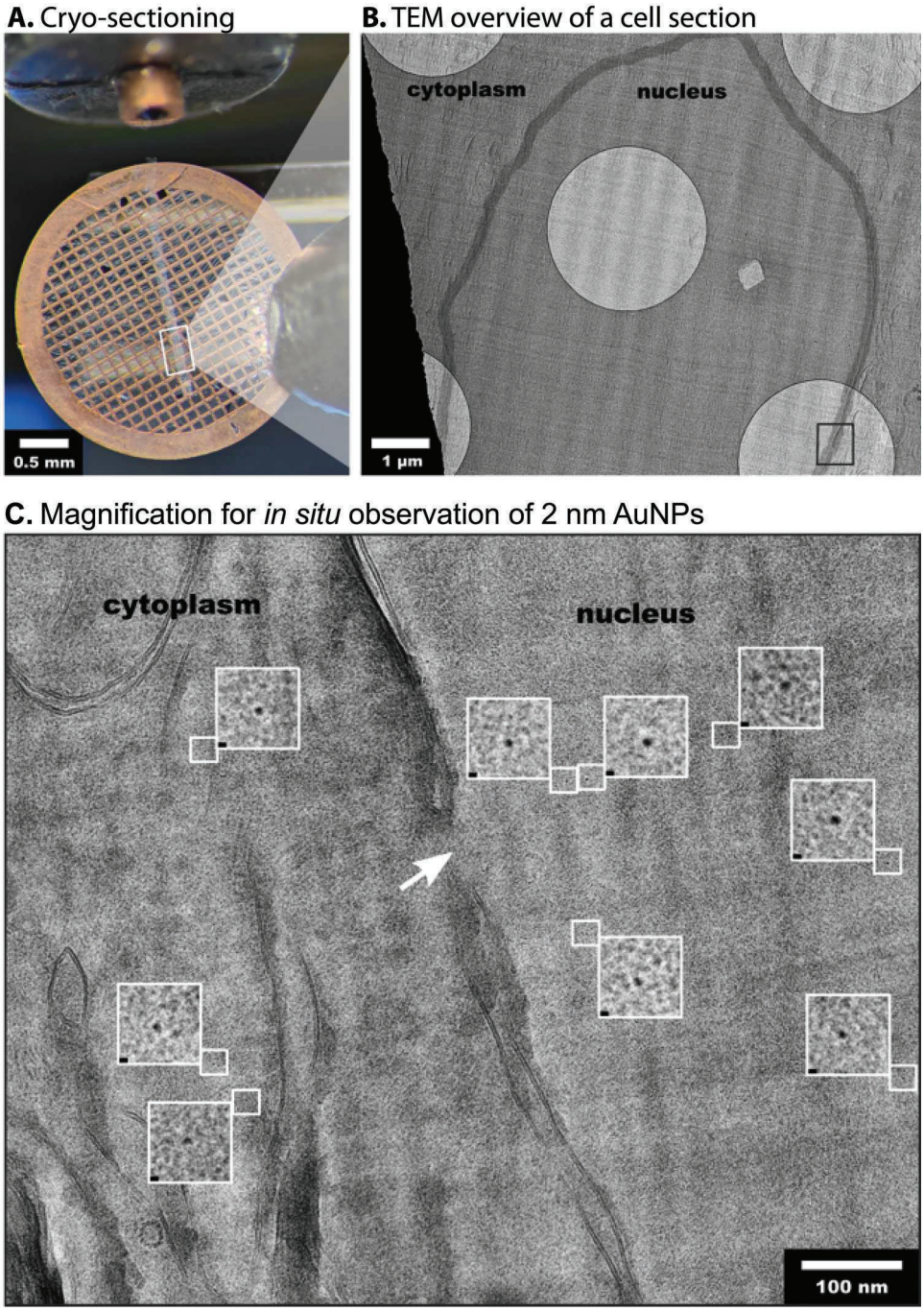


**Figure 7.** Cryo-EM workflow of high-pressure frozen HeLa cells electroporated with AuNLSPEG50%. A)The vitrified specimen was sectioned in cryogenic conditions using a cryo-ultramicrotome. The resulting translucent ribbon was deposited on a copper grid covered with a perforated carbon film and observed in cryo-Electron Microscopy. B)Cryo-EM micrograph showing a portion of cell centered on its nucleus where the nuclear envelope is highlighted. C)Magnified area around the nuclear envelope (black rectangle in (B)) showing subcellular structures including a nuclear pore (white arrow) separating the cytoplasm (left side) from the nucleus (right side). Gold particles in small boxesare enlarged 4 times (large inserts with 2nm black scale bars on bottom left corners) for better visibility.

unstained and fully hydrated cell nucleus by Cryo-Electron Microscopy Of Vitreous Sections (CEMOVIS).[1,46] The functionalized AuPEGNLS50% were delivered into the cytoplasm of living cells by electroporation and the cells were grown for 18 h before vitrification by high pressure freezing. Ribbons of vitreous cell sections were obtained using a cryo-ultramicrotome, collected on EM grids and imaged in cryo-EM (**Figure 7**).

At low magnification (Figure 7B), the cryo-TEM image showed a cell section centered on the nucleus and surrounded by the cytoplasm. The light grey holes correspond to transmitted

23669608, 2023, 6, Downloaded from https://onlinelibrary.wiley.com/doi/10.1002/smtd.202300098 by Cochrane France, Wiley Online Library on [06/01/2025]. See the Terms and Conditions (https://onlinelibrary.wiley.com/terms-and-conditions) on Wiley Online Library for rules of use; OA articles are governed by the applicable Creative Commons License

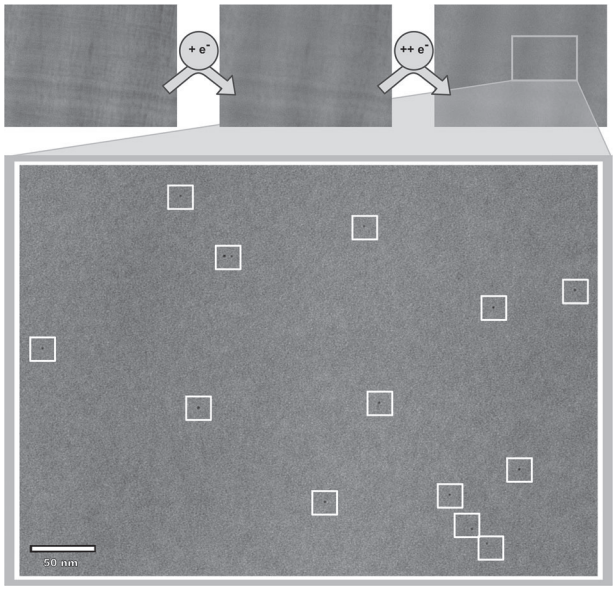


**Figure 8.** Identification of gold particles in the nucleoplasm after radiolysis of biological structures by irradiation with a high electron dose. The structural aspect of the vitreous section gradually changes after irradiation by 20, 80, 120$e^{-}$ $Å^{-2}$ (upper row). Gold particles are the only high contrast structural features remaining after high dose irradiation.

information through the specimen only whereas the dark grey corresponds to an image of the specimen plus the carbon film. Magnification into a hole crossed by the nuclear envelope was performed to observe a nuclear pore and electron dense dot-like structures compatible with the size of AuNPs (Figure 7C). The contrast of these single dots was higher than for subcellular structures such as biological membranes but expectedly faint. To verify that these densities indeed represent the AuNPs, we applied a higher electron dose to the sections (120 e $Å^{-2}$) than one normally used for imaging (10 e $Å^{-2}$) (**Figure 8**). This treatment results in radiolysis of biological molecules but not of inorganic materials. The 2 nm-sized densities remained after radiolysis and became even more contrasted, thus confirming the presence and the ability to detect 2 nm gold particles in two-dimensional cryo-EM images of a crowded cellular section. All detected particles appeared as single and non-aggregated entities. Furthermore, and in agreement with our light microscopy results, a higher concentration of AuNPs was observed within the cell nucleus.

## 3. Conclusion

To use functionalized gold nanoparticles for intracellular labeling and cryo-EM observations, the penetration and diffusion abilities of the probe must be worked out in concert. We report the optimization of the surface coverage of 2 nm TAB-, TNB-protected AuNPs with bioactive NLS ligands and surface-protecting PEG in a controlled way through thiolate exchange. We then delivered these AuNPs into living cells by electroporation. The PEG coverage considerably limited intracytosolic clustering and non-specific adherence to cellular components ensuring a robust SV40 NLS targeting of the nuclear import pathway and the shuttling of the gold particle into the nucleus. Direct detection of individual 2 nm AuNPs within the nuclei of cryo-fixed cells, proves that 2 nm-sized AuNPs provide sufficient contrast to be detected even when embedded within the crowded environment of the cell nucleus. We strongly believe that this identified size range and PEG coverage opens multiple possibilities to generate specific gold immunolabelling tools for deciphering the distribution of intracellular components within living cells after delivery using a convenient electroporation procedure.

## 4. Experimental Section

*General*: Materials and additional protocols were described in the supporting information. The staining profile was measured using Image J[47] by plotting the gray value profiles underneath the indicated lines spanning the cell nuclei.

*Synthesis of AuPEGNLS50%*: A solution of 10 µM 2 nm AuZ[30] (90 µL, 0.9 nmol) was mixed with 1 M HEPES pH 7.4 (10 µL) and then rapidly added to a freshly mixed solution containing 10 mM CALNNGAGP-KKKRKVED peptide (4 µL, 40 nmol), 5 mM tris(-2-carboxyethyl)phosphine, pH 7.4 (8 µL, 40 nmol), and 20 mM thiolated PEG 2000 (PEGSH; 2 µL, 40 nmol) into a 0.5 mL polypropylene tube. The mixture was incubated at room temperature for 16 h. The crude mixture was then purified by size exclusion chromatography (Sephadex G-25, PBS as elution buffer) followed by 7 cycles of ultrafiltration (dilution in sterile PBS) using a 0.5 mL Microcon® centrifugal filter device with 30 kDa cut-off (Merck, Molsheim). At the end of the process, a 60 µL volume was recovered containing AuPEGNLS50% at an estimated concentration of 12 µM (0.72 nmol; 80% recovery yield). The other AuPEGNLSs at different NLS percentage were prepared using the same procedure and an identical [NLS thiolate peptide+PEGSH]/AuZ ratio of 80/0.9. After ultracentrifugation, the AuPEGNLS50% was obtained at a concentration of 30 µM.

*Synchronization of HeLa Cells*: Adherent HeLa cells were synchronized using a double thymidine block method.[44] Thymidine (Sigma) was added to the cell culture media at a final concentration of 2 mM from a 100 mM stock solution in water. The cells were incubated for 16 h at 37 °C, after which the culture media was removed, the cells were washed three times with sterile PBS and normal growth medium was added again. Following 8 h at 37 °C, thymidine was added a second time at a final concentration of 2 mM for additional 16 h.

*Electroporation Protocol*: Transient permeabilization of the plasma membrane of living cells was conducted using the Neon$^{R}$ transfection system[39] with three 10 ms pulses at 517 V $cm^{-1}$.[40] For a final electroporation volume of 10 µL, HeLa cells ($2 \times 10^5$ cells in 10 µL of the Neon Buffer R) were mixed with each functionalized gold nanoparticle (50 pmol at 5 µL of a 10 µM solution in PBS). After electroporation, the cells were diluted into prewarmed cell culture medium with 10% fetal calf serum (FCS) but without antibiotics (1 mL). The cells were pelleted by gentle centrifugation (100 RCF), suspended into warmed cell culture medium with 10%FCS without antibiotics (0.5 mL) and added into 24-well plates containing 13 mm diameter cover glass or into 35 mm Ibidi dishes (Ibidi: ref 80 136 or 80 156). Plates or dishes were then placed inside a cell culture incubator at 37 °C, 5% $CO_2$ for cell adherence and growth.

*Cell Viability Assay*: The assay was done according to a published procedure.[34] Electroporated cells and untreated cells were diluted in 0.5 mL cell culture medium and divided in fractions of 100 µL in a 96-well plate. The cells were incubated at 37 °C, 5% $CO_2$, for 24 h before addition of thiazolyl blue tetrazolium bromide solution in PBS (10 µL of a 5 mg $mL^{-1}$) for quantification of the released formazan.

*Cellular Specimen preparation for Light Microscopy*: The treated cells, grown on cover glasses or Ibidi dishes, were washed twice in PBS (2×1 mL). The cells were then fixed with 2.0% glutaraldehyde in 100 mM Sorenson's buffer (1 mL) for 4 h. After removal of the fixative and 3 PBS washes (1 mL), unreacted aldehydes were blocked by incubation with a 100 mM Sorenson's buffer, pH 7.4 containing 50 mM glycine (1 mL, 20 min). The plasma membrane was permeabilized using 0.1 M Sorenson's buffer pH 7.4 containing 0.1% (w/v) saponin (1 mL, 15 min)



23669608, 2023, 6, Downloaded from https://onlinelibrary.wiley.com/doi/10.1002/smtd.202300098 by Cochrane France, Wiley Online Library on [06/01/2025]. See the Terms and Conditions (https://onlinelibrary.wiley.com/terms-and-conditions) on Wiley Online Library for rules of use; OA articles are governed by the applicable Creative Commons License

before proceeding for silver-mediated amplification of the gold particles according to a modified Danscher protocol using silver acetate and propyl gallate.[48] Briefly, the phosphate-buffered solution was replaced by a 0.1 M citrate solution, pH 6.7 containing 2% sucrose (5 washes). Silver-enhancement of the specimen was then done in a dark room for 8 min using a freshly prepared 6 mM silver acetate solution in 0.16 M sodium citrate, pH 6.7 containing 2 mM propyl gallate and 20% gum arabic. The silver-mediated AuNP staining solution was then removed from the specimens with extensive washes using 0.16 M sodium citrate solution, pH 6.7 (1 mL) and then PBS (0.5 mL). The specimens on the cover glasses were finally mounted onto 3×1 inch microscope slides (knittelglass.com) using Fluoromount-G (Southern Biotech, Ref. 0100–01, batch I2819-WC79B). Observations were carried with Leica DM5500B microscope equipped with HCX PL Apo 63×1.40 oil PH3CS objective and a Leica DFC350FX camera. When cells were grown on 35 mm Ibidi dishes, the observations were carried out with an Olympus IX83 equipped with LUCPLFLN 40×0.6 objective and a CMOS Hamamatsu Orca Fusion camera (C144440-20UP) directly after the silver-enhanced procedure.

## Supporting Information

Supporting Information is available from the Wiley Online Library or from the author.

## Acknowledgements

This research was supported by the ITI Innovec (IdEx (ANR-10-IDEX-0002), SFRI (ANR-20-SFRI-0012)), the French Infrastructure for Integrated Structural Biology (FRISBI ANR-10-INBS-05), and the ITMO Cancer (ColorME, 22P096-00). N.G. received a Ph.D. fellowship from the IdEX Unistra (Université de Strasbourg and Investissements d'Avenir). V.H. received a fellowship from the CNRS. Robert Drillien styleedited the text.

## Conflict of Interest

The authors declare no conflict of interest.

## Data Availability Statement

The data that support the findings of this study are available in the supplementary material of this article.

## Keywords

bioconjugation, electroporation, gold labeling, gold particles, nuclear import, transduction

Received: February 10, 2023
Revised: March 9, 2023
Published online: April 10, 2023

[1] A. Al-Amoudi, J.-J. Chang, A. Leforestier, A. McDowall, L. M. Salamin, L. P. O. Norlén, K. Richter, N. S. Blanc, D. Studer, J. Dubochet, *EMBO J.* **2004**, *23*, 3583.
[2] J. Mahamid, S. Pfeffer, M. Schaffer, E. Villa, R. Danev, L. K. Cuellar, F. Förster, A. A. Hyman, J. M. Plitzko, W. Baumeister, *Science* **2016**, *351*, 969.
[3] Z. Jiang, X. Jin, Y. Li, S. Liu, X.-M. Liu, Y.-Y. Wang, P. Zhao, X. Cai, Y. Liu, Y. Tang, X. Sun, Y. Liu, Y. Hu, M. Li, G. Cai, X. Qi, S. Chen, L.-L. Du, W. He, *Nat. Methods* **2020**, *17*, 937.
[4] E. Silvester, B. Vollmer, V. Pražák, D. Vasishtan, E. A. Machala, C. Whittle, S. Black, J. Bath, A. J. Turberfield, K. Grünewald, L. A. Baker, *Cell* **2021**, *184*, 1110.
[5] I. Orlov, A. Schertel, G. Zuber, B. Klaholz, R. Drillien, E. Weiss, P. Schultz, D. Spehner, *Sci. Rep.* **2015**, *5*, 8324.
[6] P. D. Jadzinsky, G. Calero, C. J. Ackerson, D. A. Bushnell, R. D. Kornberg, *Science* **2007**, *318*, 430.
[7] Y. Levi-Kalisman, P. D. Jadzinsky, N. Kalisman, H. Tsunoyama, T. Tsukuda, D. A. Bushnell, R. D. Kornberg, *J. Am. Chem. Soc.* **2011**, *133*, 2976.
[8] C. J. Ackerson, P. D. Jadzinsky, J. Z. Sexton, D. A. Bushnell, R. D. Kornberg, *Bioconjug. Chem.* **2010**, *21*, 214.
[9] C. J. Ackerson, P. D. Jadzinsky, G. J. Jensen, R. D. Kornberg, *J. Am. Chem. Soc.* **2006**, *128*, 2635.
[10] C. L. Heinecke, T. W. Ni, S. Malola, V. Mäkinen, O. A. Wong, H. Häkkinen, C. J. Ackerson, *J. Am. Chem. Soc.* **2012**, *134*, 13316.
[11] V. Marjomaki, T. Lahtinen, M. Martikainen, J. Koivisto, S. Malola, K. Salorinne, M. Pettersson, H. Häkkinen, *Proc. Natl. Acad. Sci. USA* **2014**, *111*, 1277.
[12] M. Martikainen, K. Salorinne, T. Lahtinen, S. Malola, P. Permi, H. Häkkinen, V. Marjomäki, *Nanoscale* **2015**, *7*, 17457.
[13] V. Postupalenko, D. Desplancq, I. Orlov, Y. Arntz, D. Spehner, Y. Mely, B. P. Klaholz, P. Schultz, E. Weiss, G. Zuber, *Angew. Chem. Int. Ed. Engl.* **2015**, *54*, 10583.
[14] M. Azubel, S. D. Carter, J. Weiszmann, J. Zhang, G. J. Jensen, Y. Li, R. D. Kornberg, *Elife* **2019**, *8*, 43146.
[15] D. Desplancq, N. Groysbeck, M. Chiper, E. Weiss, B. Frisch, J.-M. Strub, S. Cianferani, S. Zafeiratos, E. Moeglin, X. Holy, A. L. Favier, S. De Carlo, P. Schultz, D. Spehner, G. Zuber, *ACS Appl. Nano Mater.* **2018**, *1*, 4236.
[16] R. Lévy, N. T. K. Thanh, R. C. Doty, I. Hussain, R. J. Nichols, D. J. Schiffrin, M. Brust, D. G. Fernig, *J. Am. Chem. Soc.* **2004**, *126*, 10076.
[17] A. A. Sousa, J. T. Morgan, P. H. Brown, A. Adams, M. P. S. Jayasekara, G. Zhang, C. J. Ackerson, M. J. Kruhlak, R. D. Leapman, *Small* **2012**, *8*, 2277.
[18] D. Kalderon, B. L. Roberts, W. D. Richardson, A. E. Smith, *Cell* **1984**, *39*, 499.
[19] W. He, M. S. Ladinsky, K. E. Huey-Tubman, G. J. Jensen, J. R. McIntosh, P. J. Bjorkman, *Nature* **2008**, *455*, 542.
[20] L. Boselli, E. Polo, V. Castagnola, K. A. Dawson, *Angew. Chem.* **2017**, *129*, 4279.
[21] J. F. Hainfeld, F. R. Furuya, *J. Histochem. Cytochem.* **1992**, *40*, 177.
[22] C. D. Walkey, J. B. Olsen, F. Song, R. Liu, H. Guo, D. W. H. Olsen, Y. Cohen, A. Emili, W. C. W. Chan, *ACS Nano* **2014**, *8*, 2439.
[23] K. Luby-Phelps, *Int. Rev. Cytol.* **2000**, *192*, 189.
[24] M. Chiper, K. Niederreither, G. Zuber, *Adv. Healthcare Mater.* **2018**, *7*, 1701040.
[25] V. Sokolova, G. Nzou, S. B. van der Meer, T. Ruks, M. Heggen, K. Loza, N. Hagemann, F. Murke, B. Giebel, D. M. Hermann, A. J. Atala, M. Epple, *Acta Biomater.* **2020**, *111*, 349.
[26] V. Sokolova, J.-F. Ebel, S. Kollenda, K. Klein, B. Kruse, C. Veltkamp, C. M. Lange, A. M. Westendorf, M. Epple, *Small* **2022**, *18*, e2201167.
[27] N. Wolff, S. Kollenda, K. Klein, K. Loza, M. Heggen, L. Brochhagen, O. Witzke, A. Krawczyk, I. Hilger, M. Epple, *Nanoscale Adv.* **2022**, *4*, 4502.
[28] J. Y. Wong, T. L. Kuhl, J. N. Israelachvili, N. Mullah, S. Zalipsky, *Science* **1997**, *275*, 820.
[29] Q. Xu, L. M. Ensign, N. J. Boylan, A. Schön, X. Gong, J.-C. Yang, N. W. Lamb, S. Cai, T. Yu, E. Freire, J. Hanes, *ACS Nano* **2015**, *9*, 9217.
[30] N. Groysbeck, A. Stoessel, M. Donzeau, E. C. da Silva, M. Lehmann, J.-M. Strub, S. Cianferani, K. Dembélé, G. Zuber, *Nanotechnology* **2019**, *30*, 184005.
[31] G. L. Ellman, *Arch. Biochem. Biophys.* **1959**, *82*, 70.

23669608, 2023, 6, Downloaded from https://onlinelibrary.wiley.com/doi/10.1002/smtd.202300098 by Cochrane France, Wiley Online Library on [06/01/2025]. See the Terms and Conditions (https://onlinelibrary.wiley.com/terms-and-conditions) on Wiley Online Library for rules of use; OA articles are governed by the applicable Creative Commons License

[32] E. Oh, J. B. Delehanty, K. E. Sapsford, K. Susumu, R. Goswami, J. B. Blanco-Canosa, P. E. Dawson, J. Granek, M. Shoff, Q. Zhang, P. L. Goering, A. Huston, I. L. Medintz, *ACS Nano* **2011**, *5*, 6434.
[33] X. Liu, M. Atwater, J. Wang, Q. Huo, *Colloids Surf. B Biointerfaces* **2007**, *58*, 3.
[34] G. Creusat, J.-S. Thomann, A. Maglott, B. Pons, M. Dontenwill, E. Guérin, B. Frisch, G. Zuber, *J. Control Release* **2012**, *157*, 418.
[35] R. Lévy, U. Shaheen, Y. Cesbron, V. Sée, *Nano Rev.* **2010**, *1*, 4889.
[36] D. Drescher, T. Büchner, P. Schrade, H. Traub, S. Werner, P. Guttmann, S. Bachmann, J. Kneipp, *ACS Nano* **2021**, *15*, 14838.
[37] S. Pinel, E. Aman, F. Erblang, J. Dietrich, B. Frisch, J. Sirman, A. Kichler, A.-P. Sibler, M. Dontenwill, F. Schaffner, G. Zuber, *J. Controlled Release* **2014**, *182*, 1.
[38] J. B. Gossart, E. Pascal, F. Meyer, E. Heuillard, M. Gonçalves, F. Gossé, E. Robinet, B. Frisch, C. Seguin, G. Zuber, *Met. Sustainability* **2017**, *1*, 1700013.
[39] J. A. Kim, K. Cho, M. S. Shin, W. G. Lee, N. Jung, C. Chung, J. K. Chang, *Biosens. Bioelectron.* **2008**, *23*, 1353.
[40] G. Freund, A.-P. Sibler, D. Desplancq, M. Oulad-Abdelghani, M. Vigneron, J. Gannon, M. H. Van Regenmortel, E. Weiss, *mAbs* **2014**, *5*, 518.
[41] S. C. Ng, D. Görlich, *Nat. Commun.* **2022**, *13*, 6172.
[42] D. Mohr, S. Frey, T. Fischer, D. Görlich, T. Güttler, *EMBO J.* **2009**, *28*, 2541.
[43] K. Ribbeck, D. Gorlich, *EMBO J.* **2001**, *20*, 1320.
[44] G. Chen, X. Deng, *Bio Protoc.* **2018**, *8*, 2994.
[45] A. P. Schuller, M. Wojtynek, D. Mankus, M. Tatli, R. Kronenberg-Tenga, S. G. Regmi, P. V. Dip, A. K. R. Lytton-Jean, E. J. Brignole, M. Dasso, K. Weis, O. Medalia, T. U. Schwartz, *Nature* **2021**, *598*, 667.
[46] T. V. Hoang, C. Kizilyaprak, D. Spehner, B. M. Humbel, P. Schultz, *J. Struct. Biol.* **2017**, *197*, 123.
[47] J. Schindelin, I. Arganda-Carreras, E. Frise, V. Kaynig, M. Longair, T. Pietzsch, S. Preibisch, C. Rueden, S. Saalfeld, B. Schmid, J.-Y. Tinevez, D. J. White, V. Hartenstein, K. Eliceiri, P. Tomancak, A. Cardona, *Nat. Methods* **2012**, *9*, 676.
[48] R. W. Burry, D. D. Vandre, D. M. Hayes, *J. Histochem. Cytochem.* **1992**, *40*, 1849.

23669608, 2023, 6, Downloaded from https://onlinelibrary.wiley.com/doi/10.1002/smtd.202300098 by Cochrane France, Wiley Online Library on [06/01/2025]. See the Terms and Conditions (https://onlinelibrary.wiley.com/terms-and-conditions) on Wiley Online Library for rules of use; OA articles are governed by the applicable Creative Commons License

# Supporting Information

## Bioactivated and PEG-protected circa 2 nm gold nanoparticles for in cell labelling and cryo-Electron Microscopy

*Nadja Groysbeck, Victor Hanss, Mariel Donzeau, Jean-Marc Strub, Sarah Cianférani, Danièle Spehner, Mounib Bahri, Ovidiu Ersen, Mikhael Eltsov, Patrick Schultz, Guy Zuber**

### Complement to Materials and Methods

The materials and methods were essentially the same as the ones reported in the supporting information of our previous publication.[1] Copies with slight edition are provided below:

**Chemicals**

- 5,5'-dithio-bis(2-nitrobenzoic acid)(DTNB) (Sigma-Aldrich D8130)
- Hydrogen tetrachloroaurate(III) trihydrate (Sigma-Aldrich 520918-1G)
- Sodium borohydride ($NaBH_4$) (Aldrich 45,288-2)
- Sodium hydroxide (Fluka 71691)
- 4-(2-Hydroxyethyl)-piperazine-1-ethanesulfonic acid, N-(2-Hydroxyethyl)piperazine-N′-(2-ethanesulfonic acid) (HEPES) (Euromedex 10-110)
- Tris-hydroxymethylaminomethane base (Tris) (Euromedex, 26-128-3094B)
- Glycine (Gly)(Euromedex 26-128-6405C)
- The thiolated peptide CALNNGAGPKKKRKVED (HS-NLS, MW 1828.13) contains the SV40 Nuclear Localization Signal (PKKKRKVED) and an optimized sequence for capping gold nanoparticles (CALNN).[2] It was purchased along with CALNNG (MW: 590.65) from GeneCust (Dudelange, Luxembourg). See Figures S12 and S13 for HPLC and Mass spectrometry analyses
- Methanol (Sigma-Aldrich 179957-5L)
- Water Bi-distilled
- Tris(2-carboxyethyl)phosphine hydrochloride (Sigma-Aldrich BioUltra 75259)
- Ammonium hydroxide 28% (EMS cat#10600 EMS group, Hatfield, PA, USA)
- Glutaraldehyde 25% solution EM grade (EMS cat#16220, EMS group, Hatfield, PA, USA)
- HSPEG (Code PEG1169-0005, MW 2015Da, Iris Biotech, Germany)
- Prestained protein standards: the Precision Plus protein dual color standards (Biorad, ref 1610374)
- 3,5-Dimethoxy-4-hydroxycinnamic acid or sinapinic acid (Merck 85429)

**Materials.** The pH-meter was a Hanna HI2210 instrument combined with a HI 1131B electrode. Centrifugation of 50 mL solutions was performed using an Eppendorf 5810R centrifuge equipped with a A-4-81 rotor. Centrifugation of small volumes (0.5 to 2 mL) was performed using a Sigma 1-15K Eppendorf centrifuge with a 12132-H rotor. For gold particle

formation, agitation was performed on a rocking platform (Heidolph Rotamax 120). The UV-vis absorbance spectra were recorded using a Varian Cary 100Bio spectrometer. Nanoparticles were purified by size exclusion chromatography (Illustra Nap-10 columns sephadex G-25 DNA grade) and concentrated using 0.5 mL Microcon® centrifugal filters (Merck, Molsheim) with cut-off of 30 kDa according to the manufacturer's specification.

**Devices.** Small volumes of aqueous solutions were dispensed using pipettes (Gilson Pipetman® classic P10, P100, P1000 models). Large volumes were dispensed using serological pipettes (Falcon® 5 10 or 25 mL) and a single channel Omega Pipette (Argos Technologies Inc, Elgin IL). Reactions were performed unless indicated in polypropylene tubes of different volumes (50 mL, 15 mL, 2.0 mL, 1.5 mL or 0.5 mL).

**Preparation of aqueous stock solutions**

- Peptides were made at 10 mM concentration in water and stored in aliquots at -20°C. For titration by PAGE, the 10 mM thiolated NLS peptide (10 µL, 100 nmol) was fully reduced 15 minutes before addition to the gold nanoparticles by addition of one molar equivalent of 0.1 M TCEP (1 µL, 100 nmol).
- Tris(2-carboxyethyl)phosphine (TCEP), 0.1 M solution, pH 7.4 was prepared by incremental addition of 2 M NaOH to a 0.2 M TCEP hydrochloride (286.65 mg in 5 mL $H_2O$) solution under stirring and by monitoring pH increase with a pH-meter. When the pH reached 7.4, the TCEP solution was set at 0.1 M and stored in aliquots at -20°C.
- 4-(2-Hydroxyethyl)-piperazine-1-ethanesulfonic acid, N-(2-Hydroxyethyl)piperazine-N′-(2-ethanesulfonic acid) (HEPES) (23.83 g, 0.1 mol) was dissolved in water (50 mL). The pH was adjusted to pH 7.4 with incremental addition of 1M NaOH and using a pH-meter. The solution was then adjusted to 100 mL and was filtered for sterilization using a 33 mm syringe-driven filter unit (0.22 µm Millex-GP, Millipore, Molsheim France). The 1M HEPES-Na solution pH 7.4 was stored at 4-8°C.
- Hydrogen tetrachloroaurate(III) trihydrate ($HAuCl_4$ -$3H_2O$) (1g, 2.539 mmol) was dissolved in water (6.35 mL) to a final concentration of 0.4 M in aurate. This stock solution was stored at 4-6°C in a brown vial and can be stored for more than 6 months.
- The 2 M ammonium acetate solution was buffered to pH 4.7 with 2 M acetic acid solution using a pH-meter.
- 5,5'-dithio-bis(2-nitrobenzoic acid) (DTNB) (198.2 mg, 50 µmol) was dissolved in 0.3 M aqueous NaOH solution (10 mL) to a final 50 mM DTNB concentration. The orange solution was used within 2 weeks and stored at 4-6°C in the dark when not freshly used.
- The 133 mM Sorenson's buffer, pH 7.4 was prepared by combining 133 mM $Na_2HPO_4$ (804 mL) with 133 mM $KH_2PO_4$ (196 mL). After verification of the pH with the pH-meter, the solution was filtered for sterilization using a 33 mm syringe-driven filter unit (0.22 µm Millex-GP, Millipore, Molsheim France).
- For electroporation, the concentrations of each gold nanoparticle solution were adjusted to 10 µM by dilution with sterile PBS. The solutions were stored at 0-4°C and appears stable for at least 2 months in regard to SDS PAGE analysis, colloidal stability and abilities to accumulate in the cell nuclei following electroporation.

**Gold nanocluster synthesis.** The synthesis was done following a described procedure. A 44.35 mM DTNB (5,5'-dithiobis-(2-nitrobenzoic acid)) aqueous solution in 0.3 M NaOH (1.08 mL, 48 µmol) and then a 0.4 M aqueous solution of hydrogen tetrachloroaurate(III)

trihydrate (70 µL, 28 µmol) were added to $CH_3CN/H_2O$ (8/2) (10.8 mL) under fast agitation. After 6h at room temperature under constant agitation, a freshly prepared 0.75 M $NaBH_4$ solution in cold water (240 µL, 180 µmol) was added to the mixture. The mixture immediately turned black. After an overnight stirring, the gold particles were recovered by centrifugation as a pellet, washed with acetonitrile and then dried. The gold particles were then suspended in 0.2 M sodium acetate pH 6.0 (5 mL) and Methanol (5 mL). The solution was then centrifuged to remove a pellet consisting of undesired gold particles that did not migrate in 10% PAGE. The desired gold particles were then precipitated by addition of more MeOH (20 mL) to the solution. The black pellet (gold nanoparticle) obtained by centrifugation was then dried, suspended in water (400 µL) and further purified by a size exclusion chromatography (Illustra Nap-10 columns sephadex G-25 DNA grade) using sterile water as the eluting phase. The concentration of the gold nanoparticles was determined by UV-vis spectrophotometry using the absorbance at 520 nm and a $\varepsilon_{520}$ of 5.1 x $10^5$ $mol^{-1}$ x L x $cm^{-1}$.[3]

**PolyAcrylamide Gel Electrophoresis.** 10 to 20% Polyacrylamide Gels (1 mm thick) were casted using the BioRad MiniProtean system in 25 mM Tris-186 mM glycine buffer pH 8.3 containing 0.1 % (w/v) Sodium Dodecyl Sulfate (SDS). For electrophoresis, the running buffer was 25 mM Tris-186 mM glycine buffer pH 8.3 containing 0.1 % SDS unless indicated otherwise. The polyacrylamide gel was pre-run for 20 min at 90V. For loading in the wells, 50% (v/v) glycerol in water was diluted to 10% into samples. The electrophoresis was run at room temperature for 45 minutes at 90V. The gold nanoclusters were observed as black-brown bands. Peptides were then visualized after Coomassie blue staining. Images were taken with an iPhone 6 and by trans-illumination using a LED panel.

**Electron Microscopy of single particles.** AuNLSPEG50% concentrated solution was diluted 1000x in pure water. 3µL of diluted gold conjugate solution was deposited and air dried on glow discharged Copper C-flat R2/2 carbon film EM grids. The grid was then imaged in a Tecnaï F20 operating at 200 kV equipped with a 2K CCD Gatan camera. Micrographs montages were recorded at 100 kX with a 2.09 Å pixel size at -0.5 µm defocus.

**MALDI-TOF mass spectrometry**. Mass measurements were carried out on an Autoflex™ MALDI-TOF mass spectrometer (Bruker Daltonics GmbH, Bremen, Germany). This instrument was used at a maximum accelerating potential of 20 kV in positive mode and was operated in linear mode at 17.7 kV. The delay extraction was fixed at 600 ns and the frequency of the laser (nitrogen 337 nm) was set at 5 Hz. The acquisition mass range was set to 10000-230000 m/z with a matrix suppression deflection (cut-off) set to 9000 m/z. The equipment was externally calibrated with a standard protein calibration mixture that contained 5 proteins (Bruker Protein Standard II #8207234, Bruker Daltonics GmbH, Bremen, Germany) covering the 10,000-70,000 m/z range. Each raw spectrum was opened with flexAnalysis 2.4 build 11 (Bruker Daltonics GmbH, Bremen, Germany) software. Sample preparation was performed with the dried droplet method using a mixture of 0.5 µl of sample with 0.5 µl of matrix solution dried at room temperature. The matrix solution was prepared from a saturated solution of sinapinic acid in water/acetonitrile 50/50 diluted three-fold in water/acetonitrile/trifluoroacetic acid 50/49.9/0.1.

**Cell culture.** The HeLa (ATCC CCL2) and U2OS (ATCC HTB-96) human cancer cell lines were maintained in Dulbecco's modified Eagles tissue culture medium (DMEM) supplemented with 10% heat inactivated FCS (Life Technologies), 2 mM L-glutamine and antibiotics. Cells were grown in humidified atmosphere at 37°C and with 5% $CO_2$. Cells were maintained in culture for less than 12 passages.

**Cellular Specimen preparation for Electron Microscopy.** 24h after the electroporation treatment, the adherent cells were washed with warmed (37°C) Sorenson's buffer (3 times 2 mL). The cells were then fixed with 2.0% glutaraldehyde (1 mL) for at least 4 hours. The cells were then washed with TEM storage solution (5x, 1 mL). Enhancement of the size of the gold particles with silver was performed using the SE-EM kit (Aurion, the Netherlands) and according to the manufacturer's protocol. The cells were then contrasted with 0.5% osmium for 20 min followed by 2% uranyl acetate both diluted in water. The specimens were then dehydrated in a solution containing increasing concentrations of ethanol and flat embedded in epon (Ladd Research Industries, Williston, Vermont, USA). The resin-embedded specimens were sectioned into 100 nm thick slices that were deposited on a 200 mesh electron microscopy grid.

**High-angle annular dark-field scanning transmission electron microscopy (HAADF-STEM).** Cellular samples were imaged using a Cs-corrected JEOL JEM-2100F scanning transmission electron microscope operating at 200 kV and equipped with a High Angle Annular Dark Field Detector.

**Cellular Specimen preparation for cryo transmission electron microscope**. Electroporation was conducted with three 10 ms pulses at 517 $V.cm^{-1}$ using a 100 µL syringe (transfection system kit Neon™ 100 µl). The freshly trypsinized cells (1 x $10^6$ cells in 60 µL Neon Buffer R) were mixed with AuPEGNLS50% (50 µL of a 30 µM in PBS). After application of the pulses, the cells were diluted in cell culture medium containing 10% FCS serum and added onto a 100 mm diameter dish for cell growth during 18h. The cells were prepared as reported.[4] Electroporated Hela cells were scraped from petri dishes and pelleted down in the presence of cryoprotectant containing 10% dextran (Sigma-Aldrich # D1662) and 10% Bovine Serum Albumin (BSA, Sigma-Aldrich). The prepared pellet was drawn inside copper specimen tubes 1.5 mm / 200 µm (Leica Microsystem) and frozen by high pressure freezing using the EMPACT 2 apparatus (Leica Microsystems). Frozen specimens were then transferred into a Leica FC6/UC6 ultramicrotome (Leica Microsystems) installed in an anti-contamination glovebox[5] and trimmed. High pressure frozen cells were then sectioned at −145°C, using a 25° diamond knife (Diatome) with a cutting feed of 75 nm. Sections were collected on Quantifoil R2/2 grids coated by a holed thin carbon film and attached to the grid using an electrostatic charging device (Crion, Leica microsystem).

**Cryo electron microscopy of vitreous section.**
Grids with sections were mounted into Autogrid rings (Thermo Fischer Scientific) and transferred into a Cs-corrected Titan Krios (Thermo Fischer Scientific) operated at 300kV equipped with a GATAN GIF Quantum SE post-column energy filter and K2 Summit direct electron detector (Gatan). Cells were mapped within sections by screening at ×2300, and movies were recorded using Serial EM software[6] at x33000 with -1 µm targeted defocus and a total dose of 16.6 $e/A^2$ total over 20 frames. The frames were aligned and summed using MotionCor2 software.[7] The radiolysis[8] was performed as the series of 6 exposures of 20 $e/A^2$ each, resulting in a total dose of 120 $e/A^2$.

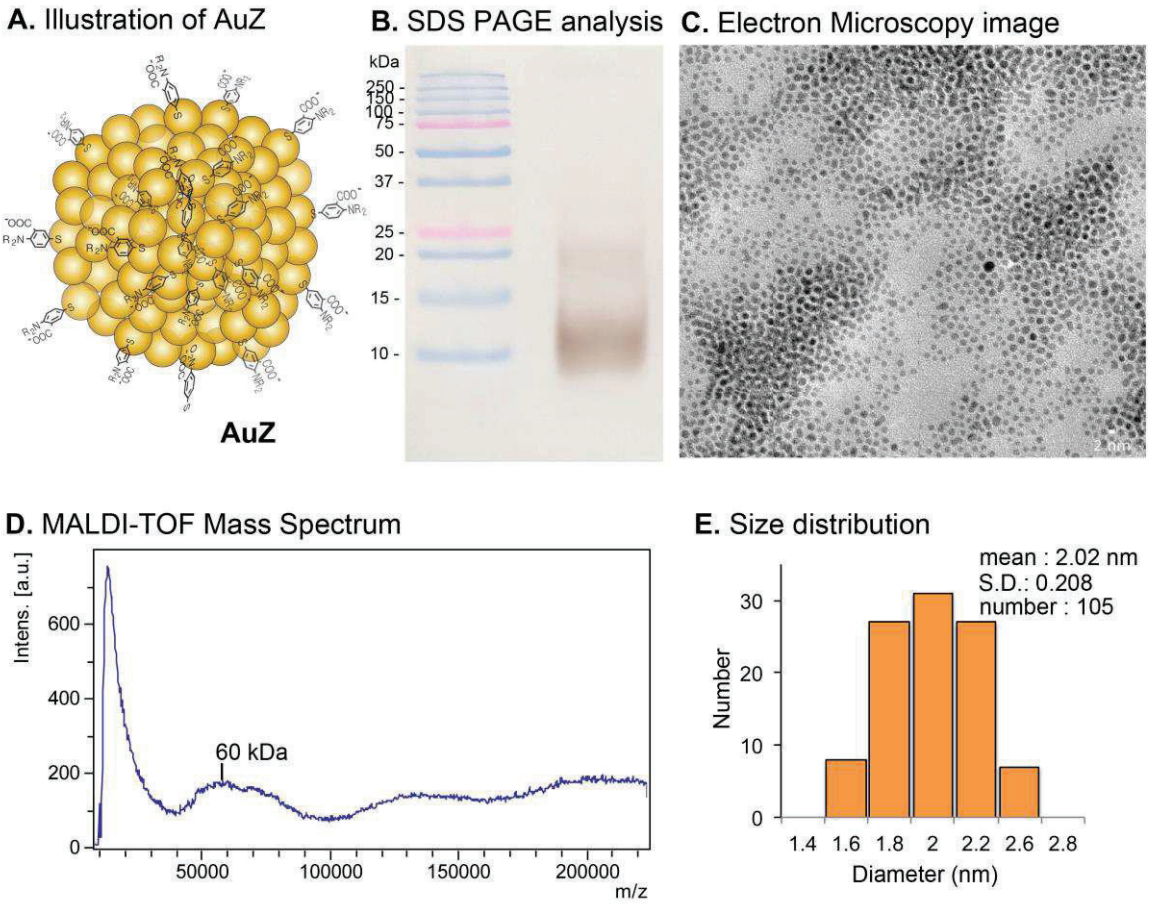


**Figure S1.** Analysis of the thioaminobenzoate- (TAB-) thionitrobenzoate- (TNB-) coated gold nanoparticle (AuZ) batch that was used for biofunctionalization. A. Illustration of the material. B. sodium dodecyl sulfate (SDS) 20% polyacrylamide gel electrophoresis (PAGE) analysis of AuZ (80 pmol). After electrophoresis, the gel was photographed. The first lane is the Precision Plus protein dual color standards (BioRad). C. Electron microscopy image of the AuZ after deposition onto Carbon film. D. MALDI-TOF Mass spectrum of AuZ. E. Size distribution analysis of AuZ. Diameters were measured from EM image.

**A.** Image of solutions 16h after mixing the peptide with AuZ at the indicated ratio

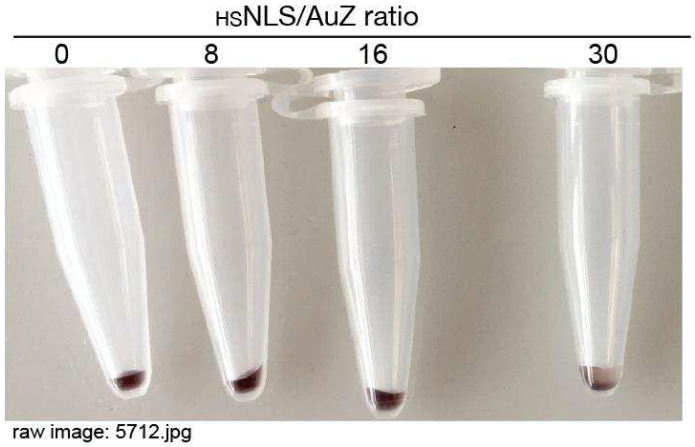


raw image: 5712.jpg

**B.** SDS PAGE analysis before Coomassie blue staining

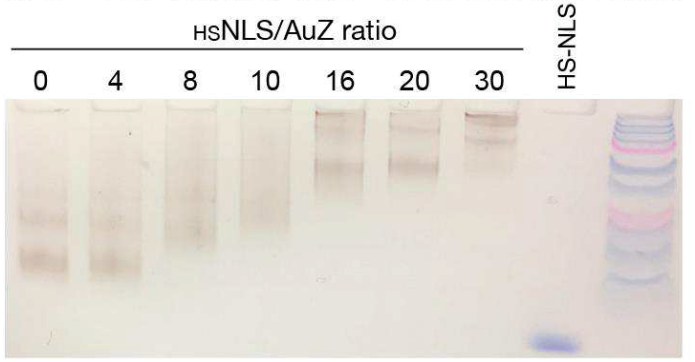


raw image: IMG_5728.jpg

**C.** SDS PAGE analysis after Coomassie blue staining

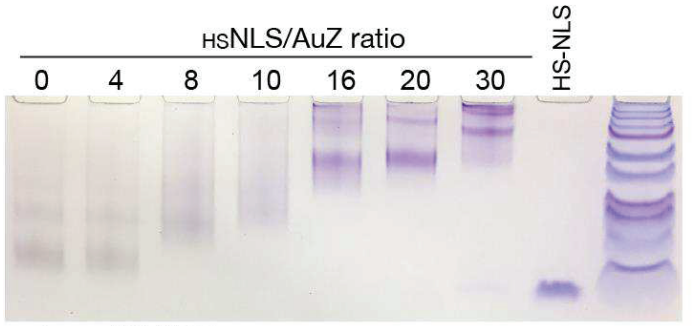


raw image: IMG_5732.jpg

**Figure S2.** Analysis of reaction products following incubation of AuZ (50 pmol) with increased amount of CALNNGAGPKKKRKVED (200 pmol to 1500 pmol as indicated) in 0.1 M HEPES pH 7.6 (6 µL) at 20°C for 16h. A. Image of tubes containing the reaction mixture at the indicated ratios after the 16h reaction time. A clear precipitation was observed at HS-NLS/AuZ ratio of 30. This colloidal instability was not seen previously with the 1.4 nm NLS-coated gold particles presenting a calculated surface of 6.15 $nm^2$ ($s=4\pi r^2$), indicating that specific functionalization of the exposed 12.6 $nm^2$ surface of 2 nm TAB-, TNB-AuNPs should already be combined with shielding elements. B and C. Images of the same gel before and after Coomassie Blue staining. Data showed new bands with decreased electrophoretic mobility suggesting formation of NLS coated gold particles with increased degree of conjugation. To note, the reaction mixture containing precipitated AuNPs (NLS/AuZ ratio of 30) was deposited into the well. Migration was likely due to the presence of sodium dodecyl sulfate (SDS) in the running buffer and in the gel.

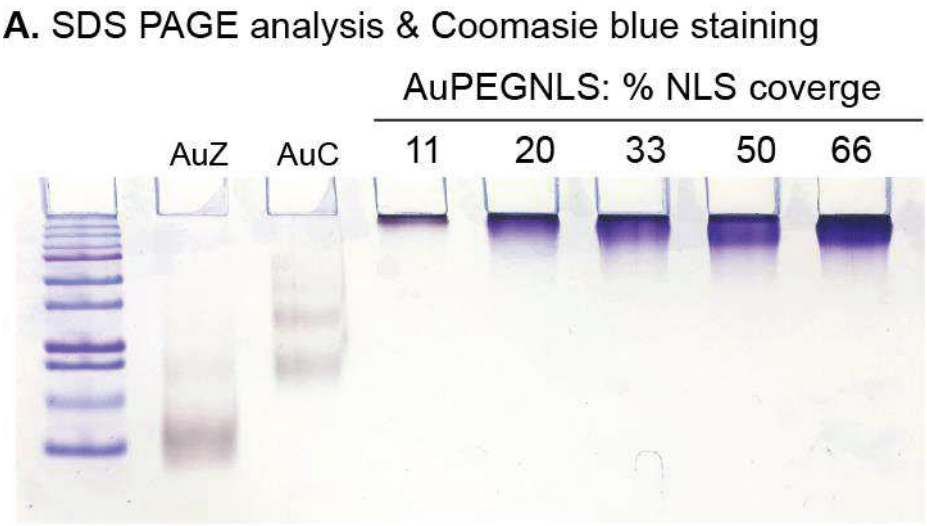


**Figure S3.** SDS PAGE analysis of the indicated gold particles after Coomassie blue staining. The blue staining intensity of AUPEGNLSs increased with increased %NLS coverage indicated that the NLS peptide is co-linked to the AuNP surface

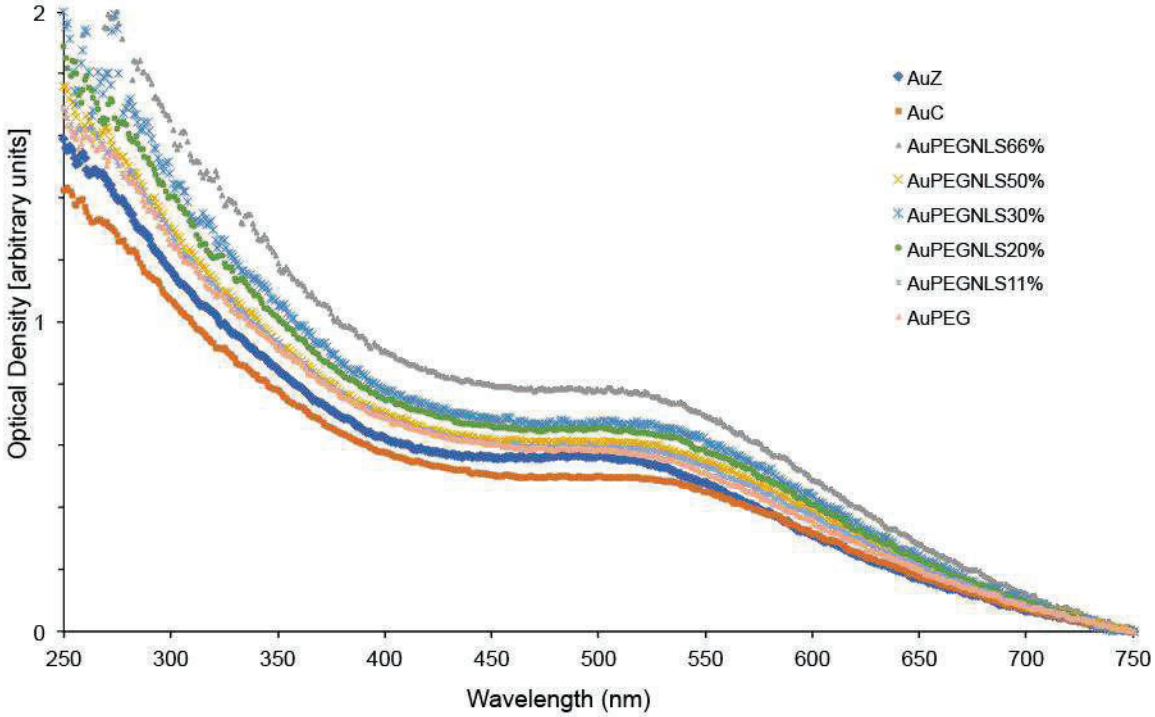


**Figure S4.** UV-visible spectra of the indicated gold nanoparticles in water. The concentrations of gold nanoparticles were estimated using an absorption coefficient of 510 000 $M^{-1}.cm^{-1}$ at 520 nm. This absorption coefficient (ε) at 520 nm [$M^{-1}.cm^{-1}$] was calculated according to the formula: $\varepsilon = e^{[3.32111.\ln D + 10.80505]}$ with D being the Diameter of the particle in nm.[3]

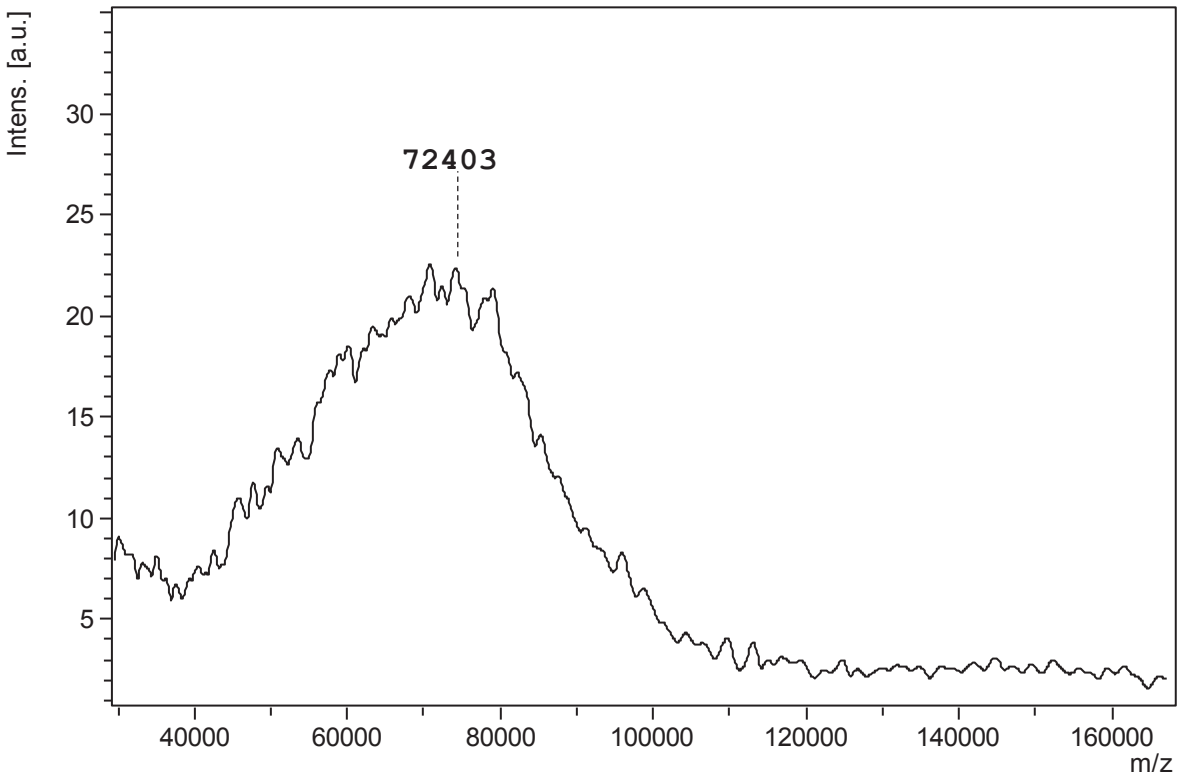


**Figure S5.** MALDI-TOF MS of AuPEG

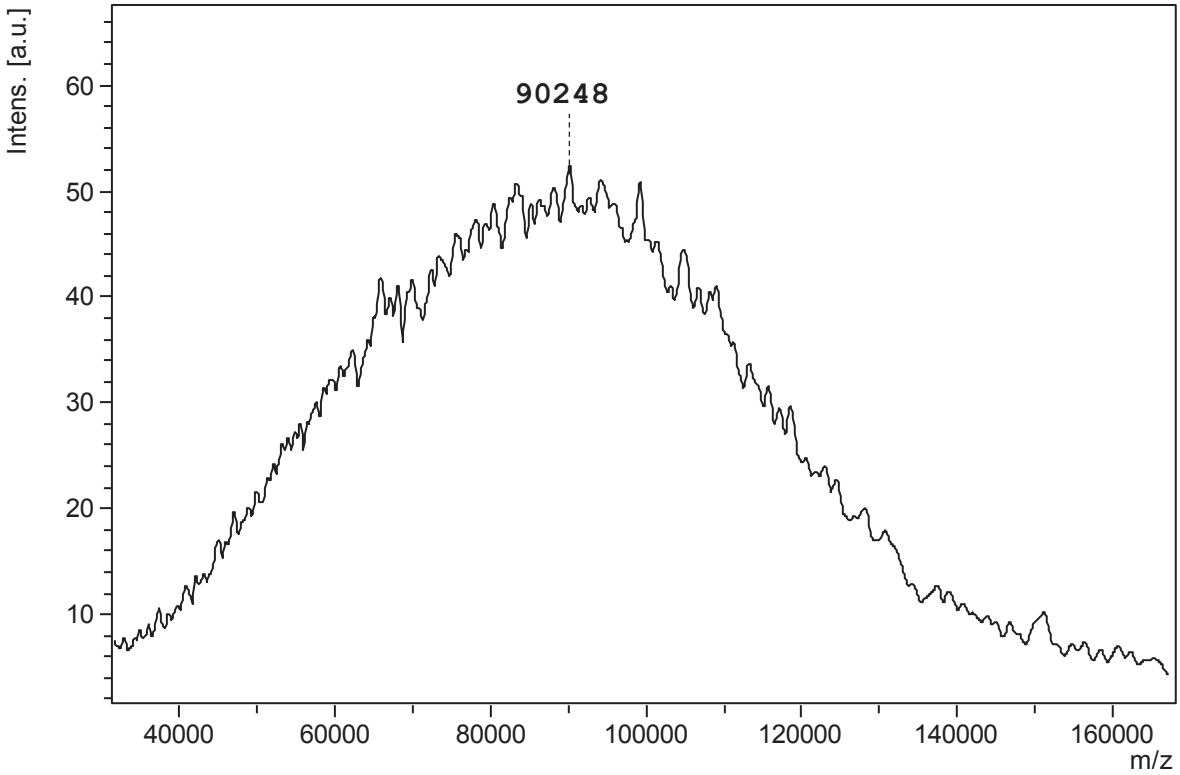


**Figure S6.** MALDI-TOF MS of AuPEGNLS 66%

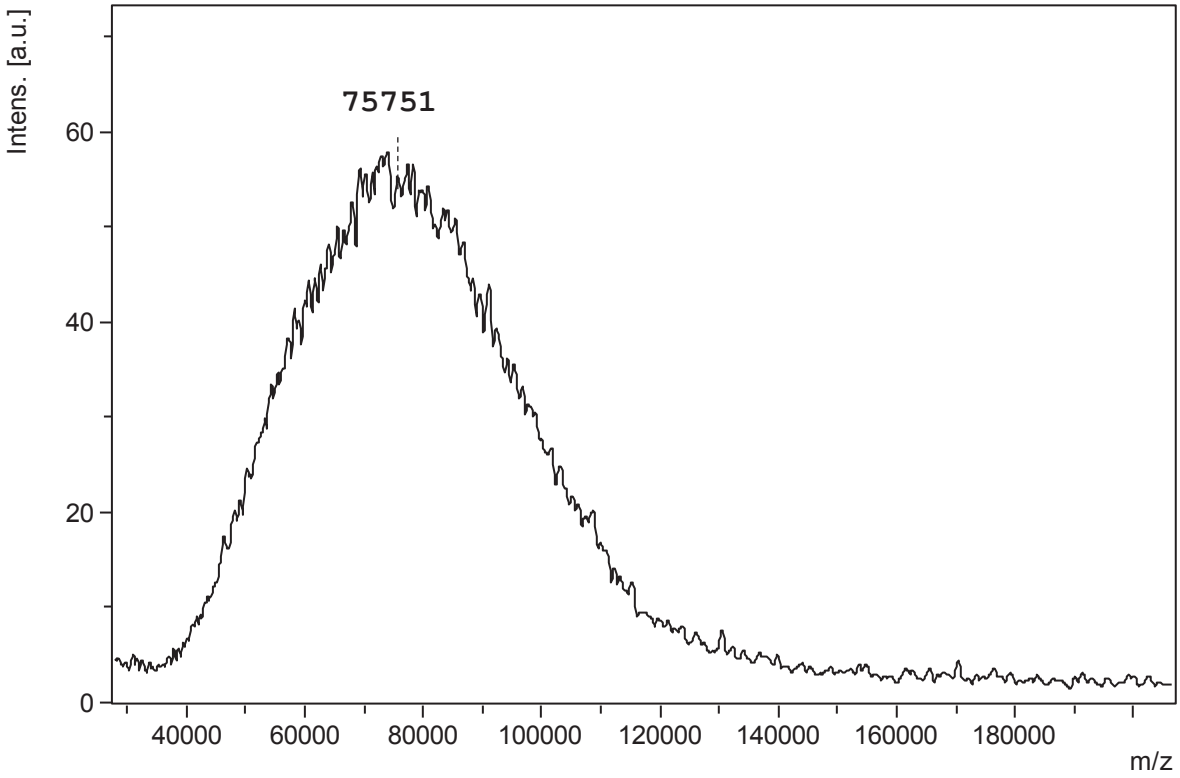


**Figure S7.** MALDI-TOF MS of AuPEGNLS 50%

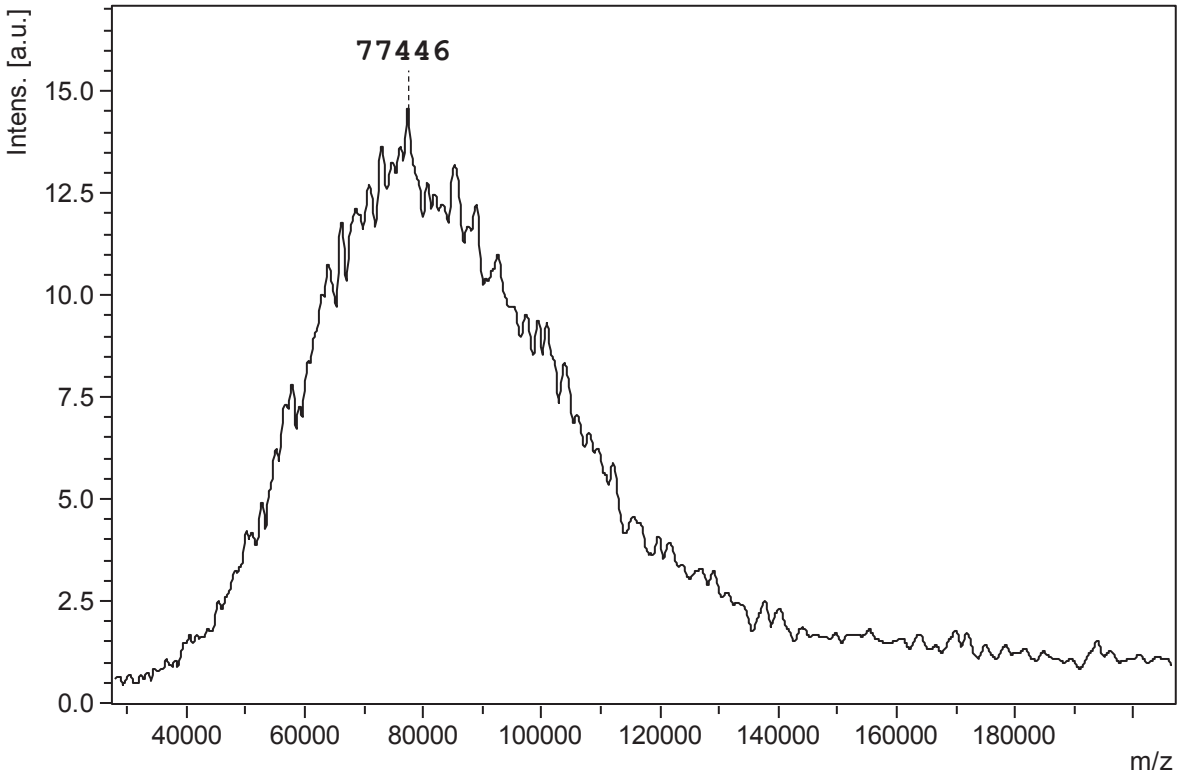


**Figure S8.** MALDI-TOF MS of AuPEGNLS 33%

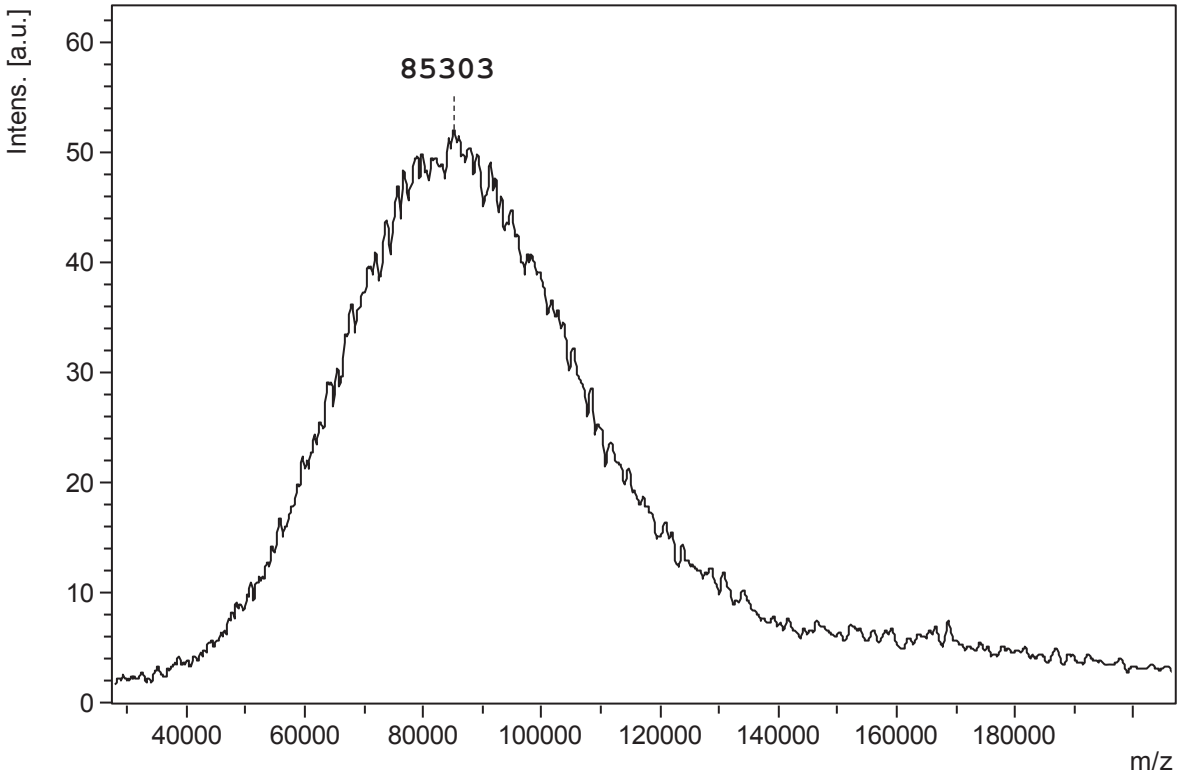


**Figure S9.** MALDI-TOF MS of AuPEGNLS 11%

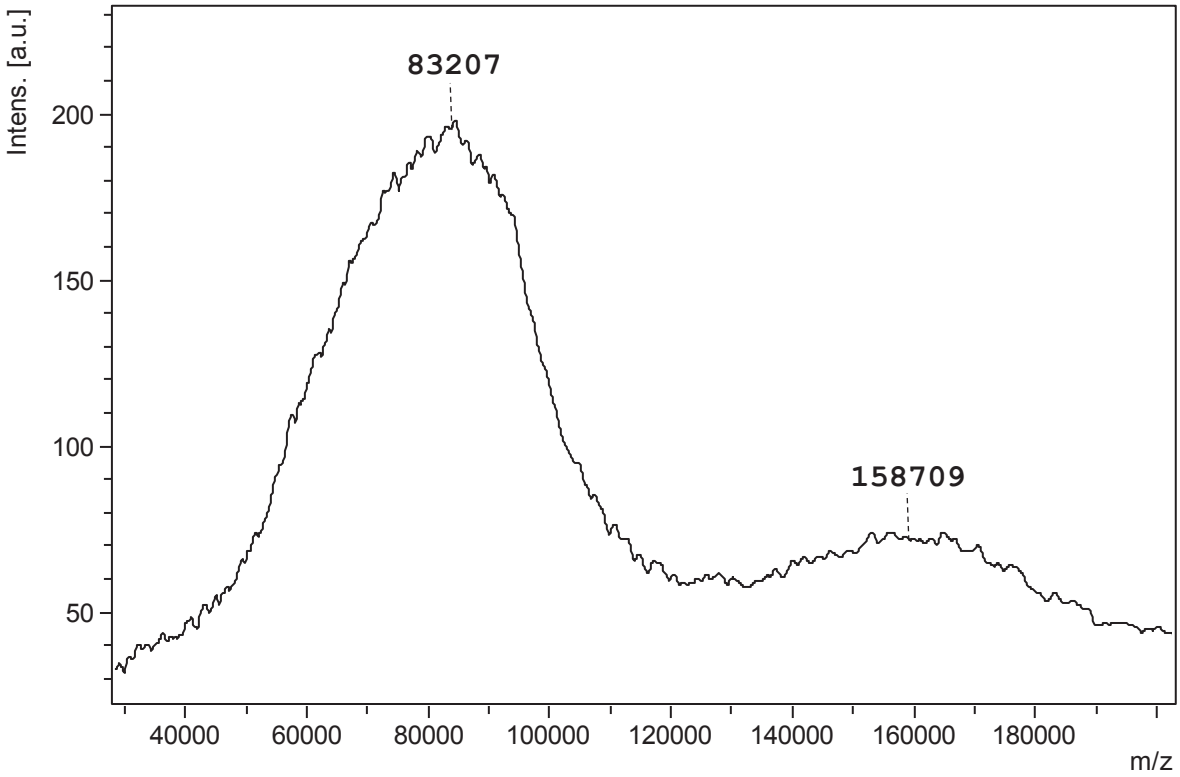


**Figure S10.** MALDI-TOF MS of AuC

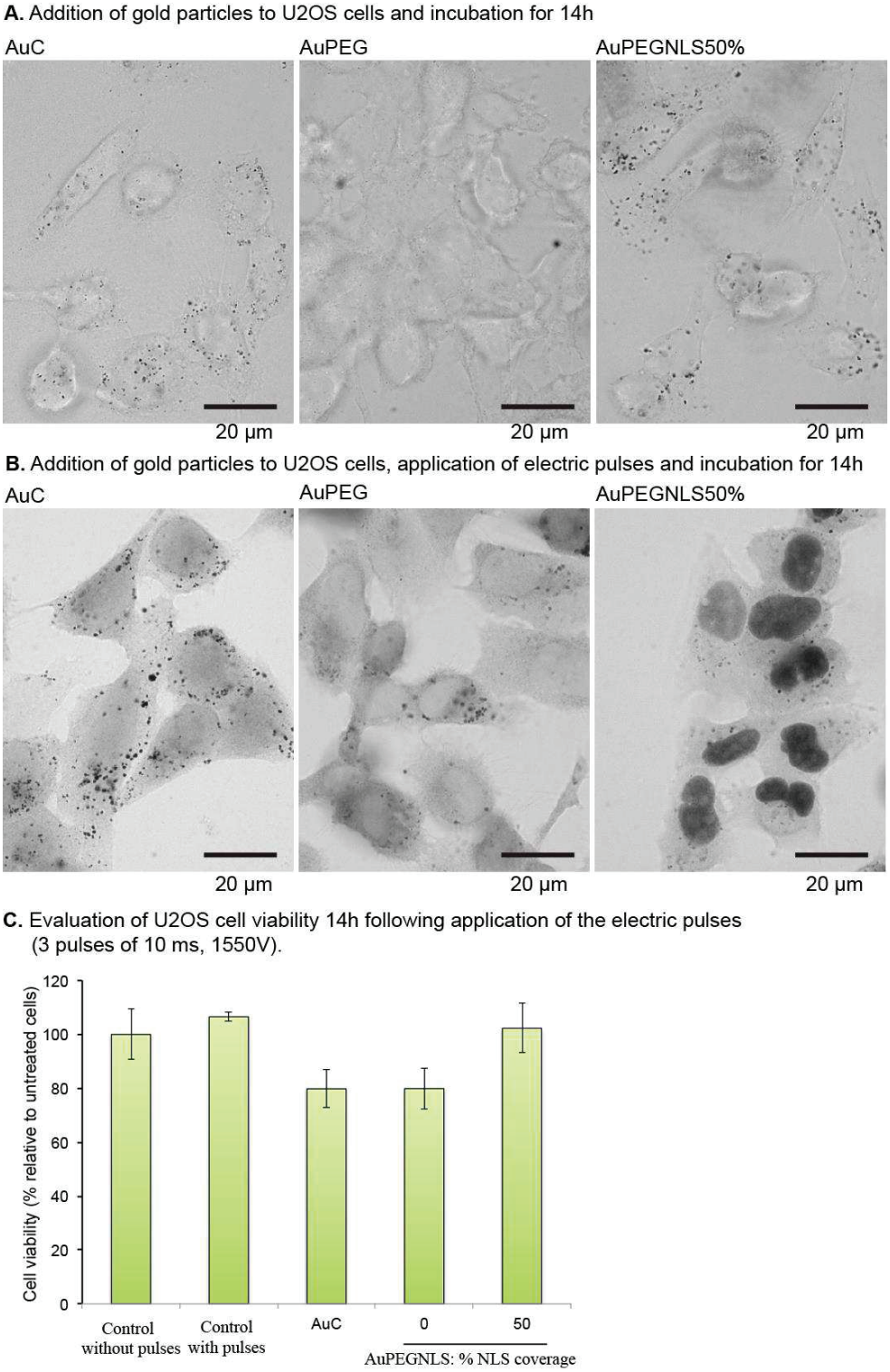


**Figure S11.** A and B. Freshly trypsinized U2OS cells ($10^5$ cells/10µL PBS) containing 5 µM of each AuNP were either directly diluted in 1 mL cell culture medium containing 10% serum or subjected to 3 electric pulses of 10 ms at 517 $V.cm^{-1}$ before dilution. Cells were collected by centrifugation and then dispatched in 0.5 mL cell culture plates for cell culture at 37°C during 14h (final concentration: 0.5 µM). Cells were fixed with 2% glutaraldehyde, permeabilized with 0.1% saponin and the gold particles were silver-enhanced for detection. C. Cell viability was estimated with the MTT assay. Values are averages and standard deviations of quintuplicates.

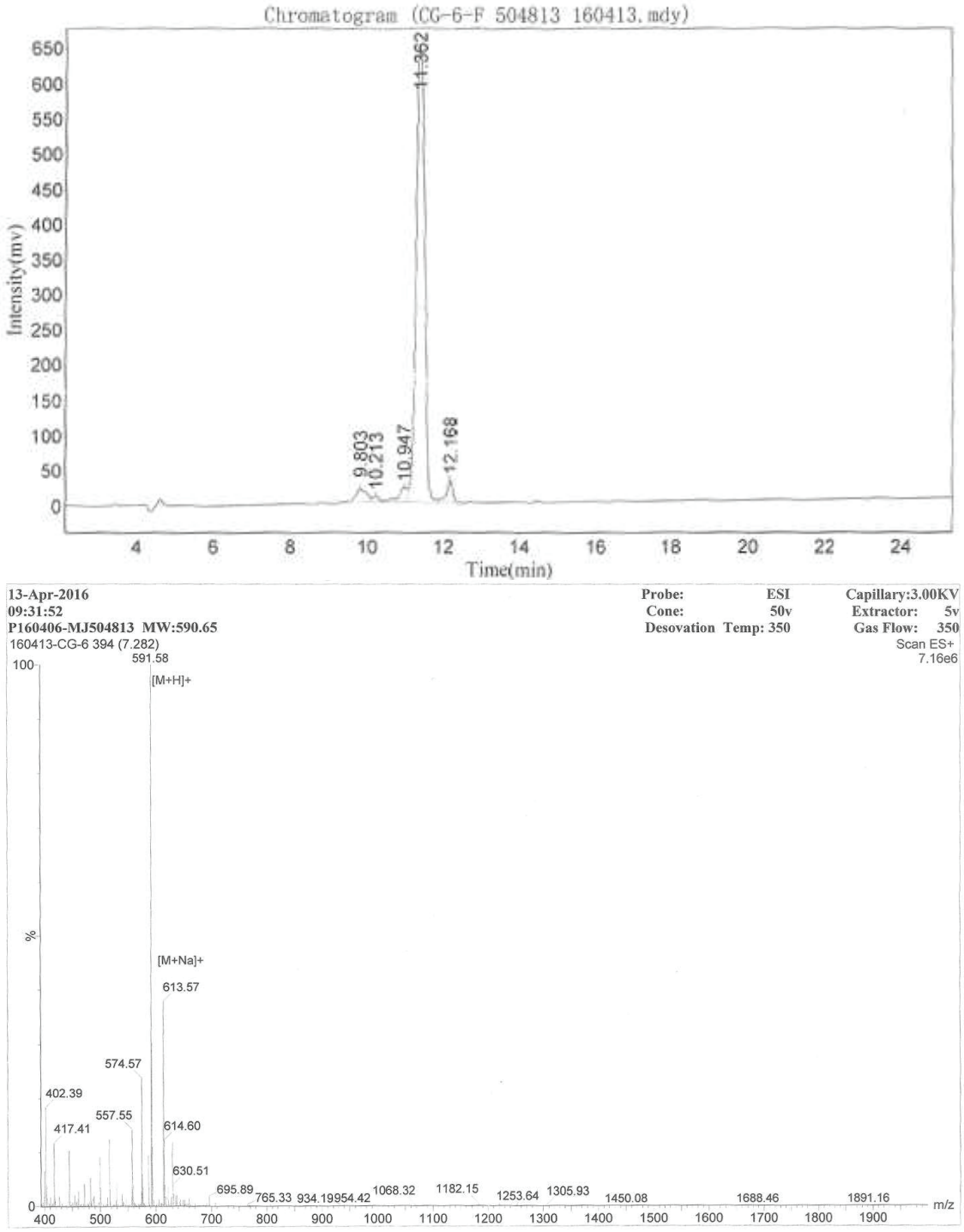


**Figure S12.** HPLC profile and mass spectrometry analysis of the Cap peptide (CALLNG, $C_{22}H_{38}N_8O_9S_1$ ; MW : 1801.06). Column: 4.6mmx250mm Diamonsil 5 µ C18. Solvent A: 0.1% TFA in 100% Acetonitrile, Solvent B : 0.1% TFA in water. Gradient: 0 to 25 min, 7 to 32% A.

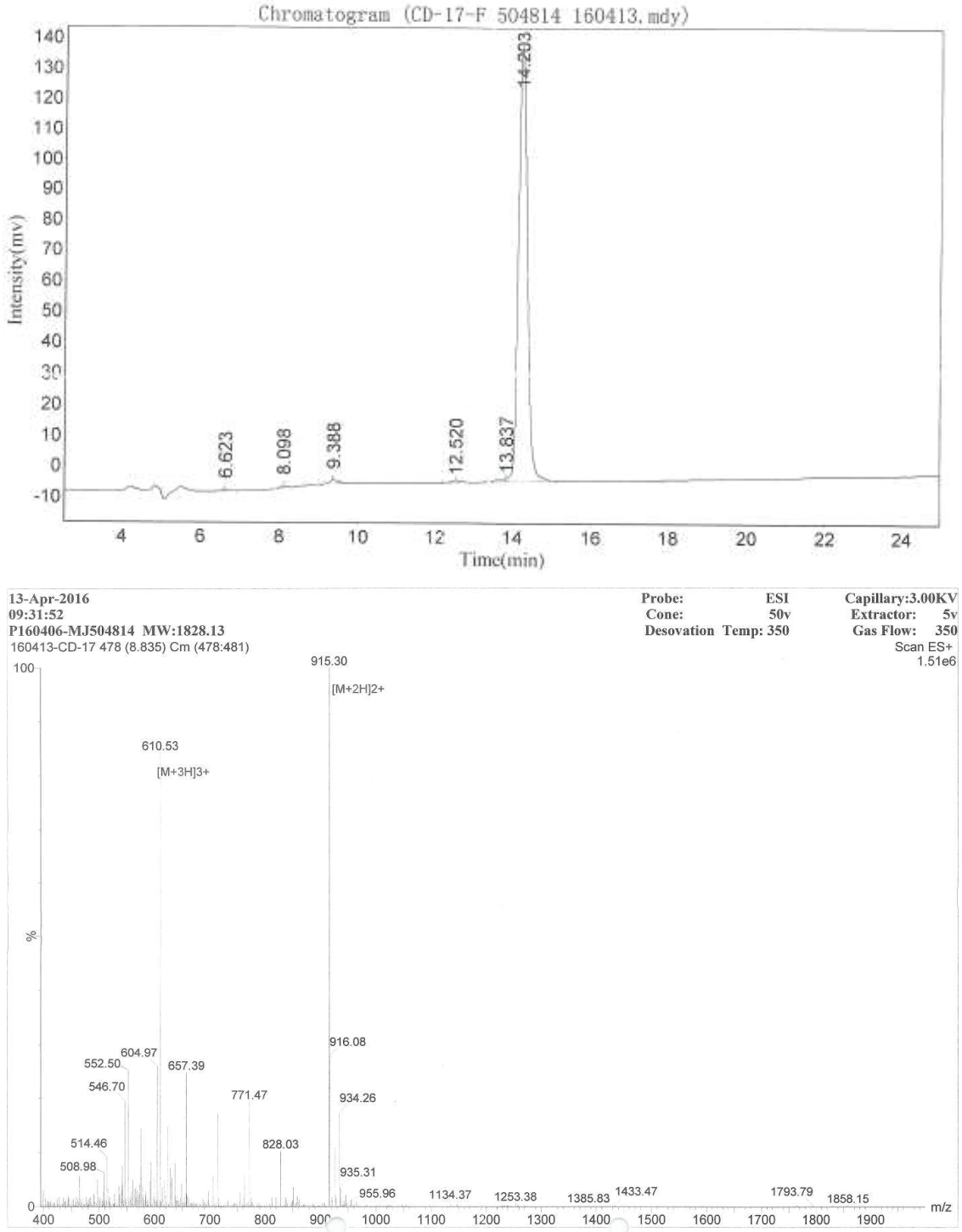


**Figure S13.** HPLC profile and mass spectrometry analysis of the NLS peptide (CALNNGAGPKKKRKVED, $C_{76}H_{134}N_{26}O_{25}S_1$ ; MW : 1828.13). Column 4.6mmx250mm Diamonsil 5 µ C18. Solvent A: 0.1% TFA in 100% Acetonitrile, Solvent B : 0.1% TFA in water. Gradient: 0 to 25 min, 7 to 32% A.

**References**

[1] D. Desplancq, N. Groysbeck, M. Chiper, E. Weiss, B. Frisch, J.-M. Strub, S. Cianferani, S. Zafeiratos, E. Moeglin, X. Holy, A. L. Favier, S. De Carlo, P. Schultz, D. Spehner, G. Zuber, *ACS Applied Nano Materials* **2018**, *1*, 4236.
[2] R. Lévy, N. T. K. Thanh, R. C. Doty, I. Hussain, R. J. Nichols, D. J. Schiffrin, M. Brust, D. G. Fernig, *J. Am. Chem. Soc.* **2004**, *126*, 10076.
[3] X. Liu, M. Atwater, J. Wang, Q. Huo, *Colloids Surf. B: Biointerfaces* **2007**, *58*, 3.
[4] T. V. Hoang, C. Kizilyaprak, D. Spehner, B. M. Humbel, P. Schultz, *Journal of Structural Biology* **2017**, *197*, 123.
[5] J. Pierson, J.-J. Fernandez, E. Bos, S. Amini, H. Gnaegi, M. Vos, B. Bel, F. Adolfsen, J. L. Carrascosa, P. J. Peters, *J. Struct. Biol.* **2010**, *169*, 219.
[6] D. N. Mastronarde, *J. Struct. Biol.* **2005**, *152*, 36.
[7] S. Q. Zheng, E. Palovcak, J.-P. Armache, K. A. Verba, Y. Cheng, D. A. Agard, *Nature Method*s **2017**, 14, 331.
[8] L. A Baker, J. L. Rubinstein, *Methods in Enzymology* **2010**, *481*, 37

## 1.2. Publication 2

Continuing the collaboration with Dr. Zuber's team (UMR7242 Biotechnology and Cell Signalling), I participated in the characterization of the new nanogold probes. These probes were created by reduction of disulfide bonds at the hing area of the mouse monoclonal antibody targeting RPB1 of RNA polII (clone 7G5), which then reacted with thiolated gold of 1.4 nm diameter by thiolate exchange. Newly synthesized conjugates are characterized by non-reducing SDS-PAGE before electroporation into cells. In the gel, the conjugates formed a near smeared band at the top of the well (Figure 2B of the paper) indicating some structural heterogeneity. We decided to explore this heterogeneity by negative staining EM. My task was to prepare the negative staining samples, image them and determine the overall structure of conjugation products. I applied Single Particle Analysis (SPA) approaches with reference-free particle picking using Eman2 software, 2D particle averaging and alignment and 2-D particle classification using xmipp3 protocols (see Materials and Methods/TEM and image analysis for detail).

My results showed that the majority of antibodies (~88%) were bound to nanogold particles, although free antibodies and single gold were still present in the preparation. Our EM analysis supported the binding of gold at the hinge region of the heavy chains. Interestingly, many classes indicated formation of complexes containing more than two heavy chains of antibodies bound together to the same nanogold particle thus forming “multibranched” structures (see Figure 2C of the paper). These observations highlight the capacities of EM combined with well established SPA tools for direct characterisation of the probes. The results confirmed the efficiency of the nanogold-antibody conjugation reaction, however the heterogeneity of the products has to be taken into account and optimized in future experiments.

The experimental procedures and results are described in detail in the following publication:

Nadja Groysbeck; Anne Marie Haeberlé; Stéphane Ory; **Victor Hanss**; Mikhail Eltsov; Patrick Schultz; Guy Zuber. 1.4 nm gold nanoparticle-antibody conjugates for *in situ* gold immunolabeling after transduction into living human cells. Comptes Rendus. Chimie, Online first (2023), pp. 1-14. doi : 10.5802/crchim.251.

*Comptes Rendus*
*Chimie*
Published online: 18 October 2023
https://doi.org/10.5802/crchim.251

Chemical Biology

# 1.4 nm gold nanoparticle-antibody conjugates for in situ gold immunolabelling after transduction into living human cells

**Nadja Groysbeck [a], Anne Marie Haeberlé [b], Stéphane Ory [b], Victor Hanss [c], Mikhael Eltsov [c], Patrick Schultz [c] and Guy Zuber [*, a]**

[a] Université de Strasbourg - CNRS, UMR7242 Biotechnologie et Signalisation Cellulaire, 300 Bd Sébastien Brant, CS 10413, 67412 Illkirch, France

[b] Centre National de la Recherche Scientifique, Université de Strasbourg, Institut des Neurosciences Cellulaires et Intégratives, F-67000 Strasbourg, France

[c] Centre for Integrative Biology (CBI), Department of Integrated Structural Biology, Institut de Génétique et de Biologie Moléculaire et Cellulaire (IGBMC), 1 rue Laurent Fries, BP10142, F-67404 Illkirch Cedex, France

*E-mails:* nadja.groysbeck@gmail.com (N. Groysbeck), haeberle@inci-cnrs.unistra.fr (A. M. Haeberlé), ory@inci-cnrs.unistra.fr (S. Ory), hanssv@igbmc.fr (V. Hanss), eltsovm@igbmc.fr (M. Eltsov), pat@igbmc.fr (P. Schultz), zuber@unistra.fr (G. Zuber)

**Abstract.** Despite advances in Electron Microscopy (EM) that enable to image protein assemblies within vitreous sections of cells at nearly atomic resolution, labelling is still necessary to locate small proteins or rare complexes. Gold immunolabelling has been used for decades to localise specific proteins within cellular sections. However, current gold particle-antibody conjugates are not built with enough chemical precision to match the current resolution offered by cryo-EM methodology. Furthermore, as a close to native specimen state can only be achieved by strict preservation of a frozen hydrated state, it is required to deliver gold labelling agents into living cells prior to their vitrification. Several 1.4 nm gold nanoparticle-antibody conjugates were synthesised. Their abilities to bind to and label their corresponding epitopes within living cells after cytosolic delivery by electroporation are documented here.

**Keywords.** Gold nanoparticle, Antibody, Conjugate, Intracellular delivery, Gold immunolabelling.

**Funding.** This research was supported by the ITI Innovec (IdEx (ANR-10-IDEX-0002), SFRI (ANR-20-SFRI-0012)), the French Infrastructure for Integrated Structural Biology (FRISBI ANR-10-INBS-05), and the ITMO Cancer (ColorME, 22P096-00). NG received a PhD fellowship from the IdEX Unistra (Université de Strasbourg and Investissements d'Avenir). VH received a PhD fellowship from the CNRS.

*Published online: 18 October 2023*

* Corresponding author.

## 1. Introduction

Understanding how multiple components of a human cell interact together to sustain the basic mechanisms of life remains mostly unknown but makes fast progress through the combination of multiple experimental approaches. Encyclopedia containing the human genome [1] and tissue-based maps of the human proteome [2] enable us to define gene expression profiles and subsequently the protein levels that compose each human cell type. Advanced quantitative methods (quantitative Polymerase Chain Reaction, mass spectrometry) estimate the abundance of mRNA and proteins per cell [3]. Progresses in microscopy allow imaging protein–protein interactions at resolution approaching (macro)molecule level for super resolution fluorescent microscopy and nanometric resolution for cryo-Electron Microscopy (EM) [4]. At nanometric dimensions, specimen preservation is crucial and dehydration or chemical cross-linking should be avoided to prevent structural reorganisation of cellular content. In this respect, eukaryotic cells, including mammalian ones, can be vitrified either by plunge freezing or by high-pressure freezing, to preserve a close-to-native frozen hydrated state, and sectioned below −140 °C for cryo-EM imaging [5]. Abundant proteins forming filaments or large assemblies such as ribosomes or nuclear pores are easily recognised in cryo-electron micrographs due to their characteristic shape [4,6]. However, less abundant biomolecular complexes or small proteins cannot be recognised unambiguously in electron tomograms and their identification relies on labelling tools. Electron-dense gold nanoparticles (AuNPs) conjugated to antibodies are popular tags for EM immunolabelling since their high electron scattering, round shape, and specific dimension provide sufficient contrast to identify the probe [7]. Colloidal AuNPs with size larger than 5 nm in diameter are readily detected even when the cellular sample is contrasted. They offer a large surface area onto which many proteins adsorb [8]. This ability has been exploited to make immunocolloids of popular usage [7]. However, size restricts penetration of those colloids in gel-like biological samples [9]. It has led to the development of gold nanoparticles with diameters below 2 nm and to modification of the gold-to-antibody conjugation because proteins do not adsorb tightly enough on the surface of gold particles below 2 nm [10]. Phosphine-coated 1.4 nm Nanogold® [11] and 0.8 nm ultrasmall AuNPs [12] have increased labelling efficiency but to the cost of an extra step consisting in increasing the size of the gold particles by silver deposition to reveal their positions in the cell sections. Due to the impermeability of the plasma membrane, labelling of specific intracellular targets is generally performed post-embedding on cell sections at temperatures above 0 °C [13]. This protocol is not consistent with high-resolution cryo-EM because vitrified cellular samples cannot be warmed up after sectioning. Therefore, the gold nanoparticles-antibody conjugates need to be delivered into living cells, prior to the vitrification step, using weakly perturbing transduction methods [14]. Ultra-small 0.8 nm AuNPs conjugated to antibodies directed against RNA polymerase II were shown to be delivered into living HeLa cells using a cationic lipid formulation, and the gold labels were detected within the nucleus by Scanning Electron Microscopy (SEM) after resin embedding and silver enhancement [15]. To develop gold particles of sizes directly visible in vitrified cell sections by cryo-EM, mercaptobenzoic acid (MBA)-coated AuNPs of defined sizes around 2 nm [16,17] appeared extremely promising [18,19]. We previously attempted to substitute MBA coating on AuNPs by thionitrobenzoate (TNB) [20] to increase ligand exchange kinetics [21]. During the synthesis of 1.4 nm AuNP with sodium borohydride, a fraction of nitro groups underwent reduction to amines, yielding AuNP with a mixed coordination layer consisting of TABs and TNBs (TAB-, TNB-AuNP) named AuZ. This mixed coverage was seen advantageous, in terms of ligand exchange with incoming thiols on the one hand, and colloidal stability on the other hand. Indeed, ligand exchange onto the AuNPs is rarely quantitative and preferentially occurs with the negatively charged TNBs, leaving zwitterionic TABs on the surface as putative protecting groups against strong associations to proteins [22].

In this study, we linked several commercial monoclonal antibodies (mAbs) to 1.4 nm AuZ gold nanoparticle to produce AuNP-mAb conjugates. First, we verified that these conjugates specifically bind to their intracellular targets using fixed and permeabilised cell lines in a classical gold immunolabelling procedure. We confirmed that shielding the

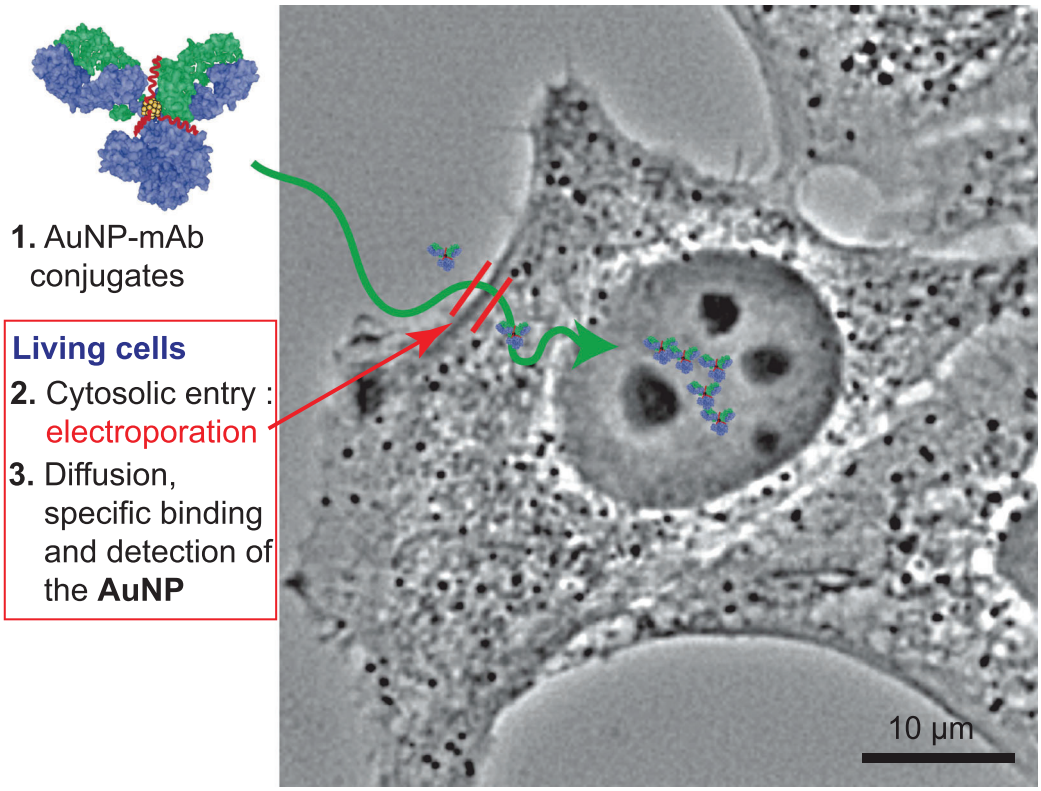


**Figure 1.** Illustration of gold immunolabelling in living cells. The strategy relies on the synthesis of specific AuNP-mAb conjugates and delivery procedure for the probes to diffuse, even into the cell nucleus, and bind to their specific targets.

gold surface of the AuNP-mAb conjugate with 2 kDa polyethyleneglycol drastically reduced unspecific adsorption of nanoparticles to extracellular constituents but also to intracellular ones [23,24]. The AuNP-mAb conjugates were then delivered inside living cells by electroporation [25,26] and the cells containing cytosolic AuNP-mAb conjugates were cultivated before monitoring the cell distribution of the probes (Figure 1). Our data demonstrate that the 1.4 nm AuNP-mAbs enter the cytoplasm where they circulate and associate to their targets. Accumulation of the probes in living cells was mAb-dependent. The accumulation patterns of the AuNP-mAb conjugates anti-GFP, anti-RPB1 (7G5, anti-RNA polymerase II) and anti-nucleoporins were analogous to the classical immunogold labelling ones indicating that the probes bind in cellulo to their targets without perturbing their function. Cytoplasmic-delivered anti-$\alpha$-tubulin and anti-$\beta$-tubulin conjugates in contrast promoted intracytoplasmic aggregates, indicating that real-time binding of these conjugates perturbs microtubule dynamics.

## 2. Results and discussion

### 2.1. *Synthesis of gold nanoparticle-antibody conjugates*

The 1.4 nm AuZ used in this study has been previously described and comprehensively characterised [20]. To conjugate the mouse monoclonal antibodies to AuZ, we took advantage of the disulfide bonds present in the hinge region. These disulfide bonds are easily reduced to sulfhydryl groups using Tris(2-carboxyethyl)phosphine (TCEP) [28], thus creating a conjugation site for the 150 kDa mAb onto TAB-, TNB-AuNP at about 7 nm of the recognised antigen paratope (Figure 2) [29]. The various reaction intermediates can be monitored using a non-reducing SDS-PAGE experiment as illustrated by the conjugation of AuZ to the 7G5 mAb (Figure 2B). The 7G5 mAb targets the 52 times-repeated YSPTSPS sequence at the C-terminal domain of the largest subunit (RPB1) of mammalian RNA polymerase II (Pol II). TCEP at a concentration of 1 mM fully cleaved the disulfide bond holding the heavy

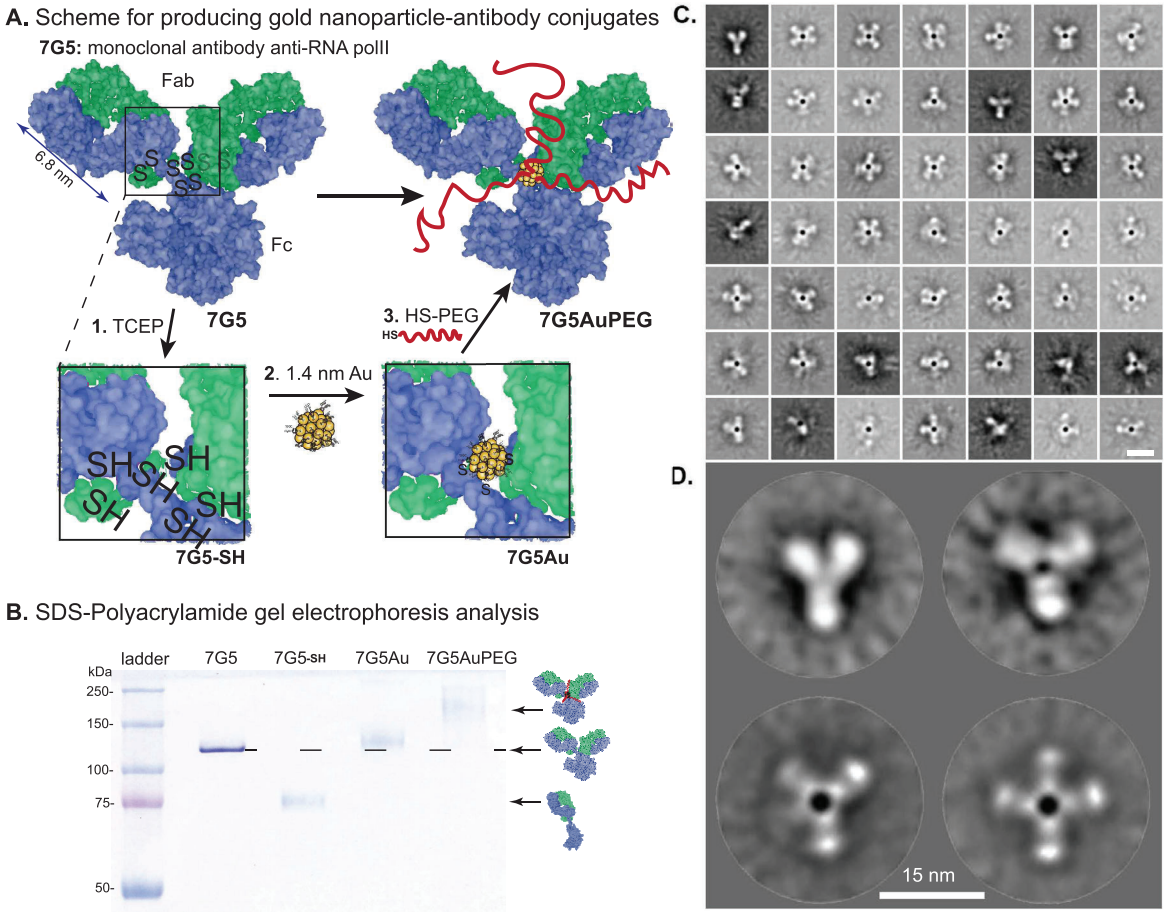


**Figure 2.** Synthesis and characterisation of the AuNP-antibody conjugate. (A) Disulfide bonds of the mouse monoclonal antibody targeting RPB1 of RNA polII (clone 7G5) are reduced at the hinge area with TCEP. The sulfhydryl groups at the hinge can then react with AuZ by thiolate exchange. After clearing the conjugate from excess AuZ, the remaining reacting thiolates on the AuNP surface are exchanged with thiolated 2 kDa polyethyleneglycol (PEG). (B) Non-reducing SDS-PAGE analysis of the reaction intermediates. Illustration of the antibody derived from protein data bank entry id 1IGY [27]. (C) Gallery of two-dimensional class averages from negatively stained 7G5AuPEG particles. (D) Representative class averages representing 2-D views of unlabelled (top) or gold-conjugated (bottom) IgG molecules. The bar represents 15 nm in C and D.

chains together as seen in the SDS-PAGE analysis (lane 7G5-SH). The mAb with an initial apparent molecular weight (MW) of 150 kDa was completely transformed into a 75 kDa protein corresponding to a single copy of the heavy and light chains. The reduced mAb was then reacted with a 1.5 molar excess of AuZ to yield a new component with an apparent MW slightly above 150 kDa (lane 7G5Au). Excess AuZ and the first released TNBs were removed by size exclusion chromatography. The purified 7G5Au was then reacted with an excess of thiolated 2 kDa polyethyleneglycol (PEG) to chemically neutralise the remaining reacting TNBs present on the gold particle surface [30] and to shield the gold surface from unspecific binding [8,23]. A material with a highly retarded electrophoretic mobility was observed (lane 7G5AuPEG), indicative of the shielding ability of PEG.

To assess the molecular organisation of the probe, the purified antibody-gold particle was visualised by transmission EM after negative staining with 2% uranyl acetate. Single particle analysis was performed to observe the position of the AuNP relative to the antibody, to determine the proportion

of Au-bound IgG molecules and to assess the integrity of the AuNP-bound antibody. The negatively stained protein moieties create a stain exclusion volume which diffuses less electrons than the surrounding medium. This property was used to select 80431 molecular images from 1125 micrographs that were aligned and clustered into 100 classes using Xmipp [31] (Figure 2C). After rejection of false positives, the remaining 36671 images were clustered into 100 classes. About 88% of the uranyl acetate-excluding materials were found associated with an electron-dense particle whose size is consistent with the input AuNP. The other images were found in classes representing characteristic views of non-conjugated IgG molecules such as 15 nm long, Y-shaped molecules (Figure 2D, top). The classes showing a dark electron-dense gold nanoparticle were heterogeneous and showed several extensions about 5 nm in size which could each correspond to Fab or Fc fragments. The 3-branched classes resemble the Y-shaped IgG molecule while the other classes are likely to represent two IgG molecules bound to the same AuNP particle with different rotational registers (Figure 2D, bottom). Strikingly, the electron-dense gold particle was always located at the centre of the multibranched structures, indicating that the AuNP associates with the hinge region of the IgG which exposes several thiolates following mild reduction step [32]. When the AuNP is bound to a single IgG molecule, the latter adopts a classical Y shape, suggesting that conjugation does not affect the molecular organisation of the antibody.

Binding of AuNP-mAb conjugates 7G5Au and 7G5AuPEG to RPB1 was first assayed using a classical immunocytochemistry procedure. HeLa cells cultivated on glass coverslips were fixed with 4% EM-grade paraformaldehyde for 20 min and their plasma membrane was permeabilised with 0.1% Triton X-100. The different 7G5 mAb conjugates were incubated with the permeabilised cells, excess probe was washed away and bound conjugates were detected with a secondary fluorescent goat anti-mouse antibody (Figure 3A). The 7G5 mAbs were found predominantly in the cell nucleus with reduced staining in the nucleolus, as expected for the nuclear RNA pol II enzyme. Enrichment of fluorescence was observed within foci in accordance with the hypothesis of transcription occurring mainly in factories or condensates containing several RNA pol II molecules [33]. A similar pattern was observed with the AuNP-mAb 7G5AuPEG component (Figure 3B). The intensity of the green fluorescence was nonetheless diminished as compared to the 7G5 mAbs signal. This feature might originate from the steric hindrance of PEGs [23] as well as from the fluorescence-quenching properties of AuNPs [34] leading to reduced association of the secondary Abs and dimming of the fluorescent signal, respectively. To map the distribution of gold nanoparticles, a similar immunolabelling experiment was performed using 7G5Au (Figure 3C) and 7G5AuPEG (Figure 3D), and a silver-enhancement procedure to reveal the AuNPs only (Supporting information, Figure S1 shows that the control HeLa cells remain unstained after incubation with the silver-enhancement solution). The 7G5Au probe showed a nuclear enrichment, but significant amounts of silver also stained the cytoplasm. Passivation of AuNPs with PEG 2 kDa diminished unspecific association to the cytoskeleton and provided a sharp nuclear gold immunolabelling in which dark spots are revealed. These dense spots might correspond to clustering of several RNA pol II molecules. The stealth property of PEGs surrounding AuZ was highly efficient since passivation of 7G5Au with the gold particle-stabilising CALNNG peptide [35] produced strong unspecific labelling of the cytoskeleton (Supporting information, Figure S2).

Commercial monoclonal antibodies (listed in Table 1) targeting RPB1 of RNA polII (7C2) [36], nucleoporins (Mab414), the trimethyl lysine 20 of histone H4 (6F8-D9), $\alpha$-tubulin (B-5-1-2), $\beta$-tubulin (TU27) and the green fluorescent protein (GFP)(2A3) were first checked for their immunofluorescence specificity (Supporting information, Figure S3). They were then conjugated to AuZ and passivised with PEG using the same protocol as for 7G5 (Supporting information, Figure S4). Gold immunolabelling experiments on adherent cell lines led to images with precise localisation of targets using bright-field microscopy. The anti-nucleoporins conjugated to pegylated AuNPs (MAb414AuPEG) labelled the Nuclear Pore Complexes embedded within the nuclear envelope (Figure 4A). The post-translational modification of histone H4 at lysine 20 was also detected in the nucleus (Figure 4B). Microtubules were also clearly revealed in the cytoplasm using the anti-$\alpha$-tubulin B-5-1-2AuPEG (Figure 4C) and the anti-$\beta$-tubulin TU27AuPEG (Figure 4D). The monoclonal anti-RPB1

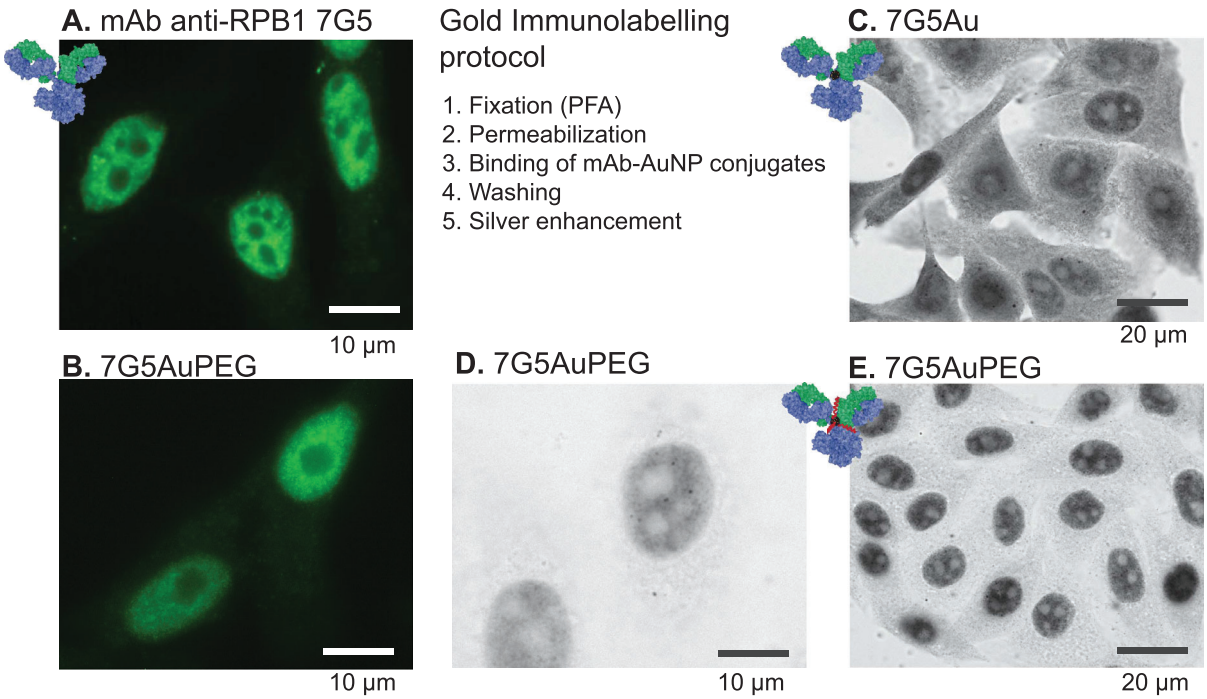


**Figure 3.** Immunofluorescence and gold immunolabelling analysis of the indicated monoclonal antibody anti-RPB1 (clone 7G5) derivatives on fixed and permeabilised HeLa cells. Images A and B: the mouse antibody was fluorescently detected with an AlexaFluo488-IgG anti-mouse conjugate. Images C, D and E: the gold particles were amplified with silver for detection by bright-field imaging. Conditions: fixation with 4% (v/v) PFA in 0.1 M phosphate buffer pH 7.6 for 20 min, permeabilisation with 0.1% (v/v) Triton X-100®, incubations with primary and secondary antibodies at 13 nM.

**Table 1.** List of antibodies used for conjugation

| Name | Target | Source |
|---|---|---|
| 7G5 | RPB1 of RNA polII $[TSPSYSP]_3$ at C ter | IGBMC |
| 7C2 | RPB1 of RNA polII $[YSPTSPS]_3$ at C ter | IGBMC |
| Mab414 | Nucleoporins (Nuclear pores) | Biolegend |
| 6F8-D9 | Histone H4 trimethyl Lysine20 (H4K20me3) | Biolegend |
| B-5-1-2 | $\alpha$-tubulin (C-t) | ThermoFisher |
| TU27 | $\beta$-tubulin (C-t) | Biolegend |
| 2A3 | Green fluorescent protein (GFP) | IGBMC |

7C2AuPEG was not as effective as 7G5AuPEG in terms of labelling sharpness (Figure 5A). Finally, the anti-GFP 2A3AuPEG [12,37] probe labelled extremely well the GFP-labelled histone H2B within the nucleus of stably transformed HeLa cells that express the GFP-H2B fusion (Figure 5C) but did not bind to wild-type HeLa devoid of GFP (Figure 5D). The importance of passivation by grafting PEG onto the gold surface to limit unspecific binding to cytoplasmic components was also confirmed for that antibody (Supporting information Figure S5).

Altogether, those first experiments demonstrated that 1.4 nm AuZ can be conjugated to several mAbs at the hinge region to produce effective gold labelling probes for classical immunocytochemistry procedures. Shielding the 1.4 nm gold nanoparticle with 2 kDa PEG was beneficial and considerably limited unspecific binding to cell components.

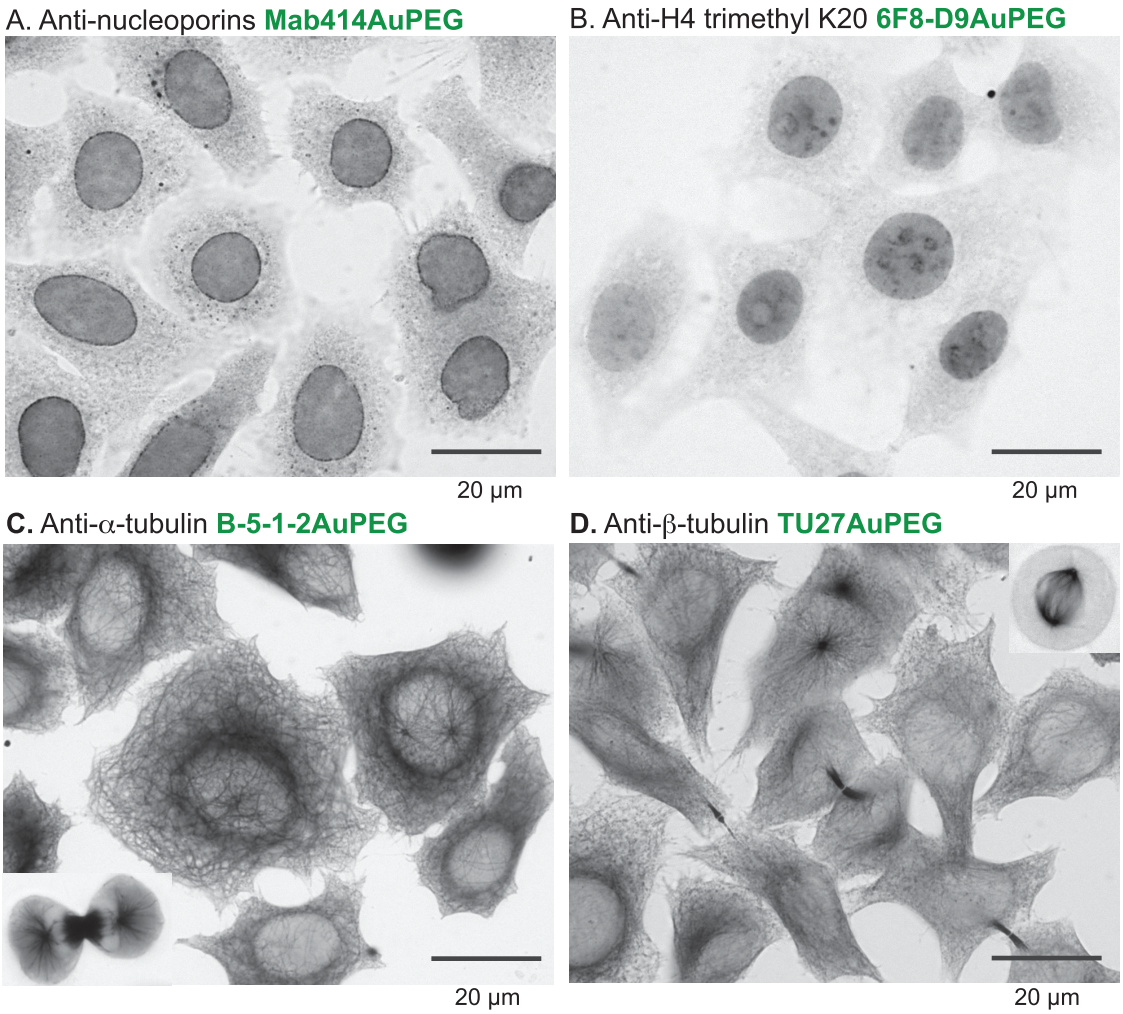


**Figure 4.** Gold immunolabelling analysis of the indicated monoclonal antibodies (mAbs) conjugated to 1.4 nm AuNP passivised with 2 kDa PEG. H2B-GFP HeLa cell line stably expresses the histone H2B fused to GFP. The gold particles were enhanced by silver for bright-field imaging.

### 2.2. *Fate of AuNP-mAb conjugates following cytosolic delivery into living HeLa cells*

The ability of the AuNP-mAb conjugates to diffuse inside living cells, bind to their targets and label them was assayed (Figure 6). To introduce the probes into the cytoplasm of living cells, transient holes in the plasma membrane of freshly trypsinised cells were created using an electroporation device and optimised pulses [26,38]. After the electric pulses and re-closure of the plasma membrane, HeLa cells containing cytoplasmic mAbs and AuNP-mAb conjugates were generally cultivated for 20 h to let them adhere onto glass coverslips. Cells were then processed for detection of antibodies and of AuNPs (Figure 6A). After delivery into the cytoplasm of HeLa cells expressing H2B-GFP, the unconjugated anti-GFP 2A3 accumulated into the cell nuclei and distributed similarly to the GFP, suggesting an effective binding of the antibody to its target (Figure 6B). Entry of 150 kDa Abs into the cell nucleus was unexpected since nuclear pore complexes usually prevent nuclear entry of proteins with a molecular weight above 60 kDa unless they are equipped with Nuclear Localisation Signals (NLS). The anti-GFP antibody is likely transported into the nucleus after binding to the NLS-containing GFP-H2B protein when it is synthetised in the cytoplasm by a piggyback mechanism [39]. When delivered into the cytoplasm of wild-type HeLa cells devoid of GFP-H2B, the

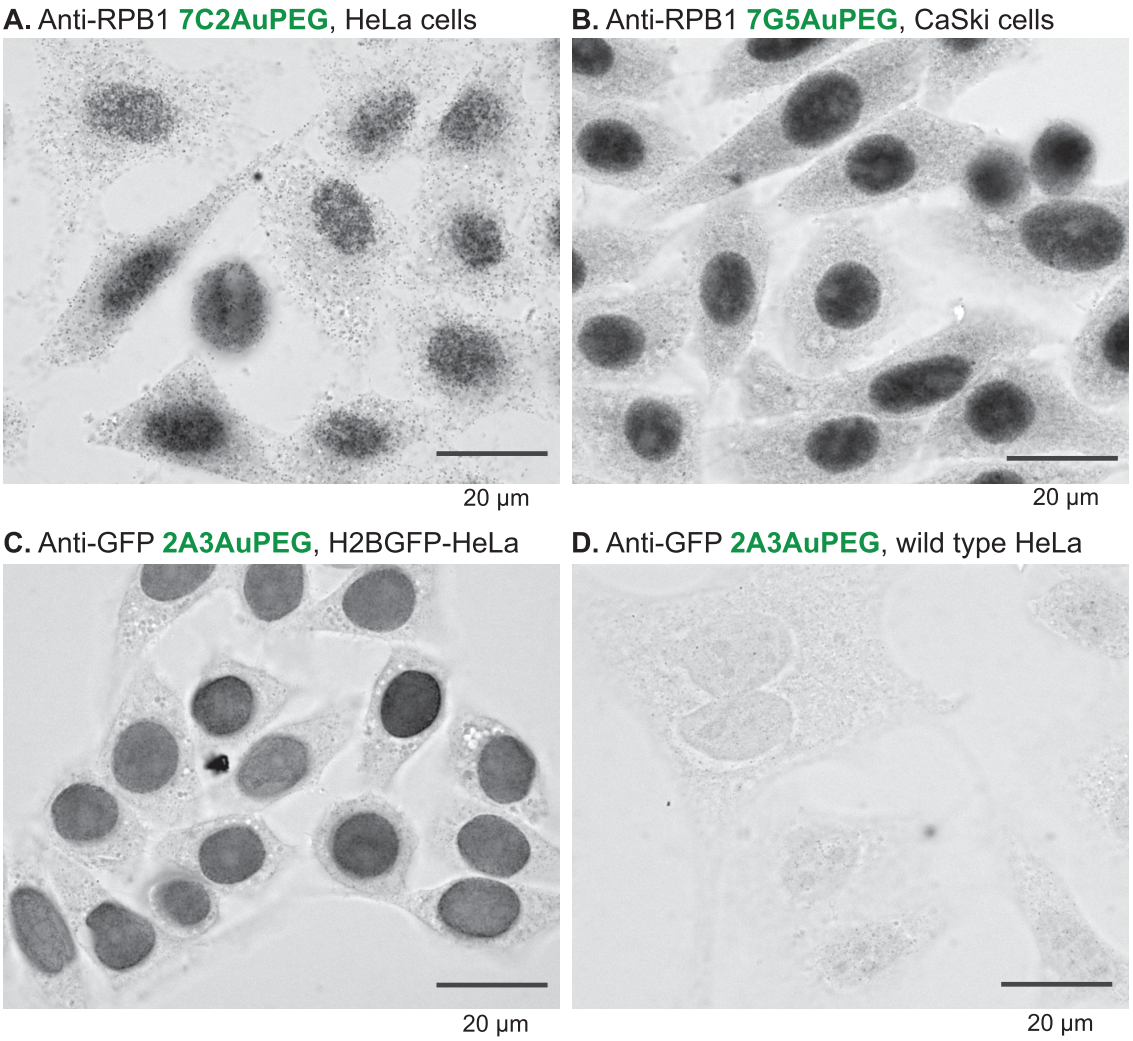


**Figure 5.** Gold immunolabelling analysis of the indicated monoclonal antibodies (mAbs) conjugated to 1.4 nm AuNP passivised with 2 kDa PEG. H2B-GFP HeLa cell line stably expresses the histone H2B fused to GFP. The gold particles were enhanced by silver for bright-field imaging.

anti-GFP 2A3AuPEG probe diffused in the cytoplasm but was excluded from the nucleus (Figure 6C). In contrast, the anti-GFP 2A3AuPEG delivered into the cytoplasm of HeLa cells expressing H2B-GFP accumulated in the nuclei in a fashion resembling 2A3 (Figure 6D), indicating that AuNP conjugation does not impair nuclear import of this specific mAb anti-GFP. The observed nuclear accumulation patterns relied on the presence of conjugates in the cytoplasm of living cells since electric pulses for electroporation were required (left-hand panels in Figure 6C and D). In cellulo labelling with anti-nucleoporins Mab414 and Mab414AuPEG yielded images (Figure 6E) which were highly reminiscent of the classical immunocytochemistry images (Figure 4A). Cytoplasmic-delivered anti-α-tubulin TU27AuPEG and anti-β-tubulin B-5-1-2AuPEG did not reveal an extensive microtubule network but rather accumulated as aggregates. This type of labelling and accumulation might be related to the dynamic nature of the microtubule network and to the electroporation procedure that involves a transient suspension of the cells using a trypsin treatment. Reshuffling of the microtubule network might take place during re-adhesion of the cells and after the electric pulses which are also known disruptors of microtubules [40,41]. The cytoplasm-delivered 7G5AuPEG and 7C2AuPEG also accumulated in the nucleus (Figure 6H) similarly to

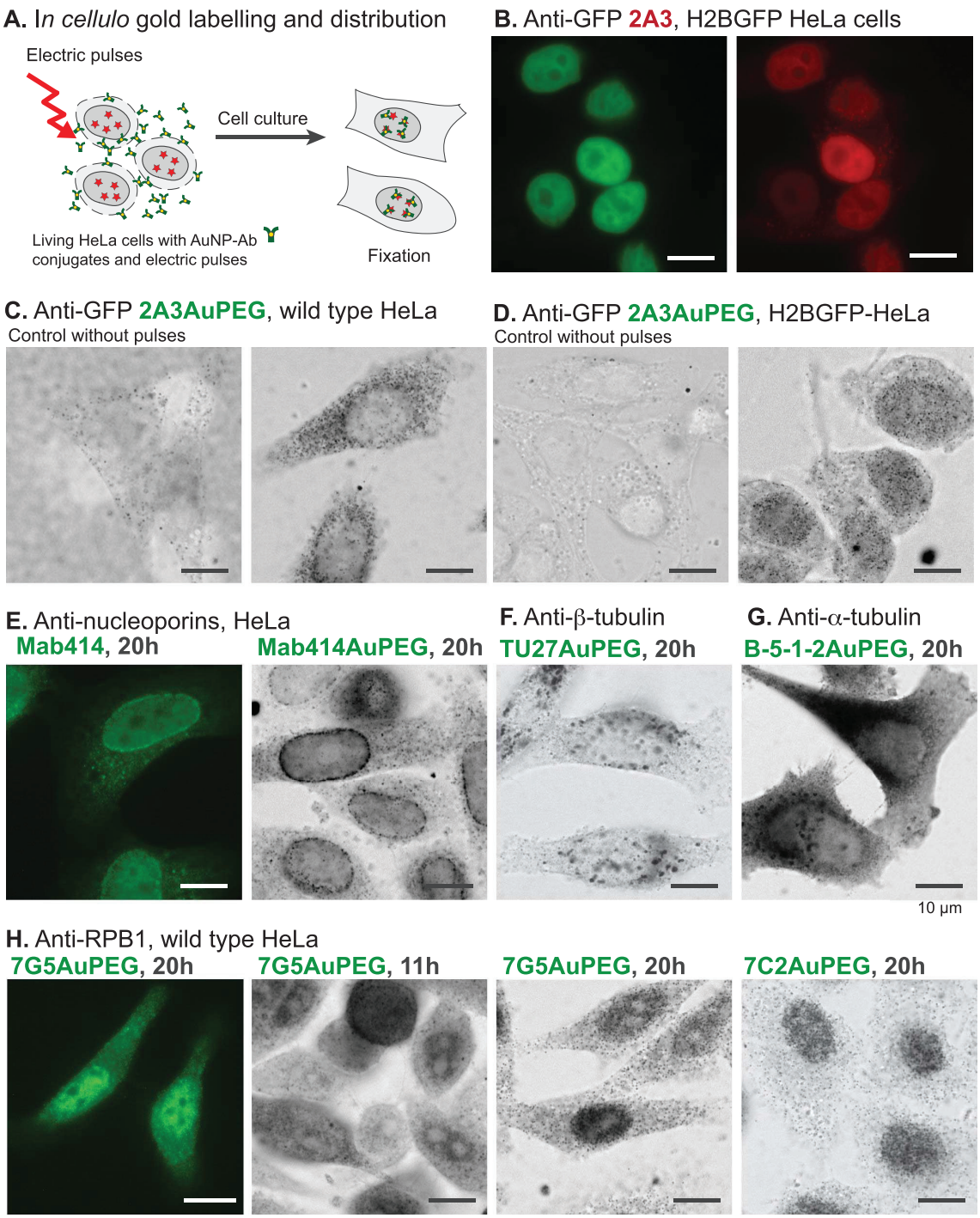


**Figure 6.** The AuNP-mAb conjugates (0.2 $\mu g \cdot \mu L^{-1}$) were delivered in HeLa cells by transient permeabilisation of the cell membrane using 3 electric pulses at 517 $V \cdot cm^{-1}$. Distribution of the mAbs and conjugates inside living cells was evaluated after culture during 20 h unless stated. Fixation: 4% PFA, 20 min. Permeabilisation: 0.1% Triton X-100. AuNPs were silver-enhanced. (A) Scheme of the procedure. (B) Images of the targeted H2B-GFP in HeLa cells (left) and of the delivered anti-GFP 2A3 (right). The mAb was detected using AlexaFluor568 goat anti-mouse (in red). (C, D) Detection of AuNPs by silver enhancement in cells incubated with 2A3AuPEG without application of electric pulses (left images) and with application of electric pulses. (E–H) Delivered mAbs were detected in cells using the antibody or the gold domain.

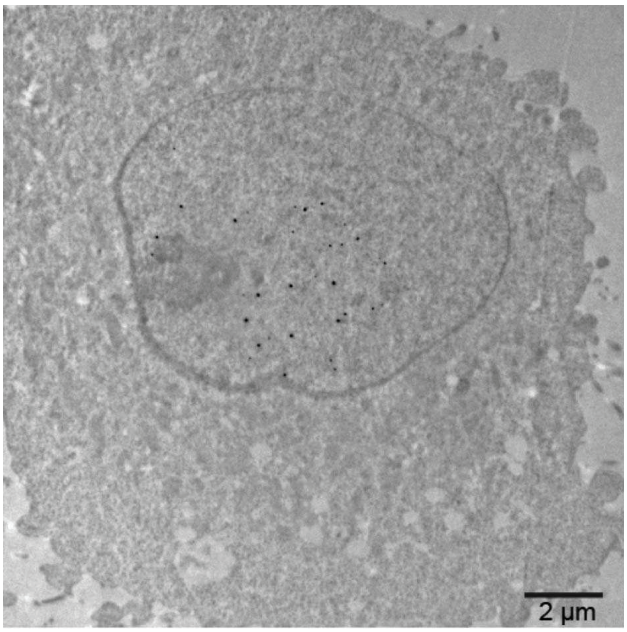


**Figure 7.** Electron micrograph of a HeLa cell section containing 7G5AuPEGs in the nucleus. Cells were incubated with 7G5AuPEG (0.2 $\mu g \cdot \mu L^{-1}$) and the plasma membrane was transiently permeabilised with 3 electric pulses at 517 $V \cdot cm^{-1}$. Cells were cultivated for 20 h, fixed with 2% glutaraldehyde and processed for classical TEM observation. Gold particles were enhanced with silver.

the unconjugated mAbs [38]. Similarly to the classical gold immunolabelling protocol, passivation of the AuNPs with PEG was also extremely useful for nuclear accumulation. Indeed, capping the AuNP of 7G5Au with CALNNG peptide did not lead to nuclear accumulation of 7G5AuC 24 h following electroporation (Figure S6). Finally, the nuclear accumulation appears not as with the anti-GFP conjugates. This property is likely related to the production of RNA pol II in the cytoplasm which is lower than that of H2B-GFP, limiting *de facto* the entry of Ab-bound RNA pol II [37,38]. The 7G5AuPEG labelling was further investigated by transmission electron microscopy (TEM) (Figure 7). Twenty hours after electroporation, cells were fixed, the gold signal was amplified by silver enhancement for better visualisation and thin sections of resin-embedded cells were observed by TEM. An image of a cell section displaying the nucleus and cytoplasm was recorded. The enhanced AuNPs were almost exclusively found in the cell nucleus, confirming that the RNA polII-driven accumulation of the corresponding AuNP-mAb occurred in this cell.

## 3. Conclusion

We hereby provide a synthesis protocol for preparing mAbs conjugated to 1.4 nm AuZ gold nanoparticles by taking advantage of the disulfide bonds which connect the hinge region of the antibody heavy chains. The reaction process can be easily monitored by non-reducing SDS-PAGE analysis which reveals the key reaction intermediates. Passivation of the gold surface with 2 kDa polyethyleneglycol provided probes with excellent gold immunolabelling properties such as solubility, absence of in vivo aggregation, good diffusion properties, and dramatically diminished the unspecific binding to cellular components. Moreover, these conjugates can be delivered into the cytoplasm of living cells by electroporation, where they diffuse and bind to their targets. The piggyback mechanism allowing nuclear entry of AuNP-mAb only upon binding to NLS-containing targets can be extremely useful as filter since unbound AuNP-mAbs remain in the cytoplasm. Our first proof of concept data demonstrated that AuNP-mAbs can be delivered into living cells, bind to their specific targets and accumulate at locations where their targets go. In principle, the anti-GFP antibody has the potential to become a rather generic gold immunolabelling probe. Standard immunolabelling procedure and silver enhancement will enable to monitor the labelling dynamic and efficiency, to adjust the amounts of the electroporated probes and the incubation time (and maybe other parameters) to ensure that the most specific labelling is observed later in cryo-EM. Specific monoclonal antibodies bind to a specific protein domain and then interfere with the functioning of their targets. After labelling with AuNPs and delivery inside living cells, these interfering probes might help decipher the function of protein/protein interactions and dynamics of exposure to Ab binding. Although the electroporation procedure is convenient and has demonstrated efficiency, the electric pulses are not neutral to cell physiology. Cells mostly recover but the cell cytoskeleton is perturbed. Alternatively, differentially disruptive liposomal formulations have been used as delivery solutions and can be employed as well.

## 4. Experimental section

### 4.1. *Materials*

The 2 kDa alpha-methoxy-omega-mercapto poly (ethylene glycol) (PEG-SH) was ordered from Iris Biotech. EM-grade paraformaldehyde (20% w/v solution) and glutaraldehyde (25% w/v solution) were purchased from Electron Microscopy Sciences. Other reagents were obtained from Sigma Aldrich, Carl Roth, VWR Chemicals, Euromedex or Honeywell. They were used without further purification unless stated otherwise. All solutions and buffers were made with water purified with a Millipore Q-POD apparatus. Precision Plus Protein Standard Dual Xtra (BioRad) was used as protein ladder for SDS-PAGE analysis. Monoclonal antibodies were purchased from commercial sources and were devoid of bovine serum albumin or gelatine. They were cleared from sodium azide or any other preservatives by size exclusion chromatography (Sephadex G-25) and eventually reconcentrated by ultracentrifugation.

### 4.2. *Gold nanoparticle synthesis*

The 1.4 nm AuZ was synthesised and characterised in a previous publication [18–20]. The concentration of gold nanoparticles was determined by UV–vis spectrophotometry using the absorbance at 520 nm and an extinction coefficient $\varepsilon_{520}$ of $2.7 \times 10^5$ $mol^{-1} \cdot L \cdot cm^{-1}$.

### 4.3. *Reduction of monoclonal antibody*

Before performing any conjugation, reduction of the monoclonal antibody at the hinge area was monitored by SDS-PAGE using a non-reducing loading buffer. The antibody (2 $\mu g \cdot \mu L^{-1}$ or 13.34 μM, 2 μL) was titrated with TCEP (final concentrations: 0.1, 0.25, 0.5, 1, and 2 mM). After 16 h incubation at 20 °C, the reaction mixtures were mixed with 30% (w/v) glycerol containing 0.1% (w/v) SDS and 0.05% (w/v) bromophenol blue (0.4 μL) and analysed by SDS-PAGE. The minimal TCEP concentration producing full disappearance of the band at about 150 kDa was selected for medium-scale synthesis.

### 4.4. *Synthesis of 7G5AuPEG*

The monoclonal antibody in PBS containing 1 mM EDTA (2 $\mu g \cdot \mu L^{-1}$ or 13.34 μM, 100 μL) was reduced by addition of 0.1 M TCEP, pH 7.0 (1 μL) to a final concentration of 1 μM. After a 12 h incubation at 20 °C, an aliquot was withdrawn for analysis and the mixture was then quickly added and mixed with Auz (25 μL of 80 μM solution). After overnight incubation at 20 °C, the crude mixture was purified by size exclusion chromatography (Biorad P100, 2 mL of resin, elution with PBS). Thiolated polyethyleneglycol 2000 (2.7 μL of a 20 mM aqueous concentration) was then added. The mixture was incubated at room temperature for 16 h and the crude mixture was purified by ultracentrifugation (7 cycles of 0.5 mL sterile PBS) using a 0.5 mL Microcon® centrifugal filter device with a 100 kDa cutoff (Merck, Molsheim). At the end of the process, the gold nanoparticle-antibody conjugate was recovered in 60 μL PBS and analysed by SDS-PAGE to estimate the concentration and conjugation efficiency. The other gold nanoparticles-antibody conjugates were similarly prepared.

### 4.5. *Electroporation protocol*

Transient permeabilisation of the plasma membrane of cells was conducted as previously described using the Neon® transfection system and three 10 ms pulses at 1550 V [20,26]. Typically, HeLa cells ($2 \times 10^5$ cells in 10 μL of the Neon Buffer R) were mixed with each antibody (2.5 μL of 2 $\mu g \cdot \mu L^{-1}$ solution in PBS). After the electric pulses, cells were diluted in prewarmed antibiotic-free cell culture medium (1 mL). The cells were recovered by gentle centrifugation, suspended into the warmed antibiotic-free complete cell culture medium and plated in 24-wells plates for cell adherence and growth onto glass coverslips and left in a cell culture incubator, usually for 18 h.

### 4.6. *Cell culture*

Cells were cultured in a 37 °C humidified incubator supplied with 5% $CO_2$. HeLa, CaSki, and stably transformed H2B-GFP HeLa cells were maintained in Dulbecco's modified Eagle medium containing 2 mM L-glutamine, 10 mM HEPES buffer, pH 7.0, 10% heat-inactivated foetal bovine serum (FBS) and 50 μg/mL gentamycin. For immunocytochemistry, immunofluorescence and pre-embedding immuno-EM experiments, cells (25,000 cells/well) were seeded into 24-well plates in 0.5 mL cell culture medium in which

13 mm diameter glass coverslips were deposited. The cells were left to adhere overnight by culture in a 37 °C humidified incubator supplied with 5% $CO_2$.

### 4.7. *Immunocytochemistry for bright-field and fluorescence imaging*

Coverslip-adhered cells were fixed with 4% PFA in 100 mM Sorenson's buffer, pH 7.6 for 20 min at 20 °C. The coverslips were then washed with PBS (3 × 0.5 mL, 5 min) containing 50 mM glycine (0.5 mL, 20 min) and cell plasma membranes were permeabilised with 0.1% Triton X-100 in PBS (0.5 mL, 5 min). Coverslips were soaked in PBS containing 10% (w/v) BSA for 1 h, washed with 0.2% acetylated BSA (BSA-c) in PBS (2 × 0.5 mL, 5 min) and then incubated with 6 to 10 nM of the conjugates in 0.2% BSA-c containing 10% FCS, 0.5 mL for 1 h. Next, cells were washed with 0.2% BSA-c (2 × 0.5 mL, 5 min) and with 80 mM citrate buffer pH 6.7 containing 2% sucrose (3 × 0.5 mL, 5 min). Gold was revealed by silver enhancement according to a modified Danscher protocol [42] using silver acetate and propyl gallate [43]. For fluorescence imaging, the primary antibodies were labelled using secondary fluorescent anti-mouse conjugates (AlexaFluor568 goat anti-mouse, Invitrogen A11031 and AlexaFluor488 goat anti-mouse, Invitrogen A11029). Fluorescence observations were carried out using a Leica DM5500B microscope equipped with an HCX PL Apo 63 × 1.40 oil PH3CS objective and a Leica DFC350FX camera.

### 4.8. *Preparation of cells containing gold nanoparticle-antibody conjugates for bright-field microscopy imaging*

After the indicated time periods following application of the electric pulses, the adherent cells cultivated on glass coverslips were washed with PBS (2 × 1 mL). The cells were fixed with 4.0% paraformaldehyde (PFA) (1 mL) for 20 min or 2% glutaraldehyde in 100 mM Sorenson's buffer, pH 7.6 for 1 h. After removal of the fixative solution and 3 PBS washes (1 mL), the plasma membrane was permeabilised using 0.1% (w/v) saponin or Triton X-100 (1 mL, 15 min) in 0.1 M Sorenson's buffer pH 7.6. The phosphate-buffered solution was replaced by a 0.1 M citrate solution, pH 6.7 containing 2% sucrose (5 washes, 1 mL). Development of AuNPs [42] was then done in a dark room for 30 min using freshly prepared 6 mM silver acetate solution in 0.16 M sodium citrate, pH 6.7 containing 20% gum arabic and 2 mM propyl gallate [43]. The silver-promoted enhancement of AuNPs was stopped with 0.16 M sodium citrate solution, pH 6.7 (1 mL, several washes). The glass coverslips were finally mounted onto 3 × 1 inch microscope slides (knittelglass.com) using Fluoromount-G (Southern Biotech, Ref. 0100-01, batch I2819-WC79B). Observations were carried out using a Leica DM5500B microscope equipped with an HCX PL Apo 63 × 1.40 oil PH3CS objective and a Leica DFC350FX camera.

### 4.9. *Cellular specimen preparation for EM*

20 h after the electroporation treatment, the adherent cells were washed with warmed (37 °C) Sorenson's buffer (3 × 2 mL). The cells were then fixed with 2.0% glutaraldehyde (1 mL) for 24 h. They were then washed with TEM storage solution (5×, 1 mL). Enhancement of the gold particles with silver was performed using the SE-EM kit (Aurion, the Netherlands) according to the manufacturer's protocol. The cells were then contrasted with 0.5% osmium for 20 min followed by 2% uranyl acetate both diluted in water. The specimens were dehydrated in a solution containing increasing concentrations of ethanol and flat-embedded in Epon (Ladd Research Industries, Williston, Vermont, USA). The resin-embedded specimens were sectioned into 100 nm thick slices which were deposited on an electron microscope grid.

### 4.10. *TEM and image analysis*

Cellular specimens were imaged on a Hitachi H7500 transmission electron microscope (Hitachi High Technologies Corporation) equipped with an AMT Hamatsu digital camera (Hamatsu Photonics). For EM imaging of 7G5AuPEG we used nickel EM grids covered with a thick holey carbon film (Quantifoil R2/2). The grids were topped with a thin continuous carbon layer and rendered hydrophilic by a 90s treatment in a Fischione 1070 plasma cleaner operating at 30% power with a gas mixture of 80% argon:20% oxygen. The 7G5AuPEG solution was diluted to a final concentration of 50 μg/mL in Buffer A (Tris 10 mM, pH 7.4, NaCl 50mM) and crosslinked for 30 s at a final glutaraldehyde concentration of 0.3%. Three μL of

this solution were deposited on the glow-discharged EM grid and the particles were allowed to adsorb for 1 min. The grid was washed once on a drop of buffer A and negatively stained with a 2% uranyl acetate solution. The sample was then imaged in a Tecnai F20 (FEI) operating at 200 kV and equipped with a 2K CCD camera (Gatan). Micrograph montages were recorded at an image magnification of 50 kX with a 2.01 Å pixel size at −2 µm defocus using the SerialEM software [44]. For single particle analysis, micrographs were imported within the Scipion framework for image processing software [45] and Fourier band-passed filtered using the xmipp3 protocol [31]. Reference-free picking was performed using the eman2 protocol to generate a dataset of 80431 particles [46]. The particle set was aligned, masked, 2-D classified, cleaned to obtain a total of 36671 molecular images and classified again into 100 classes using xmipp3 protocols.

## Declaration of interests

The authors do not work for, advise, own shares in, or receive funds from any organization that could benefit from this article, and have declared no affiliations other than their research organizations.

## Supplementary data

Supporting information for this article is available on the journal's website under https://doi.org/10.5802/crchim.251 or from the author.

## References


[1] The ENCODE Project Consortium, *Nature*, 2012, **488**, 57-74.

[2] M. Uhlen, L. Fagerberg, B. M. Hallstrom, C. Lindskog, P. Oksvold, A. Mardinoglu, A. Sivertsson, C. Kampf, E. Sjostedt, A. Asplund *et al.*, *Science*, 2015, **347**, article no. 1260419.

[3] B. Schwanhäusser, D. Busse, N. Li, G. Dittmar, J. Schuchhardt, J. Wolf, W. Chen, M. Selbach, *Nature*, 2011, **473**, 337-342.

[4] J. Mahamid, S. Pfeffer, M. Schaffer, E. Villa, R. Danev, L. K. Cuellar, F. Förster, A. A. Hyman, J. M. Plitzko, W. Baumeister, *Science*, 2016, **351**, 969-972.

[5] A. Al-Amoudi, J.-J. Chang, A. Leforestier, A. McDowall, L. M. Salamin, L. P. O. Norlén, K. Richter, N. S. Blanc, D. Studer, J. Dubochet, *EMBO J.*, 2004, **23**, 3583-3588.

[6] A. P. Schuller, M. Wojtynek, D. Mankus, M. Tatli, R. Kronenberg-Tenga, S. G. Regmi, P. V. Dip, A. K. R. Lytton-Jean, E. J. Brignole, M. Dasso *et al.*, *Nature*, 2021, **598**, 667-671.

[7] W. P. Faulk, G. M. Taylor, *Immunochemistry*, 1971, **8**, 1081-1083.

[8] M. P. Monopoli, C. Aberg, A. Salvati, K. A. Dawson, *Nat. Nanotechnol.*, 2012, **7**, 779-786.

[9] G. Mayer, M. Bendayan, *Progr. Histochem. Cytochem.*, 2001, **36**, 3-84.

[10] L. Boselli, E. Polo, V. Castagnola, K. A. Dawson, *Angew. Chem.*, 2017, **129**, 4279-4282.

[11] J. F. Hainfeld, *Science*, 1987, **236**, 450-453.

[12] J. M. Robinson, T. Takizawa, D. D. Vandre, *J. Histochem. Cytochem.*, 2000, **48**, 487-492.

[13] R. C. N. Melo, E. Morgan, R. Monahan-Earley, A. M. Dvorak, P. F. Weller, *Nat. Protoc.*, 2014, **9**, 2382-2394.

[14] M. Chiper, K. Niederreither, G. Zuber, *Adv. Healthc. Mater.*, 2018, **7**, article no. e1701040.

[15] I. Orlov, A. Schertel, G. Zuber, B. Klaholz, R. Drillien, E. Weiss, P. Schultz, D. Spehner, *Sci. Rep.*, 2015, **5**, article no. 8324.

[16] Y. Levi-Kalisman, P. D. Jadzinsky, N. Kalisman, H. Tsunoyama, T. Tsukuda, D. A. Bushnell, R. D. Kornberg, *J. Am. Chem. Soc.*, 2011, **133**, 2976-2982.

[17] M. Azubel, J. Koivisto, S. Malola, D. Bushnell, G. L. Hura, A. L. Koh, H. Tsunoyama, T. Tsukuda, M. Pettersson, H. Häkkinen *et al.*, *Science*, 2014, **345**, 909-912.

[18] M. Azubel, S. D. Carter, J. Weiszmann, J. Zhang, G. J. Jensen, Y. Li, R. D. Kornberg, *Elife*, 2019, **8**, article no. e43146.

[19] V. Postupalenko, D. Desplancq, I. Orlov, Y. Arntz, D. Spehner, Y. Mely, B. P. Klaholz, P. Schultz, E. Weiss, G. Zuber, *Angew. Chem. Int. Ed. Engl.*, 2015, **54**, 10583-10586.

[20] D. Desplancq, N. Groysbeck, M. Chiper, E. Weiss, B. Frisch, J.-M. Strub, S. Cianferani, S. Zafeiratos, E. Moeglin, X. Holy *et al.*, *ACS Appl. Nano Mater.*, 2018, **1**, 4236-4246.

[21] R. L. Donkers, Y. Song, R. W. Murray, *Langmuir*, 2004, **20**, 4703-4707.

[22] N. Zhan, G. Palui, M. Safi, X. Ji, H. Mattoussi, *J. Am. Chem. Soc.*, 2013, **135**, 13786-13795.

[23] J. Y. Wong, T. L. Kuhl, J. N. Israelachvili, N. Mullah, S. Zalipsky, *Science*, 1997, **275**, 820-822.

[24] N. Groysbeck, V. Hanss, M. Donzeau, J.-M. Strub, S. Cianferani, D. Spehner, M. Bahri, O. Ersen, M. Eltsov, P. Schultz *et al.*, *Small Methods*, 2023, **7**, article no. e2300098.

[25] H.-Y. Wang, C. Lu, *Biotechnol. Bioeng.*, 2008, **100**, 579-586.

[26] G. Freund, A.-P. Sibler, D. Desplancq, M. Oulad-Abdelghani, M. Vigneron, J. Gannon, M. H. Van Regenmortel, E. Weiss, *mAbs*, 2014, **5**, 518-522.

[27] L. J. Harris, E. Skaletsky, A. McPherson, *J. Mol. Biol.*, 1998, **275**, 861-872.

[28] A. Makaraviciute, C. D. Jackson, P. A. Millner, *J. Immunol. Methods*, 2016, **429**, 50-56.

[29] N. Groysbeck, A. Stoessel, M. Donzeau, E. C. da Silva, M. Lehmann, J.-M. Strub, S. Cianferani, K. Dembélé, G. Zuber, *Nanotechnology*, 2019, **30**, article no. 184005.

[30] R. Guo, Y. Song, G. Wang, R. W. Murray, *J. Am. Chem. Soc.*, 2005, **127**, 2752-2757.

[31] J. M. de la Rosa-Trevín, J. Otón, R. Marabini, A. Zaldívar, J. Vargas, J. M. Carazo, C. O. S. Sorzano, *J. Struct. Biol.*, 2013, **184**, 321-328.

[32] M. M. C. Sun, K. S. Beam, C. G. Cerveny, K. J. Hamblett, R. S. Blackmore, M. Y. Torgov, F. G. M. Handley, N. C. Ihle, P. D. Senter, S. C. Alley, *Bioconjug. Chem.*, 2005, **16**, 1282-1290.

[33] W.-K. Cho, N. Jayanth, B. P. English, T. Inoue, J. O. Andrews, W. Conway, J. B. Grimm, J.-H. Spille, L. D. Lavis, T. Lionnet *et al.*, *Elife*, 2016, **5**, article no. e13617.
[34] C. Xue, Y. Xue, L. Dai, A. Urbas, Q. Li, *Adv. Opt. Mater.*, 2013, **1**, 581-587.
[35] R. Lévy, N. T. K. Thanh, R. C. Doty, I. Hussain, R. J. Nichols, D. J. Schiffrin, M. Brust, D. G. Fernig, *J. Am. Chem. Soc.*, 2004, **126**, 10076-10084.
[36] S. Besse, M. Vigneron, E. Pichard, F. Puvion-Dutilleul, *Gene Expr.*, 1995, **4**, 143-161.
[37] N. Groysbeck, M. Donzeau, A. Stoessel, A.-M. Haeberle, S. Ory, D. Spehner, P. Schultz, O. Ersen, M. Bahri, D. Ihiawakrim *et al.*, *Nanoscale Adv.*, 2021, **3**, 6940-6948.
[38] S. Conic, D. Desplancq, A. Ferrand, V. Fischer, V. Heyer, B. Reina San Martin, J. Pontabry, M. Oulad-Abdelghani, N. K. Babu, G. D. Wright *et al.*, *J. Cell Biol.*, 2018, **217**, 1537-1552.
[39] N. Mosammaparast, K. R. Jackson, Y. Guo, C. J. Brame, J. Shabanowitz, D. F. Hunt, L. F. Pemberton, *J. Cell Biol.*, 2001, **153**, 251-262.
[40] J. Teissié, M. P. Rols, *Ann. N. Y. Acad. Sci.*, 1994, **720**, 98-110.
[41] C. Kanthou, S. Kranjc, G. Sersa, G. Tozer, A. Zupanic, M. Cemazar, *Mol. Cancer Ther.*, 2006, **5**, 3145-3152.
[42] G. Danscher, J. O. Nörgaard, *J. Histochem. Cytochem.*, 1983, **31**, 1394-1398.
[43] R. W. Burry, D. D. Vandre, D. M. Hayes, *J. Histochem. Cytochem.*, 1992, **40**, 1849-1856.
[44] D. N. Mastronarde, *J. Struct. Biol.*, 2005, **152**, 36-51.
[45] J. M. de la Rosa-Trevín, A. Quintana, L. del Cano, A. Zaldívar, I. Foche, J. Gutiérrez, J. Gómez-Blanco, J. Burguet-Castell, J. Cuenca-Alba, V. Abrishami *et al.*, *J. Struct. Biol.*, 2016, **195**, 93-99.
[46] G. Tang, L. Peng, P. R. Baldwin, D. S. Mann, W. Jiang, I. Rees, S. J. Ludtke, *J. Struct. Biol.*, 2007, **157**, 38-46.

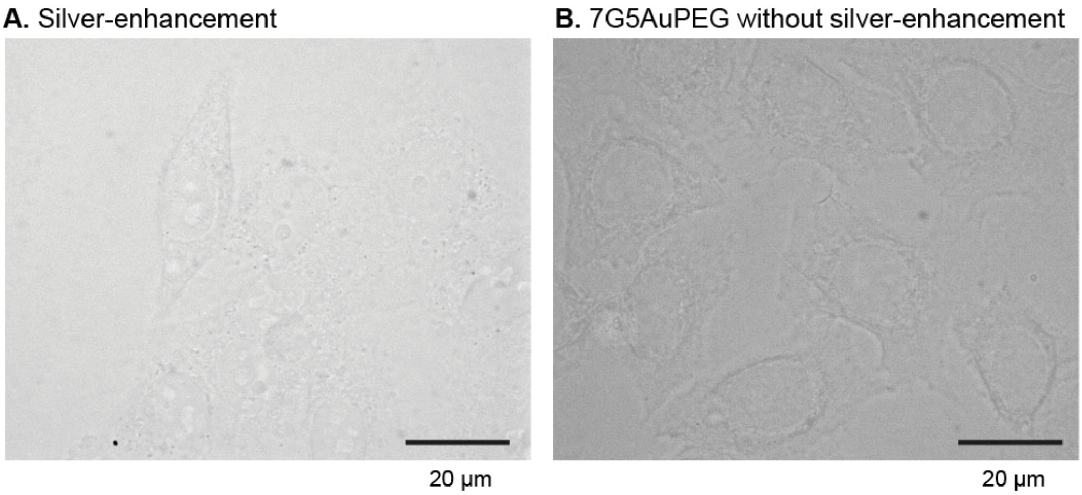


**Supplementary Figure S1.** Controls experiments. Image of 4% PFA-fixed and 0.1% Triton X-100 permeabilized HeLa cells. (A) After permeabilization, the cells were treated with silver-enhancement solution. (B) Gold immunolabelling of HeLa with the 7G5AuPEG anti-RPB1 without silver-enhancement solution.

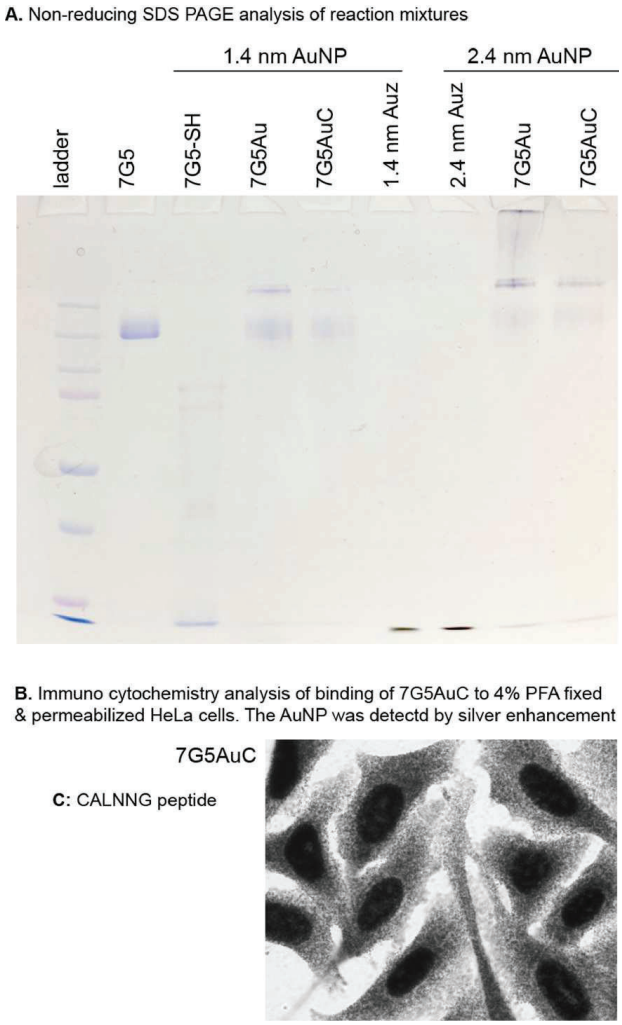


**Supplementary Figure S2.** Analysis of the production of 7G5AuC and binding specificity using fixed HeLa cells. (A) The 7G5 was firstly reduced with TCEP, reacted with Auz and purified by size-exclusion chromatography. The purified conjugate was then reacted for passivation with the peptide CALNNG (C). (B) The CALNNG appeared to promote unspecific binding of the probe the fixed cell ultrastructure.

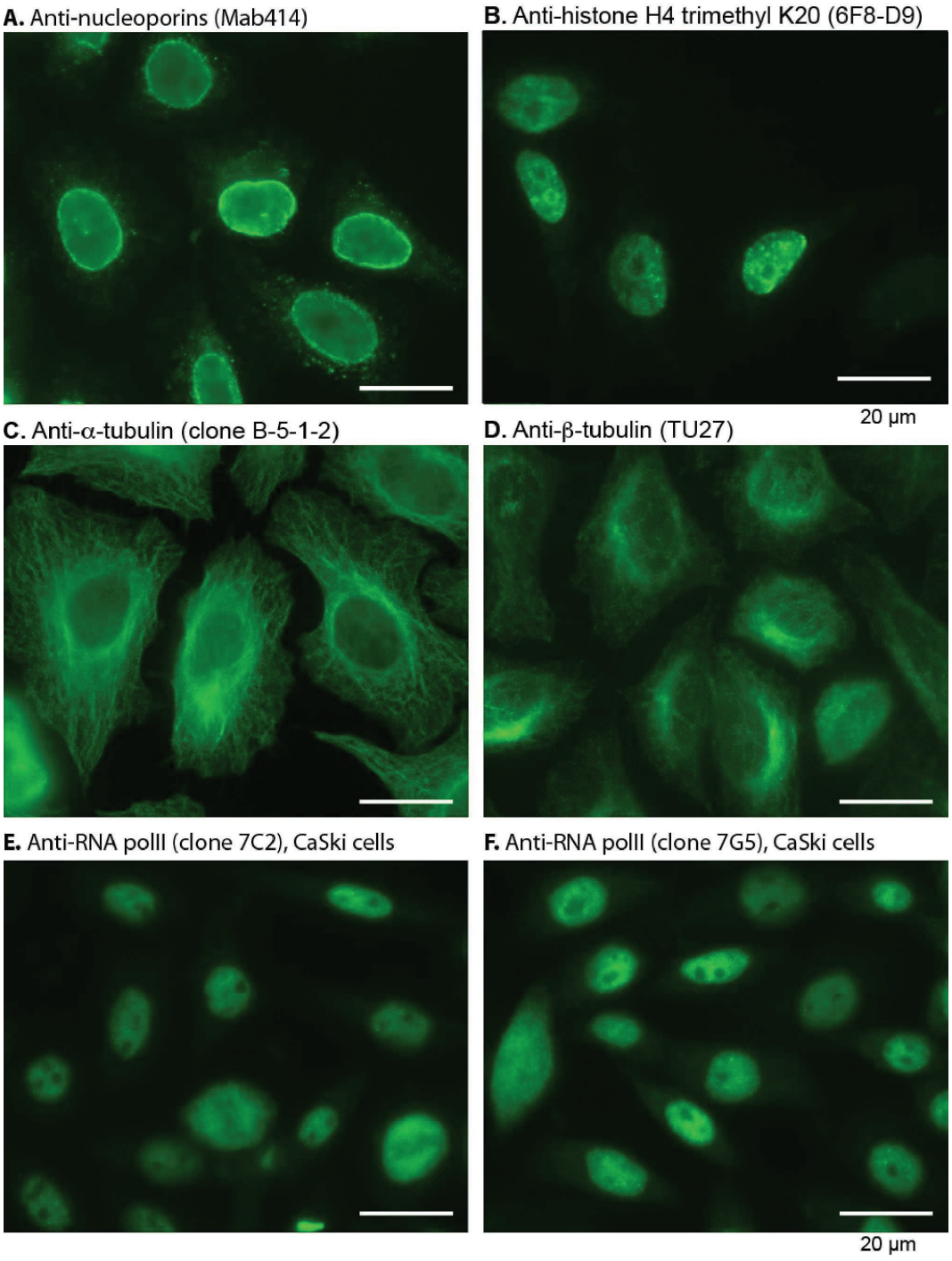


**Supplementary Figure S3.** Immunofluorescence imaging. Otherwise indicated, HeLa cells adhered onto glass coverslips were fixed with 4% PFA for 20 min. The plasma membrane was permeabilized with 0.1% Triton X-100 before incubation with the indicated primary mouse mAbs in PBS containing 10% FBS. The mouse antibody was detected with a goat anti-mouse AlexaFluor488-antibody conjugate.

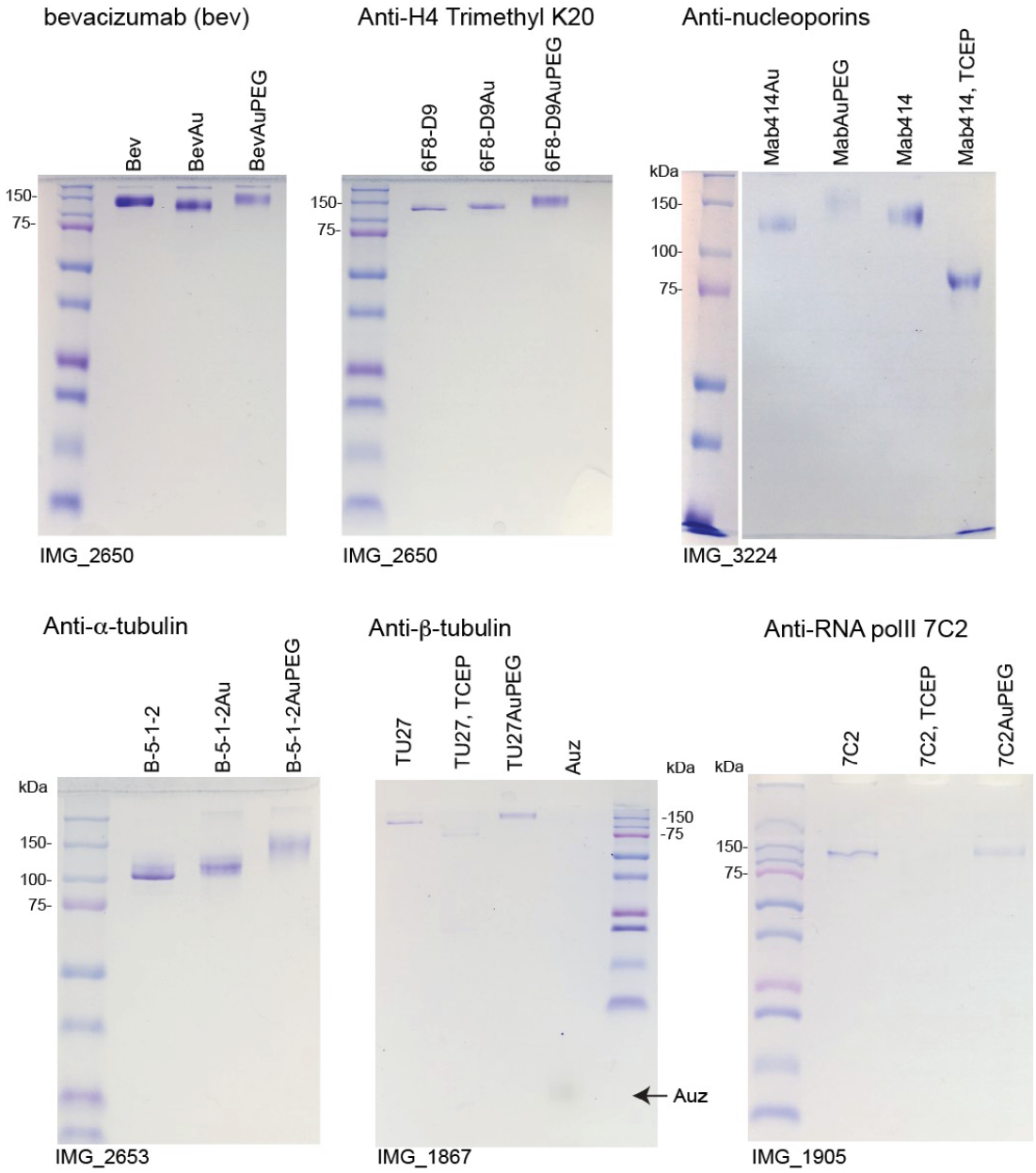


**Supplementary Figure S4.** Non-reducing SDS-PAGE analysis of the indicated AuNP-mAb conjugates. The proteins were stained with Coomassie blue.

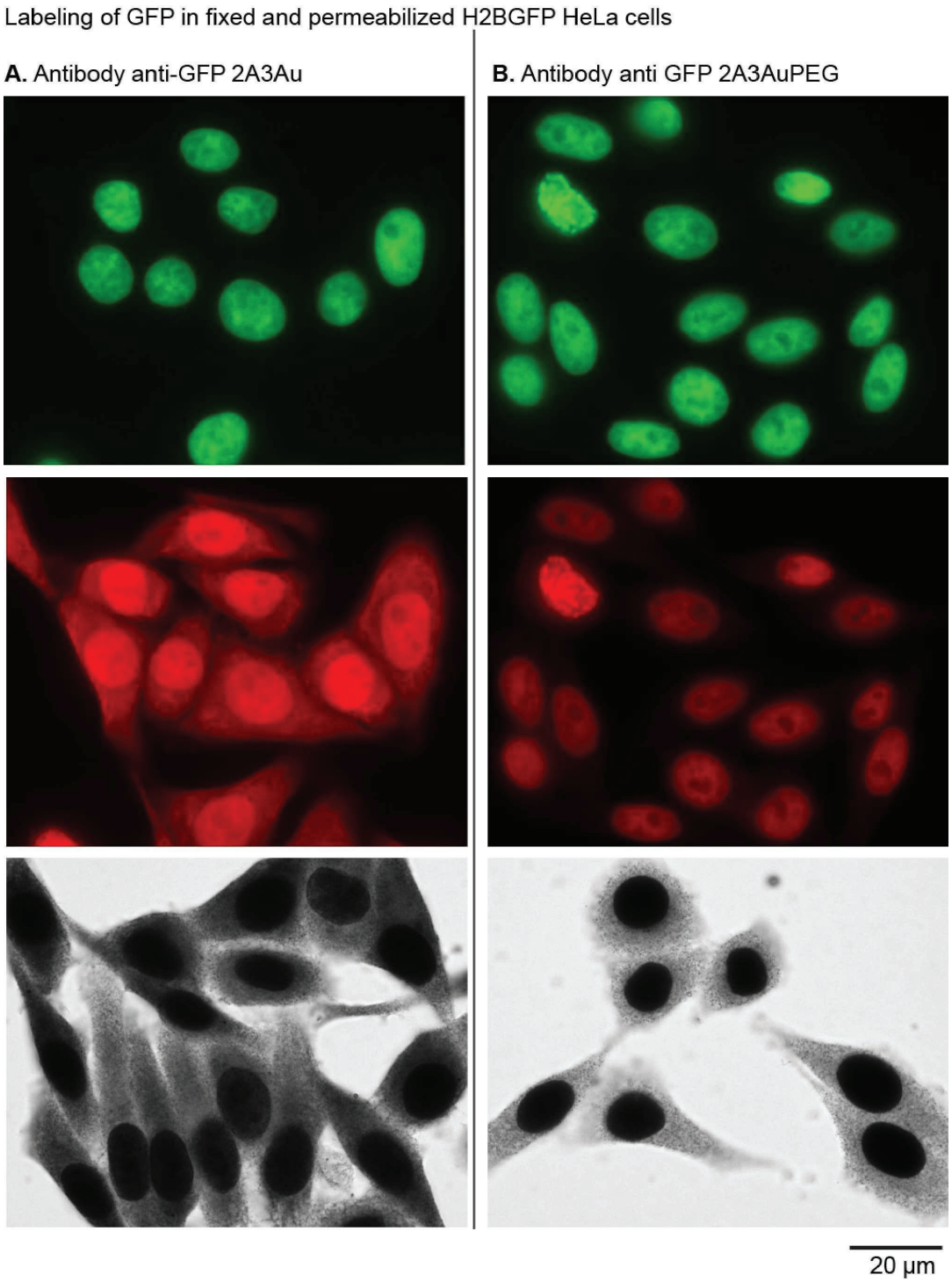


**Supplementary Figure S5.** HeLa cells stably expressing H2B-GFP were fixed with 4% PFA for 20 min, permeabilized with 0.1% Triton X-100. The H2BGFP fusion protein was then detected by binding of 2A3Au and 2A3AuPEG conjugates to the GFP. Detection was done either directly using the GFP green fluorescence (top images), an anti-mouse AlexaFluor-594-Ab conjugate (middle images) or the AuNP via a silver enhancement procedure. Results showed that coating of the AuNP with PEG limit unspecific binding.

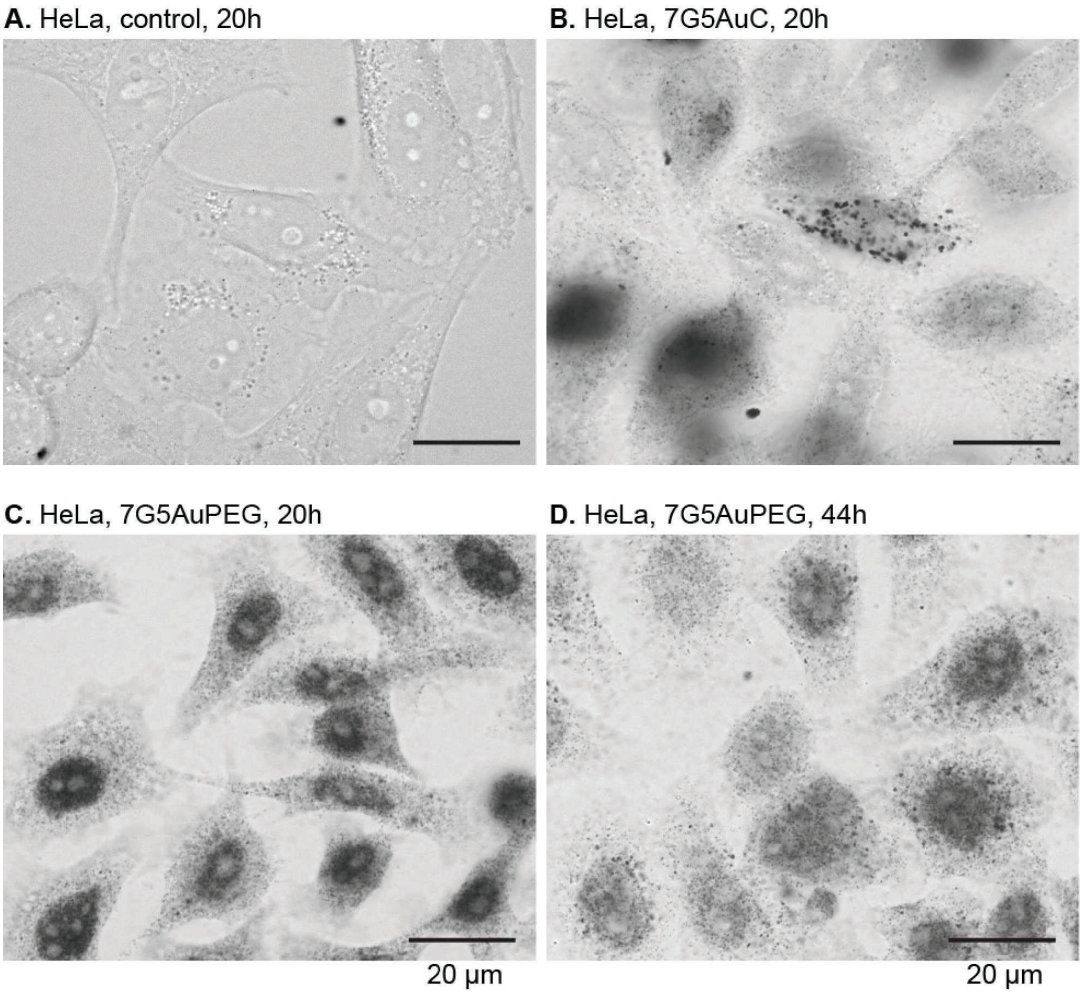


**Supplementary Figure S6.** HeLa cells were incubated with the indicated AuNP-7G5 conjugates and treated with three pulses of 10 ms at 517 $V \cdot cm^{-1}$. After 20 h or 44 h of cell culture, the cells were fixed with 4% PFA for 20 min, permeabilized with Triton X-100 and the gold particles were enhanced with silver.

## 1.3. Optimization of the probe delivery by electroporation

My initial results with *in situ* cryo-EM visualization of Au•NLS (Publication 1) was encouraging, I used the probes synthesized by our collaborators and provided the foundation for further methodological development. Building on these findings, I gained expertise in the complete workflow of probe preparation and electroporation. However, my exploratory experiments revealed significant limitations in applying these techniques to my long-term goal: *in situ* cryo-EM mapping of Pol II. In this section, I detail the optimization of critical electroporation steps to address these challenges.

**Synthesis of gold nanoparticles.** I used a gold nanoparticle (AuNP) synthesis protocol derived from Levy-Kalisman and coworkers (Levi-Kalisman et al., 2011), were the anionic mercaptobenzoic acid (MBA) stabilization agent was replaced by the Ellman reactive that forms a less negative outer coating layer (Desplancq et al., 2018). This outer layer is populated by 2/3 of zwitterionic thioaminobenzoic acids (TAB) and 1/3 of the anionic thionitrobenzoic acids (TNB). They can be easily exchanged by any other thiol molecules to form a strong Au-S bond. This can be used for binding of a thiolated protein to a nanogold particle to form a gold-protein conjugate. I produced AuNPs of different sizes which were controlled by direct observation in electron microscopy. Finally, I produced AuNPs with a size of  2 nm diameter. Previous experiments showed that larger particles impaired nuclear import and were concentrated in endosomes, while smaller particles were difficult to detect in electron tomograms. 2.4 nm AuNPs have been successfully conjugated to Nuclear Localization Signal (NLS) peptides to drive their nuclear import before (Desplancq et al., 2018; Groysbeck et al., 2023) and in my experiments described below, gold nanoparticles were synthesized following the protocol published by Groysbeck et al. (Groysbeck et al., 2023). The conjugation step was slightly adapted for each protein. Purification of the conjugation products (conjugates) yielded varying amounts. The labeling efficiency was evaluated using two complementary methods. The first involved silver enhancement of chemically fixed electroporated cells: the silver precipitates around the probe's gold nanoparticle, creating visible dark spots creating black spots whose size varies according to the incubation time, making their locations more visible. The second method employs fluorescent labeling with secondary antibodies conjugated to fluorophores, highlighting the protein component of the conjugates. Together, these methods target all the elements of the conjugate separately, the gold nanoparticles and the affinity proteins, and ensures the specificity of the probing and the integrity of the conjugates of co-localization when both imaging methods are co-localizing.

**Electroporation experiments.** My initial cryo-FIB milling results showed that HeLa used in Publication 1 produces a very rough crystalline ice in the nucleus after plunge freezing, because their nuclear areas are too thick. I decided to switch to U-2 OS cells that are flatter. It turned out, however, that the electroporation protocol used successfully in Publication 1 for HeLa cells (three 10 ms pulses at 1550 V) resulted in great mortality of U-2 OS cells. I also extensively tested the thermofisher online protocol to electroporate U-2 OS cells. In my hands, it could not get better than 50% or less of cell survival with heterogenous transfection rates. I explored every possible option: changing the special buffer provided with the Thermo transfection system (Buffer R) to PBS, changing the cell concentration and the probe concentration, but nothing improved the viability, efficiency and homogeneity of transfection. It has to be noted that Thermofisher online protocol was optimised for plasmid DNA delivery (Table 1). It is possible that the high negative charge, larger size, and relative flexibility of DNA molecules influence the impact of electroporation on cell viability. Consequently, electroporation protocols may require modification for use with different probes and cell lines.

| Cell line | Pulse voltage (V) | Pulse width (ms) | Pulse number | Cell density (c/mL) | Transfection efficiency | Viability |
|---|---|---|---|---|---|---|
| HeLa | 1 005 | 35 | 2 | $5 \times 10^6$ | 90% | 87% |
| U-2 OS | 1 230 | 10 | 4 | $5 \times 10^6$ | 82% | 72% |
| K-562 | 1 000 | 50 | 1 | $1.51 \times 10^7$ | 83% | 90% |
| | 1 350 | 10 | 4 | $1.51 \times 10^7$ | 85% | 88% |
| | 1 450 | 10 | 3 | $1 \times 10^7$ | 90% | 90% |
| MEF | 1 350 | 30 | 1 | $5 \times 10^6$ | 80% | 75% |
| | 1 650 | 20 | 1 | $5 \times 10^6$ | 70% | 70% |

**Table 1.** Online Thermo Fisher scientific electroporation parameters for Neon ™ transfer system using 10 µL tips type for different cell lines transfected with 0.5 µg of a plasmid encoding EGFP. (https://www.thermofisher.com/order/transfectionselect/#!/citations).

I decided to explore the modification of voltage and number of pulses. I had several discussions with Mariel Donzeau (TRAVE's Team in IGBMC) about electroporation protocols that help me to obtain homogeneous transfection rate while ensuring high cell survival. She highlighted a protocol employing a single pulse at 1400 V for 10 ms, arguing that multiple or prolonged pulses used in our previous experiments (Publication 1 and 2) can adversely affect cell viability and reduce transfection efficiency. She suggested that increasing the voltage can help balance pulse parameters and improve transfection efficiency. Furthermore, in her hand, this single pulse protocol has demonstrated consistent success across multiple cell lines (Juncker et al., 2023).

The reason for reducing electroporation to a single short pulse of 10 ms lies in minimizing cell damage. This approach is grounded in the following considerations:

1. Increasing cell permeability by the application of an electric field is promoting molecular exchanges between the cell cytoplasm and the electroporation mix. High density crowding of differentially charged macromolecules in the cytoplasm will escape the cell upon electroporation in two different ways : (i) through osmolarity difference between the cytoplasm and the electroporation mix; and (ii) the presence of charged molecules that migrate to one of the electrodes and leave the cytoplasmic environment. These effects will obviously have a stronger impact on the cell integrity after several pulses. However with one pulse, cells seem to largely recover from a partial loss of cytoplasmic content.

2. In an non-uniform electric field, the voltage is directly linked to the potential difference between two points such as:

$$\Delta V = -\int_{r0}^{r} E dr$$

where $\Delta V$ is the potential difference in volts, $E$ is the electric field function and $r$ is the radial distance. Increasing the voltage of the system is increasing the work per unit of charge. In other words, modifying the voltage alters the energy transferred to a unit of charge over a given distance. Voltage is often described as the amount of pressure applied to charges in a circuit or an electric field between two electrodes. Simply put, within a single pulse frame of 10 ms, increasing the voltage can accelerate the movement of charges from one electrode to the other, thereby trapping more probes within the cell's cytoplasm.

My electroporation assays were conducted using the same U-2 OS cell line. An identical number of cells was collected by trypsinization and prepared at a consistent concentration of $1 \times 10^7$ cells/mL in the electroporation mix. After electroporation, the cells were allowed to attach to coverslips and to recover for 12 to 18 hours. Chemical fixation was then performed using 4% formaldehyde for 20 minutes, followed by silver enhancement for 15 minutes. The silver enhancement protocol was performed exactly as previously described (see Publication 1). It is

important to note that the optical density of silver accumulation cannot be used for quantitative comparisons of transfection efficiency, as the development of silver stain does not progress linearly depending on the initial gold nanoparticle concentration. However, it was sufficient for a brief qualitative assessment of the overall transfection efficiency to guide parameter optimization.

| Cell line | Pulse voltage (V) | Pulse width (ms) | Pulse number | Cell density (c/mL) | Label |
|---|---|---|---|---|---|
| U-2 OS | 1200 | 10 | 4 | $1 \times 10^7$ | **Online** |
| U-2 OS | 1000 | 10 | 2 | $1 \times 10^7$ | **L.V.** |
| U-2 OS | 1400 | 20 | 1 | $1 \times 10^7$ | **M.V.** |
| U-2 OS | 1600 | 20 | 1 | $1 \times 10^7$ | **H.V.** |

**Table 2.** Electroporation conditions used in my experiments: Online, reproduced from Table 1 for U-2 OS; L.V., low voltage; M.V. medial voltage; H.V., high voltage.

All the electroporation experiments presented below were performed on U-2 OS cell lines using AU-NLS probes, introduced in the section “1.1. Publication 1”. Electroporation using the online supplier protocol for U-2 OS cells (Table 2, Online) led to a high transfection rate with a high cell mortality (see Figure 1 Online section). The high mortality was manifested by a low number of cells present in the field of view (Figure 1 left images, compare Online and M.V. sections). Dark nuclei compared to relatively low cytoplasmic background indicated a high efficiency of transfection. Aiming to reduce cell mortality, I evaluated two sets of electroporation conditions, designated as L.V. and M.V. (Table 2).

As shown in Figure 1, the density of cells remaining on coverslips was comparable between the L.V. and M.V. protocols, whereas the Online protocol resulted in approximately three times fewer cells. All three protocols differed by increments of roughly 200 V (Table 2) but between the 1000 V of the L.V. protocol and the 1400V of the M.V protocol, the applied voltage did not significantly impact the vitality rate of transfected cells. However, the Online protocol, which used an intermediate voltage of 1,200 V, yielded the lowest vitality rate. Unlike the L.V. and M.V. protocols, which employed two 10 ms pulses and one 20 ms pulse, respectively, the Online protocol utilized four 10 ms pulses, doubling the cumulative electroporation time. These findings suggest that the total electroporation time and or the number of pulses are more critical for cell vitality than the applied voltage.

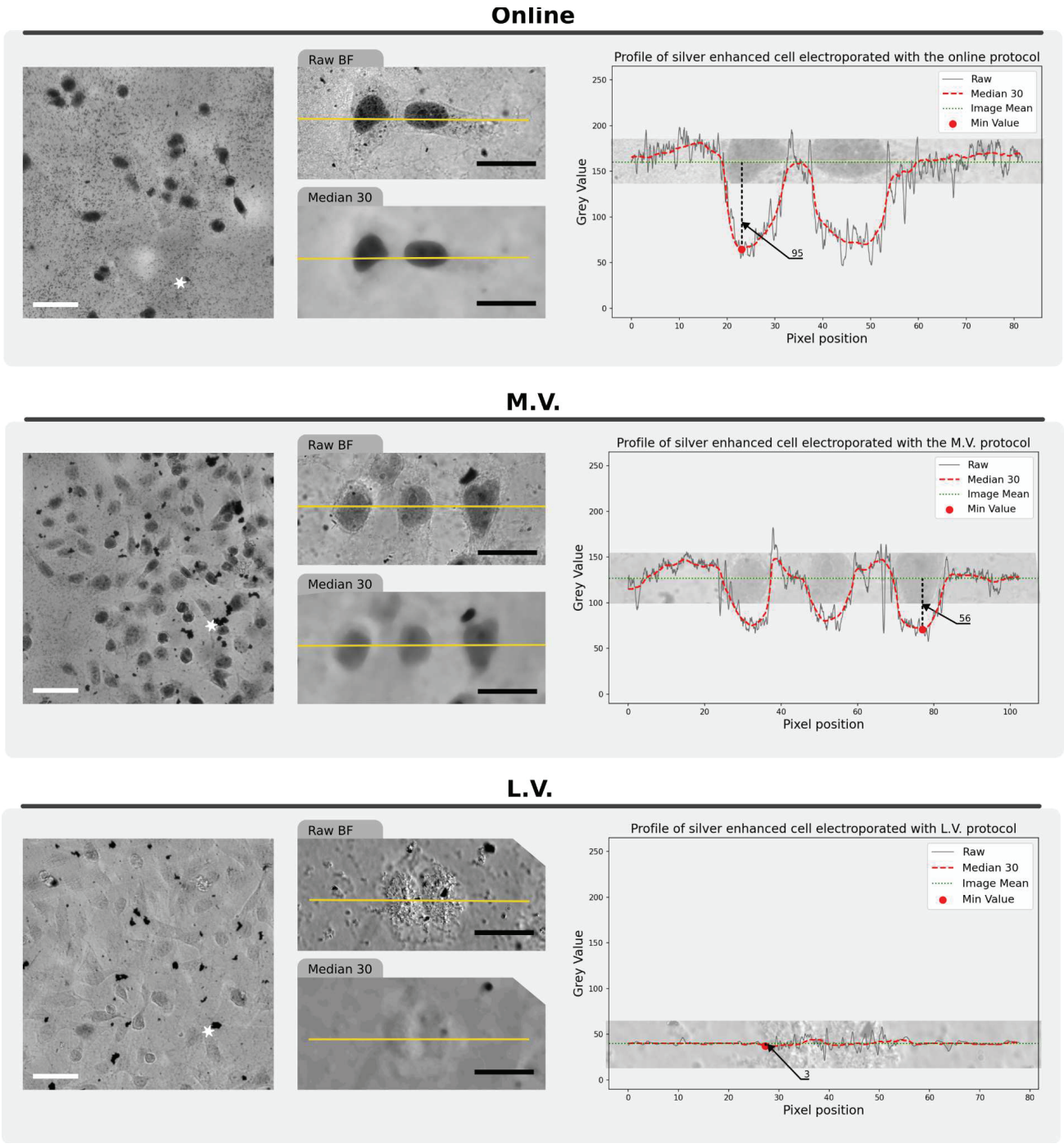


**Figure 1**.Characterization of the electroporation protocols: Online, M.V.(medium voltage), and L.V. (low voltage, see Table 2 for detail). Images represent U-2 OS cells after electroporation with the Au•NLS probe for different electroporation protocols, chemical fixation and silver enhancement. The left column shows a low magnification bright field image, the middle top, high magnification bright field image with a yellow line representing the position of the intensity profile, middle bottom, median filter with 30 pixels diameter applied to the middle top image.The right column shows profile plots with superimposition of the raw and filtered profiles curves with the minimum to mean ratio highlighted by a vertical dashed black line. The white scale bar represents 40 µm, the black scale bar represents 20 µm, white stars indicate debris coming from silver enhancement protocol or cell debris.Pixel values of the images analysed here are 8 bit encoded where 255 is the brightest white value and 0 the darkest back value.

To assess the electroporation efficiency, I analysed the linear intensity profiles drawn through the nuclei and cytoplasm of electroporated cells (Figure 1, central column; see Supplementary Materials and Methods for details). In each protocol, the median-filtered profile data, represented by the red curve (Figure 1, right plots), provided a smoothed representation of the noisy raw image profile data (Figure 1, right plots grey curves). The alignment of the median-filtered curve and nuclei contours indicates that the median filtering did not distort the shape of the nucleus. Correspondingly, the median-filtered profiles closely represent the raw data and are easier to compare, and thus, they were used to interpret the results. The transfection efficiency between protocols was compared using the difference between the minimum grey value of nucleus pixels and the global image mean intensity, referred to as the "minimum-to-mean" value. The Online protocol resulted in nuclei that were approximately twice as dark as those transfected using the M.V. protocol, with minimum-to-mean values of 95 and 56, respectively (Figure 1). In contrast, the L.V. protocol showed no significant staining of the nucleus, yielding a minimum-to-mean value of 3. These results indicate that the electroporation can occur only above a certain threshold of voltage, since no usable electroporation was seen at 1000 V. However, the results obtained at 1200 V and 1400 V show again that the number of pulses or their electroporation cumulative time have a higher effect than the voltage. Among the three conditions - online, M.V., and L.V. - the M.V. protocol offers the best compromise, maintaining a good vitality rate alongside moderate transfection efficiency.

Although the amount of probe electroporated into cells is lower under M.V. conditions compared to the online protocol, the reduced cell mortality offers a significant advantage for cryo-ET applications involving vitreous cryo-sectioning. This technique requires the formation of a large cell pellet that is completely vitreous. Conversely, cell number might be less critical for cryo-FIB milling sample preparation approaches, as these methods currently enable precise targeting of individual cells of interest by in-chamber fluorescence imaging. Under these circumstances, maximizing electroporation efficiency may be prioritized, even at the expense of increased cell mortality.

To further improve the efficiency of probe transfer, I used the M.V. parameters as a reference and explored the effect of higher voltage on both transfection efficiency and cell vitality. Specifically, I increased the voltage of the M.V. protocol by 200 V, bringing it to 1,600 V, while maintaining a single 20 ms pulse (H.V. protocol in Table 2). Additionally, I investigated the impact of the resuspension buffer on transfection efficiency by comparing PBS with the Neon™ resuspension buffer R (Figure 2). Four conditions were tested: the M.V. protocol using either PBS or Buffer R, and the H.V. protocol using PBS or Buffer R. In each condition, $10^7$ cells/mL of U-2 OS cells were electroporated with the Au-NLS probe. Following electroporation, cells were processed in the same way as the previous experiment series (Figure 1): they were placed on glass coverslips, chemically fixed, and stained using the same silver amplification protocol.

I observed no significant differences in cell viability between the M.V. and H.V. protocols. Similarly, there were no noticeable changes in cell shape or distribution on the glass surface that would suggest prolonged cell stress or damage following electroporation. The choice of PBS or Buffer R as the resuspension electroporation buffer did not significantly impact transfection efficiency. However, the voltage difference between the protocols appears to influence transfection efficiency. The H.V. protocol showed a minimum-to-mean ratio twice as high as the M.V. protocol for both PBS and Buffer R (Figure 2). Compared to the Online protocol, the H.V. protocol achieved similar transfection efficiency without a significant decrease in cell viability (Figure 2). In this experiment, I can only judge viability by comparing the cell densities between M.V. and H.V. images and due to an unfortunate higher dilution of cells made before transfer to coverslips, it is not possible to directly compare Figure 1 with Figure 2.

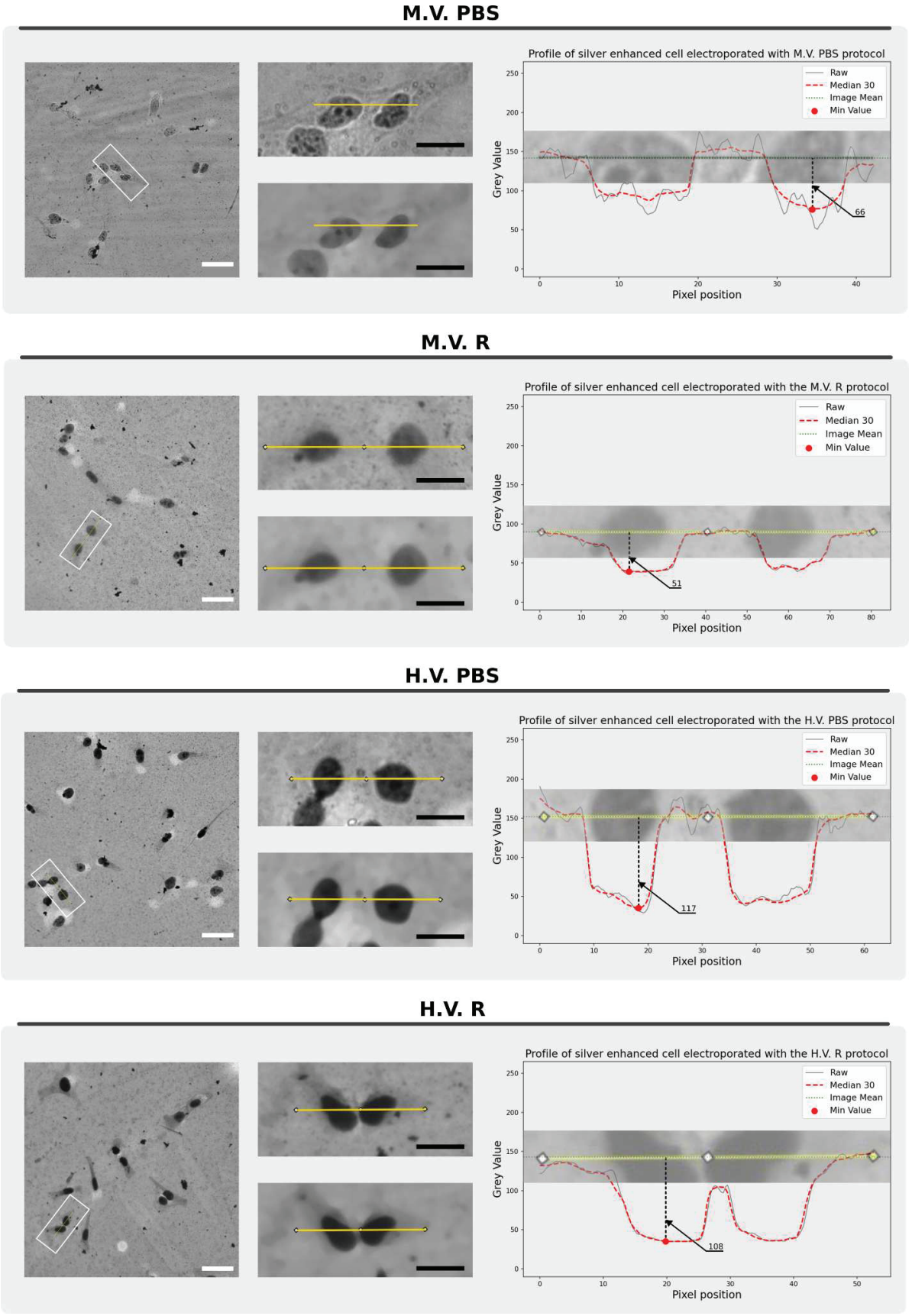


**Figure 2**.The impact of electroporation voltage and buffer composition was evaluated using two different buffers, PBS and Buffer R, and two protocols, M.V. and H.V. Sample preparation, imaging, profile analysis, and all measurements were performed as described for Figure 1. The white scale bar represents 50 µm, while the black scale bar represents 20 µm. White boxes on the left image correspond to the region magnified in the middle top and middle bottom images.

## 1.4 Towards *in situ* localization of Pol II nanogold probes

Aiming to establish a robust pipeline for the *in situ* localization of Pol II at the molecular resolution, I explored several labeling strategies. My initial approach used a well-characterized monoclonal antibody targeting the C-terminal domain (CTD) of the largest Pol II subunit. This approach was initialized in the Schultz team (IGBMC) in combination with conventional EM imaging a long time ago (Orlov et al., 2015). Although this approach is more established than others, it presents challenges related to probe specificity, potential interference with Pol II enzymatic function, and the stability of the antibody-antigen complex. To address these limitations, I explored alternative labeling methods. Additionally, I proposed the development of more universal probes suitable for a broader spectrum of target molecules.

**1.4.1 The 7G5 monoclonal antibody, 7G5 and f7G5 Conjugates**. In order to localize Pol II *in situ*, I initially used the 7G5 mouse monoclonal antibody (mAb) that was produced three decades ago. This antibody recognizes the C-terminal terminal domain of the largest Pol II subunit. It was raised against the conserved Tyr-Ser-Pro-Thr-Ser-Pro-Ser heptapeptide which is repeated 52 times in the human RPB1 gene. This long, intrinsically disordered domain of Pol II is expanded outside of the complex (Zaborowska et al., 2016) thus facilitating its localization by the antibody.

**The Piggyback mechanism.** A major challenge for the *in vivo* labeling is ensuring that the gold conjugates transfected into living cells specifically bind to their target protein of interest. Discriminating between specifically bound gold conjugates and non-specifically bound or free gold particles is critical for a successful labeling experiment, particularly under conditions where unbound probes cannot be washed away. Previous experiments showed that the nuclear transport can be used for filtering out free and non-specifically bound antibodies. It has been shown that free antibodies, and immunogold conjugates do not diffuse freely into the nucleus because the diffusion barrier of nuclear pores is around 100 KDa for uncompacted globular-like proteins (Wang and Brattain, 2007). Antibodies or immunogold conjugates are not actively imported into the nucleus, as they lack a nuclear localization signal (NLS) within the immunogold probe sequence. However, *in situ* labeling of Pol II using fluorescently labeled 7G5 antibodies has been shown to result in nuclear fluorescence accumulation (Freund et al., 2013). To explain this nuclear co-localization of 7G5 antibodies with Pol II, it has been proposed that, upon delivery into the cell, 7G5 antibodies interact with their freshly translated Pol II target in the cytoplasm before the target is imported into the nucleus. The labeled Pol II subunit is subsequently recruited to the nuclear pore and actively transported into the nucleus, effectively carrying the immunogold probe along with it, a process described as "piggybacking" (Freund et al., 2013; Orlov et al., 2015; Roozbahani et al., 2024).

Earlier experiments performed in the team showed that 0.8 ultrasmall gold conjugated to the 7G5 monoclonal antibody were delivered in human living human cells and are imported into the cell nucleus as was observed for fluorescent antibodies, thus demonstrating that gold-based probes

behave as as free antibodies *in vivo* and are likely to use the same piggyback mechanism (Orlov et al., 2015).

**7G5 antibody fragments.** The 7G5 mouse mAb is an IgG molecule with a molecular mass of 150 kDa consisting of two heavy chains, each interacting with a light chain. An IgG molecule, in principle, can bind to two Pol II complexes, which may result in unwanted artificial aggregation. It can be avoided by using isolated Fragment antigen-binding (Fab) regions of an antibody. FAbs are derived from mAbs by peptidic digestion. They have a molecular mass of about 50 kDa and contain half of the heavy chain interacting with a light chain. FAbs retain all the antigen recognition properties but are monovalent and therefore may prevent *in situ* aggregation issues.

**Conjugation to AuNPs.** The heavy and the light chains interact through disulfide bonds, while additional intra-chain disulfide bonds stabilize and IgG domains. The presence of a reducing agent in controlled quantities favors the partial protonation of sulfurs involved in disulfide bonds. Protein chains are then partially open and newly formed thiol groups are accessible for interaction with gold nanoparticles (Groysbeck et al., 2019; Makaraviciute et al., 2016). The 7G5 mAbs and Fabs have been conjugated using this protocol which is difficult to control precisely. The result of the conjugation process is monitored by gel electrophoresis which reveals the amount of gold-coupled IgG molecules. The difference in size between an f7G5•gold conjugate and excess gold is smaller than between the 7G5•gold conjugate and excess gold. The size exclusion chromatography purification step is thus less effective in isolating f7G5•gold.

Our purification attempts resulted in only small quantities only sufficient to verify the probe specificity on **non** electroporated fixed and permeabilized cells. The probe was too scarce to electroporate the number of cells needed for the rest of the workflow.

**1.4.2. Production of recombinant Fab fragments.** Several considerations encouraged us to produce recombinant Fab fragments derived from the 7G5 monoclonal antibody. MAbs are purified from ascites liquid which are subjected to legal issues about animal welfare. In addition the partial protonation of the disulfide bonds connecting the heavy and light subunits is extremely sensitive to the activity of the reducing agent used for the conjugation process, that has to be precisely controlled since it may affect intra-chain disulfide bonds important for chain folding. The conjugation process is thus likely to generate unwanted probe species such as partially unfolded molecules (see **1.2. Publication 2** part). In collaboration with Arnaud Poterszman we decided to clone the two chains of the IgG molecules and to express the recombinant form of the Fab (rFab) in insect cells. The possibility to express a recombinant form of the Fab opens numerous new perspectives. First of all one can introduce small protein tags such as a his-tag or a strep-tag to facilitate affinity purification of the probe. Second additional functions can be incorporated into the probe such as fluorescent probes for correlative light and electron microscopy. Importantly, we also introduced an additional SH group at the N-terminus of the light chain to facilitate gold conjugation without use of reducing agents that may alter the structure of the IgG domains. Unfortunately, due

to time constraints, I was unable to fully complete the development and characterization of these probes.

**1.4.3. Spycatcher/SpyTag based probes.** Nuclear accumulation of the nanogold probe provides strong evidence that the immunogold conjugate was specifically bound to its target in the cytoplasm and was effectively imported into the nucleus via the piggyback mechanism. However, we cannot entirely rule out the possibility that the probe dissociates from its target within the nucleus during the 24-hour incubation period. We therefore explored the possibility to use a probing system that takes advantage of the covalent bond formed during the interaction between a globular 15 kDa protein called spycatcher and its specific SpyTag ligand (RSGAHIVMVDAGSR) (Zakeri et al., 2012). A slightly modified system SpyCatcher003 has been used in a modified K562 cell line expressing the pol II Rpb3 subunit tagged with a SpyTag003. A cysteine was introduced in the SpyCatcher003 sequence through a S49C substitution that was originally designed for dye attachment (Keeble et al., 2019). However, this mutation was used as an anchor point for gold nanoparticle conjugation. I was able to efficiently produce and conjugate the spycatcher protein to gold nanoparticles but I was unable to characterize this probe *in situ*.

**1.4.4. Targeting a different Pol II subunit.** The CTD of the largest subunit is the subject of multiple regulation mechanisms involving the phosphorylation of Ser2 and Ser5 of the heptapeptide repeat. Although no cytotoxic effect was observed with increasing amounts of transfected 7G5 MAbs, it cannot be excluded that the binding of the immunogold probed interferes with Pol II activity and for example prevents it from entering the elongation phase. To address this issue we will use the above mentioned genetically modified K562 cell line that expresses a RBP3 subunit fused to a SpyTag (see 1.4.3).

**1.4.5. Development of *in situ* universal labeling probes.** The above described immunolabeling probes rely on the availability of an antibody displaying a highly specific interaction mode to avoid coupling to non-specific proteins and a high affinity to prevent dissociation of the antibody from its target molecule. Home-made monoclonal antibodies require a long optimization and selection time without guarantee that both objectives can be reached. On the other hand biomolecular recognition systems have been optimized that provide exquisite affinity and specificity, and can be tested for *in vivo* studies. Such systems require a prior genetic modification of the cell line to introduce specific tags, which is now possible with the advent of genome editing tools such as Crispr-Cas9 (Jinek et al., 2012). We mentioned above the SpTag/Spycatcher system which can lead to a covalent bond between the gold probe and the target protein. Here I describe additional systems that I started working with during my thesis project and would like to focus on in the future if the opportunity arises.

**Recombinant anti-GFP antibodies.** The scientific community designed a large number of cell lines with individual GFP labeled proteins, either in an overexpressed form, but more and more frequently in an genetically engineered version where the endogenous gene is replaced by a modified version, thus giving rise to the same expression levels than the wild-type protein. A recombinant Fab fragment directed against GFP has been cloned and has been conjugated to AuNPs. Even more interesting is the design of a single chain nanobody with nanomolar affinity for GFP. This reagent can be produced in large amounts in *E.coli* and has the advantage of being of small size. This engineered anti-GFP nanobody contains an additional Sulfhydryl group for joining to nanagold without the problematic partial reduction step. Nanobodies do not contain disulfide bonds that can be opened without affecting the stability or function of the nanobody.

**Au-K3_E3-NanoBody.** The E3-K3 assembly system was used as a linker in the conjugation of a nanobody targeting GFP (nGFP) to gold in an Au•K3-E3nGFP architecture. This linker avoids using the disulfide bonds of the nanobody for conjugation and distances the gold to reduce its potential steric impact on the nGFP function. A modified U2OS cell line expressing the NUP96-GFP fusion nucleoporin was electroporated with Au•K3-E3nGFP. Preliminary fluorescence and silver enhancement controls (Figure 1) show that the probe localizes to the periphery of the nucleus. This probe was used at the end of my thesis, and I did not have time to push the workflow towards tomography. I used the system Au-K3_E3-NanoBoby that was previously shown to work using a nanoboy against GFP (nGFP) in the following construction $(Nb\text{-}E3)_2$:$(K3)_2$AuNP (Groysbeck et al., 2021; Vigneron et al., 2019). Although this probe was shown to recognize a transiently expressed recombinant GFP protein in PFA fixed and permeabilized HeLa cells it was not tested as an *in vivo* probe in the context of sample preparation for *in situ* cryo ET. In my thesis project, I explore the compatibility of this probe *in vivo* after electroporation and could validate it as a potential versatile probe for later cryo-ET. I electroporated the $(nGFP\text{-}E3)_2$:$(K3)_2$AuNP probe into a U2OS cell line engineered to stably express the NUP96-GFP fusion nucleoporin and shown that the probe is localized at the site of the NUP96 nucleoporin and that the cell line withstand this probing for 20 H after electroporation with good cell viability rate and thus validating this universal probe as a good candidate for further *in situ* cryo ET study (Figure 3).

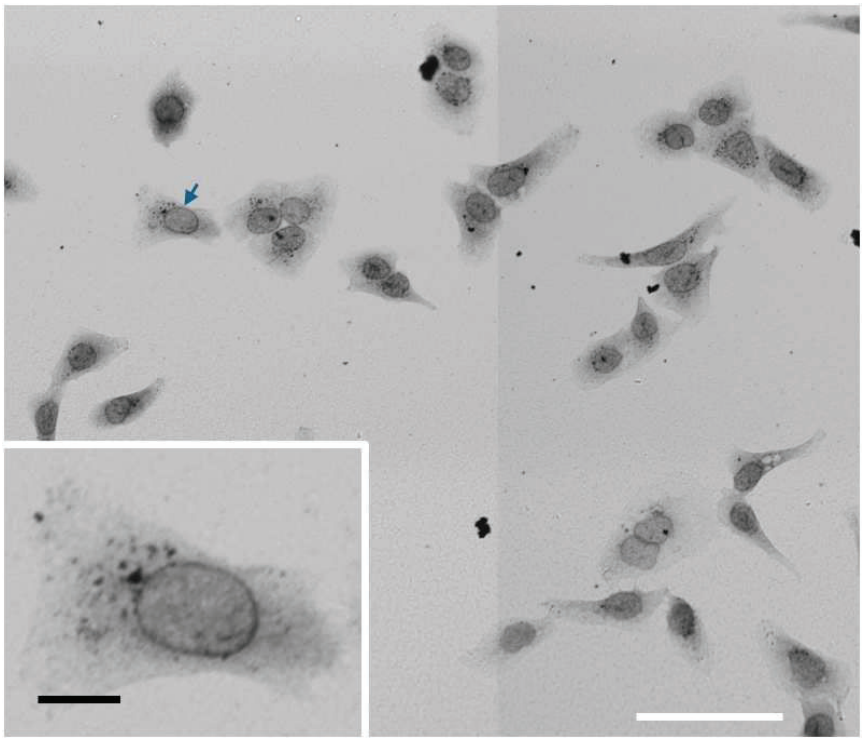

**Figure 3.** U2OS cells expressing NUP96-GFP electroporated with $(nGFP\text{-}E3)_2$:$(K3)_2$AuNP probe. The cells shown after chemical fixation and silver enhancement. The probe bound to nuclear pores clearly depicts the contour of the nucleus. Some background labeling is present in cytoplasm and likely in endosomes. The inset shows a magnified view of the cell marked by an arrow. The white scale bar represents 50 μm, while the black scale bar represents 10 μm.

## 1.5. Post transfection sample preparation for Cryo ET

Having achieved promising results in nanogold visualization at the start of my project, I proceeded to optimize various steps of the workflow related to sample preparation of electroporated cells for cryo-ET. The equipments available at the institute were more conducive to developments in the direction of cryo-FIB-SEM, as we had a fully equipped Auriga 60 (Carl Zeiss Microscopy GmbH) microscope for cryo-FIB milling, along with all the necessary accessories for cryo-transfer and cryo-sputtering. However, the cryo-FIB milling workflow had not yet been established at the institute. Therefore, I focused on setting up the cryo-FIB workflow from scratch and optimizing it for the goals of my project.

Under the guidance of Mikhail Eltsov and with the assistance of Daniel Spechner for FIB-SEM operations, I implemented these technologies at the cryo-EM platform of IGBMC and at my projects. My optimization directions included:

- Seeding cells on EM grids;
- Cryo-immobilization using plunge-freezing;
- Using In-Lens SE detector for localizing of cells in cryo conditions within the FIB-SEM system and for evaluation of freezing quality;
- Waffle technique for complete vitrification of nuclear regions of adherent cells.

**1.5.1. Seeding cells on EM grids.** Proper adherence and maximal spreading of adherent cells on an EM grid are essential for reducing sample thickness, which is critical for achieving high-quality freezing via plunge-freezing. Here, I use the term freezing rather than vitrification because, in the absence of additional cryoprotectants (e.g., glycerol (Bäuerlein et al., 2021)), complete vitrification can only be achieved in very thin cellular extensions of mammalian cells, such as lamellipodia, which are typically thinner than 500 nm. In contrast, thicker regions, such as the nuclear area, do not vitrify fully. However, structural interpretations remain possible in the presence of polycrystalline ice, depending on the "fineness" of the ice crystals (see for example (Mahamid et al., 2016)).
At the beginning of my project I used HeLa cells then I switched to the U-2 OS system. I reproduced the available approaches of seeding cells on 200 mesh Quantifoil gold grids covered with perforated carbon coated with fibronectin (Lam and Villa, 2021; Mahamid et al., 2016 ; Figure 4A). I observed that when carbon support films with large holes and narrow spacing are used—for instance, 2 µm holes with 2 µm inter spacing—cells tend to avoid the centers of the grid squares (Figure 4B). This behavior makes such samples unsuitable for cryo-lamella fabrication, as lamellae can only be milled near the centers of the grid squares, not in the thicker metal grid bars. I solved it by switching to smaller holes- larger spacing grids holes of 1 µm diameter with an interspace of 4 µm (QUANTIFOIL™ R 1/4 ).

**1.5.2. Plunge freezing.** The thermofisher Vitrobot plunge freezer (Iancu et al., 2006) was the well established plunge freezing method in the institute. It provides great automation features such as humidity controlled chamber, automatic blotting with tunable blotting time and blotting force and of course automatic plunging. However, this equipment surfers from serious drawbacks such as mandatory simultaneous back and front blotting, unstable chamber humidity, non reproducible blotting from one grid to another using the same blotting parameters.

Front blotting of cell-seeded EM grids can potentially damage cells before freezing. To address this issue, we designed custom Teflon adapters for the Vitrobot's front arm, enabling back-blotting only. This approach has been widely reported as an effective method for blotting cell-seeded EM grids using the Vitrobot (Wagner et al., 2020) and was recently shown to work efficiently for bacteria-seeded grids (Lien et al., 2024). However, in our experiments, this method did not yield satisfactory results. Most grids prepared with back blotting alone retained excessive water between the Teflon sheet and the cells, leading to inadequate blotting. This resulted in poor freezing quality and thick ice formation.

At the beginning of my second year of PhD, I started using a homemade manual plunge freezer that is built of a weighted aluminum arm, holding any loaded fine tweezer, reproducing the original Marc Adrian's guillotine. The blotting is performed manually in open air, without humidity control. Although this method does not provide reproducible blotting or freezing, it produced sufficiently good freezing quality to visualize nanometric biological structures, such as macromolecular complexes, after post-freezing sample processing (see Section 1.5.5). Diffractograms recorded at different positions on manually plunge-frozen samples revealed that very few, if any, achieved amorphous ice quality within the nuclei of mammalian cells. The micro-damages caused by water microcrystals in these samples likely prevent the recovery of high-resolution information, severely impacting the final resolution of reconstructed 3D maps.

I concluded that manually plunge-frozen, cell-seeded EM grids are adequate for obtaining rough 3D environmental descriptions within tomograms. However, achieving the high-resolution standards required for accurate subtomogram averaging of macromolecular complexes demands freezing of mammalian cells in a more uniformly vitreous state. Recently, halfway through my fourth PhD year the institute has acquired a Leica EM GPT 2 plunge freezer that enabled more reproducible freezing of adherent mammalian cells, however it does not resolve the vitrification problems that can be only solved by implementation of high-pressure freezing (see 1.5.5).

I also observed that, in addition to freezing quality, the "roundness" of cells affects cryo-FIB lamella fabrication in our instrumental setup (Figure 4C, D). The lowest milling angle achievable with our equipment is 10°. Under these conditions, milling rounder cells, such as HeLa, results in shorter lamellae (Figure 4C). In contrast, flatter cells, such as U-2 OS, allow for significantly larger lamella areas (Figure 4D). Larger lamellae enable the collection of more tilt series from a single lamella, thereby improving data collection throughput.

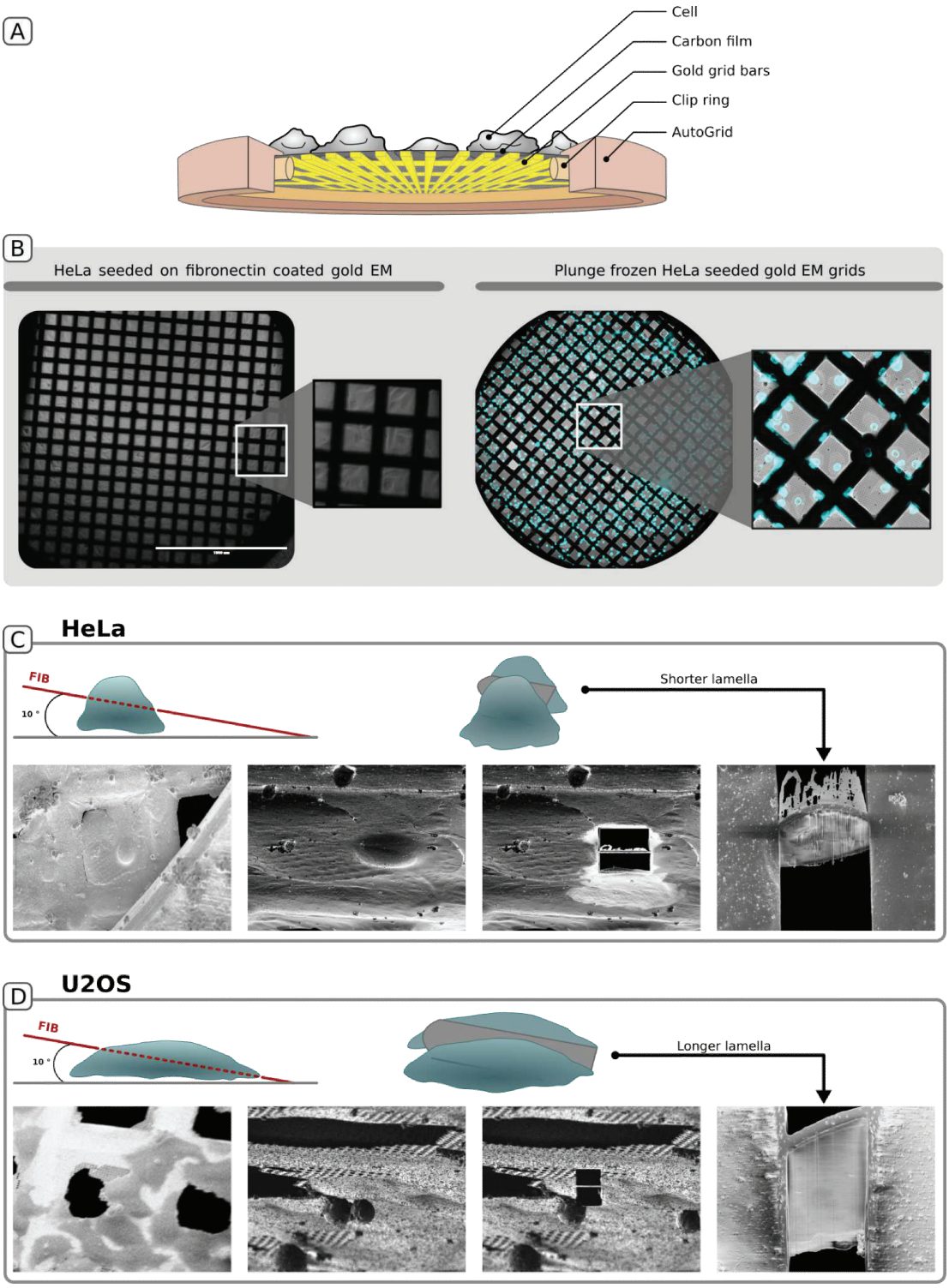


**Figure 4**. **(A)** The current setup for processing adherent cells for cryo-FIB milling involves the use of 200-mesh gold grids with perforated carbon support films. Cells are seeded on the carbon-coated side of the grid, and after plunge freezing, the grids are mounted into Autogrid rings for further processing. **(B)** When grids with larger-hole and smaller interspacing are used (here QUANTIFOIL™ R 2/2 ), cells preferentially adhere to the grid bar regions rather than the centers of the perforated carbon. This behavior is evident when cell nuclei are visualized using Hoechst fluorescence. **(C and D)** The geometry of the lamella is significantly influenced by the "roundness" of the cells. Flatter cells, such as U-2 OS, enable the production of larger lamella areas compared to rounder cells like HeLa. The increased lamella area achievable with flatter cells facilitates higher data collection throughput.

**1.2.3 Use of the In-Lens detector for screening cells and lamellae in cryogenic conditions.** InLens SE (secondary electrons) column detectors are placed around the incident electron beam path within the SEM column between the condenser and the objective lenses. In this particular setup, a boosting tension of 8 kV is applied from within the SEM column to its tip (pole piece) a few millimeters away from the sample surface (working distance, WD). This boosting voltage is highly efficient for collecting low energy SE as they are accelerated toward the InLens detector. SE within the low energy range are affected by topological deformations that are imprinted in the recorded micrographs where In-Lens imaging results in resolution and high contrast topographic images (Kumagai and Sekiguchi, 2009 ; Carl Zeiss Microscopy GmbH, Auriga® series instruction manual, revision en05, 2012 p43-46). From a practical point of view I could experience that this detector is really sensitive to surface charges whether they are due to the charging effect of prolonged acquisitions of a fixed area or charge removal by surface erosion ionization introduced by ion imaging using FIB (Figure 5A). The combination of charge sensitivity and high topographic contrast is convenient to spot cells on a frozen hydrated cell-seeded grid (Figure 5B). A field of view of 2.8 x 2.1 mm using sub µm pixel size is suitable to image the entire surface of the grid using a fine enough pixel size to precisely sample cells and distinguish carbon holes to select the best region for milling lamellae.

To the best of our knowledge, this type of cell imaging has not been demonstrated to date, as the majority of instruments used for cryo-FIB milling are equipped with less advanced optics and lack an In-Lens detector. The ability to directly visualize cell contours before initiating milling provides a significant advantage, enabling precise targeting of lamellae to select the most suitable regions for tomographic data acquisition, particularly within nuclei. We are currently exploring the integration of In-Lens imaging for rapid localization of target cells in combination with cryo-fluorescence imaging. This workflow, which can be performed after plunge-freezing, holds great potential for enhancing the efficiency and accuracy of cryo-FIB milling.

I also observed that In-Lens imaging is sensitive to ice roughness (Figure 5C). While we currently lack an explanation for how charge accumulation is linked to ice crystal size, this sensitivity offers a fast and convenient method for assessing the freezing quality of samples.

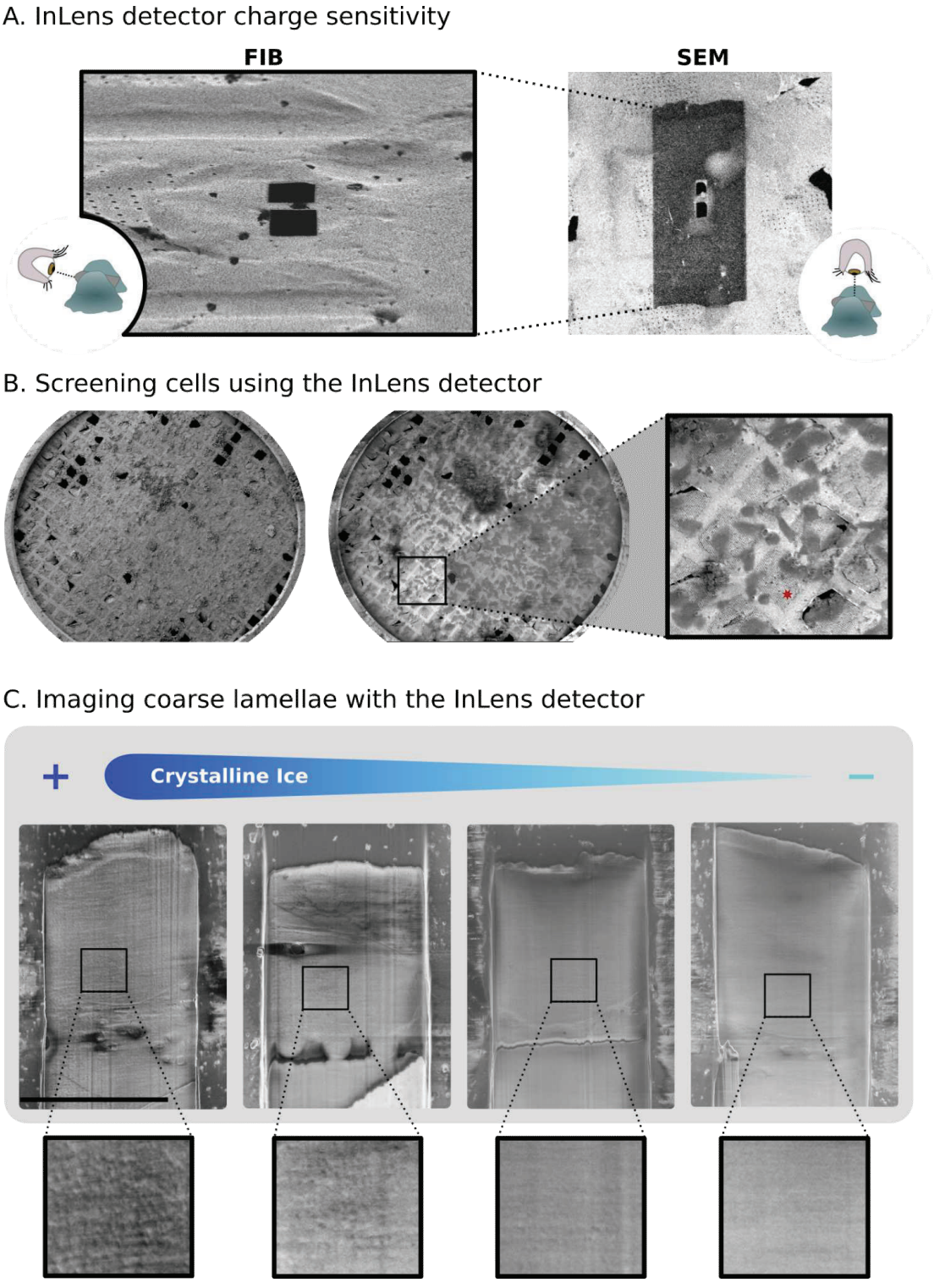


**Figure 5.** InLens detector available in Auriga 60 provides us with useful options for cryo-sample analysis while cryo-FIB lamella fabrication. (A) InLens detector visualizes surface charges (rSEM) remaining after a short image taken using gallium ion beam (FIB). The eye icon indicates the orientation of the FIB and SEM imaging.(B) Visualization of the cells contours by In-Lens detector. (C) Detection of the polycrystalline ice roughness by In-Lens detector.

**1.5.4 Waffle method.** In this method, a cell pellet is applied directly on the EM grid and allowed to fill the volume between the grid bars before being high pressure frozen (Kelley et al., 2022). I tried to deploy this method quite early in the workflow using the Leica EM PACT2 high pressure freezer. This apparatus is designed to freeze biological material within copper tubes or deposited on flat specimen carriers of 2.8 mm diameters (Figure 6A). To get the best cooling properties, I used thin 1.45 mm diameter membrane carriers with 0.1 mm cavity and 0.16 mm of total thickness. The membrane carriers were coated using 0.5% phosphatidylcholine diluted in chloroform. The carbon coated EM grids were razor cut to a rectangle with semicircles on the opposite width sides looking like a racetrack shape (Figure 6). These cuts were needed to fit the EM grid on the EM PACT 2 insertion tool that was engineered to load 2.8 mm diameter specimen carriers, smaller than the 3.05 mm diameter commercial EM grid. The racetrack shaped EM grid prepared with cell pellets is then mounted between the two flat faces of fatty membrane carriers constituting a sandwich loading onto the EM PACT 2 and high pressure frozen. The high pressure frozen sandwich is easily dismantled in liquid nitrogen thanks to the fatty properties of the coated membrane carriers where the EM grid is recovered, clipped and stored.

The vitrified suspension of cells in this setup has the thickness of 100 µm. To obtain the reliable vitrification the cells 10% of dextran 40 kDa and 10% BSA were added. The vitrified pellet appears as a pill on the grid surface (Figure 6B). The thickness of the sample was too high to make proper lamellae, but I successfully created initial trenches (Figure 6B). Imaging the block faces of these trenches revealed recognizable structural features of the cells, including nuclei (Figure 6B).

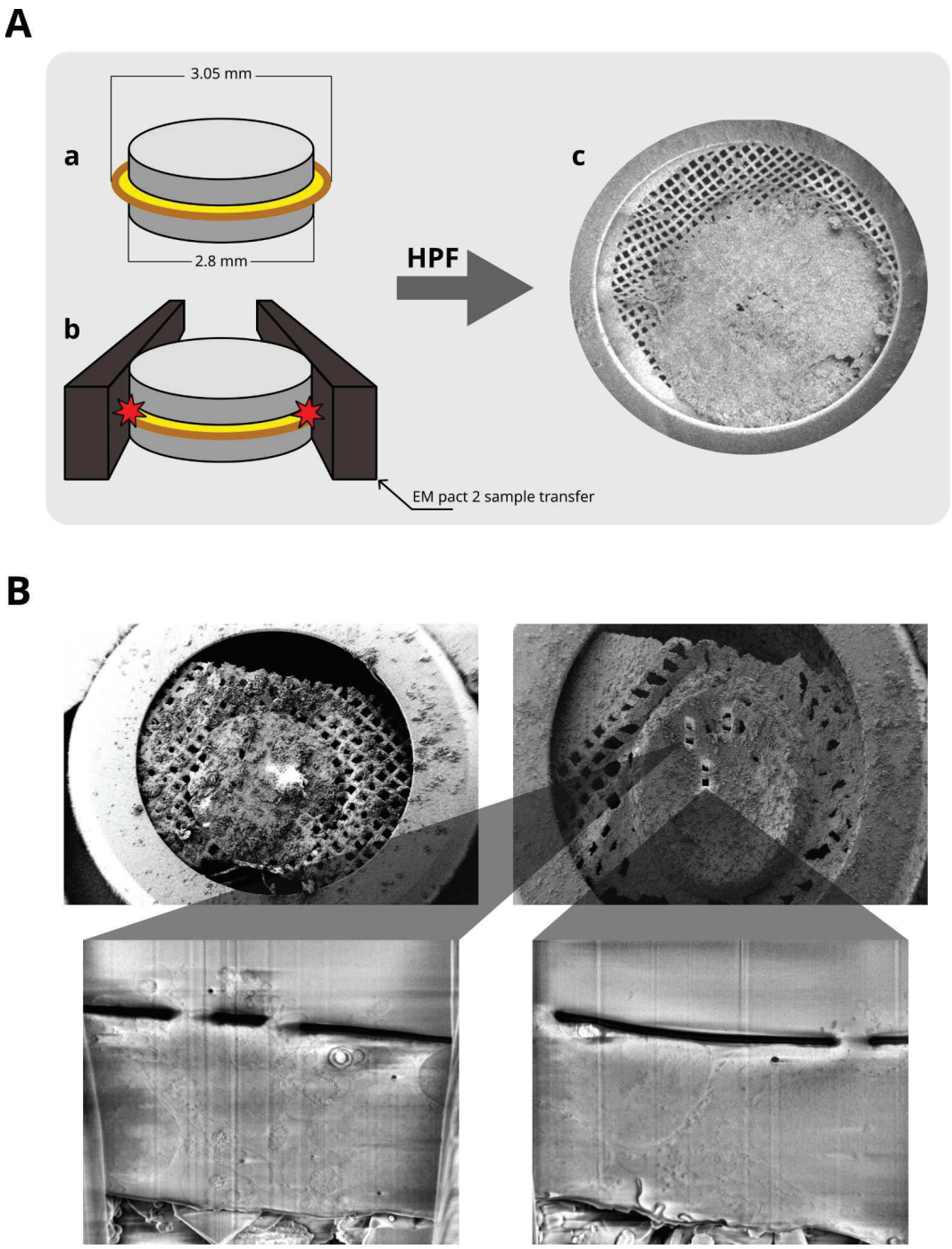


**Figure 6.** Firsts waffles attempts using the Leica EM PACT 2 HPF. (A) Illustration of a fitting problem between the small Leica EM PACT 2 specimen carriers and classical 3.05 mm EM grids. (A.a) Representation of the montage required to perform waffle HPF using Leica EM PACT 2 specimen carriers. These carriers, represented in grey, are 2.8 mm in diameter but classical EM grids, represented in yellow, are 3.05 mm and they protrude out of the waffle montage leaving the grid edge prone to deformations. (Ab) The loading of samples for high pressure freezing into the EM pact 2 using the Rapid Transfer System (RTS) requires the waffles to be mounted on a specific loading tool with a special forceps tip represented by brown bars. The EM grids protrusions out of the waffles are squished by the loading system tip, represented by red stars, leading to deformations that are visible in the SEM scan displayed in (Ac) which highlight a badly warped grid that encountered the problems illustrated in **A.a** and **A.b**. (B) First cellular features imaged on HPF waffles. To reduce the problems induced by the difference of diameter between the EM grid and the specimen carriers, the EM grid was cut out using a razor blades and placed in the waffle montage in a way that the Leica EM PACT 2 loading system can grip to the specimen carriers without entering in contact with any EM grid protrusions, thus reducing deformations. The results of this manipulation is visible in the (B top row), where the razor blades cuts in the EM grids are visible as well as the HPF frozen cell pellet forming a thick disk in the middle. (B bottom row) Cellular features imaged on block faces milled out of the waffles.

When the HPM-010 high pressure freezing apparatus became available, I performed a second round of experiments. Three different coating materials were compared. 0.5 % soja lecithin, phosphatidylcholine and paraffin. The paraffin showed the highest hydrophobicity properties in such a way that it was very difficult to have the EM grid stay on the flat coated surface of the specimens carriers. Both soja lecithin and phosphatidylcholine showed a visually similar relative hydrophobicity with the EM grid staying on the coated surface. Once high pressure frozen, paraffin coated sandwiches opened very easily where soja lecithin and phosphatidylcholine-coated sandwiches were slightly more difficult but overall were easy enough. We decided to move forward using soja lecithin and phosphatidylcholine coated specimen carriers as their respective high pressure sandwiches were easier to assemble.

After high-pressure freezing the sandwiches usually disassemble spontaneously when removed from the freezing tip of the machine (Figure 7). The waffle grids immediately got covered with ice contamination likely because of electrostatic effects (Figure 7A). I found that this contamination can be efficiently removed when the waffle is transferred into cryo-FIB-SEM. The entire sample surface can be cleaned by rapidly browsing over it with a 2 or 4 nA FIB probe (Figure 7Ba,Bb). This quick FIB pass minimally damages the waffle's surface while effectively removing ice balls contamination through the "ion wind" effect, similar to how ionizers repel contamination in cryo-ultramicrotomy. This likely happens because of the charging effects created by the ion beam (see Figure 5A). In agreement with this hypothesis, ice balls remain above the conductive grid bars.

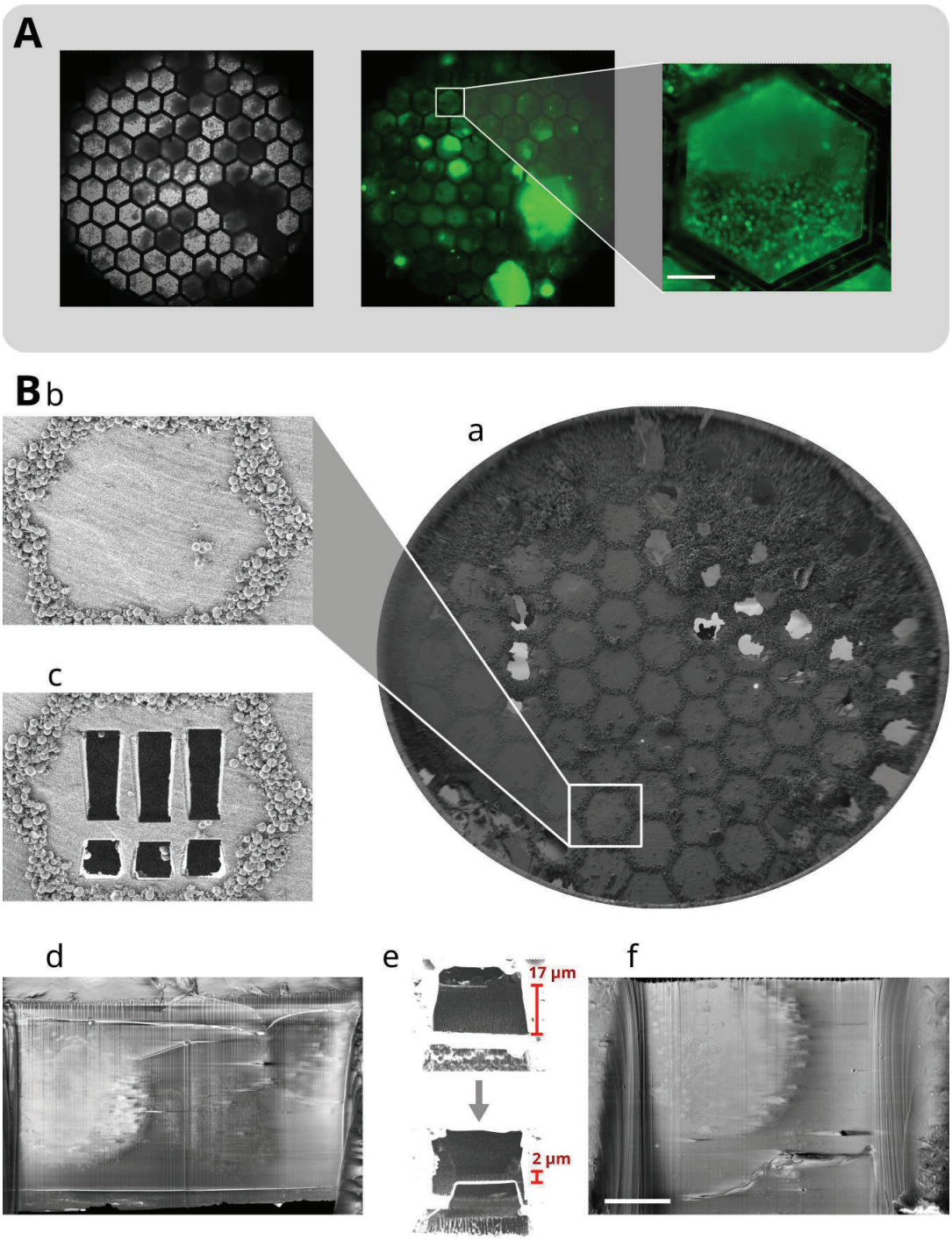


**Figure 7.** In house deployment of the waffle methods with cryo milling optimization. (A) Light microscopy images of “waffles” taken by the Leica cryo CLEM microscope. To prepare the "waffle," a gold 100-hexagonal mesh EM grid was coated with a thin Formvar film, produced in-house using a ready-to-use solution of Formvar diluted in ethylene dichloride. A pellet of trypsinized U2OS cells expressing H2B-GFP was then deposited onto the EM grid from the grid bar side, filling all available spaces until saturation. The grid was sandwiched between two phosphatidyl-coated hydrophilic Type B carriers, with the flat sides of the carriers enclosing the grid. This configuration, referred to as a "waffle," was subsequently high-pressure frozen using an HPM010 high-pressure freezing apparatus.The left image represents a bright field montage of the surface of the waffled grid after spontaneous disassembly of the sandwich. The large untransparent regions are clamps of ice contamination. The middle image shows a montage showing GFP fluorescence. The right image shows a magnified view of GFP fluorescence. Cell nuclei are round because of cell trypsinization. Scale bar 50 µm. (B) Procedure of lamellae production from waffled samples, optimized for our instrument. (Ba) SEM overview of the "waffle,"

prepared from a 3T3 MEF pellet on a 100-hexagonal mesh gold EM grid coated with Formvar. Before acquiring the scan, the entire sample surface was cleaned by rapidly browsing over it with a 2 or 4 nA FIB probe. (Bb) Magnified grid's hexagone, where the ice balls were removed, and preparatory milling was done for 3 regions of interest (Bc). The exclamation-like shape of the milled areas were drawn on purpose as we need to remove the material as deep to see the complete thickness of the vitrified sample. It is done before starting lamella milling after turning the block at 14 or 16° from the surface. It has to be noticed that the exclamation-like shape is not made of a rectangle and a square but from two trapeziums with the slope compensating for redeposition in order not to obstruct the milling window for the lamella. (Bd) Block face scan of one of the three regions of interest using the In-Lens detector in order to screen its surface content. A cell in good condition is present on the left with great contrast; we can distinguish its nucleus and its cytoplasm, membrane-like features from potent degraded cells are present in the middle and a potential third cell is visible on the top right of the block face. (Be) The sample surface is placed at 14 or 16 ° compared to the FIB beam in order to mill a coarse lamella through the desired block face. The upper image shows the complete waffle thickness (17 µm) before starting lamella shaping. The lower one shows a coarse lamella of 2 µm thickness. (Bf) A SEM scan of the surface of the coarse lamella using the In-Lens detector in order to screen its content to decide whether or not it is worthy to move toward further lamella thinning and polishing steps.

We were unable to obtain thinner lamellae on our instrument, as the subsequent mamella thickness refining steps often resulted in lamellae loss. The destressing patterns shown in (Kelley et al., 2022) might be essential but were not tried yet. The inability to obtain thinner lamellae on our instrument may also result from the absence of a block face coating or sputtering, which would enhance smoothness and conductivity. Without this, the repeated exposure of the block face to ion beams during lamella polishing steps could negatively affect the integrity of the final lamella. During my visit to eBIC to attempt milling lamellae from waffled specimens, I had an insightful conversation with James Gilchrist. We hypothesized that additional in-chamber sputtering after coarse lamella milling could positively impact later polishing steps. Unfortunately, our current system lacks the capability to perform this safely for the sample.

We could obtain several lamelas from the waffled samples in eBIC. It was not possible to target milling by built in fluorescence in their instrument, therefore we have to place lamellas blindly. They show complete vitrification, but unfortunately did not contain intact cells (Figure 8). We could only identify multilamellar structures likely from phosphatidylcholine-coating of carriers (Figure 8B). In this context, it has to be emphasised that lamella milling in waffled samples differs from well established approaches developed for plunge-frozen samples. In case of waffles, the initial milling has to be done from the top of the block face (Figure 6Be, bright trench) rather than from the width of the block face (Figure 6Be, darker trench), which was the approach attempted here. A 14° or 16° lamella made from the top or even the corner of the block face rarely reaches the nucleus, often capturing only its periphery. To increase the likelihood of milling lamellae that include the nucleus in waffled samples, we need to develop a strategy that targets the milling to the "meat" of the block rather than limiting the milling at its surface.

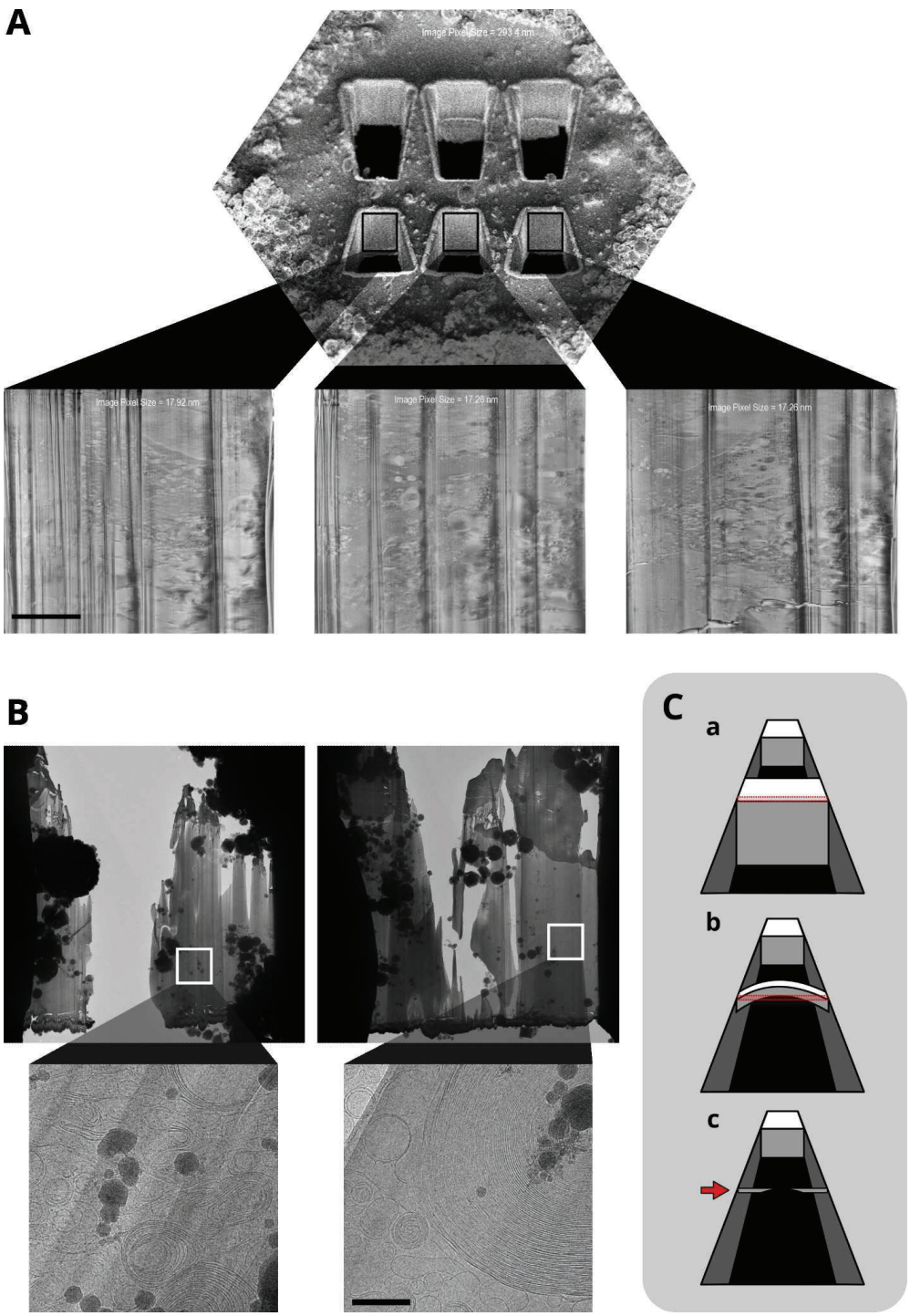


**Figure 8.** Milling of waffles at IGBMC and at eBIC. (A) SEM screening of milled block face from a waffle sample made with HPM-010 as for Figure 7. (A) top : 3 block faces milled out of a waffle sample in a hexagon of 100 hexagonal mesh EM gold grids. (A bottom left to bottom right) Magnified scans of each block face displaying a high membrane-like and vesicle-like complexity. In the top left corner of the (A bottom right) image, cellular-like features with a potent nucleus surrounded by membranes and vesicles without any distinguishable cytoplasmic membrane. The scale bar represents 5 µm. (B) TEM montages of waffle's lamella leftovers. The waffles here are duplicates of samples shown in (A). (B top row) TEM montage of damaged lamella milled from the top of the blockface (see C). (B bottom row) magnification of lamella areas showing multilamellar structures. (C) schematics showing stress related bending effect of lamella upon thinning that leads to damage in their central area. (Ca) : 3D perspective schematics of a waffle's block face with the targeted final thin lamella shown highlighted by a dotted red square. (Cb) Bending of the block face as it gets thinner upon milling before it reaches the desired width highlighted by a dotted red square. (Cc) Bending effects are so deforming that the milling procedures chop away the central section that moved outwards of the final preserved lamella region leading to lamella amputated from its central region with milling artefacts on what remains (see also B top row).

**1.5.5 Visualization of the labeling of Au•NLS Conjugate in cryo-lamellas.** U2OS cells electroporated with Au•NLS conjugates using M.V. protocol. A major part of cell suspension was seeded on EM grid, whereas a small part of the suspension was seed to cover slips for evaluation of the electroporation efficiency. Silver enhancement controls confirmed that the probe is present in the nucleus. The cell adherent to EM grids were cryo-immobilized by plunging into liquid ethane and thinned into lamellae by cryo FIB-SEM. The tilt-series recorded at different places in different lamellas and samples can be used to assess the freezing quality. The tomograms reconstructed from the tilted series allowed me to identify objects with the most intense contrast between 2 and 3 nm in diameter (Figure 9A). I identified these objects as Au•NLS probes. Vesicles, organelles, the nuclear envelope with nuclear pores are recognizable from the raw images. Denoising the tomograms using approaches like neural network based architectures eases the identification of certain proteins by eye, such as ribosomes, nucleosomes, and proteasomes. Gold particles remain visible even after denoising, but become more difficult to distinguish, because the contrast of biological molecules is amplified (Figure 9B). The projection of the standard deviation of each row of pixels along the Z-axis of a tomogram highlights the extreme grayscale values of pixels in those rows. Such projections allowed me to easily identify the presence and localization of gold particles in the xy-plane (Figure 9C). The particles are indeed present in the nucleus of electroporated cells and more rarely in the cytoplasm near the nuclear border.

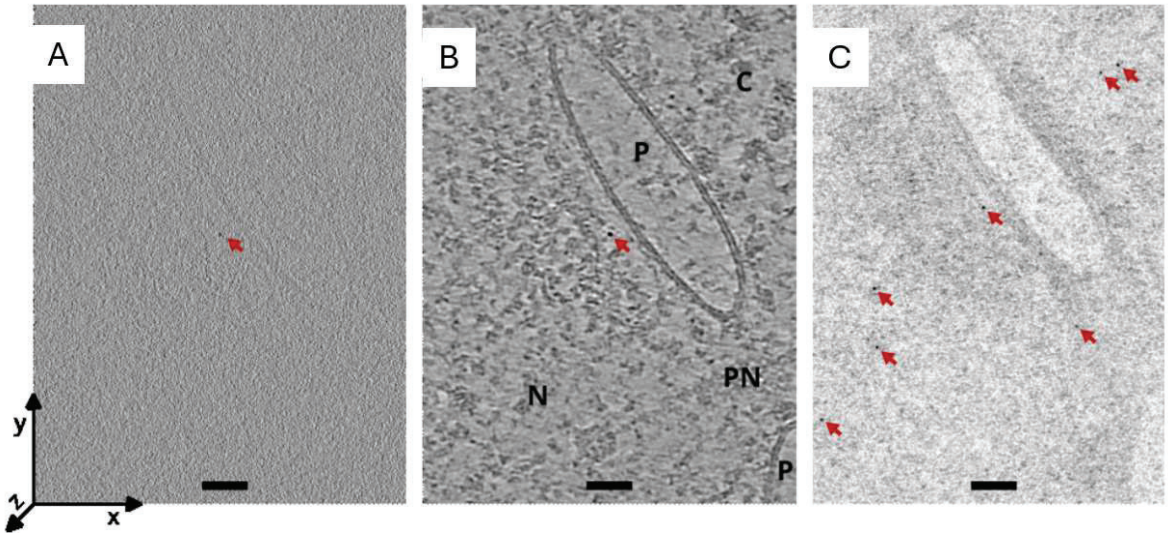


**Figure 9.** (A) Raw central slice of a tomogram showing the nuclear periphery of a U2OS cell nucleus electroporated with the Au•NLS probe. (B) The same slice after denoising with cryoCARE. d : A projection of the raw reconstruction from which the slice is derived, along the Z-axis, using ImageJ standard deviation z-projection command (https://imagej.net/software/fiji/). It calculates the standard deviation of pixel intensities along each Z column of voxels. Notice that the gold particle (red arrow) is readily identifiable in (A), but becomes more challenging to distinguish from other structures after denoising. The standard deviation projection, however, highlights the overall distribution of nanogold within the volume, revealing a higher concentration of particles in the nucleus compared to the cytoplasm. PN: nuclear pore, P: nuclear membrane, C: cytoplasm, N: nucleus, red arrows : AU•NLS conjugates. The scale bars represent 100 nm distance.

# Bibliography


Bäuerlein, F.J.B., Renner, M., Chami, D.E., Lehnart, S.E., Pastor-Pareja, J.C., Fernández-Busnadiego, R., 2021. Cryo-electron tomography of large biological specimens vitrified by plunge freezing. https://doi.org/10.1101/2021.04.14.437159

Desplancq, D., Groysbeck, N., Chiper, M., Weiss, E., Frisch, B., Strub, J.-M., Cianferani, S., Zafeiratos, S., Moeglin, E., Holy, X., Favier, A.L., De Carlo, S., Schultz, P., Spehner, D., Zuber, G., 2018. Cytosolic Diffusion and Peptide-Assisted Nuclear Shuttling of Peptide-Substituted Circa 102 Gold Atom Nanoclusters in Living Cells. ACS Appl. Nano Mater. 1, 4236–4246. https://doi.org/10.1021/acsanm.8b00988

Freund, G., Sibler, A.-P., Desplancq, D., Oulad-Abdelghani, M., Vigneron, M., Gannon, J., Van Regenmortel, M.H., Weiss, E., 2013. Targeting endogenous nuclear antigens by electrotransfer of monoclonal antibodies in living cells. mAbs 5, 518–522. https://doi.org/10.4161/mabs.25084

Groysbeck, N., Donzeau, M., Stoessel, A., Haeberle, A.-M., Ory, S., Spehner, D., Schultz, P., Ersen, O., Bahri, M., Ihiawakrim, D., Zuber, G., 2021. Gold labeling of a green fluorescent protein (GFP)-tag inside cells using recombinant nanobodies conjugated to 2.4 nm thiolate-coated gold nanoparticles. Nanoscale Adv. 3, 6940–6948. https://doi.org/10.1039/d1na00256b

Groysbeck, N., Hanss, V., Donzeau, M., Strub, J.-M., Cianférani, S., Spehner, D., Bahri, M., Ersen, O., Eltsov, M., Schultz, P., Zuber, G., 2023. Bioactivated and PEG-Protected Circa 2 nm Gold Nanoparticles for in Cell labeling and Cryo-Electron Microscopy. Small Methods 7, 2300098. https://doi.org/10.1002/smtd.202300098

Groysbeck, N., Stoessel, A., Donzeau, M., Da Silva, E.C., Lehmann, M., Strub, J.-M., Cianferani, S., Dembélé, K., Zuber, G., 2019. Synthesis and biological evaluation of 2.4 nm thiolate-protected gold nanoparticles conjugated to Cetuximab for targeting glioblastoma cancer cells via the EGFR. Nanotechnology 30, 184005. https://doi.org/10.1088/1361-6528/aaff0a

Iancu, C.V., Tivol, W.F., Schooler, J.B., Dias, D.P., Henderson, G.P., Murphy, G.E., Wright, E.R., Li, Z., Yu, Z., Briegel, A., Gan, L., He, Y., Jensen, G.J., 2006. Electron cryotomography sample preparation using the Vitrobot. Nat. Protoc. 1, 2813–2819. https://doi.org/10.1038/nprot.2006.432

Jinek, M., Chylinski, K., Fonfara, I., Hauer, M., Doudna, J.A., Charpentier, E., 2012. A Programmable Dual-RNA–Guided DNA Endonuclease in Adaptive Bacterial Immunity. Science 337, 816–821. https://doi.org/10.1126/science.1225829

Juncker, T., Chatton, B., Donzeau, M., 2023. The Prodigious Potential of mRNA Electrotransfer as a Substitute to Conventional DNA-Based Transient Transfection. Cells 12, 1591. https://doi.org/10.3390/cells12121591

Keeble, A.H., Turkki, P., Stokes, S., Khairil Anuar, I.N.A., Rahikainen, R., Hytönen, V.P., Howarth, M., 2019. Approaching infinite affinity through engineering of peptide-protein interaction. Proc. Natl. Acad. Sci. U. S. A. 201909653. https://doi.org/10.1073/pnas.1909653116

Kelley, K., Raczkowski, A.M., Klykov, O., Jaroenlak, P., Bobe, D., Kopylov, M., Eng, E.T., Bhabha, G., Potter, C.S., Carragher, B., Noble, A.J., 2022. Waffle Method: A general and flexible approach for improving throughput in FIB-milling. Nat. Commun. 13, 1857. https://doi.org/10.1038/s41467-022-29501-3

Kumagai, K., Sekiguchi, T., 2009. Sharing of secondary electrons by in-lens and out-lens detector in

low-voltage scanning electron microscope equipped with immersion lens. Ultramicroscopy 109, 368–372. https://doi.org/10.1016/j.ultramic.2009.01.005

Lam, V., Villa, E., 2021. Practical Approaches for Cryo-FIB Milling and Applications for Cellular Cryo-Electron Tomography, in: Gonen, T., Nannenga, B.L. (Eds.), cryoEM, Methods in Molecular Biology. Springer US, New York, NY, pp. 49–82. https://doi.org/10.1007/978-1-0716-0966-8_3

Levi-Kalisman, Y., Jadzinsky, P.D., Kalisman, N., Tsunoyama, H., Tsukuda, T., Bushnell, D.A., Kornberg, R.D., 2011. Synthesis and Characterization of Au102(p-MBA)44 Nanoparticles. J. Am. Chem. Soc. 133, 2976–2982. https://doi.org/10.1021/ja109131w

Lien, Y.-W., Amendola, D., Lee, K.S., Bartlau, N., Xu, J., Furusawa, G., Polz, M.F., Stocker, R., Weiss, G.L., Pilhofer, M., 2024. Mechanism of bacterial predation via ixotrophy. Science 386, eadp0614. https://doi.org/10.1126/science.adp0614

Mahamid, J., Pfeffer, S., Schaffer, M., Villa, E., Danev, R., Cuellar, L.K., Förster, F., Hyman, A.A., Plitzko, J.M., Baumeister, W., 2016. Visualizing the molecular sociology at the HeLa cell nuclear periphery. Science 351, 969–972. https://doi.org/10.1126/science.aad8857

Makaraviciute, A., Jackson, C.D., Millner, P.A., Ramanaviciene, A., 2016. Considerations in producing preferentially reduced half-antibody fragments. J. Immunol. Methods 429, 50–56. https://doi.org/10.1016/j.jim.2016.01.001

Orlov, I., Schertel, A., Zuber, G., Klaholz, B., Drillien, R., Weiss, E., Schultz, P., Spehner, D., 2015. Live cell immunogold labeling of RNA polymerase II. Sci. Rep. 5, 8324. https://doi.org/10.1038/srep08324

Vigneron, M., Dietsch, F., Bianchetti, L., Dejaegere, A., Nominé, Y., Cordonnier, A., Zuber, G., Chatton, B., Donzeau, M., 2019. Self-Associating Peptides for Modular Bifunctional Conjugation of Tetramer Macromolecules in Living Cells. Bioconjug. Chem. 30, 1734–1744. https://doi.org/10.1021/acs.bioconjchem.9b00276

Wagner, F.R., Watanabe, R., Schampers, R., Singh, D., Persoon, H., Schaffer, M., Fruhstorfer, P., Plitzko, J., Villa, E., 2020. Preparing samples from whole cells using focused-ion-beam milling for cryo-electron tomography. Nat. Protoc. 15, 2041–2070. https://doi.org/10.1038/s41596-020-0320-x

Zaborowska, J., Egloff, S., Murphy, S., 2016. The pol II CTD: new twists in the tail. Nat. Struct. Mol. Biol. 23, 771–777. https://doi.org/10.1038/nsmb.3285

Zakeri, B., Fierer, J.O., Celik, E., Chittock, E.C., Schwarz-Linek, U., Moy, V.T., Howarth, M., 2012. Peptide tag forming a rapid covalent bond to a protein, through engineering a bacterial adhesin. Proc. Natl. Acad. Sci. 109. https://doi.org/10.1073/pnas.1115485109

# Chapter II

# FIB-SEM imaging and sample processing deployment in CBI

Upon developing cryo-FIB-SEM milling for my project (see chapter I), I gained a unique expertise in handling the Instrument and became its most experienced user. I was in charge of the interaction with the service engineers of the manufacturer in case of failure and contributed to solving numerous technical problems. I was interested in implementing the imaging modalities of the instrument associated with the SEM part which allows for volumetric imaging of whole cells or tissues at nanometric resolution.

To visualize the 3D organization of whole cells and tissues at nanometric resolution, electron microscopy is an essential tool to grasp the whole cellular context, and not only the fluorescently labeled probe, thus providing images with a high information content. As discussed in the introduction, TEM provides an excellent x-y resolution but is limited by the thickness of resin cell sections which cannot exceed 100 nm. FIB-SEM bases volumetric imaging uses a focused ion beam to mill away a thin layer of the sample surface while the scanning electron beam is used to image the newly created block face (Kizilyaprak et al., 2014) with high and isotropic spatial resolution (5 nm) and over a depth of several tenths of micrometers. FIB-SEM observations were performed using a dedicated instrument installed at the IGBMC (Auriga 60, Carl Zeiss Microscopy GmbH).

The volumetric imaging modes provide a wealth of information about the size, shape and distribution of all cellular components at the scale of whole cells and tissue sections up to 300 µm in thickness. In order to extract quantitative 3D information on each cell type in different physiological conditions cellular images need to be segmented and annotated; a laborious process which precludes the extraction of all available information and the full interpretation of the images. The Heitz (iCube, Strasbourg) and Schultz teams have developed dedicated segmentation algorithms based on deep neural networks for FIB-SEM images. These algorithms enable multiclass organelle segmentation (mitochondria, endoplasmic reticulum, outer cell membrane, cell nucleus, endosomes) with excellent accuracy (Meyer et al., 2021) provided that sufficient examples (i.e. manually delineated images) are available.

In this program, I contributed to volumetric data acquisition on a large number of specimens and normalized sample preparation methods to reduce image heterogeneity due to embedding or staining variations. I further contributed to the implementation and testing of the DeepSCEM program, a user-friendly application that allows training of a deep learning model on electron microscopy images.

These developments have a large number of applications and we expect that several IGBMC research teams in the institute will benefit from the possibility to record volumetric cellular images and to extract quantitative information after organelle segmentation.

## 1.1 Volumetric Imaging of resin-embedded samples

In collaboration with the team of Fabien Alpy (IGBMC) and the group of Benoit Naegel and Etienne Baudrier (iCube, Strasbourg), the Schultz team aims at setting up a workflow for the quantitative interpretation of volumetric information. The advent of FIB-SEM imaging techniques has enabled nanometric spatial resolution image acquisition – including volumetric information on whole cells or tissue – and resulted in very large datasets with high information content. The dynamic behavior, the morphological parameters and the intracellular distribution of organelles (membrane-bound cell compartments) can now be studied quantitatively and can be time-resolved by recording snapshots of any process of interest. However, the size and complexity of these data sets makes a complete manual annotation of all data not feasible, and our consortium developed a U-Net based architecture and obtained very good performance in supervised segmentation tasks.

Our objective was to quantitate morphological changes in a defined cellular system that can be perturbed to assess statistically significant changes in the three-dimensional (3D) organization, interactions and dynamics of organelles visualized at high spatial resolution by FIB-SEM imaging. We mostly focused on the endosomal and lysosomal compartments for which Fabien Alpy has gathered preliminary 2D results. The lysosome is considered as the degradation and recycling center of the cell and is also involved in food uptake and in responses against bacteria, viruses and other antigens. This compartment is highly dynamic and interacts with the secretion or endosomal pathway, thus leading to a large variability of vesicle morphologies associated with specific functions.

Inter-organelle membrane contacts sites (MCSs) are specific subcellular regions favoring the exchange of metabolites and information. Dr Alpi is investigating the potential role of the late-endosomal membrane-anchored proteins StAR related lipid transfer domain-3 (STARD3) and STARD3 N-terminal like (STARD3NL) in the formation of MCSs involving late-endosomes (LEs) (Wilhelm et al., 2017, p. 3). His team demonstrated that both STARD3 and STARD3NL create MCSs between LEs and the endoplasmic reticulum (ER). STARD3 and STARD3NL use conserved two phenylalanines in an acidic tract (FFAT)-motif to interact with ER-anchored VAP proteins.

Together, they form an LE–ER tethering complex allowing heterologous membrane apposition (Alpy et al., 2013). This LE–ER tethering complex affects organelle dynamics by altering the formation of endosomal tubules.

As a proof of concept, our consortium aimed to record a small number of volumetric datasets of HeLa cells in wild type conditions, after expression of a mutated version of the STARD3 protein and after overexpression of STARD3. The objective is to extract volumetric information and morphological parameters.

## 1.2 Resin sample evaluation and imaging set up for nanotomography

The whole FIB-SEM acquisition workflow leads to a high image variability. Variation in cell states, preparation protocols including fixatives, contrasting agents and resins, and acquisition conditions on the FIB-SEM instrument result in different organelle appearance which renders their automated analysis more complex. As a result of this variability our automated segmentation tests showed that the currently available U-net architectures fail when trained on a given FIB-SEM database and applied on images from another laboratory.

My task was to assess structural preservation of embedded samples and to optimize image acquisition conditions to reduce image variability and optimize image contrast (see Supplementary Materials and Methods for details). The samples I have screened and evaluated consisted of Hela cells grown on sapphire discs, high pressure frozen to preserve the structural integrity of the cell and cryo-substituted to reveal the detailed structure of cellular organelles.

## 1.3 Publication 3

The goal of this project was to develop a user-friendly tool for segmenting volumetric data from resin-embedded samples. The tool uses supervised training of a deep learning model, which can be easily set up and validated by biologists without programming skills through a graphical user interface. My role involved (i) beta testing the software using FIB-SEM stacks I recorded under different conditions, (ii) creating a manual segmentation training dataset to evaluate the training process, and (iii) conducting various tests and providing feedback to the lead author/developer to troubleshoot and optimize initial versions. The manuscript has been submitted for peer review to a special edition of Biology of the Cell focused on Emerging Methods in Microscopy Data Processing for Life Sciences.

The experimental procedures and results are described in detail in the following manuscript, submitted to revisions.

# DeepSCEM : A User-Friendly Solution for Deep Learning-Based Image Segmentation in Cellular Electron Microscopy

## Running title

Deep Learning-based image segmentation

Cyril Meyer[1], Victor Hanss[3], Etienne Baudrier[2], Benoît Naegel[2], Patrick Schultz[3]

1. IRIMAS, Université de Haute-Alsace
2. ICube, UMR 7357 CNRS
3. IGBMC, Université de Strasbourg, CNRS, Inserm, IGBMC *UMR 7104- UMR-S 1258, 67400 Illkirch, France*

## Abstract

Deep learning methods using convolutional neural networks are very effective for automatic image segmentation tasks with no exception for cellular electron micrographs. However, the lack of dedicated easy-to-use tools largely reduces the widespread use of these techniques. Here we present DeepSCEM, a straightforward tool for fast and efficient segmentation of cellular electron microscopy images using deep learning with a special focus on efficient and user-friendly generation and training of models for organelle segmentation.

## Keywords

software, segmentation, deep learning, electron microscopy, cellular imaging, organelles

## Introduction

The internal organization of the cell into membrane bound compartments defines functional domains named organelles whose number, distribution, shape and mode of interaction reflect the cellular identity and its pathophysiologic state. The morphological description of organelles benefits from the high spatial resolution of electron microscopes that oversteps Abbe's diffraction limit of standard light microscopes. Early transmission electron microscopy (TEM) observations of cellular structures were essentially two-dimensional (2D) projections of ~ 100 nm thin resin-embedded cellular slices that lacked volumetric information. Stereological methods were first used to extrapolate 2D measurements to the whole cellular volume (Weibel et al., 1966), but these predictions were limited by the complex shape and uneven distribution of organelles. To reach 3D information on whole cells or tissues, serial sectioning protocols were developed to image successive physical slices of the sample, but this approach is technically very demanding and suffers from section distortions (Williams & Kallman, 1955). In electron tomography the specimen is discretely tilted over a range of angles in the microscope to record multiple views that can be back projected into a high resolution tomographic

reconstruction. This method is limited to 500 nm thick sections, but may be combined with serial sectioning to reach larger volumes.

Advances in Scanning Electron Microscopy (SEM) enabled rapid imaging of resin-embedded thick specimens at nanometric scale. Three-dimensional information was first achieved by sequentially removing the top slice with an ultramicrotome fitted in a SEM chamber and repeatedly imaging the new block face (serial block face, SFB-SEM) (Leighton, 1981). The top slices can be removed in finer increments using focused gallium ion beam (FIB) milling thus leading to FIB-SEM tomography (Heymann et al., 2006). FIB-SEM imaging enables recording high-resolution 5x5x5 nm isotropic images on 40 x 40 µm large image areas and over a depth of several tenths of micrometers (Narayan et al., 2014; Wei et al., 2012) and has become a powerful tool to obtain undistorted volume information (Bosch et al., 2015; Cretoiu et al., 2015).

The morphological parameters and intracellular distribution of organelles can now be studied quantitatively on large portions of cells or on whole tissue. However, image interpretation requires a segmentation step to annotate the cellular compartments and organelles in order to extract quantitative information such as size, distribution, interactions and morphology from these delimited regions. A human expert can identify and annotate these cellular domains interactively, but this task is very tedious and may take several days for each cell. In a context of massive datasets, the size and complexity of these image stacks prevents manual annotation, therefore biologists need computer-aided methods to identify and segment cellular organelles.

In the field of image analysis, the rise of deep learning approaches allowed us to develop U-Net based models with very good performance in supervised segmentation tasks (Meyer et al., 2021, 2023). These methods are now the standard to solve complex analyses of medical and biological images, in particular in the field of cellular electron microscopy (Heinrich et al., 2018; Ronneberger et al., 2015; Xiao et al., 2018). Deep learning based segmentation of cellular organelles for EM images has been applied to mitochondria, endoplasmic reticulum and other organelles on images with possible anisotropy. Recently, results were shared on the OpenOrganelle web repository on FIB-SEM images at 4 nm spatial resolution for over 35 organelles and macromolecular structures (Heinrich et al., 2021).

However, the use of supervised methods based on deep learning in the field of FIB-SEM imaging faces high image variability arising from the large diversity of cell lines, the various preparation protocols including different fixatives or cryo-preservation conditions and a large panel of contrasting agents and resins. Variations in the appearance, contrast and texture of organelles can further arise from FIB-SEM image acquisition conditions. Altogether, variations in organelle aspect affect the efficiency of their automated detection and analysis.

Our tests showed that the currently available U-net architectures are very powerful to predict organelle identity when the training and the prediction sets are generated in the same laboratory with the same protocoles, while they generally fail when trained on a given FIB-SEM database and applied on images from another laboratory. These observations led us to conclude that semi-automated segmentation is performed most efficiently when training and prediction are performed on a similar dataset which reduces image variability. As training of a U-net architecture is not straightforward, we developed and describe here the interactive DeepSCEM tool to train your own model on your own dataset. This tool accepts as entries a training dataset composed of a representative set of 2D slices of a volumetric dataset associated with annotated organelles or regions of interest. DeepSCEM will train a model that will be used to automatically segment any related volumetric datasets and produce annotated

segmentation files. An evaluation set composed of a few manually annotated sections can be used to evaluate the accuracy of the predictions qualitatively and quantitatively.

Existing tools, such as ilastik (Berg et al., 2019) or DeepMIB (Belevich & Jokitalo, 2021) already address the segmentation issue, but our program differs in several aspects. Firstly, DeepSCEM was designed to be very user-friendly especially for the evaluation of its performances by a non-expert user. It can be operated through a few clicks in a Windows environment thanks to a dedicated distribution of the software binaries. This means that DeepSCEM can be evaluated for a given problem in just a few hours by a non computer-expert. The second property of DeepSCEM is its modularity. Being written in Python and using the widely-used TensorFlow library, new models and parameters can be easily added, increasing the possibilities for more advanced users. For example, any TensorFlow model which has valid input and output shapes can be loaded, trained and used for prediction in DeepSCEM. The third property of the software lies in its performance. As our software is dedicated to the particular task of organelle segmentation, it has been optimized to perform this task. Thanks to its software architecture, DeepSCEM can be used with or without any graphical interface. This means that a specific process can easily be set up by system administrators.

# Results

In this section, a description of the DeepSCEM application and its usage is provided. We will first present the general workflow followed by examples of how the program is used, illustrated on a representative FIB-SEM image stack. More information about the imaging conditions and the tools used for initial image segmentation are available in the methods section.

## Workflow

In this subsection, we describe the general usage of DeepSCEM, for automated segmentation of cellular electron microscopy images. The process can be divided into five main steps (Fig. 1).

(i) A training image dataset is selected from the original image stack and the corresponding annotations need to be created. Annotation corresponds to a manual segmentation of the organelles in which image features that allow the recognition of a particular cellular ultrastructure are associated with the corresponding organelle class or instance. When analyzing a large 3D stack of several hundred images, the training set typically represents a few tens of images that should be representative of the different types of structures of interest, and should be large enough to train a robust neural network model. In order for the deep learning process to make a good prediction, the instance of interest must be present several times on several images. The accuracy of the prediction increases with the number of annotations, and weak or unsatisfactory predictions can be improved by increasing the number of the annotated instances. Annotations can be provided using software products like MIB (Belevich et al., 2016), ilastik (Berg et al., 2019) or any other tool that allows manual annotation of the images and generates binary images of the region of interest in TIF format.

(ii) A neural network model for segmentation is then created. DeepSCEM provides a model generator which, in the current version, can create 2D and 3D U-Net based models with various parameters including number of filters per layer, model depth and use of residual connections. By default, the program provides a standard neural network model, but users can

also create their own custom models using TensorFlow and load them directly into DeepSCEM.

(iii) The model is then trained on the annotated dataset to recognize the distinctive features of the object of interest. Briefly, small image patches are extracted within the annotated area to be used by the deep learning process using a loss function. The application allows the user to select the patch size, batch size, loss function and the number of steps to train the model.

(iv) The performance of the training model can be assessed quantitatively by using a separate set of manually segmented images. This validation dataset consists of a few images extracted from the 3D image stack. The aim of this step is to compare the segmentation performed by an expert, also called ground truth, with the predicted segmentation. Quantitative values using F1-score and intersection-over-union metrics can be used to prevent overfitting and to select the best-performing training model.

(v) The trained model can now be used to segment cellular images coming either from the remaining images of the same stack or from different image stacks.

DeepSCEM provides tools to visualize the results of the segmentation, allowing the user to make a quick qualitative evaluation.

## Examples

In this section, we present two case studies to illustrate the use of DeepSCEM to segment organelles in cellular electron microscopy images. All the data used for these examples and the exact results presented in this section are publicly available (Meyer, 2024a, 2024b; Meyer & Schultz, 2023). We present qualitative and quantitative results for different classes (organelles) to illustrate the accuracy of the implemented method.

**User case 1**: The aim of this first example is to train a model to automatically segment mitochondria in a 3D stack of 600 consecutive FIB/SEM images of a HeLa cell (see Material and Methods). The training set consists of 40 images in which mitochondria were manually segmented by contouring the external mitochondrial membrane using the MIB program that produced the annotation set as a separate TIF file for each annotated image where the inside of the mitochondria is marked with 1 and the outside with 0. This mask is used to extract image patches that are representative of the region of interest to be used for the training process. Alternatively, the mask may delineate only the contour of the ROI, or characteristic membrane-less textures. To start the training process, the training set and the corresponding annotation are first loaded using the DeepSCEM interface (Fig. 2). The number of slices annotated for training may vary according to the complexity of the object of interest, the noise level, or the abundance of the feature of interest.

The next step is to generate a starting model. For this experiment, we used the default U-Net architecture implemented in DeepSCEM which is a 2D U-Net with 32 filters in the first layers and residual connections. We use the Dice loss function for training during 64 epochs of 256 batches with a batch size of 8 (Fig. 3). In most cases these default values will produce a useful trained model, but these default values such as batch size, loss function or number of training steps can be modified to optimize the training model.

Then the starting model can be trained on the annotated dataset (Fig. 4). The program also provides opportunities for runtime data augmentation, modifications made to the original data during the training phase. In our case these corresponded to image rotations and flips. Within the annotated “mitochondria” region, representative and non-overlapping image patches that describe the texture and intrinsic features of this class of organelles are extracted and used in

the learning process. The patch size can be adapted to the object of interest, it should include as many characteristic features of the object, and as little surrounding noise, as possible.

To evaluate the performance of the trained model, a validation dataset has to be prepared. In this case we select and annotate the next 20 slices of the image stack to assess whether the model correctly predicts the presence of mitochondria. The validation set must contain the feature of interest and can be a selection of non-consecutive image patches representing the mitochondria in different conditions. Annotations must be provided by the experts as contoured mitochondria, and are loaded into DeepSCEM along with the validation set and the trained model (Fig. 5).

As a measure of predictive performance, we use the F1-score which is calculated from the precision and recall of the test, where the precision is the number of true positives divided by the number predicted positives and the recall is the number of predicted positives divided by the number of all positives. The intersection-over-union (IOU) metrics can also be used to measure how well pixels predicted to be mitochondria align with the ground truth.In the case of mitochondria, the predictions are of high quality (F1 score of 0.950) and the trained model is close to optimal.

Further optimization can be performed by changing parameters in DeepSCEM such as (i) the size of the patch that holds the characteristic features of the ROI; they can be changed to include more information or less noise, (ii) the type of loss function used during the training process and (iii) the number of iterations of the learning process. In the case of mitochondria segmentation, the effect of changing these parameters had negligible effects on the prediction score (data not shown). Changing the operator who annotates manually the validation dataset, which defines the “ground truth”, had similar effects on the prediction score suggesting that the difference between ground truth and prediction are within interpretation errors.

The last step is to apply the trained model to the remaining 560 images of the stack. One has to enter the prediction mode of DeepSCEM, select the trained model to be used and load the stack of images on which a segmentation prediction is to be performed. If such a prediction is made on images that have already been annotated, such as a validation set, a test score can be computed to compare the manual annotation with the prediction. To do this, the evaluation mode has to be entered to select the images to be compared which then allows to compute the F1-score.

**User case 2**: The aim of this second example is to train a model to automatically segment multiple organelles in the same 3D stack. The training set consisted of 40 images where each organelle was segmented separately resulting in a different mask file for each organelle and for each annotated image (Fig. 6A). Mitochondria were segmented as described above, and endoplasmic reticulum (ER) as well as endo-lysosomes were annotated in the training set. In addition, we also annotated the external cell membrane (plasma membrane) which separates the cell boundary from the external matrix. In this case only the cell contour appeared in the mask as a continuous line whose width was three times the size of the membrane.

In order to train a model for multiple objects the number of labels has to be set accordingly. In the DeepSCEM environment, labels correspond to segmented masks of the objects of interest. Each mask as well as the raw images are loaded separately, listed in the DeepSCEM “Dataset” section and organized as a sample. A new model is generated as for user case 1.

When the model is trained with two classes, mitochondria and ER, using default parameters and a patch size of 256x256, the prediction score for mitochondria remains similarly high (F1-score of 0.951) while ER is less accurately predicted (F1-score of 0.709)(Fig. 5B and C). This reflects the lower detection limit of the organelle boundaries even for a trained expert. Indeed,

two independent experts perform only slightly better and their compared annotation yields a F1-score of 0.751. Changing the patch size to 512x(&é slightly degrades the F1 score for both organelles (0.947 for mitochondria and 0.691 for ER) possibly because including more contextual information adds more noise than signal. We also trained the model with three classes, namely mitochondria, endosomes and plasma membrane which yielded F1 values of 0.966, 0.836 and 0.740, respectively. The relatively poor score for endosomes may be related to their pleiotropic shapes and internal organization. A larger training set representing the whole variability in shape and textures is likely to provide better predictions.

# Conclusion

Here we describe DeepSCEM, a new tool to train a deep learning model for automatic segmentation of volumetric electron microscopy images. This tool was illustrated by FIB/SEM images for Hela cells but can be adapted to any kind of cellular or tissue system as well as for other modalities for volumetric images such as block phase SEM images or serial sectioning. The trained model can be further used to predict segmentations for image stacks of similar cell types and preparation conditions. More expert transfer learning approaches will be developed in the future to overcome the prediction failure when the cells are very different or are prepared with different staining or fixation conditions. Considering the limited time required to train a model, it may be possible to overcome this limitation by calculating a dedicated model for each preparation condition.

DeepSCEM is intended to be evolutive and to be extended to comply with state of the art deep learning architectures, computing of losses and additional options to optimize the deep learning models, but also to adapt to the diverse needs of future users. For this purpose, users are widely encouraged to contact the authors using the GitHub issue page in order to propose improvements to the software.

The program delivers predicted segmentations of cellular features that may be adapted to specific cell types or cellular features. These results can be loaded into volume-rendering tools to visualize the cellular architecture. More importantly the segmented areas provide quantitative information on key properties of the organelles such as their volume, their distribution or their interactions. These quantitative morphological values can be used to compare the cell state in normal or diseased states and, in case of known mutations, may provide molecular clues to the observed phenotypic variations.

# Materials and Methods

### Sample preparation

The sample consists of HeLa cells stably expressing the protein STARD3 (Wilhelm et al., 2017) and processed after high pressure freezing and freeze substitution. Hela cells were grown on carbon-coated sapphire disks in DMEM containing 10 percent Foetal Calf Serum before being high pressure frozen (HPM 10 Abra Fluid AG) in liquid nitrogen. The samples are then freeze-substituted (AFS, Leica) and embedded in Lowicryl HM20 as previously described (Spiegelhalter et al., 2010). The samples were dehydrated at -90°C for 9 h in dry acetone containing 0.25 percent uranyl acetate and 0.1 percent glutaraldehyde. Temperature was raised to -45°C over 18 hours with a slope of 2.5°C/h. The cells were then rinsed with acetone and infiltrated in 10 percent and 25 percent resin (Lowicryl HM20) for 2h each bath. When the

resin concentration reached 25 percent, the temperature was raised to -25°C and the resin concentration raised to 100 percent in three successive steps. The samples were then placed in 3 consecutive baths of pure resin lasting 8 h each before UV polymerization at -25°C for 48 h and warming to 20°C during 9 hours.

## Cellular electron microscopy

Focused Ion Beam (FIB) milling and Scanning Electron Microscopy (SEM) observations were performed using the Auriga 60 instrument (Carl Zeiss Microscopy GmbH, Oberkochen). For 3D reconstruction, 15 nm thick slices of the resin embedded sample were removed by FIB milling and the freshly exposed cross-section was imaged in a serial manner with a lateral pixel size of 7.5 nm. The analyzed image stack is 2048 by 1536 pixels in size corresponding to 15.3 by 11.5 µm and consists of 600 slices corresponding to a depth of 9 µm. For FIB milling the probe current was set to 2nA at 30kV acceleration potential. For noise reduction line averaging with line averaging count number N=11 and scan speed 4 was used. The resin block was glued on an aluminum stub using silver paint (Silver dag 1415, Plano GmbH, Wetzlar). First all side walls beside the block face were covered by silver paint and then the block face was sputter-coated with a few nanometer thick metal film to avoid resin charging. The SEM acceleration voltage was set to 1.5kV, the SEM aperture was 60 µm and high current mode was turned on. For SEM imaging the Energy selective Back-scattered electron (EsB) detector was used with a retarding EsB grid voltage of 1155 volts. The gray level scale was reversed in order to obtain a TEM like image contrast.

The complete data (images and annotation) are accessible on Zotero (Meyer & Schultz, 2023). The data is available for public research and noncommercial use, to access the data, users must request access to confirm those requirements.

## Annotations

Annotations have been generated using software products such as MIB (Belevich et al., 2016), ilastik (Berg et al., 2019) or any other tool which allows manual annotation of the images and generates binary images of the region of interest in TIF format. Closed regions of interest such as mitochondria, nuclei, endosomes, endoplasmic reticulum are segmented to encompass all pixels that are part of the structure. External cell membranes or nuclear membranes are segmented as continuous lines with a suitable line thickness. For the validation set, each instance has been interactively annotated by two experts in order to estimate the inter-expert decisional variation.

## Deep learning

*Hardware configuration*

The analysis shown here has been performed on a workstation equipped with 64 Go of RAM, a NVIDIA RTX 2080 Ti GPU and an Intel Xeon W-2135 CPU. Using this configuration, the average training time was 59 minutes, ranging between 2 hours for a large model containing 64 filters, instead of the standard 32, and less than 30 min for models containing 16 filters. The prediction time on a test set of 40 slices was 40s, but the prediction time for a stack of 600 images 2048 by 1536 pixels in size was 20 minutes. A total processing time of 1 hour is therefore to be expected, not counting the annotation time. DeepSCEM can also run on a less powerful hardware configuration but, in order to load large datasets and train bigger models, the amount of memory should be proportional to the dataset size and model parameters. Although not required, the GPU card significantly improves the computation time, especially for the training process.

*Architecture*

In the biomedical field, the most common architectures include U-Net (Ronneberger et al., 2015), DeepLab and its evolutions, DeepLabV3+ (Chen, Papandreou, et al., 2018; Chen, Zhu, et al., 2018). The U-Net architecture has quickly become popular as the model is easy to implement, and extend. The original article presents a high-performing network with a small amount of training data, thanks to data augmentation techniques. Also, as the model can be implemented as a fully convolutional neural network, its input and output shapes can be adapted to user prerequisites.

The U-Net uses the principle of an encoder-decoder architecture with long skip connections between the convolutional blocks of the same level. Many variants of the U-Net model have been proposed that modify the processing blocks (He et al., 2016a, 2016b) or the types of connections (Chaurasia & Culurciello, 2017). However, regardless of the variations proposed, the overall architecture remains the same: an encoder-decoder model with connections between the encoder and the decoder.

To give a simplified idea of how the elements of the model work together, it can be summarized as follows. The encoder extracts features from the input image. It consists of a series of convolutional blocks, each of which is composed of convolutional layers and various optional layers such as batch normalization (Ioffe & Szegedy, 2015). The number of filters in the convolutional layers is increased as the image is downsampled, allowing the network to capture more complex features. The decoder is responsible for generating the segmentation mask from the features extracted by the encoder. It is in essence the symmetry of the encoder, where downsampling is replaced by upsampling to generate a segmentation mask with the same resolution as the input image. The long skip connections are concatenations between the convolutional blocks of the same level in the encoder and in the decoder. These connections allow the network to preserve the spatial information and fine details of the input image to generate a more accurate segmentation mask.

The U-Net architecture can be easily parametrized to fit specific tasks. You can for example change the number of filters per layer, the depth (number of downsampling/upsampling steps in the encoder/decoder) or the processing blocks composition by adding residual connections or batch normalization layers. Those changes can allow us to create a very coarse model for a specific easy task, but also to create a very large and efficient model for a more complex task. The architecture can be used with either 2D or 3D processing blocks.

*Training*

Once we have a segmentation model, it is classically initialized with random weights and the model needs to be trained. In order to train a model, a dataset with images and their corresponding annotations are required. During the training phase, the model is presented with batches of images (patches) and their corresponding annotations. The loss function measures the difference between the predicted segmentation mask and the reference segmentation. The weights of the model are updated based on this difference using an optimization algorithm based on stochastic gradient descent, like Adam (Kingma & Ba, 2015). To improve the performance of the model, various techniques can be used during training, like data augmentation, which involves applying transformations to the images and annotations. Overfitting is a common issue in deep learning that can be simply explained as the model starting to memorize the training data instead of learning the underlying patterns. This can lead to poor performance on unseen data. To prevent overfitting, we use a validation set during training. The validation set is a subset of data that is not used for updating the weights of the model, but to monitor the performance of the model. The validation can be used to stop a training which is getting worse due to overfitting or divergence, but more importantly to select the best overall model on this validation set. The performance on the validation set can also be used to determine the best hyperparameters for training, such as learning rate, number of layers, batch size, etc.

After the model is trained, it can be used for automated segmentation of the images. We may further use a final image subset, the testing set which should not have been used for training or validation, to determine the performance of the model. If the model is only evaluated on the training and validation set, it may appear to perform well, but may not generalize well.

# Acknowledgement

We are grateful to Véronique Mallouh and Danièle Spehner for helpful discussions and manual annotations, and to Fabien Alpy for giving access to standardized resin-embedded samples. We acknowledge support from the Institut National de la Santé et de la Recherche Médicale (INSERM), the Centre National pour la Recherche Scientifique (CNRS), the Ligue contre le Cancer and to IGBMC (ANR-10-LABX-0030-INRT). This work of the Interdisciplinary Thematic Institute IMCBio+, as part of the ITI 2021-2028 program of the University of Strasbourg, CNRS and Inserm, was supported by IdEx Unistra (ANR-10-IDEX-0002), and by SFRI-STRAT'US project (ANR-20-SFRI-0012) and EUR IMCBio (ANR-17-EURE-0023) under the framework of the France 2030 Program. We acknowledge the use of resources of the French Infrastructure for Integrated Structural Biology FRISBI (ANR-10-INBS-0005) and of Instruct-ERIC.

# Conflict of Interest statement

The authors declare that they have no conflict of interest. Correspondence should be addressed to C.M. (cyril.meyer@uha.fr).

## Data and Code Availability Statement

The data presented and used in the example of the article are available on the Zenodo platform (Meyer & Schultz, 2023). The software and its source code is available on GitHub (https://github.com/Cyril-Meyer/DeepSCEM) and shared under MIT license. If you use our tool to perform automatic segmentation for your projects, please cite this paper as a reference of our work.

## Author roles

EB, BN and PS have designed the study and supervised the work, CM created the application, VH tested the application, PS and CM wrote the manuscript with inputs from all the authors.

## References


Belevich, I., Joensuu, M., Kumar, D., Vihinen, H., & Jokitalo, E. (2016). Microscopy Image Browser: A Platform for Segmentation and Analysis of Multidimensional Datasets. *PLOS Biology*, *14*(1), e1002340. https://doi.org/10.1371/journal.pbio.1002340

Belevich, I., & Jokitalo, E. (2021). DeepMIB: User-friendly and open-source software for training of deep learning network for biological image segmentation. *PLOS Computational Biology*, *17*(3), e1008374. https://doi.org/10.1371/journal.pcbi.1008374

Berg, S., Kutra, D., Kroeger, T., Straehle, C. N., Kausler, B. X., Haubold, C., Schiegg, M., Ales, J., Beier, T., Rudy, M., Eren, K., Cervantes, J. I., Xu, B., Beuttenmueller, F., Wolny, A., Zhang, C., Koethe, U., Hamprecht, F. A., & Kreshuk, A. (2019). ilastik: Interactive machine learning for (bio)image analysis. *Nature Methods*, *16*(12), 1226–1232. https://doi.org/10.1038/s41592-019-0582-9

Bosch, C., Martínez, A., Masachs, N., Teixeira, C. M., Fernaud, I., Ulloa, F., Pérez-Martínez, E., Lois, C., Comella, J. X., DeFelipe, J., Merchán-Pérez, A., & Soriano, E. (2015). FIB/SEM technology and high-throughput 3D reconstruction of dendritic spines and synapses in GFP-labeled adult-generated neurons. *Frontiers in Neuroanatomy*, *9*. https://doi.org/10.3389/fnana.2015.00060

Chaurasia, A., & Culurciello, E. (2017). LinkNet: Exploiting encoder representations for efficient semantic segmentation. *2017 IEEE Visual Communications and Image Processing (VCIP)*, 1–4. https://doi.org/10.1109/VCIP.2017.8305148

Chen, L.-C., Papandreou, G., Kokkinos, I., Murphy, K., & Yuille, A. L. (2018). DeepLab: Semantic Image Segmentation with Deep Convolutional Nets, Atrous Convolution, and Fully Connected CRFs. *IEEE Transactions on Pattern Analysis and Machine Intelligence*, *40*(4), 834–848. https://doi.org/10.1109/TPAMI.2017.2699184

Chen, L.-C., Zhu, Y., Papandreou, G., Schroff, F., & Adam, H. (2018). Encoder-Decoder with Atrous Separable Convolution for Semantic Image Segmentation. In V. Ferrari, M. Hebert, C. Sminchisescu, & Y. Weiss (Eds.), *Computer Vision – ECCV 2018* (pp. 833–851). Springer International Publishing. https://doi.org/10.1007/978-3-030-01234-2_49

Cretoiu, D., Gherghiceanu, M., Hummel, E., Zimmermann, H., Simionescu, O., & Popescu, L. M. (2015). FIB-SEM tomography of human skin telocytes and their extracellular vesicles. *Journal of Cellular and Molecular Medicine*, *19*(4), 714–722.

https://doi.org/10.1111/jcmm.12578
He, K., Zhang, X., Ren, S., & Sun, J. (2016a). Deep Residual Learning for Image Recognition. *2016 IEEE Conference on Computer Vision and Pattern Recognition (CVPR)*, 770–778. https://doi.org/10.1109/CVPR.2016.90
He, K., Zhang, X., Ren, S., & Sun, J. (2016b). Identity Mappings in Deep Residual Networks. In B. Leibe, J. Matas, N. Sebe, & M. Welling (Eds.), *Computer Vision – ECCV 2016* (pp. 630–645). Springer International Publishing. https://doi.org/10.1007/978-3-319-46493-0_38
Heinrich, L., Bennett, D., Ackerman, D., Park, W., Bogovic, J., Eckstein, N., Petruncio, A., Clements, J., Pang, S., Xu, C. S., Funke, J., Korff, W., Hess, H. F., Lippincott-Schwartz, J., Saalfeld, S., & Weigel, A. V. (2021). Whole-cell organelle segmentation in volume electron microscopy. *Nature*, 1–6. https://doi.org/10.1038/s41586-021-03977-3
Heinrich, L., Funke, J., Pape, C., Nunez-Iglesias, J., & Saalfeld, S. (2018). Synaptic Cleft Segmentation in Non-isotropic Volume Electron Microscopy of the Complete Drosophila Brain. In A. F. Frangi, J. A. Schnabel, C. Davatzikos, C. Alberola-López, & G. Fichtinger (Eds.), *Medical Image Computing and Computer Assisted Intervention – MICCAI 2018* (pp. 317–325). Springer International Publishing. https://doi.org/10.1007/978-3-030-00934-2_36
Heymann, J. A. W., Hayles, M., Gestmann, I., Giannuzzi, L. A., Lich, B., & Subramaniam, S. (2006). Site-specific 3D imaging of cells and tissues with a dual beam microscope. *Journal of Structural Biology*, *155*(1), 63–73. https://doi.org/10.1016/j.jsb.2006.03.006
Ioffe, S., & Szegedy, C. (2015). Batch Normalization: Accelerating Deep Network Training by Reducing Internal Covariate Shift. *Proceedings of the 32nd International Conference on Machine Learning*, 448–456. https://proceedings.mlr.press/v37/ioffe15.html
Kingma, D. P., & Ba, J. (2015). Adam: A Method for Stochastic Optimization. In Y. Bengio & Y. LeCun (Eds.), *3rd International Conference on Learning Representations, ICLR 2015, San Diego, CA, USA, May 7-9, 2015, Conference Track Proceedings*. http://arxiv.org/abs/1412.6980
Leighton, S. B. (1981). SEM images of block faces, cut by a miniature microtome within the SEM - a technical note. *Scanning Electron Microscopy*, *Pt 2*, 73–76.
Liu, J., Li, L., Yang, Y., Hong, B., Chen, X., Xie, Q., & Han, H. (2020). Automatic Reconstruction of Mitochondria and Endoplasmic Reticulum in Electron Microscopy Volumes by Deep Learning. *Frontiers in Neuroscience*, *14*. https://doi.org/10.3389/fnins.2020.00599
Meyer, C. (2024a). *DeepSCEM: Examples datasets* [dataset]. Zenodo. https://doi.org/10.5281/zenodo.12168941
Meyer, C. (2024b). *DeepSCEM: Examples results* [dataset]. Zenodo. https://doi.org/10.5281/zenodo.12518270
Meyer, C., Baudrier, É., Schultz, P., & Naegel, B. (2023). Combining Max-Tree and CNN for Segmentation of Cellular FIB-SEM Images. In B. Kerautret, M. Colom, A. Krähenbühl, D. Lopresti, P. Monasse, & B. Perret (Eds.), *Reproducible Research in Pattern Recognition* (pp. 77–90). Springer Nature Switzerland. https://doi.org/10.1007/978-3-031-40773-4_7
Meyer, C., Mallouh, V., Spehner, D., Baudrier, É., Schultz, P., & Naegel, B. (2021). Automatic Multi Class Organelle Segmentation For Cellular Fib-Sem Images. *2021 IEEE 18th International Symposium on Biomedical Imaging (ISBI)*, 668–672. https://doi.org/10.1109/ISBI48211.2021.9434075

Meyer, C., & Schultz, P. (2023). *IGBMC ICube LW4-1: Image and annotations* [dataset]. Zenodo. https://doi.org/10.5281/zenodo.8344292

Narayan, K., Danielson, C. M., Lagarec, K., Lowekamp, B. C., Coffman, P., Laquerre, A., Phaneuf, M. W., Hope, T. J., & Subramaniam, S. (2014). Multi-resolution correlative focused ion beam scanning electron microscopy: Applications to cell biology. *Journal of Structural Biology*, *185*(3), 278–284. https://doi.org/10.1016/j.jsb.2013.11.008

Ronneberger, O., Fischer, P., & Brox, T. (2015). U-Net: Convolutional Networks for Biomedical Image Segmentation. In N. Navab, J. Hornegger, W. M. Wells, & A. F. Frangi (Eds.), *Medical Image Computing and Computer-Assisted Intervention – MICCAI 2015* (pp. 234–241). Springer International Publishing. https://doi.org/10.1007/978-3-319-24574-4_28

Spiegelhalter C, Tosch V, Hentsch D, Koch M, Kessler P, Schwab Y, Laporte J. (2010) From dynamic live cell imaging to 3D ultrastructure: novel integrated methods for high pressure freezing and correlative light-electron microscopy. *PLoS One*.;5(2):e9014. doi: 10.1371/journal.pone.0009014.

Wei, D., Jacobs, S., Modla, S., Zhang, S., Young, C. L., Cirino, R., Caplan, J., & Czymmek, K. (2012). High-Resolution Three-Dimensional Reconstruction of a Whole Yeast Cell Using Focused-Ion Beam Scanning Electron Microscopy. *BioTechniques*. https://doi.org/10.2144/000113850

Weibel, E. R., Kistler, G. S., & Scherle, W. F. (1966). PRACTICAL STEREOLOGICAL METHODS FOR MORPHOMETRIC CYTOLOGY. *Journal of Cell Biology*, *30*(1), 23–38. https://doi.org/10.1083/jcb.30.1.23

Wilhelm LP, Wendling C, Védie B, Kobayashi T, Chenard MP, Tomasetto C, Drin G, Alpy F. (2017). STARD3 mediates endoplasmic reticulum-to-endosome cholesterol transport at membrane contact sites. *EMBO J*. 36(10):1412-1433. doi:10.15252/embj.201695917.

Williams, R. C., & Kallman, F. (1955). INTERPRETATIONS OF ELECTRON MICROGRAPHS OF SINGLE AND SERIAL SECTIONS. *The Journal of Biophysical and Biochemical Cytology*, *1*(4), 301–314. https://doi.org/10.1083/jcb.1.4.301

Xiao, C., Chen, X., Li, W., Li, L., Wang, L., Xie, Q., & Han, H. (2018). Automatic Mitochondria Segmentation for EM Data Using a 3D Supervised Convolutional Network. *Frontiers in Neuroanatomy*, *12*. https://doi.org/10.3389/fnana.2018.00092

# Figures

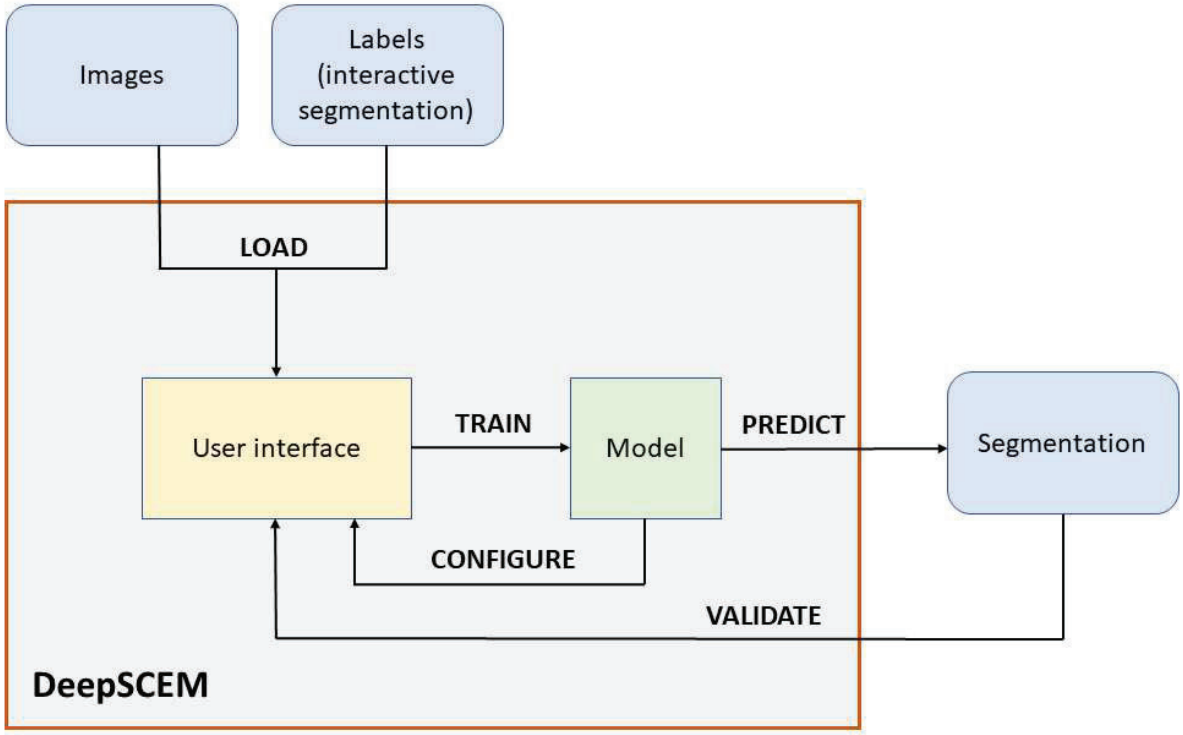


Figure 1 | General workflow of the DeepSCEM application.

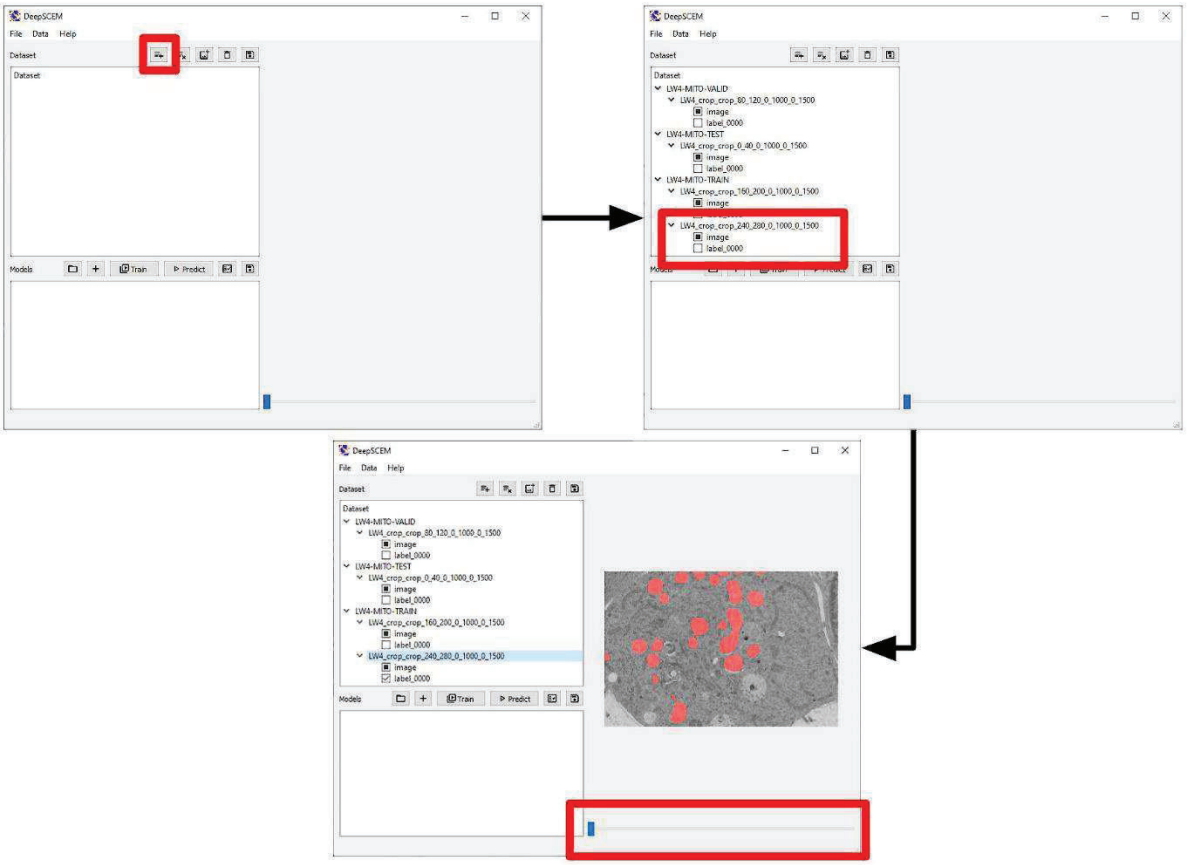


Figure 2 | Graphical interface used to visualize the image dataset. The icon highlighted in red is used to select the dataset which can be scrolled using the bar framed in red.

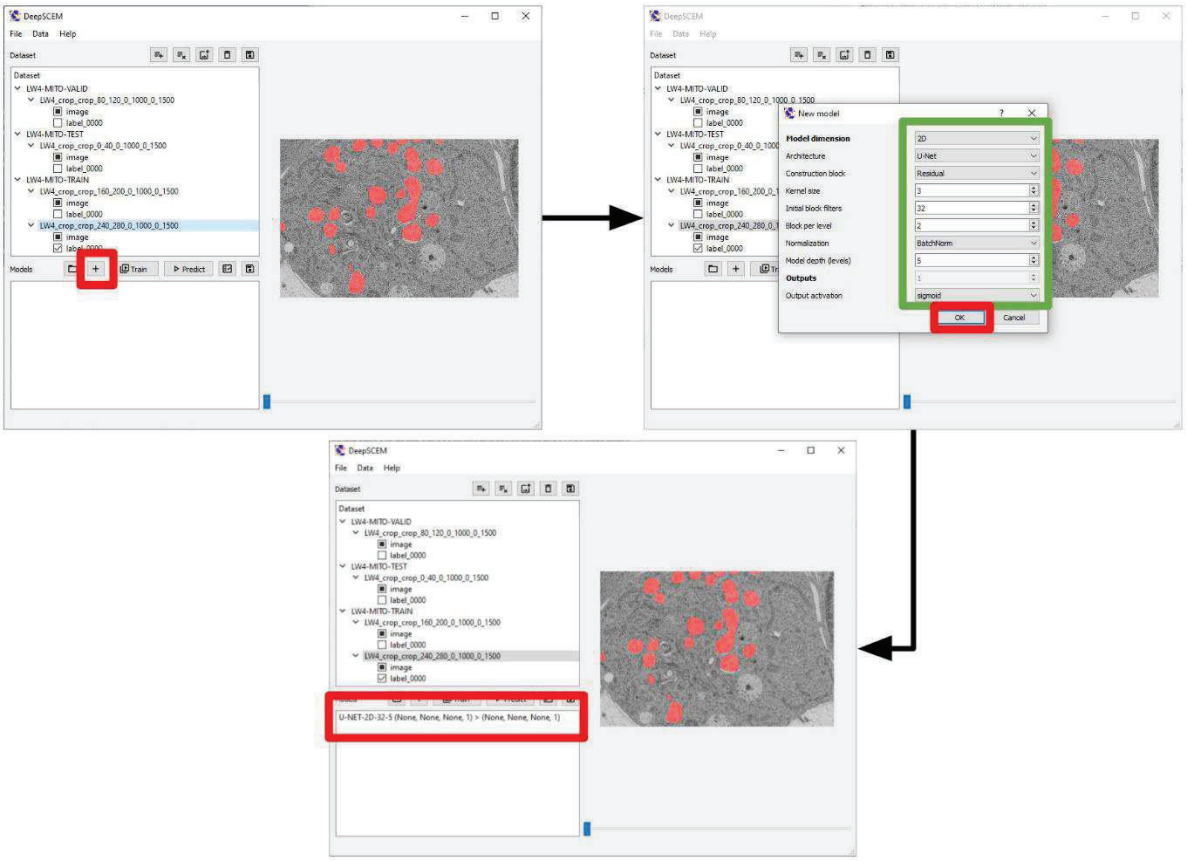


Figure 3 | Creation of a starting model. By selecting the icon framed in red a starting model can be selected and several parameters can be adjusted and saved.

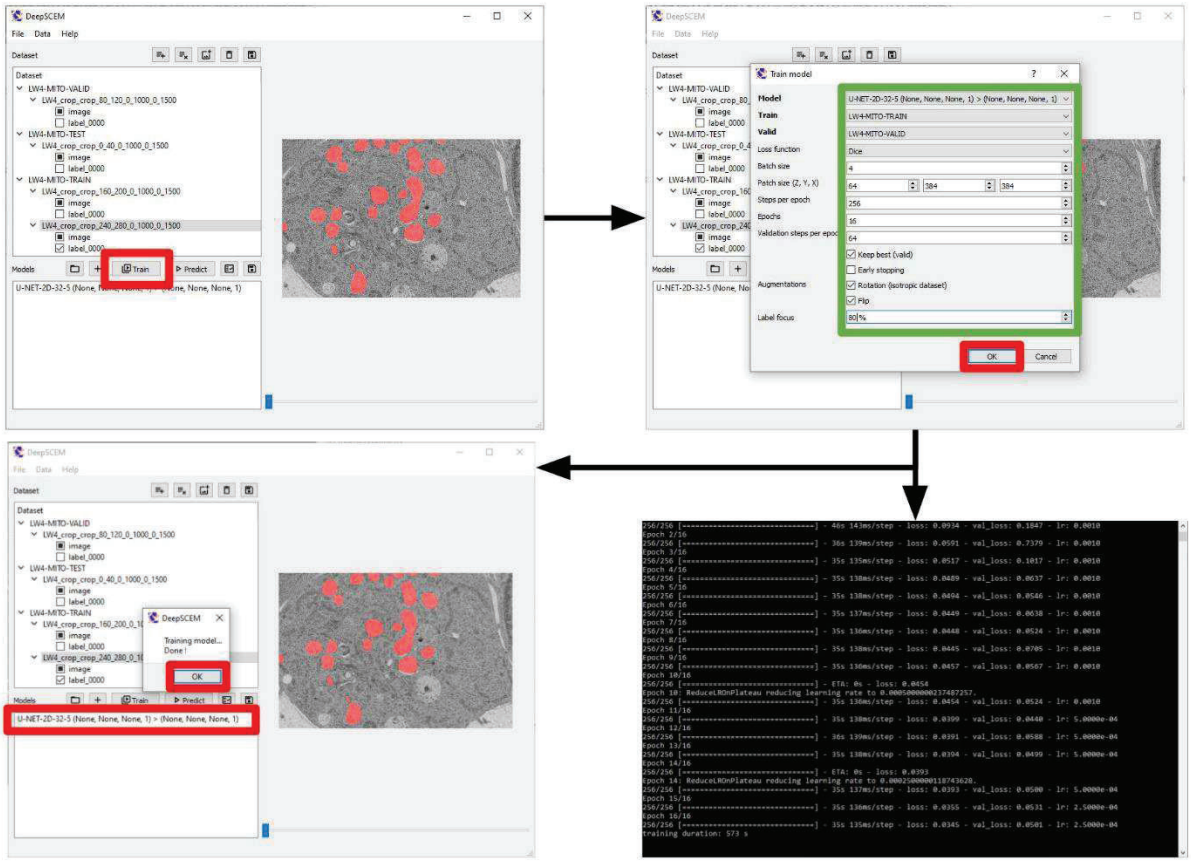

Figure 4 | Training of the model. The training mode is selected by the icon highlighted in red. The next window defines basic training parameters. Images and masks are selected.

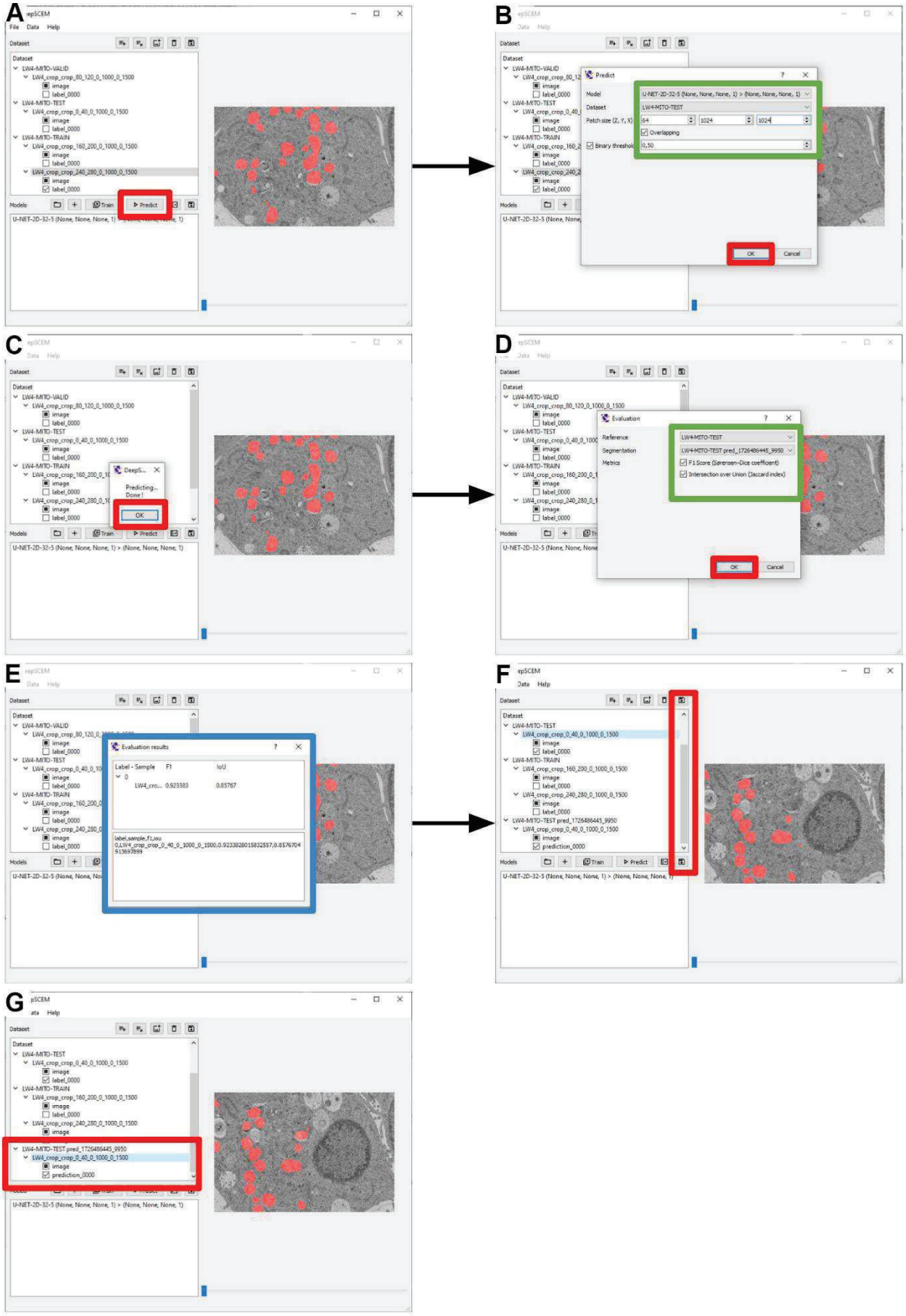


Figure 5 | Evaluate and view predictions.

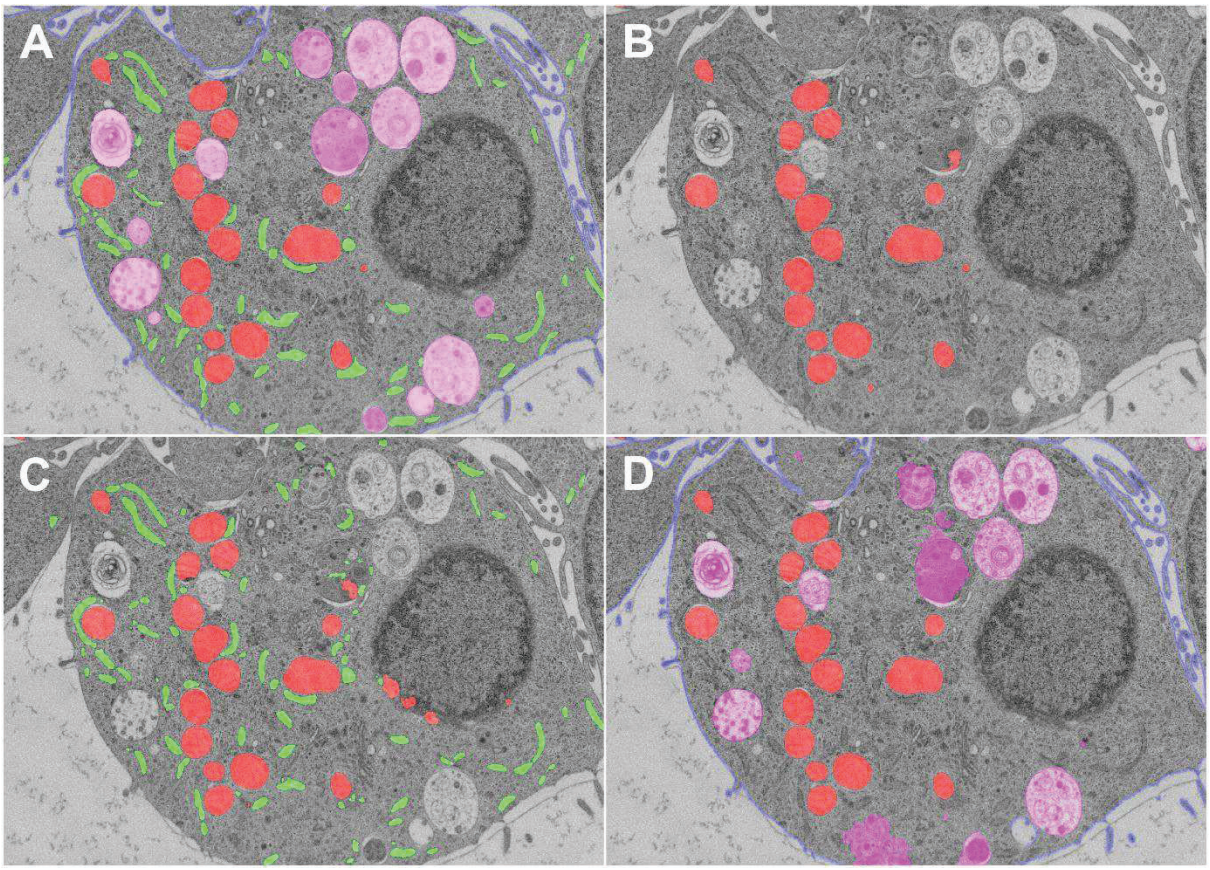


Figure 6 | Qualitative segmentation predictions. A. reference segmentation of mitochondria (red), endoplasmic reticulum (green), endosomes (pink) and plasma membrane (blue). B. Mitochondria segmentation prediction using a binary model. C. Mitochondria and endoplasmic reticulum segmentation predictions using a model trained on two classes. D. Mitochondria, endosomes and plasma membrane segmentation predictions using a model trained on three classes.

# Bibliography

Alpy, F., Rousseau, A., Schwab, Y., Legueux, F., Stoll, I., Wendling, C., Spiegelhalter, C., Kessler, P., Mathelin, C., Rio, M.-C., Levine, T.P., Tomasetto, C., 2013. STARD3/STARD3NL and VAP make a novel molecular tether between late endosomes and the ER. J. Cell Sci. jcs.139295. https://doi.org/10.1242/jcs.139295

Kizilyaprak, C., Daraspe, J., Humbel, B.M., 2014. Focused ion beam scanning electron microscopy in biology. J. Microsc. 254, 109–114. https://doi.org/10.1111/jmi.12127

Meyer, C., Mallouh, V., Spehner, D., Baudrier, E., Schultz, P., Naegel, B., 2021. Automatic Multi Class Organelle Segmentation For Cellular Fib-Sem Images, in: 2021 IEEE 18th International Symposium on Biomedical Imaging (ISBI). Presented at the 2021 IEEE 18th International Symposium on Biomedical Imaging (ISBI), IEEE, Nice, France, pp. 668–672. https://doi.org/10.1109/ISBI48211.2021.9434075

Wilhelm, L.P., Wendling, C., Védie, B., Kobayashi, T., Chenard, M., Tomasetto, C., Drin, G., Alpy, F., 2017. STARD 3 mediates endoplasmic reticulum-to-endosome cholesterol transport at membrane contact sites. EMBO J. 36, 1412–1433. https://doi.org/10.15252/embj.201695917

# Discussion

## Current work achievements

I have validated the different steps of a workflow for *in situ* labeling of a target molecule using electroporation as a probe delivery system, plunge freezing of seeded cells or the waffle method followed by high pressure freezing for cultured cell pellets, cryo sections and cryo-lamella milling using a cryo FIB-SEM instrument, high resolution cryo electron tomography and detection of the gold nanoparticles. Time was short and instruments lunatic, therefore all planned experiments could not be performed.

I am convinced that the 2 nm nanogold probes are detectable in 2D images of vitreous cryo-sections of cells as I demonstrated for the AuNLS probe (Publication 1). In this context, the ability to routinely obtain thin sections (<100 nm) is a significant advantage of this method. Although cryo-sectioning introduces compression artifacts that can affect subtomogram averaging, it remains a valuable technique when appropriate equipment, such as a humidity-controlled environment, is available. Cryo-sectioning combined with brief 2D imaging using cryo-EM offers a rapid and efficient approach to assess labeling efficiency with nanogold probes. To further optimize this approach, the attachment of sections to EM grids has to be improved. In its current state, the attachment is variable but still acceptable for screening purposes. However, this variability hinders the acquisition of tomographic data. Optimizing the attachment will unlock the full potential of this method, enabling its use for high-throughput tomographic data collection.

This observation is also fascinating, as each image represents a projection of a ~100 nm thick volume, indicating that the contrast provided by 2 nm nanogold particles is significantly stronger than that of biological molecules. However, it seemed to be at the limit of visual recognition, at least to my eyes. In 2D images obtained with defocus based phase contrast, CTF results in a complex interference pattern that together with summing biological densities along the projection axis, makes the nanogold particles not always strikingly recognizable (see Figure 7 of the Publication 1). In my opinion, using particles smaller than 2 nm would likely be impossible to recognize visually. However, I do not rule out the possibility that this limitation could be mitigated through advanced data processing tools. This is supported by my subsequent experiments with 3D data (see Chapter 1.5.5), which demonstrated that using the standard deviation projection approach in ImageJ enhances nanogold visibility in raw data. Additionally, thinner sections, which the method permits, could further improve recognition. Finally, the “ironing” of sections using a high electron dose, which destroys most structural details, can serve as an effective method for initial brief screening (Figure 8 of Publication 1). Combining information from a low-dose image (<50 $e^{-}/Å^{2}$), which

preserves structural details, with a high-dose image (>100 $e^-/Å^2$) for “ironing,” which highlights the positions of gold particles, can be used to optimize 2D screening on vitreous sections.

Detection of the gold nanoparticles should improve upon 3D tomographic reconstruction since the scattering of the gold will not be superimposed with the signal of cell content, thus opening the possibility to detect even smaller particles. This was not obvious in our first experiments and in our hands the gold particles could not be detected better. More experiments are required to address this question thoroughly. One concern being that some reports described movements of gold nanoparticles within the sample during tilt series recording (Comolli and Downing, 2005). Internal movements can lead to the fading of the gold signal, reducing its contrast in the tomogram. If these movements are caused by increased absorption of energy from electrons, resulting in localized water mobility, it could also impact the structure of biological molecules, thereby limiting resolution.

It will be important to address these concerns in future experiments; however, I anticipate they will not be critical. In my opinion, even under optimal conditions, detecting all gold particles within a given volume is unlikely. Similarly, not every Pol II complex is expected to be labeled with a gold probe. Furthermore, saturated labeling could potentially interfere with transcription or disrupt the nuclear distribution of Pol II complexes. A more realistic scenario is that the primary use of gold probes will be to identify initial structural references for *in situ* Pol II analysis, such as the localization of Pol II-containing clusters or condensates (Cisse et al., 2013; Zlotorynski, 2024). These putative entities have not been structurally characterized in close to native frozen-hydrated conditions. We cannot fully rely on the vision of them as the dense bodies - transcription factories that were previously suggested by conventional EM observations of nuclei extracted at non physiological conditions (Cook, 1999; Iborra et al., 1996). Once these condensates are located by nanogold labeling, their putative “nanoanatomy” features may become recognizable and used for their future localization and analysis. Furthermore, we expect that Pol II interacts with many other factors *in situ* forming complexes. Those organizations might be different from one predicted from *in vitro* studies. Nanogold probes to Pol II will help to locate such structures without need or bias of priori knowledge. The mapping of such complexes through gold labeling will provide us with initial low-resolution references for further implementation of shape-based search by deep-learning based tools (Harastani et al., 2024; Zeng et al., 2023).

My experiments confirmed that the cell nucleus cannot be vitrified through plunge freezing, nevertheless the sample with a fine polycrystalline ice can be used for initial cryo-ET mapping of nanogold probes. The plunge freezing instruments that allow blotting of the grid from one side allow reproducible freezing of cells adherent to EM grids. I demonstrated that the In-Lens detector (Chapter I, Section 1.2.3) in the Auriga 60 microscope allows precise localization of cells and assessment of polycrystalline ice roughness directly within the SEM instrument. Since ice quality can vary significantly between cells, this helps to improve data collection efficiency.

The pellets of cells for vitreous sectioning were incubated with 10% dextran 40 kDa and 10% BSA as external cryoprotectants. This is unavoidable for high-pressure freezing in bulk, as in 300 micron tubes as it was done for these experiments. These conditions are not fully natural and could cause osmotic effects leading to a higher density of the cellular content. This is not favourable for visualization of nanogold. The waffle method, though unfortunately incompatible with vitreous cryo-sectioning, could potentially overcome these limitations. Unlike bulk samples, waffles have grid bar thicknesses of less than 30 microns. My most recent experiments with these samples demonstrated that vitrification of waffles can be achieved without the need for external cryoprotectants (Chapter I, Section 1.5.4), as the cell culture medium typically contains 5% glucose. I am convinced that the waffle method is the way to go towards studies of molecular organization of the cell nucleus *in situ*, but it requires further optimization, which I will discuss below (see “Challenges and Perspectives” section).

From the beginning of my work, I used Au•NLS conjugates as a test probe towards developing the *in situ* labeling of Pol II. My experiments demonstrated that the available protocols well established for the most frequent applications of electroporation - transfection with DNA or RNA, are not efficient for nanogold probes. Moreover, protocols for transfection of HeLa cells with nanogold probes established by Guy Zuber team, turned out to be not optimal for U-2 OS cells. We decided to switch to U-2 OS because a number of (i) relevant genetically modified lines are available and (ii) these cells are flatter providing better geometry for lamella milling (Chapter I, Section 1.5.2). Using Au•NLS conjugates, I optimized electroporation settings to achieve a high transfection rate with minimal cell mortality. I found that single-pulse strategies are less stressful for U-2 OS cells, while voltages 1400 V and 1600 V are effective for nanogold probe uptake (Chapter 1, Section 1.3). Recently, I successfully applied these settings to electroporate cells with n(nGFP-E3)$_2$:(K3)$_2$AuNP conjugates targeting NUP96-GFP, achieving specific staining with low cell mortality. Although waffles were prepared for these samples, lamellae could not be obtained due to equipment issues.

During my thesis, I explored various concepts of probe design for *in situ* gold labeling. Initially, I planned to use Au conjugates with complete monoclonal antibodies, but producing these probes in sufficient quantities was challenging. Additionally, my negative staining analysis (Publication 2) revealed significant structural heterogeneity, indicating that more than two sets of heavy/light chains bound to the same gold nanoparticle. This polyvalence is unwanted for *in vivo* labeling due to the risks of target crosslinking and aggregation.

Current genome editing tools offer new solutions to overcome the limitations of probes using monoclonal antibodies. I began exploring two approaches: (i) SpyCatcher/SpyTag-based probes and (ii) nanogold conjugates with recombinant anti-GFP nanobodies. In my opinion, both approaches have to be explored. My NUP96-GFP labeling experiment using

$(nGFP\text{-}E3)_2$:$(K3)_2$AuNP yielded promising results (Chapter I, Section 1.4.5), opening the way for future applications of this labeling strategy for *in situ* Pol II localization.

# Challenges and perspectives

Based on my observations and experiments I have identified several steps in my workflow that would benefit from further improvement and optimization. Hereby I describe these weak points and propose some perspectives

## 1. Probe synthesis

### 1.1. Estimating gold probe concentration.

During my thesis, I encountered difficulty estimating the concentration of gold probes, which was essential for determining the molar amount of protein to be conjugated. To measure protein concentration, UV-visible spectrophotometric tools are commonly used in biochemistry labs. These rely on the Beer-Lambert law: $log_{10}(I_0 / I) = A = \varepsilon lc$, where $I_0/I$ is transmittance, A is absorbance, ε is the molar absorption coefficient, c is molar concentration, and l is light path length. Proteins absorb light at 280 nm, and nucleic acids absorb at 260 nm, a principle used in NanoDrop™ technology.

Gold nanoparticles, with a 2.4 nm diameter, absorb light at 280 nm, overlapping with the protein absorption. The absorbance is additive, and by taking absorbance measurements at two different wavelengths, it's possible to calculate the concentration of both the gold and conjugated protein, provided their extinction coefficients are known. A mathematical system can be formed to solve for gold and conjugate concentrations. However, the extinction coefficient for gold nanoparticles is determined experimentally, and the only known data are for pure gold nanoparticles at 506 nm. The extinction coefficient for 2 nm gold nanoparticles is 492410 M-1.cm-1, and for 2.4 nm nanoparticles, it is 902187 $M^{-1}.cm^{-1}$. This makes it difficult to directly use this method for estimating purified gold probe concentration at the same wavelength as protein.

Other methods like the Bradford assay, with absorption at 595 nm, are also ineffective due to the broad absorbance spectrum of gold nanoparticles (250-700 nm). Protein concentration can be estimated via SDS-PAGE gels, where the protein is stained with Coomassie blue or silver ions. These stains, however, interfere with nanogold signals during electrophoresis, making it challenging to correlate with a BSA gradient for concentration estimation. Techniques such as Qubit™ (Invitrogen™ ThermoFisher) and BCA assays cannot be used either due to similar interference from gold nanoparticles.

Western blotting with radioactivity-based immunodetection could be another option, but it requires generating specific IgG for non-IgG proteins, which would be time-consuming and costly. Circular dichroism (CD) measurements, which compare the absorption differences of left and right circularly polarized light, can estimate chiral object concentration. While gold nanoparticles are achiral and don't influence CD measurements at low concentrations, higher concentrations would cause too much light scattering.

An alternative method involves calibrating CD spectra for the molecular part of the conjugate, allowing the concentration of the gold probe to be calculated. Another idea is to reduce an aliquot of the purified conjugate to separate the gold nanoparticles from the protein, saturate the protein surface with SDS, and run the sample on an SDS-PAGE gel alongside a protein concentration gradient. Densitometric analysis of the gel could then estimate the protein concentration.

More recently a new biophysical characterisation method has been developed to estimate the molecular mass of single particles by mass photometry. Mass photometry measures the interference between the light scattered by the molecule and the light reflected by the measurement surface. The signal measured is called the mass photometry contrast (or interferometric contrast) and is directly correlated with molecular mass (Young et al., 2018). Most published studies have applied mass photometry to proteins, to study protein-protein interactions (Higuchi et al., 2021) or protein oligomerization mechanisms (Naftaly et al., 2021). It would be of highest interest to use this method and characterize the population of gold particles coupled to proteins in order to assess the homogeneity of the probe, the number of bound components and the valency of the probe.

**1.2. Better controlled conjugation**

The reduction step leading to a covalent link between the gold nanoparticle and the bait needs to be optimized for each protein. The process is particularly tricky for full IgG molecules or Fab fragments since reduction of intramolecular SH-bonds is required without affecting intermolecular bonds essential for the folding of the IgG domains. The availability of recombinant baits on which highly accessible SH groups can be engineered at defined position opens the possibility to control in a more efficient way this process and to improve probe homogeneity.

**1.3. Au•Conjugates purification.** After conjugation a large excess of single gold nanoparticles may be contaminating the mix. It is essential to separate the uncoupled gold nanoparticles from the final conjugate aliquot to avoid producing non-specific gold signals in the final micrographs which could result in misleading results. To do so, the conjugation may be performed in excess of bait to make sure that all AuNPs are conjugated, but still a fraction of AuNPs may not be reactive for binding any bait. In collaboration with A. Poterszman, we explored the possibility to graft an affinity tag on the recombinant antibody that is conjugated to the AuNPs to allow a further affinity purification step to select those AuNPs that have a bound bait. First experiments were not

successful and it is possible that the affinity tag was not accessible to interact with the resin. Additional constructs need to be tested to optimize this step.

**1.4. Impact of conjugation on probe affinity.** It has been observed for some nanobodies that their conjugation to the gold surface completely abolished further interaction with the target molecules (Groysbeck et al., 2021). The ability of the gold conjugates to recognize their target is generally assessed on native protein gel electrophoresis followed by an interaction with the gold probe whose binding is revealed by silver enhancement. A more quantitative affinity measurement would be useful to show that the conjugation reduced significantly the affinity of the bait for its target. In unfavorable cases, a protein or a polyethylène glycol linker could be introduced between the bait and the gold surface to remedy this issue.

## 2. labeling and electroporation

**2.1. Electroporation.** The physical events making electroporation successful at transfecting molecules in living cells is still under investigation. Our experiments indicate that cell survival is weakly affected and that most of the cells not only survive the process but can undergo further cell divisions suggesting that cell integrity is not affected or is recovering quickly after electroporation.

After electroporation some of the probe is encapsulated in endo-lysosomes reducing the *in vivo* labeling efficiency. However, electroporation behaves much better in this respect than lipid-based approaches for probe delivery for which a large fraction of the probe is sequestered in the endo-lysosomal compartment. Adding glycerol to the cell media induces a hypertonic shock inducing stress on the cells as they shrink upon partial dehydration. Getting back to isotonic condition by removing the glycerol excess was reported (Wang et al., 2020) to induce endo-lysosomal membrane permeabilization causing encapsulated molecules to be delivered in the cytoplasm. Our workflow could implement this step post electroporation in trying to increase the *in vivo* labeling efficiency.

**Electroporation and cell damage**. Although cytotoxicity is weak in controlled electroporation conditions, the process is likely to affect cell homeostasis. Electroporation increases the level of Ca2+ uptake and might be correlated to electron-dense features that we have seen in the mitochondria in some of our tomograms. These features may correspond to Ca2+ granules that have been observed previously (Weinbach and Von Brand, 1965). Other reports mention that many very short electric pulses may lead to cell damage or death (Kotnik et al., 2019; Peng et al., 2024). This study shows that electric pulses generate reactive oxygen species (ROS) and oxidative damage of unsaturated lipids. Other studies revealed that both F-actin and β-tubulin proteins in the cytoskeleton are disrupted by electropermeabilization-inducing pulses and that the cytoskeleton recovers within hours. The main effect of electric pulses on cortical actin is not its depolymerization but rather its impaired attachment to the membrane.

**Probe integrity after electroporation.** It has never been tested whether electroporation is damaging the probe or the conjugation of the ligand to the gold nanoparticle. Our experiments with the gold-NLS particles suggest that most of the probe is delivered to the nucleus thus suggesting that the probe is not affected by the electroporation. For larger proteins, it could be of interest to submit the probe to the electroporation conditions and to control whether the protein is still conjugated to the AuNP.

**Electrophoretic properties of the probe.** Gold nanoparticles coupled to proteins are showing electrophoretic properties in SDS-PAGE and whether or not the probes are showing the same behaviour during electroporation is discussed here. If potential interaction of negatively charged SDS with the probe is ignored, nanogold•Protein probe migration downwards within a SDS-PAGE, towards the positive electrodes, would indicate that the overall probe is negatively charged. The same hypothesis was emitted by the author that issued the synthesis protocol of the 2.4 nm gold nanoparticles I used (Groysbeck et al., 2019). The first version of these nanogold particles were synthesized using a slightly different protocol which resulted in smaller 1.4 nm nanoparticles (Desplancq et al., 2018). The small gold was characterized and found to be composed of a cluster of 102 gold atoms coated by multiple copies of two organic compounds, 30 thioaminobenzoic acids (TAB) and 14 anionic thionitrobenzoic acids (TNB) giving to the raw nanogold particles an overall negative charge. This explanation is only valid for raw nanogold particles: final probes are made of proteins or molecules interacting with neutralized or passivated gold. In my work I used a high concentration of 2kDa PEG-SH to saturate the remaining interaction site of the gold and we don't know whether PEG-SH will preferentially exchange more with TNB or TAB and thus we cannot determine the final overall charge of the conjugate. Anyway, for a neutral conjugate, we can hypothesize that the difference of concentration of the probe in the electroporation mix compared to the inner cell will build an osmotic pressure that will lead to transfection. Now, in the case of an overall negatively charged probe, the transfection rate would be low. At the beginning of the electroporation pulse, the plasma membrane difference of potential will increase with positive charges stacking on the outside and negative charges aggregating on the inside until saturation. At this point, negatively charged probes will be attracted towards the outer cell membrane and the positive electrode. With electrostatic pressure building up as the electric field intensifies (until it stabilizes), plasma membrane breaks, positively charged elements rush inside the cell. At the end of the pulse, the potential difference across the plasma membrane will slowly recover. During this reequilibration of the membrane charges, anionic elements were shown to be excreted by the cell (Sözer et al., 2018). It seems like they would be a competition between diffusion and osmotic pressure against electrophoretic forces of negatively charged probes thus lowering their potential transfection rates

**Cellular effect of the electroporation mix**. Labeling a molecule of interest in a living cell is a crucial and challenging step for not messing with the environment and keeping the impact of the interacting probe minimal on the local interaction area structure. We cannot have information on

how the probe is affecting the structure of the probed molecules in the complexes it is involved in but having a constant cell vitality rate and cell dividing time is a good indicator that the probing is not perturbing the cell cycle and gives hope in not interfering with the organisation of cell processes such as transcription condensates for instance.

*In vivo* labeling of cells should use only bio-compatible medium and chemical. All reagents used for the probe synthesis should be washed off before transfection as reducing agents, EDTA and other chemicals will have a bad impact on the cell vitality.

The probes are stored in PBS at -20°C, for a short amount of time, or -80°C with 10% glycerol as soon as they are purified. Prior to electroporation, the probe solution is brought to 4°C on ice and mixed with cells (diluted in the resuspension buffer R) and the electroporation buffer T. Depending on the proportion of the probe solution in the electroporation mix there is a great amount of glycerol electroporated inside living cells. The impact of glycerol in living cells is poorly understood as well as its impact on transfection efficiency. It would be great to compare electroporation efficiencies of electroporation mixes prepared with a probe solution containing 10% of glycerol and electroporation mixes prepared with a centricon cleaned probe solution with traces of glycerol. Despite that glycerol is a cryoprotectant that could help with later freezing steps (Zhang et al., 2022), it is suspected to hinder cell proliferation (Wiebe and Dinsdale, 1991) and to induce osmotic stress that can lead to cell death (Armitage and Mazur, 1984). Whether or not glycerol reduces transfection efficiency, it seems that it should be avoided in electroporation mix as it can impact the recovery of already weak electroporated cells. The greater transfected healthy cells the better for later cryo sample preparation steps.

**Estimate probe delivery.** It is currently difficult to estimate the cellular concentration of the probe after electroporation. This parameter is crucial to optimize the binding efficiency of the probe to the target. In the case of Pol II it is impossible to determine whether the probe delivered is sufficient to label all Pol II molecules or only a subset of them. Coupling the probe with a fluorescent dye engineered onto the ligand protein as suggested for the recombinant Fabs would not only allow for correlated light and electron microscopy, but would also raise the possibility to quantify the transfected fluorescence and estimate the intracellular concentration of the probe.

## 3. Sample Freezing

**Loading cells with care on freezing apparatus.** Cell stress can induce unwanted morphological changes. It is therefore of particular importance to handle the cells carefully before freezing by keeping an optimal temperature close to 36 °C, a good humidity and an optimal 5 % $CO_2$ concentration. This can be obtained by using $CO_2$ buffered media or by having an incubator close to the freezing apparatus. Loading the grid inside the freezing apparatus is a critical step as it is prone to stress : cells are taken out of the medium, the $CO_2$ and humidity controlled environment

and loaded on a grid holder at room temperature (tweezer for plunge freezing, specimen carriers and holder for high pressure freezing). Plunge or waffle freezing time is not compressible but it needs to be performed in a matter of two seconds. The impact of these stresses on the *in situ* pol II distribution and interactome are likely to be minimal as no major stress specific transcription will start in such a short period of time. These cell stresses can be partially prevented by pre-warming all the tools in direct contact with the cell seeded grid : tweezers for plunging, specimen carriers, tip holders for the high pressure freezing. A $CO_2$ buffered media can compensate for the lack of $CO_2$ during the sample handling before freezing. A drop of media can be added to the grid loaded on the plunging tweezers to keep enough of media and $CO_2$ to protect the cells, waffles are less impacted as the grid is squeezed between two specimen carriers thus reducing the amount of evaporation.

## 4. Sample thinning

A central issue in cellular electron microscopy at molecular scale is to generate a window for the observation of a thin sample in transmission electron microscopy which is currently the most suitable method to obtain high resolution information. The cryo-sectionning and the FIB-SEM milling technologies have been proposed to date and I had the unique opportunity to be in contact with both methods and to compare their respective advantages and drawbacks.

**Cryo-sectioning.** This method was originally proposed as a follow up of traditional sectioning methods for cellular electron microscopy. It opens the possibility to create very thin sections, and to generate serial sections to address long range organizational principles. However in cryogenic conditions, this method is hampered by three main technical difficulties. First the sections are shrinking by up to 30% in the sectioning direction as a result of diamond knife compression effects. It is not clear to what extent this compression affects the molecular structure of biomolecules. It is well possible that compression of a still fluid vitreous sample simply results in a thickening without affecting the molecular organisation of the supramolecular complexes. It would be of highest interest to show that high resolution structures can be obtained on test objects such as ribosomes from cryo sections. The second difficulty comes from the poor adhesion of cryo-section to the EM grids which results in movements during tomographic series acquisition and poor resolution in tomograms. Recent improvements have been obtained in this respect and will be published soon. The third limitation is the need of very skilled operators, a problem that can only be solved by adequate training.

**Cryo FIB-SEM and Waffle method.** Cryo FIB-SEM milling became the most popular method to create lamellas for cryo ET. It delivers a deformation free cellular section but is presently not compatible with serial milling since the volumes above and below of the lamella are milled away. I implemented this method at IGBMC but noticed that it needs a proper machine. The Auriga 60

machine is not adapted for high throughput lamella milling. Its operation is slow, the cryo-transfer system is not user-friendly and difficult to handle even for an expert user. Despite all these difficulties I was able to produce some lamellae from which decent tomograms could be obtained. A new generation of instruments with increased automation and optimized specimen transfer is now available, which should speed up and rationalize the production of cryo-lamellae. To further optimize the Waffle method, it will also be crucial to incorporate a halfway deposition step, enabling better access to the cells and overcoming the challenges associated with top-face lamella milling.

## 5. Cryo-ET sampling power: finding Nemo

**Cryo-lamella contains only a small portion of the nucleus.** FIB-SEM based sample thinning of cellular specimen for cryo-ET imaging will not create more than 10 or 8 µm wide lamella per cell as too close lamella will contaminate each other during milling due to redeposition of milled material that occurs few micrometers away from the border of the milling shapes. Considering a HeLa nucleus with an estimated volume of 350 $\mu m^3$ (Maul and Deaven, 1977), a classical lamella of 8 µm wide, 8 µm deep and 0.2 µm thick or less will roughly contain 1/30th of the nuclear content. The TEM recording constraints will not allow this full lamella volume to be sampled by successive tilt-series recordings. These recordings have to be spaced out to avoid one recording to damage the next one and we can estimate that two recording regions have to be spaced by one camera length in x and one camera wide in y. Taking into account our falcon 4i 4096 x 4096 pixel detector and a recording pixel size of 2.058 Angstrom, one recording field of view will be about 0.84 x 0.84 µm and sample about 0.14 $\mu m^3$ or 1/2500th of the nuclear volume.

At best a lamella has about 10 recording fields of view in its x and y dimensions. Taking into account the gaps, only 5 x 5 fields of view will be recorded in x and y. 25 recorded tomograms of 0.84 x 0.84 x 0.2 µm will narrow down the total screened nucleus volume to 3.5 $\mu m^3$ : 1/100th of its total volume. This scenario is only valid for flat cells from which a 8 µm deep lamella can be milled and that will contain only nuclear material. Although it may seem like an almost impossible task, recent advancements, such as the parallel cryo-electron tomography (PACE-tomo) method, supported by the high optical stability of modern cryo-ET instruments, enable a throughput of less than 5 minutes per tilt series (Eisenstein et al., 2023).

**How many Pol II can we expect to detect in a tomogram?** A number of reports have tried to estimate the number of Pol II molecules per HeLa cell as well as the proportion of actively transcribing ones. These values are of interest since they allow us to estimate the number of pol II molecules that one can expect to see in a cell section or lamella. Analysis of cell extracts estimated the number of the polymerase II largest subunit rpb1 to be present around ~320,000 copies in a single nucleus, part of them are involved in active polymerases that were found to be roughly 65.000 (Kimura et al., 1999). Some Pol II molecules are probably freely diffusing in the cell nucleus

and a significant number have been reported to be stalled at gene promoters for subsequent activation. Based on these rough estimations, one can expect to detect about 128 Pol II molecules per tomogram, 26 of them being actively transcribing.

These approximate values allow us also to estimate the concentration of pol II which is of importance with regard to the affinity of the probe to have a stable interaction. With 65.000 molecules in 0.35 $e^{-12}$ µL of nucleus volume, the concentration of active pol II molecules can be estimated to 0.3 µM and the total pol II is roughly at 1.5 µM. Taking for granted the piggyback mechanism, it is important to reach a high concentration of probe to the cytoplasm and to have a low dissociation constant (Kd) between the probe and the target to have a chance to label the target molecule. Once imported into the nucleus, KDs in the 1 to 50 nanomolar range will be important to have a stable interaction.

## Summary

To summarize, the workflow for *in situ* labeling at the molecular resolution combines multiple experimental steps that are technically state-of-the-art but still require significant optimization. My work has provided critical proof-of-principle observations supporting the feasibility of this approach. Specifically, I demonstrated the detectability of gold nanoparticles in cryo-EM data *in situ*, developed cell electroporation strategies tailored for gold nanoparticle conjugates, and achieved proof-of-principle labeling using versatile nanobody-based probes. Additionally, I initiated the optimization of cryo-ET sample preparation for the Waffle technique, advancing its practical applicability for visualization of probes by cryo-ET. While further refinement is needed, I am confident that this method is now significantly closer to practical implementation for *in situ* mapping of Pol II, and potentially to other molecular targets in the crowded nuclear environment.

# Bibliography


Armitage, W.J., Mazur, P., 1984. Toxic and osmotic effects of glycerol on human granulocytes. Am. J. Physiol.-Cell Physiol. 247, C382–C389. https://doi.org/10.1152/ajpcell.1984.247.5.C382

Cisse, I.I., Izeddin, I., Causse, S.Z., Boudarene, L., Senecal, A., Muresan, L., Dugast-Darzacq, C., Hajj, B., Dahan, M., Darzacq, X., 2013. Real-Time Dynamics of RNA Polymerase II Clustering in Live Human Cells. Science 341, 664–667. https://doi.org/10.1126/science.1239053

Comolli, L.R., Downing, K.H., 2005. Dose tolerance at helium and nitrogen temperatures for whole cell electron tomography. J. Struct. Biol. 152, 149–156. https://doi.org/10.1016/j.jsb.2005.08.004

Cook, P.R., 1999. The Organization of Replication and Transcription. Science 284, 1790–1795. https://doi.org/10.1126/science.284.5421.1790

Desplancq, D., Groysbeck, N., Chiper, M., Weiss, E., Frisch, B., Strub, J.-M., Cianférani, S., Zafeiratos, S., Moeglin, E., Holy, X., Favier, A.L., de Carlo, S., Schultz, P., Spehner, D., Zuber, G., 2018. Cytosolic Diffusion and Peptide-Assisted Nuclear Shuttling of Peptide-Substituted Circa 102 Gold Atom Nanoclusters in Living Cells. ACS Appl. Nano Mater. 1, 4236–4246. https://doi.org/10.1021/acsanm.8b00988

Eisenstein, F., Yanagisawa, H., Kashihara, H., Kikkawa, M., Tsukita, S., Danev, R., 2023. Parallel cryo electron tomography on in situ lamellae. Nat. Methods 20, 131–138. https://doi.org/10.1038/s41592-022-01690-1

Groysbeck, N., Donzeau, M., Stoessel, A., Haeberle, A.-M., Ory, S., Spehner, D., Schultz, P., Ersen, O., Bahri, M., Ihiawakrim, D., Zuber, G., 2021. Gold labeling of a green fluorescent protein (GFP)-tag inside cells using recombinant nanobodies conjugated to 2.4 nm thiolate-coated gold nanoparticles. Nanoscale Adv. 3, 6940–6948. https://doi.org/10.1039/d1na00256b

Groysbeck, N., Stoessel, A., Donzeau, M., Da Silva, E.C., Lehmann, M., Strub, J.-M., Cianferani, S., Dembélé, K., Zuber, G., 2019. Synthesis and biological evaluation of 2.4 nm thiolate-protected gold nanoparticles conjugated to Cetuximab for targeting glioblastoma cancer cells via the EGFR. Nanotechnology 30, 184005. https://doi.org/10.1088/1361-6528/aaff0a

Harastani, M., Patra, G., Kervrann, C., Eltsov, M., 2024. Template Learning: Deep Learning with Domain Randomization for Particle Picking in Cryo-Electron Tomography. https://doi.org/10.1101/2024.03.20.585905

Higuchi, Y., Suzuki, T., Arimori, T., Ikemura, N., Mihara, E., Kirita, Y., Ohgitani, E., Mazda, O., Motooka, D., Nakamura, S., Sakai, Y., Itoh, Y., Sugihara, F., Matsuura, Y., Matoba, S., Okamoto, T., Takagi, J., Hoshino, A., 2021. Engineered ACE2 receptor therapy overcomes mutational escape of SARS-CoV-2. Nat. Commun. 12, 3802. https://doi.org/10.1038/s41467-021-24013-y

Iborra, F.J., Pombo, A., Jackson, D.A., Cook, P.R., 1996. Active RNA polymerases are localized within discrete transcription ‘factories’ in human nuclei. J. Cell Sci. 109, 1427–1436. https://doi.org/10.1242/jcs.109.6.1427

Kimura, H., Tao, Y., Roeder, R.G., Cook, P.R., 1999. Quantitation of RNA polymerase II and its transcription factors in an HeLa cell: little soluble holoenzyme but significant amounts of polymerases attached to the nuclear substructure. Mol. Cell. Biol. 19, 5383–5392. https://doi.org/10.1128/MCB.19.8.5383

Kotnik, T., Rems, L., Tarek, M., Miklavčič, D., 2019. Membrane Electroporation and

Electropermeabilization: Mechanisms and Models. Annu. Rev. Biophys. 48, 63–91. https://doi.org/10.1146/annurev-biophys-052118-115451

Maul, G., Deaven, L., 1977. Quantitative determination of nuclear pore complexes in cycling cells with differing DNA content. J. Cell Biol. 73, 748–760. https://doi.org/10.1083/jcb.73.3.748

Naftaly, A., Izgilov, R., Omari, E., Benayahu, D., 2021. Revealing Advanced Glycation End Products Associated Structural Changes in Serum Albumin. ACS Biomater. Sci. Eng. 7, 3179–3189. https://doi.org/10.1021/acsbiomaterials.1c00387

Peng, W., Polajžer, T., Yao, C., Miklavčič, D., 2024. Dynamics of Cell Death Due to Electroporation Using Different Pulse Parameters as Revealed by Different Viability Assays. Ann. Biomed. Eng. 52, 22–35. https://doi.org/10.1007/s10439-023-03309-8

Sözer, E.B., Pocetti, C.F., Vernier, P.T., 2018. Transport of charged small molecules after electropermeabilization — drift and diffusion. BMC Biophys. 11, 4. https://doi.org/10.1186/s13628-018-0044-2

Wang, S., Jin, S., Li, G., Sun, R., Shu, Q., Wu, S., 2020. Decompression Process of Glycerol Shock Treatment Can Overcome Endo-Lysosomal Barriers for Intracellular Delivery. ACS Omega 5, 33133–33139. https://doi.org/10.1021/acsomega.0c04771

Weinbach, E.C., Von Brand, T., 1965. The isolation and composition of dense granules from Ca++-loaded mitochondria. Biochem. Biophys. Res. Commun. 19, 133–137. https://doi.org/10.1016/0006-291X(65)90131-2

Wiebe, J.P., Dinsdale, C.J., 1991. Inhibition of cell proliferation by glycerol. Life Sci. 48, 1511–1517. https://doi.org/10.1016/0024-3205(91)90275-G

Young, G., Hundt, N., Cole, D., Fineberg, A., Andrecka, J., Tyler, A., Olerinyova, A., Ansari, A., Marklund, E.G., Collier, M.P., Chandler, S.A., Tkachenko, O., Allen, J., Crispin, M., Billington, N., Takagi, Y., Sellers, J.R., Eichmann, C., Selenko, P., Frey, L., Riek, R., Galpin, M.R., Struwe, W.B., Benesch, J.L.P., Kukura, P., 2018. Quantitative mass imaging of single biological macromolecules. Science 360, 423–427. https://doi.org/10.1126/science.aar5839

Zeng, X., Kahng, A., Xue, L., Mahamid, J., Chang, Y.-W., Xu, M., 2023. High-throughput cryo-ET structural pattern mining by unsupervised deep iterative subtomogram clustering. Proc. Natl. Acad. Sci. 120, e2213149120. https://doi.org/10.1073/pnas.2213149120

Zhang, P.-Q., Tan, P.-C., Gao, Y.-M., Zhang, X.-J., Xie, Y., Zheng, D.-N., Zhou, S.-B., Li, Q.-F., 2022. The effect of glycerol as a cryoprotective agent in the cryopreservation of adipose tissue. Stem Cell Res. Ther. 13, 152. https://doi.org/10.1186/s13287-022-02817-z

Zlotorynski, E., 2024. Condensates burst the bridge for transcription. Nat. Rev. Mol. Cell Biol. 25, 159–159. https://doi.org/10.1038/s41580-024-00711-5

# General Conclusion

My thesis work explored and optimized a workflow for *in situ* labeling with nanogold probes and imaging of cellular structures at the molecular resolution in the native functional environment by cryo-ET. Although the original aim of mapping Pol II in the cell nucleus was not fully achieved, I believe that significant advancements were made in various stages of the workflow, from probe delivery to imaging.

It is important to highlight that this workflow required the implementation of cutting-edge technically challenging equipment nodes, including high-pressure freezing, vitreous cryo-sectioning, FIB-SEM, and high-resolution cryo-ET. Mastering these advanced instruments presented significant challenges and time investments, requiring optimization of both operational parameters and sample handling protocols. Among these, the most challenging was FIB-SEM, as its functional pipelines were not previously integrated into the routines of the cryo-EM platform or research teams of IGBMC. As a result of my work, I successfully carried on FIB-SEM pipelines for conventional resin-embedded samples and implemented cryo-lamella milling at the institute level, establishing an initial methodology core and teaching materials that now support further advancements in FIB-SEM workflows at IGBMC.

I also consider as my key achievement the definition of electroporation settings for efficient nanogold probe uptake in U-2 OS cells, which provide favorable geometry for lamella milling. Electroporation protocols were optimized to minimize cell mortality while achieving a working labeling intensity. The successful use of Au·NLS conjugates demonstrated the feasibility of detecting 2 nm gold probes in 2D cryo-EM images of vitreous cryo-sections and later in 3D cryo-tomographic volumes. My exploration of nanogold probes labeling strategies revealed limitations in traditional monoclonal antibody-based probes, directed me to the development of alternative strategies. Promising results were obtained using SpyCatcher/SpyTag-based probes and, especially recombinant anti-GFP nanobodies. Using the later nanobodies conjugates, I successfully performed proof-of-principle labeling experiments, demonstrating their potential applicability for the *in situ* localization of Pol II and other molecular targets.

Despite the challenges in vitrifying the cell nucleus by plunge freezing, I found that samples containing polycrystalline ice were still useful for initial cryo-ET mapping of nanogold probes. However, our current method of choice is the waffle technique, which allows vitrification of the complete cell without the need for external cryoprotectants. It showed great potential for studying molecular organization *in situ* but still requires further optimization to reach its full capability. My work has also revealed significant challenges related to reproducibility of nanogold probes synthesis and to the estimation of their concentration, which will require further attention.

The next essential challenge has its origin in the limited sampling capacity of high-resolution cryo-ET. The number of rare target molecules, such as Pol II in our case, can be fewer than a hundred in a highly crowded tomographic reconstruction of the cell nucleus. This crowded nuclear environment contains numerous frequent complexes, such as nucleosomes, and a variety of other molecules, making the task of identifying specific targets particularly difficult. The difficulty of finding Pol II in this data is reminiscent of Marlin's difficulty in finding his son in the vastness of the Great Barrier Reef (from the animated film "Finding Nemo"). On one hand, the rarity of the target requires efficient labeling strategies to find it, and on the other hand, it raises the question of how many Pol II molecules we can realistically label. Despite this challenge, as I noted earlier, unsaturated labeling of Pol II is already capable of providing new essential observations on (i) localization of Pol II clusters/condensates; (ii) initial characterisation of Pol II and Pol-II containing association with chromatin and splicing machineries *in situ*. I believe that combining our labeling method with shape-based tomographic data mining approaches, such as template matching or deep learning-based tools, will provide valuable insights into transcription organization at the molecular scale *in situ*.

# Supplementary Materials and Methods

## Chapter I, Section 1.3.

**Profile analysis**. In the following steps, the images were processed using ImageJ Version 1.54j 12 June 2024 with java 1.8.0_172 (64 bit). Photonic images were first converted to 8-bit images and duplicated. Duplicates were filtered using a median filter with a radius of 30 pixels. Small series of the same cells were selected in both the original images and filtered duplicates. Using the “straight” option in the tools bar I drew a line passing over the centre of the cell's nucleus starting and ending with the coverslip background used in both the raw and the median filtered images. These lines were used for a profile analysis using the “plot profile” tool. The resulting datasets were exported in csv format, imported and plotted using a python script with python 3.8 using packages matplotlib version 3.4.2 and numpy 1.24.4 (https://github.com/VictorHanss/Thesis/tree/main/). For illustration purposes images have been processed using contrast-limited adaptive histogram equalization (CLAHE) algorithm with a blocksize of 127, histogram bins of 256 and a maximum slope of 2 and filtered further using a fast fourier bandpass filter with a large structures filtering down to ¼ of the images pixel width and a small structures filtering of 1 pixel, only to remove very low resolution illumination gradient noise.

## Chapter II, Section 1.2

**Recording software.** Smart SEM (version 6.00 ; 09-Jun-16) is the main software of the FIB-SEM microscope handling both FIB and SEM usage. This software is fitted with multiple tools allowing to align both FIB and SEM probes, create navigation map, tilt compensation for image, dynamic focus to get the complete field of view of tilted region of interest in focus and more. This primary software gives the option to perform nanotomography using slice and view for volume imaging, but in a primitive way, where all the fields of view have to be recorded. The nanotomography tool of the Zeiss atlas engine software (version 5.3.5.27) was preferentially used to perform volume imaging on resin embedded samples. For cryo lamella applications, the microscope was operated with Smart SEM.

**Image acquisition.** Using the secondary electron SESI detector first. Then SESI and InLens as InLens gave a better overall sharp image : better resolving power. Having this couple of detectors allowed us to combine images to get dinner details. The secondary electrons imaged with this combo of detectors was sensitive to surface deformation and defects decreasing the image quality as the surface defects are hiding biological information. Bac-scattered electrons, generated within the sample are less impacted by surface deformations and retrieve all the biological information of the field of view. Backscattered electrons being rare, BSE images are noisier but the combo of SE and BSE can relatively compensate for surface deformation and noise.

## Image processing

**Pre-processing.** Raw SEM images recorded with the SE and BSE detector were weighted and combined. The resulting images were in some cases denoised using the fiji embedded mean filter with a small sigma between 0.5 and 2. The contrast of the resulting images were in some cases increased using the CLAHE algorithm (Pizer et al., 1990, 1987). The final processed images are cropped out of useless 0 value pixels and saved for later alignment. All the previous steps are being taken care of using an imageJ script that I designed as a small GUI to select whether or not to perform CLAHE contrast enhancement or Mean filtering for noise reduction. This macro was designed to extract images from stacks and process them one at a time in a way that does not use much computer resources but is time consuming. This choice was made so that the macro can be run on the FIB-SEM 4 Go RAM computer at the end of an acquisition for FIB-SEM users. This script can be found on my github page at https://github.com/VictorHanss/Thesis/tree/main/imageJScripts.

**Alignment.** Rough alignment was performed using the SIFT algorithm (Lowe, 2004) embedded within the ImageJ Version 1.54j 12 June 2024 with java 1.8.0_172 (64 bit) (Schneider et al., 2012). Fine alignments were performed using AMST (Hennies et al., 2020) embedded within MIB (Belevich et al., 2016).

**Segmentation.** The segmentation was performed using deep learning solution DeepSCEM. X stacks of 825x753x50 x,y,z, were manually annotated using the fiji plugin “segmentation editor” and fed inside DeepSCEM for model training using the following parameters : 2D model with U-Net architecture of a kernel size of 3 using 64 initial block filters, 2 block per level and a model depth of 4 levels. 3 different models were trained to segment rough endoplasmic reticulums, mitochondria and endosomes using the following parameters : batch size of 4, patch size of 400 by 400 x-y 125 steps per epoch, 64 Epochs and 64 validations steps per epoch, rotation and flip augmentation activated and a label focus of 95 %. A stack of interest was then fed into DeepSCEM to perform prediction using the 3 previously introduced models. The predicted segmentation is saved as an

hdf5 file embedding the segmentation map as a binary 0 - 1 pixel value image stack and the raw SEM volume images as a 32 bit stack.

**3D Rendering**. The 3D rendering of the segmentation and movie recording with the dynamic super imposition of the SEM volumetric images with the 3D segmentation model was performed using chimerax (version 1.9rc202411111853, 2024-11-11 ; Pettersen et al., 2021). The predicted segmentation hdf5 file is imported within chimerax, the segmentation binary stack is displayed as a surface using a sampling step of 2, a smoothing factor of 1 and 50 iteration using the following command line :

> ***seg surf*** *#model_ID* ***step*** *1* ***smooth*** *true* ***smoothingIterations*** *40* ***smoothingFactor*** *0.9*

A single plane of the SEM stack was displayed at a time with the possibility to browse through the entire volume. The slices are fully opaque, displayed with bit depth of 8 with the contrast adjusted through threshold level points applied to the image histogram as followed :

> ***vol*** *#model_ID* ***region*** *0,0,0,Xmax,Ymax,Zmax* ***step*** *1* ***colorMode*** *auto8* ***imageMode*** *“full region”* ***level*** *0,0* ***level*** *x,y* ***level*** *1,1* ***transparency*** *0*

# Bibliography


Belevich, I., Joensuu, M., Kumar, D., Vihinen, H., Jokitalo, E., 2016. Microscopy Image Browser: A Platform for Segmentation and Analysis of Multidimensional Datasets. PLOS Biol. 14, e1002340. https://doi.org/10.1371/journal.pbio.1002340

Hennies, J., Lleti, J.M.S., Schieber, N.L., Templin, R.M., Steyer, A.M., Schwab, Y., 2020. AMST: Alignment to Median Smoothed Template for Focused Ion Beam Scanning Electron Microscopy Image Stacks. Sci. Rep. 10, 2004. https://doi.org/10.1038/s41598-020-58736-7

Lowe, D.G., 2004. Distinctive Image Features from Scale-Invariant Keypoints. Int. J. Comput. Vis. 60, 91–110. https://doi.org/10.1023/B:VISI.0000029664.99615.94

Pettersen, E.F., Goddard, T.D., Huang, C.C., Meng, E.C., Couch, G.S., Croll, T.I., Morris, J.H., Ferrin, T.E., 2021. UCSF ChimeraX : Structure visualization for researchers, educators, and developers. Protein Sci. 30, 70–82. https://doi.org/10.1002/pro.3943

Pizer, S.M., Amburn, E.P., Austin, J.D., Cromartie, R., Geselowitz, A., Greer, T., Ter Haar Romeny, B., Zimmerman, J.B., Zuiderveld, K., 1987. Adaptive histogram equalization and its variations. Comput. Vis. Graph. Image Process. 39, 355–368. https://doi.org/10.1016/S0734-189X(87)80186-X

Pizer, S.M., Johnston, R.E., Ericksen, J.P., Yankaskas, B.C., Muller, K.E., 1990. Contrast-limited adaptive histogram equalization: speed and effectiveness, in: [1990] Proceedings of the First Conference on Visualization in Biomedical Computing. Presented at the [1990] First Conference on Visualization in Biomedical Computing, IEEE Comput. Soc. Press, Atlanta, GA, USA, pp. 337–345. https://doi.org/10.1109/VBC.1990.109340

Schneider, C.A., Rasband, W.S., Eliceiri, K.W., 2012. NIH Image to ImageJ: 25 years of image analysis. Nat. Methods 9, 671–675. https://doi.org/10.1038/nmeth.2089

**Victor HANSS**

# Sample preparation and method development towards new nanometric probes for cryo electron tomography

## Résumé

La cellule eucaryote est un système compact et hétérogène et dans ce contexte, l'imagerie à haute résolution par cryo-tomographie électronique (cryo-ET) a permis de révéler des aspects structurels macromoléculaires in situ qui ne pouvait être atteint par l'analyse de molécules isolées in vitro. Cependant, dans l'environnement cellulaire encombré, l'identification de biomolécules est une tâche difficile. Pour repérer les molécules individuelles en imagerie à haute résolution, les macromolécules sont ciblées in vivo avec des sondes conjuguées à des nanoparticules d'or.

Nous avons choisi l'ARN polymérase II (pol II) comme cible. La pol II est chargée de transcrire l'information stockée sous forme d'ADN en ARN messager chez les organismes eucaryotes. Aucune image à ce jour n'a permis de visualiser ou de localiser directement la pol II in situ. La détermination de l'organisation des condensats de Pol II et leur interaction avec la chromatine et les machineries d'épissage fournirait des informations essentielles sur la transcription eucaryote. Pol II est une protéine globulaire de taille moyenne, rare en dehors des sites de transcription. Le développement de procédures de marquage avec des sondes nanométriques permettrait d'obtenir sa localisation. Pour atteindre ces objectifs, j'ai abordé les défis techniques suivants :

- Marquage in vivo

- Vitrification complète de la cellule

- Amincissement des cellules pour la cryo-ET

Ces optimisations et procédures ont été intégrées dans un workflow qui m'a permis de visualiser et de localiser les particules d'or des conjugués in situ.

**Mots clés :**

Cryo-tomographie électronique, Cryo-ET, in situ Cryo-ET, Cryo FIB-SEM, CEMOVIS, Immunogold

**Résumé (1000 caractères maximum) et mots clés en anglais / Summary (maximum 1,000 characters) and keywords in English :**


**Summary :**

The eukaryotic cell is a compact, heterogeneous system, and in this context, high-resolution imaging by cryo-electron tomography (cryo-ET) has made it possible to reveal *in situ* macromolecular structural aspects that could not be achieved by single particle analysis *in vitro*. However, in the dense cellular environment, biomolecule identification is a difficult task. To spot individual molecules in high-resolution imaging, macromolecules are targeted *in vivo* with probes conjugated to gold nanoparticles.

We chose RNA polymerase II (pol II) as our target. Pol II is responsible for transcribing information stored as DNA into messenger RNA in eukaryotic organisms. To date, no images have made it possible to directly visualize or localize pol II *in situ*. Determining the organization of Pol II condensates and their interaction with chromatin and splicing machinery would provide essential information on eukaryotic transcription. Pol II is a medium-sized globular protein, rare outside transcription sites. The development of labelling procedures with nanometric probes would make it possible to obtain its localization. To achieve these goals, I tackled the following technical challenges:

In vivo labelling

Complete cell vitrification

Cell thinning for cryo-ET

These optimizations and procedures were integrated into a workflow that enabled me to visualize and localize the conjugate gold particles in situ.



**Keywords :**
Cryo-electron tomography, Cryo-ET, *in situ* Cryo-ET, Cryo FIB-SEM, CEMOVIS, Immunogold